Department of Physical Chemistry

Faculty of Science

PALACKY UNIVERSITY, OLOMOUC

Pyrite type transition metal dichalcogenides for oxygen evolution

Doctoral dissertation

By

Yunpeng Zuo, MSc

Under

Study program: Chemistry, P1417

Field of study: Nanomaterial Chemistry, 1407V023

Supervisor: Ing. Kment Štěpán, PhD.

Olomouc 2022

.

Declaration

I declare that this dissertation entitled “Pyrite type transition metal dichalcogenides for oxygen evolution” is my original work performed during my doctoral study. I further declare that I have a major contribution in the publications [i], [ii], and [iii] listed in the author’s publications, which described in experimental part of the submitted dissertation.

In Olomouc on …10-03-2022… Yunpeng Zuo ……………………………

Acknowledgements

I would like to express my sincere gratitude to my supervisor, Ing. Kment Štěpán, Ph.D. for the professional guidance, inspirational advices and help. Further, I would like to thank to Prof. Radek Zbořil, the head of the laboratory, for the opportunity to work in the Centre of Regional Centre of Advanced Technologies and Materials. I would extend my thanks to everyone who gave me help during my doctoral studies. Last but not least, I would like to thank my family for all their love and support during my whole studies. This work was supported by the Operational Programme Research, Development and Education–European Regional Development Fund, Project no. CZ.02.1.01/0.0/0.0/15_003/0000416 of the Ministry of Education, Youth and Sports of the Czech Republic.

BIBLIOGRAPHICAL IDENTIFICATION

Author's name: Yunpeng Zuo

Title: Pyrite type transition metal dichalcogenides for oxygen evolution

Type of thesis: Ph.D. thesis

Department: Department of Physical Chemistry

Supervisor: Ing. Kment Štěpán, Ph.D.

The Year of Presentation: 2022

Abstract

Electrocatalytic water splitting is a green pathway to produce hydrogen in large quantities, which involves two half reactions: hydrogen evolution reaction (HER) and oxygen evolution reaction (OER). OER is the kinetic bottleneck of water splitting, which requires a high standard overpotential with the four–electron–proton–coupled processes, thus it is particularly important to develop OER catalysts. Pyrite–type transition metal dichalcogenides (MX_2, where M = Fe, Co, Ni et al., and X = S or Se) have been promising electrocatalytic materials for the OER, but the catalysts still require further improvement due to the easy oxidization of surface atoms and the intrinsically low activity.

Ongoing research found that multimetallic compounds generally have better water splitting activity than single metal compounds. Furthermore, boron–doping can effectively optimize the adsorption energy of OER intermediates. The present thesis is focused on developing boron doping advanced multimetal pyrite–type transition metal dichalcogenides (PT–TMDs) for boosted OER. Herein, we synthesized the FeCoNiBS *in situ* coated by amorphous $FeCoNiB_x$ and fabricated heteroepitaxial pyrite Ni–selenide through dual–cation substitution and boron doping as the efficient and durable heterogeneous catalysts for OER. The spherical aberration–corrected transmission electron microscopy clearly shows that the obtained sulfides exhibit different phases with an approximately 2 nm amorphous layer on the external surface. This hybrid catalyst exhibits superior OER activity with an attractive overpotential of 419.4 mV vs. RHE at 100 mA cm^{-2} in 1 M KOH solution and excellent stability over 10 h. The fabricated Ni–pyrite selenides showed a special crystalline−amorphous structure. After dual–cation substitution and boron doping, the overpotential improved from 543 mV to 279.8 mV at 10 mA cm^{-2} with Tafel slope from 161 to 59.5 mV dec^{-1}.

Within the framework of this thesis, we focused on building efficient catalysts for OER. The cations and boron doping can modulate the intrinsic electronic structure of pyrite–type sulfide/selenide for highly active OER performance. The discoveries underscore the importance of modulating OER property by using multiple elements, which provides an advantageous method for engineering the electrical structure of pyrite–type sulfide/selenide for superior OER catalysis, as well as general guidance on the minimization of activity loss with valence engineering.

Keywords: OER, pyrite–type TMDs, boron doping, amorphous, valence engineering, spatially confined, theoretical calculations

Number of Pages/Appendices: 115/V

Language: English

BIBLIOGRAFICKÉ IDENTIFIKACE

Jméno: Yunpeng Zuo

Název práce: Dichalkogenidy přechodných kovů pyritového typu pro vývoj kyslíku

Typ práce: Disertační práce

Katedra: Katedra fyzikální chemie

Školitel: Ing. Kment Štěpán, Ph.D.

Rok obhajoby: 2022

Abstrakt

Elektrokatalytické štěpení vody je zelená cesta k produkci vodíku ve velkých množstvích, která zahrnuje dvě poloviční reakce: reakci evoluce vodíku (HER) a reakci evoluce kyslíku (OER). OER je kinetickým úzkým hrdlem štěpení vody, které vyžaduje vysoký standardní nadpotenciál u procesů spojených se čtyřmi elektrony a protony, a proto je zvláště důležité vyvinout katalyzátory OER. Dichalkogenidy přechodných kovů pyritového typu (MX_2, kde M = Fe, Co, Ni a kol. a X = S nebo Se) byly slibnými elektrokatalytickými materiály pro OER, ale katalyzátory stále vyžadují další vylepšení kvůli snadné oxidaci povrchových atomů a skutečně nízké aktivitě.

Probíhající výzkum zjistil, že multikovové sloučeniny mají obecně lepší schopnost štěpit vodu než jednotlivé kovové sloučeniny. Kromě toho může dopování borem účinně optimalizovat adsorpční energii meziproduktů OER. Tato práce je zaměřena na vývoj pokročilých dichalkogenidů přechodných kovů (PT–TMD) s dopováním borem pro zesílené OER. Zde jsme syntetizovali FeCoNiBS *in situ* potažený amorfním $FeCoNiB_x$ a vyrobili jsme heteroepitaxní pyrit Ni–selenid prostřednictvím substituce dvou kationtů a dopování borem jako účinné a odolné heterogenní katalyzátory pro OER. Transmisní elektronová mikroskopie s korekcí sférické aberace jasně ukazuje, že získané sulfidy vykazují různé fáze s přibližně 2 nm amorfní vrstvou na vnějším povrchu. Tento hybridní katalyzátor vykazuje vynikající OER aktivitu s atraktivním nadměrným potenciálem 419,4 mV vs. RHE při 100 mA cm^{-2} v 1 M roztoku KOH a vynikající stabilitou po dobu 10 hodin. Vyrobené selenidy Ni–pyritu vykazovaly speciální krystalicko–amorfní strukturu. Po dvoukationtové substituci a dopování borem se nadměrný potenciál zlepšil z 543 mV na 279,8 mV při 10 mA cm^{-2} s Tafelovou strmostí ze 161 na 59,5 mV dec^{-1}.

V rámci této práce jsme se zaměřili na vybudování účinných katalyzátorů pro OER. Kationty a dopování borem mohou modulovat vnitřní elektronickou strukturu sulfidu/selenidu pyritového typu pro vysoce aktivní výkon OER. Tyto objevy podtrhují důležitost modulace vlastnosti OER pomocí více prvků, což poskytuje výhodnou metodu pro inženýrství elektrické struktury sulfidu/selenidu pyritového typu pro vynikající katalýzu OER, stejně jako obecný návod na minimalizaci ztráty aktivity pomocí valenčního inženýrství.

Klíčová slova: OER, TMD pyritového typu, doping borem, amorfní, valenční inženýrství, prostorově omezené, teoretické výpočty

Počet stran/příloh: 115/V

Jazyk: Anglický

CONTENT

1. Introduction

Environmental problems based on the combustion of fossil fuel are the great challenges for the sustainable development of society that humans have to face for the next decades.[1,2] Developing a green pathway to replace fossil fuel and reducing the hazardous gases emission can effectively improve the existing problems.[3,4] Although the development and application of renewable energy, such as wind, tidal, solar, has been stimulating for a long time, the low energy delivery efficiency limited the large–scale application of sustainable energy.[5–8] Apart from the development of advanced energy conversion devices, converting renewable energy into chemical energy will be more conducive to the commercial application of sustainable energy. As the typical green energy source with the highest gravimetric energy, hydrogen is the ideal sustainable gas to replace fossil fuels in various industries.[9,10] Currently, electrocatalytic water splitting is an implementable method for hydrogen generation, and this electrolytic process has been widely studied that contains two half–reactions oxygen evolution reaction (OER) and hydrogen evolution reaction (HER).[11–13] Concerning HER and OER, the OER process undergoes four–electron−proton to form one O_2 molecular, which requires a large overpotential ($\eta \approx 1.23$ V vs standard reduction potential) for the whole water−splitting reaction. Thus, the OER is regarded as the rate–limiting step of electrocatalytic water splitting, compared to HER. Based on this mentioned reason, enormous studies devoted to the development of highly effective OER catalysts to relieve the sluggish kinetics and increase the energy conversion efficiency.[14,15] However, at present, the water−splitting reaction, especially the OER, still suffers from low efficiency and insufficient stability to meet the requirement of the practical application. So it is particularly important to develop highly active HER/OER catalysts.[16, 17]

A large number of researchers discovered the pH of the electrolyte is strongly related to the mechanism of OER. In an acidic solution, OER proceeds in four steps shown in the equations.[18,19] In an acidic environment, H_2O will form OH^* on the surface of the active sites (Equation 1), then further interact with water molecules to produce O^* and OOH^* intermediates (Equation 2 or Equation 3).[20,21] Different from the acid solution, OH^* will generate from the OH^- instead of H_2O in an alkaline environment (Equation 5–7).[22] Finally the oxygen gas will generate based on the OOH^* intermediates (Equation 4 and 8). It is worth noting that the $OH^* \rightarrow O^*$ and $O^* \rightarrow OOH^*$ processes are the rate–limiting steps with a higher energy barrier value of 3.2 eV.[20,21] Thus, if the catalysts can effectively reduce the energy barrier of these steps, they will be the advantageous candidates for the superior OER. To date, most of the commercial catalysts of OER are noble metal oxides (e.g., IrO_2, RuO_2), possessing small reserves, high cost, and challenging large–scale application.[20, 23]

In an acidic system,

$2H_2O \rightarrow OH^* + H_2O + H^+ + e^-$ (1)

$OH^* + H_2O \rightarrow O^* + H^+ + H_2O + e^-$ (2)

$O^* + H_2O \rightarrow OOH^* + H^+ + e^-$ (3)

$OOH^* \rightarrow O_2 + H^+ + e^-$ (4)

In an alkaline system,

$4OH^- \rightarrow OH^* + 3OH^- + e^-$ (1)

$OH^* + 3OH^- \rightarrow O^* + 2OH^- + H_2O + e^-$ (2)

$O^* + 2OH^- + H_2O \rightarrow OOH^* + OH^- + H_2O + e^-$ (3)

$OOH^* + OH^- + H_2O \rightarrow O_2 + 2H_2O + e^-$ (4)

* denotes the surface adsorption sites

Pyrite–type transition metal dichalcogenides (PT–TMDs) have emerged as one of the most valuable candidates for the highly effective OER catalysts.[24,25] It is worth noting that the PT–TMDs nanomaterials have special physical properties covered from conductor, semiconductor, and insulator, with a wide range of applications.[26,27,28] The PT–TMDs display a crystal system of isometric with the octahedral coordination which contains cations and dianion units.[25, 29] The intrinsic electronic configuration of the PT–TMDs nanocatalysts are favorable for the OER application, but the catalytic performance still suffers from the unstable surface composition (easy to be oxidized) and sluggish charge transfer.[30,31]

Valence engineering has been adopted as the regular strategy and easily implemented approach to alleviating the shortcomings. Especially, the 3d heteroatoms doping or alloying in the PT–TMDs can effectively modify its electronic modulation to be suitable for the OER process.[32–33] Considerable polymetal pyrites were developed as substantial materials during the past decades for the enhanced OER catalysts relative to the monometal sulfides.[34–36] As the most common PT–TMDs, the pyrite sulfides, and selenides with 3d transition metal atoms doping have been widely reported in OER application. V–doped pyrite NiS_2 nanosheets have been synthesized by the simple chemical method, and the physical property of this material changed from representative semiconductor to conductive material, which exhibited superior OER performance.[37] Similarly, the Fe–dopant mediated novel pyrite NiS_2 mesocrystals presented a boosted OER activity with an overpotential from 351 mV to 252 mV vs. RHE at 10 $mAcm^{-2}$ in alkaline solution.[38]

Additionally, non–metallic atom doping in the PT–TMDs can attract the electrons of the metal sites in the material, forming the high valence sites which would facilitate the adsorption of O–containing intermediates, thus improving catalytic activity.[39,40] Moreover, the structural stability of the PT–TMDs could be further modified by coating a carbon layer or amorphous membrane.[41,42] It had discovered the B–doping in the PT–TMDs significantly changed the d orbital electronic configuration of the transition metals science the electronic hybridized between the metal d orbitals and B 2p orbitals, resulting in the delocalization of the electrons on active sites.[43] This special electronic configuration was beneficial for OER process, especially the intermediate steps. As another big challenge, the dissolution of surface cations and oxidation of external species of PT–TMDs during the OER seriously affect the structural stability of the material. So it is very important to develop some methods or strategies to fabricate a stable surface structure for remarkable catalytic durability. Coating the PT–TMDs with the conductive active layers, such as amorphous borides and carbon membrane, could effectively prevent the ripening or aggregation of the material, and finally enhance the stability and activity of PT–TMDs. Tingting Li et al. successfully prepared the Co_3O_4 nanoneedle arrays supported on the Ni foam (NF@Co_3O_4).[44] Next, the NF@Co_3O_4 was covered by the Ni–B membrane to generate core–shell hybrid. Benefiting from the special interface interaction, NF@Co_3O_4@NiB presented excellent electrochemical performance. In addition, Jingwei Chen and co–workers synthesized the Co_xFe_yS@C compound with a thin carbon layer on the surface based on the prussian blue precursor.[41] The coated carbon layer effectively promotes the energy storage capacity of the Co_xFe_yS@C material. Thus developing more appropriate synthesis approaches for novel PT–TMDs could effectively expand the application in electrocatalysis.

2. Literature overview

2.1 The structure of the pyrite–type transition metal dichalcogenides (PT–TMDs)

PT–TMDs are an interesting group of materials towards HER and OER with low–cost, adjustable electronic configuration, and rich component combination.[45–49] The class members in PT–TMDs are widely distributed in the earth's crust, covering from semiconductors to metallic compounds, which can act as a promising catalyst for OER. Typical PT–TMDs phase contains many kinds of materials with the formulation of $M^{2+}(X_2)^{2-}$ type.[50] The metal elements include Mn, Fe, Co, Ni, Cu, Zn, Ru, Rh, Pd, Cd, Os, and Ir (purple area in **Figure 1**), while the anions are S, Se, and Te located on the pink area of the periodic table in **Figure 1**. Notably, part of the TMDs consisting of the same elements in the selected region that can present 2D arrangement type except for pyrite structure. For this thesis, we only focused on sulfides and selenides (X=S, Se, cyan–blue area).

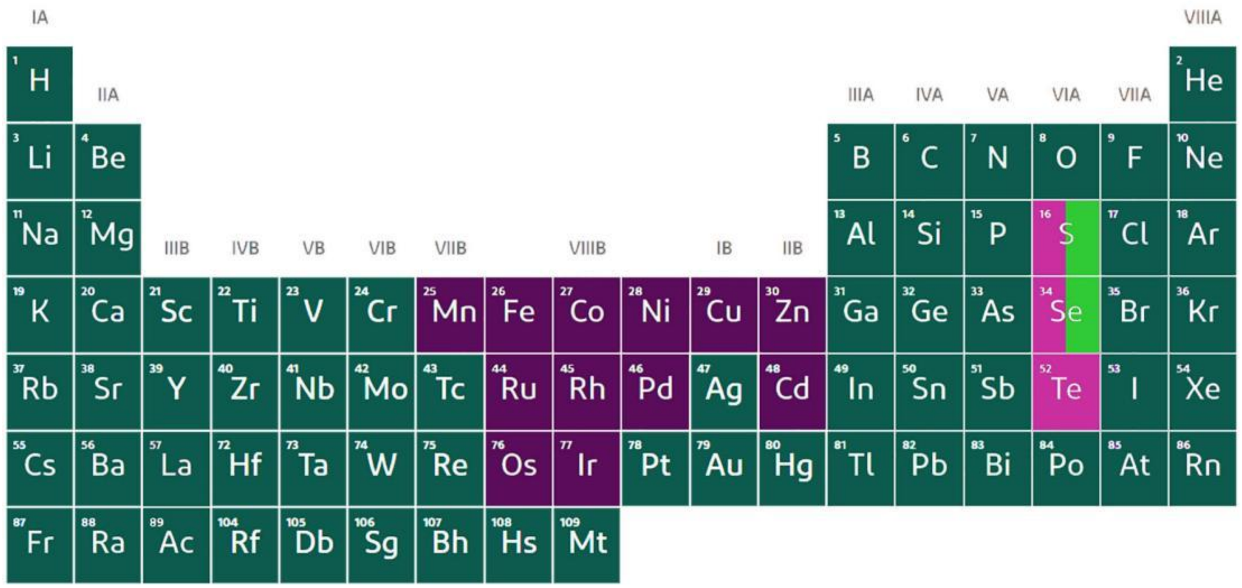

Figure 1: Classification of the PT–TMDs showing the cations (purple area) and anions (pink area) under the formulation of $M^{2+}(X_2)^{2-}$ type.

The PT–TMDs phases have been widely studied in the past decades with the formulation of $M^{2+}(X_2)^{2-}$, showing the cations occurring in octahedral coordination. The properties of the PT–TMDs cover from insulators, semiconductors, metals to superconductivity.[25] In recent years, there were plenty researches focused on the morphologies and components of high–efficiency PT–TMDs electrocatalysts, which greatly expands the range of PT–TMDs catalysts and their applications.[51–54] The electronic structures of PT–TMDs are strongly depend on the electrons distributed in *d* orbitals, which can be controlled by the doping of metal atoms or non–metal elements.[32–33] Pyrite–type transition metal sulfides/selenides including monometallic and multimetallic compounds have been identified as two promising low–cost OER catalysts based on the reported materials.

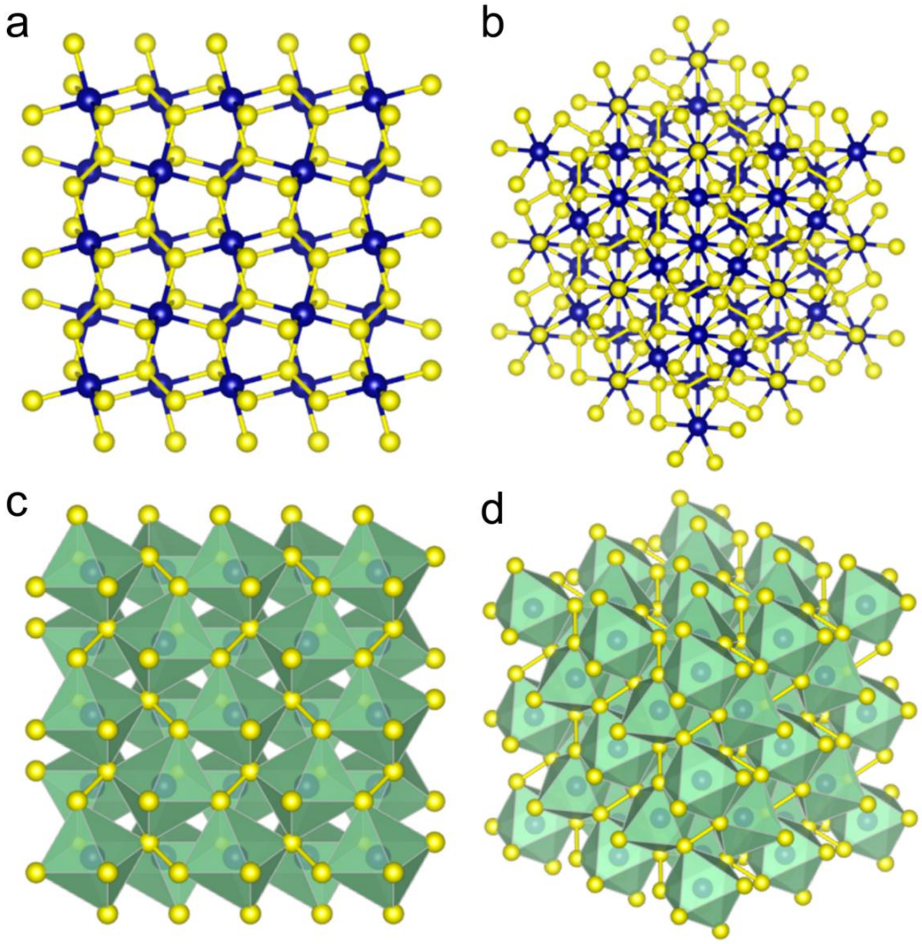

Figure 2: (a–d) Typical crystal structure of PT–TMDs. The blue ball represents metal elements while the yellow ball is S or Se.

Conventional pathways to obtain high–quality pyrite–phase sulfides and selenides materials in nanoscale commonly need high temperature, high pressure, or long reaction. Currently, the rapid development of the hydro– and solvothermal reactions successfully accelerated the low temperature synthesis technique for pyrite–phase sulfides and selenides.[25] The size, dimensional and morphological can be regulated to diversity at the low temperature under 200 ℃ in a closed reaction system. Importantly, various ingenious synthesis methods have been developed to synthesize pyrite–phase sulfides and selenides of different shapes and sizes, as well as the complex catalytic interface structure, for achieving satisfying water–splitting catalytic performance.[54,55] However, the development of commercial–grade OER/HER catalysts still needs to be accelerated to meet the commercial application requirements. It will be meaningful to develop the novel technical routes and synthetic pathways to promote the commercialization process, thereby reducing dependence on traditional fossil energy and reducing hazardous gas emissions, thereby further improving the environment.

2.2 Synthesis of pyrite–type transition metal sulfides (PT–TMS)

Sulfides are widely distributed in nature with controllable costs, driving it can be applied to commercial fields on a large scale. Establishing new technologies and methods to synthesize nano–level PT–TMSs will play a decisive role to resolve the dilemma. The most common metal sulfides cover monometallic sulfides, polymetallic sulfides, and non–metal doping sulfides. Two common synthesis approaches, a hydrothermal reaction in the high–pressure reactor and a sulfurization reaction in a tube furnace, have been identified as the main feasible options. In this thesis, we will investigate the recent progress in developing these PT–TMSs from different methods, techniques, and precursors. Systematically discuss their appealing properties and related water splitting activity (OER and HER) in acidic or alkaline solutions. We then speculate on some future development opportunities of PT–TMSs.

2. 2. 1 Synthesis of monometallic PT–TMSs

Particularly, three basic monometallic sulfides (NiS_2, CoS_2, FeS_2) have attracted extensive attention in electrocatalytic water splitting, batteries, supercapacitors, optical fields, due to the relatively easy to prepare, low cost, and good intrinsic properties.[48,56,57] Each monometallic sulfide contains many different species of compounds. For example, the nickel sulfides have four compounds with different compositions, including NiS_2 (pyrite), Ni_3S_2 (heazlewoodite), Ni_3S_4 (polydymite), and NiS (millerite).[48,56] All the phases have been investigated as OER catalysts, but the pyrite–type nickel sulfides are relatively easy to synthesize by the common synthetic methods, such as gas–phase sulfuration, hydrothermal and electrochemical methods.[48] An interesting solution–based approach was investigated by Wendi Xiang and co–workers through a facile solvothermal strategy.[56] The $Ni(CH_3COO)_2 \cdot 4H_2O$ and sulfur were added into the mixture of N, N–Dimethylformamide (DMF), and ethanol solution. After vigorous stirring, the mixture was transferred to the Teflon reactor and reacted under 180 ℃ for 12h. The solution–based method to synthesize pyrite–type NiS_2 microspheres were shown in Scheme 1. The prepared NiS_2 microspheres had an average diameter of 1.6 μm based on the SEM results (see Figure 3a), which displays a remarkable OER activity with an overpotential of 311 mV under 10 $mAcm^{-2}$ in 1M KOH.[56]

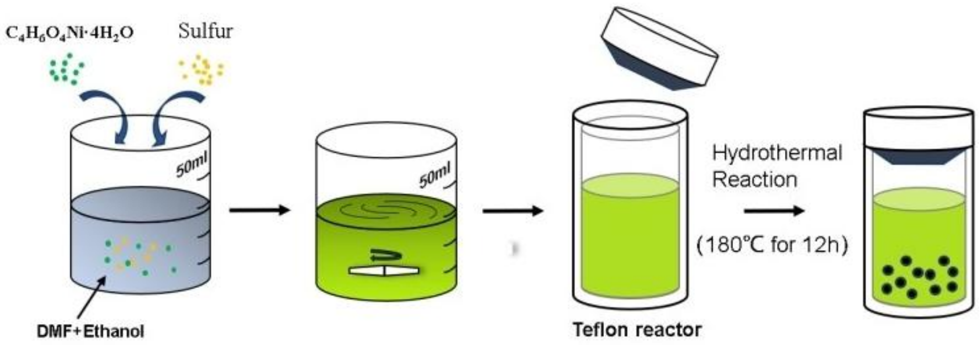

Scheme 1. The preparation process of NiS_2 microsphere. Taken from Ref. 56 and modified.

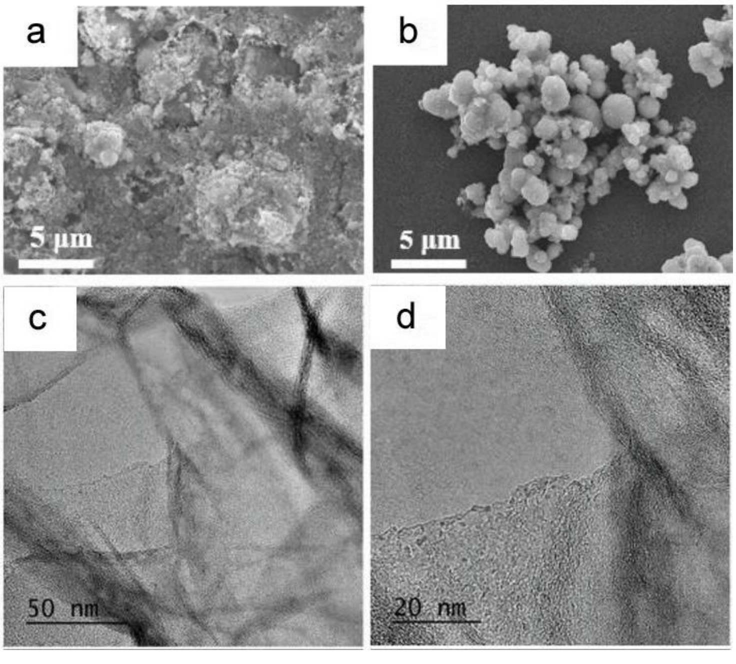

Figure 3. (a, b) SEM images of the NiS_2 microspheres with different reaction time of 1 h and 3h.[56] (c, d) Enlarged TEM images of NGO/Ni_7S_6.[57] Taken from Ref. 56, 57 and modified.

Kolleboyina Jayaramulu et al. prepared porous N–doped graphene oxide/nickel sulfide sheets (NGO/Ni_7S_6) used metal–organic framework (MOF) as a template.[57] The nickel–based metal–organic framework (NiMOF–74) comprised of Ni(II) and 2,5–dihydroxyterephthalate (DHT) was mixed with nitrogen–doped graphene oxide (NGO) as depicted in Scheme 2. The mixture was added into a Teflon bottle together with thiourea and heated to 200 °C for 24 h. After *in situ* sulfurations, NGO/Ni_7S_6 sheets were successfully prepared with the highly dispersed layer structure. (Figure 3c,d) The electrocatalytic performance of NGO/Ni_7S_6, tested in 0.1 M KOH solution, and as expected, the NGO/Ni_7S_6 sheets showed remarkable OER activity than commercial RuO_2, with a smaller overpotential (380 mV) than RuO_2 (390 mV).[57] The special MOF precursor offered the porous hollow structure for the NGO/Ni_7S_6 that was beneficial for enhancing the intrinsic OER activity. Those results indicate the loading catalysts on layer substrate could effectively promote its dispersion and fully expose its active sites. Moreover, the hybrid materials riched organic molecular chains in the structure can usually bring many porous units after high temperature treatment, revealing a valuable approach to build specified catalysts for water splitting. Compared to nickel sulfide described above, many other nickel sulfides are suitable for OER. Yang et al. synthesized the Ni_9S_8, Ni_9S_8–$NiS_{1.03}$ alloy, and $NiS_{1.03}$ by changing the sulfidation process. They found the OER performance of the three catalysts gradually improved with the increase of high–valence Ni species.[58] The $NiS_{1.03}$ exhibited an overpotential ~270 mV at 10 $mAcm^{-2}$, significantly lower than that of Ni_9S_8 (~310 mV), Ni_9S_8–$NiS_{1.03}$ (~290 mV), and RuO_2 (~320 mV).[58]

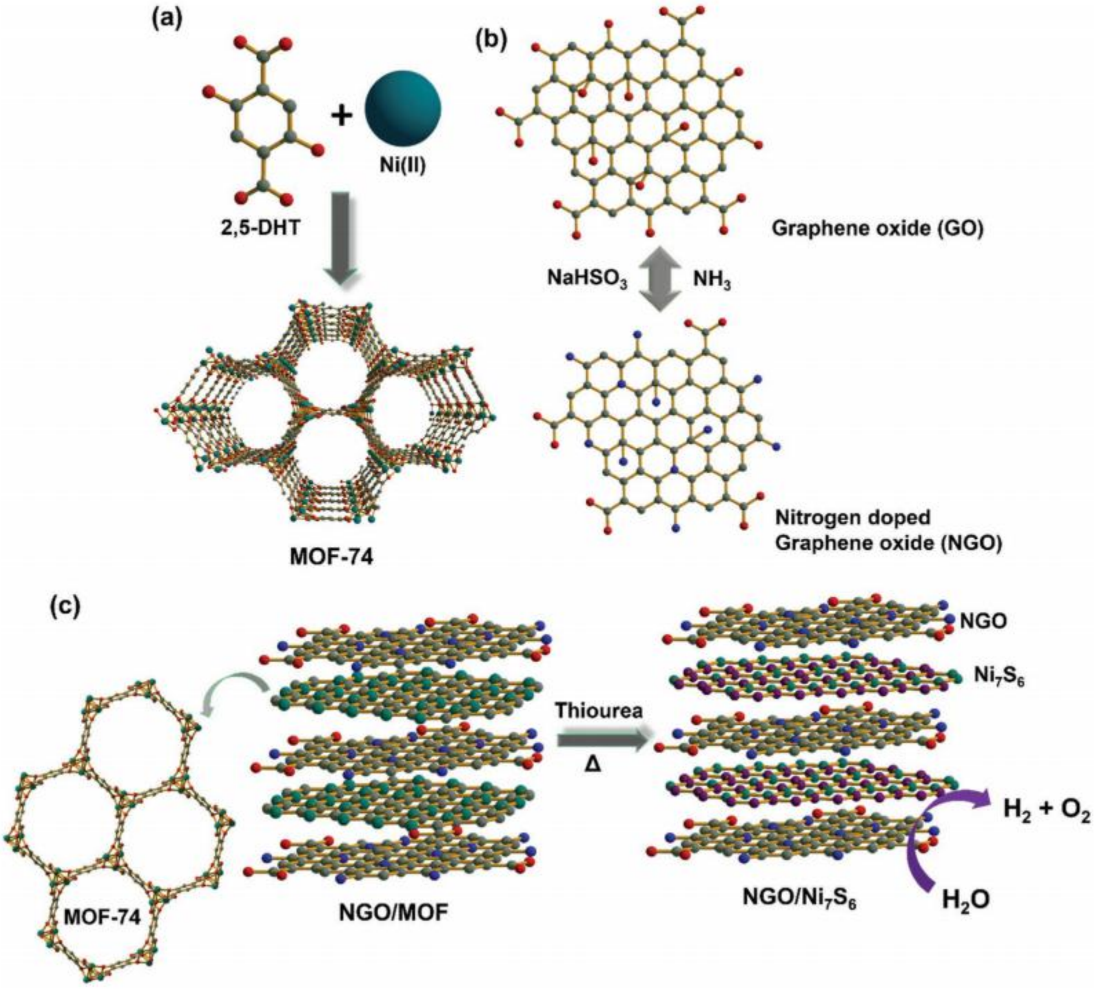

Scheme 2. Illustration of the prepare process of (a) MOF–74, (b) NGO and (c) NGO/Ni_7S_6. Taken from Ref. 58 and modified.

Apart from the single component nickel sulfide, Jingjing Wang et al. developed hollow Ni_3S_2/NiS nanoparticles coated by MOF.[48] The Ni_3S_2/NiS core was made by the regulated sulfuration of colloidal Ni particles. Notably, the Ni_3S_2/NiS could serve as Ni precursor which would react with terephthalic acid, thus finally *in situ* generating a thin Ni–MOF layer on the surface of the hollow Ni_3S_2/NiS nanoparticles. (see **Scheme 3**)[48] This heterogeneous nanostructure served as superior OER catalysts with a small overpotential of 298 mV under the current density of 10 mA·cm^{-2}.[48] This result suggests that there may be abundant Ni^{n+} ion or high–valent Ni species on the surface composition of the obtained materials, which may become active sites for the OER or other electrocatalytic application.

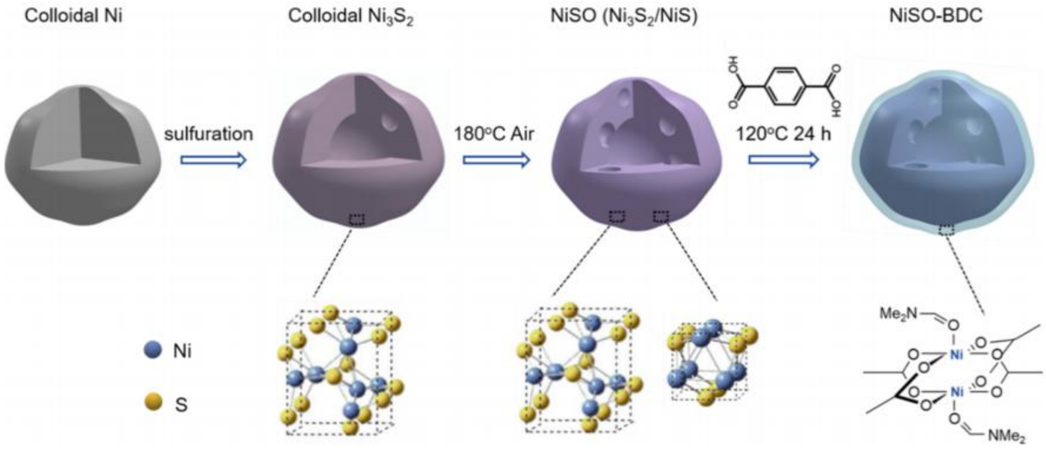

Scheme 3. Preparation process of hollow Ni_3S_2/NiS nanoparticles coated by Ni–MOF. Taken from Ref. 48 and modified.

Xiangkai Shi and co–workers studied the valence state of external Ni elements in the pyrite–type NiS_2 catalysts.[59] They adopted one–step hydrothermal approach to synthesize nickel sulfide nanospheres evolved from the nanosheets. A series of nickel sulfides (NiS, Ni_3S_4 and NiS_2) were fabricated with similar morphology and size.[59] The three kinds of nickel sulfides had different structures including hexagonal, cubic, and pyrite phases as shown in Figure 4.[59] The X–ray photoelectron spectroscopy (XPS) results of these catalysts indicated the pyrite–type NiS_2 contained the highest Ni^{3+} content, due to the adsorbed oxygen. Simultaneously, the NiS_2 presented advantageous OER activity with an ultra–low overpotential of 241 mV at 10 mAcm^{-2} in 1M KOH solution, which was significantly lower than those of NiS (322 mV), Ni_3S_4 (270 mV), and commercial RuO_2 catalyst (310 mV).[59] The author further assembled an overall water–splitting device that used the prepared NiS_2 as both the anode and cathode catalysts (NiS_2 + NiS_2) compared to the combination of the commercial catalyst (Pt/C + RuO_2) in the 1M KOH solution with a scan rate of 5 mV/s.[59] The required potential for this overall water–splitting device is 1.66 V at 10 mAcm^{-2}, approximately 30 mV lower than that of Pt/C and RuO_2 combination (1.69 V).[59] Moreover, the device kept only a 4.8% drop of the current during the chronopotentiometry stability test under 10 mAcm^{-2} for 37 h, much better than Pt/C + RuO_2, revealing the considerable durability of NiS_2 + NiS_2 catalysts in the overall water–splitting application.[59] Density functional theory (DFT) investigated that the octahedrally coordinated Ni^{3+}–S_6 center in the pyrite–type NiS_2 could optimize the reaction between the active site and OH* intermediates, thus reducing the activation energy of the OER and accelerating the slow kinetics.[59] Among these catalysts, the surface morphology also played an important factor for the final catalytic activity, by increasing the reaction between the exposed active sites and catalytic intermediates.

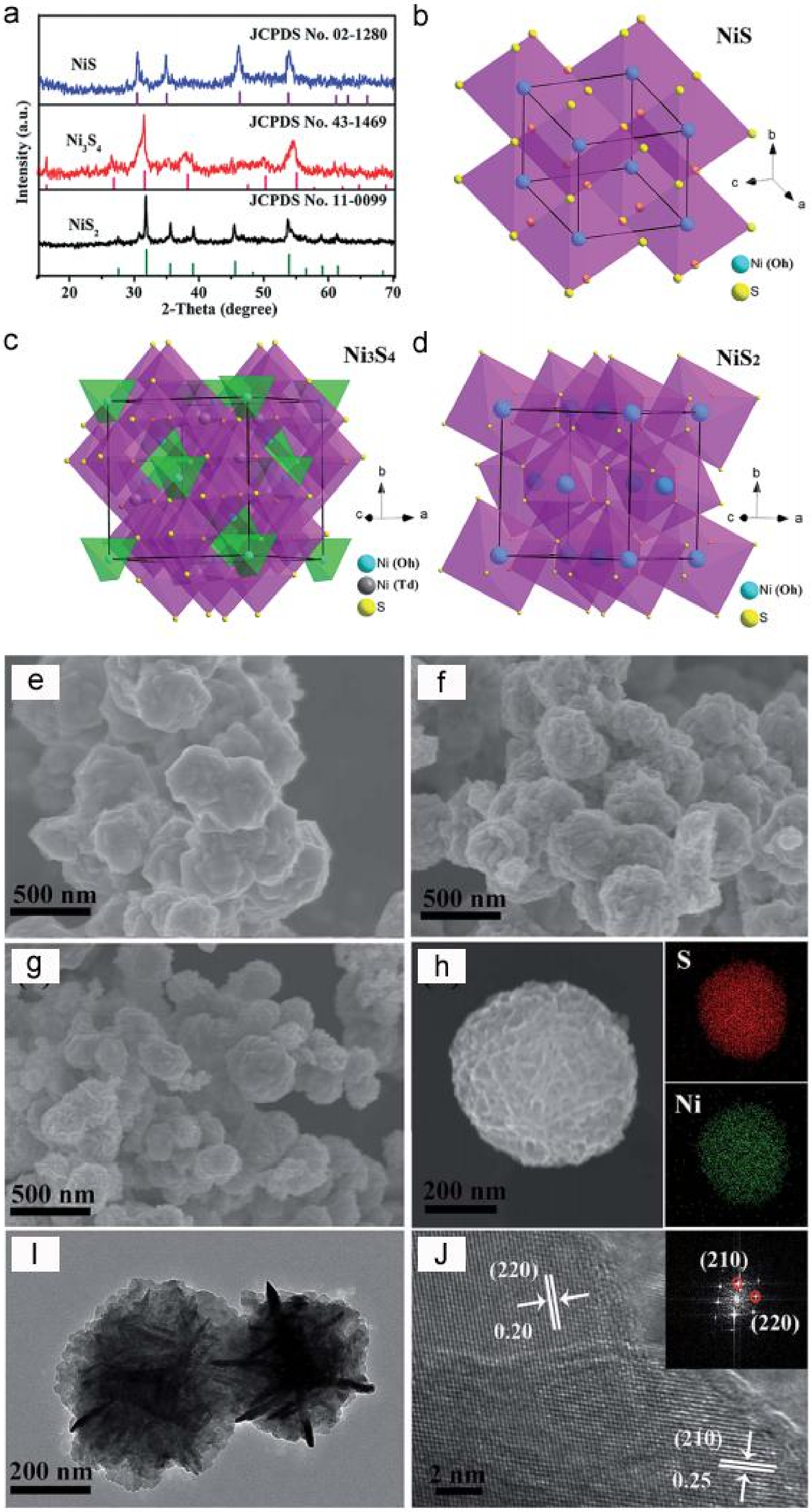

Figure 4. (a) The XRD and (b, c, d) Different crystal structures of NiS, Ni_3S_4, and NiS_2. (e–g) SEM images of NiS, Ni_3S_4, and NiS_2. (h) SEM–EDS Elemental mapping. (I, J) HRTEM images of NiS_2. Taken from Ref. 59 and modified.

Apart from nickel sulfides, pyrite iron sulfide (FeS_x) and cobalt sulfide (CoS_x) also can offer big capabilities for the application of electrocatalytic water splitting. Similar to Ni sulfides, extensive research focused on the morphology and composition of the FeS_x and CoS_x. Matias Villalba et al. reported a further strategy to design pyrite FeS_2 nanoparticles for pH dependence on water splitting.[60] The $FeCl_3$ and thiourea were dissolved in 1,2–propanediol solution. Then the mixture was heated to 180 ℃ and reacted for 12 h, finally, the FeS_2 nanoparticles were obtained with micron–level size. The monometallic pyrite FeS_2 nanoparticles demonstrated big potential for HER under the broad pH range.[60] Because of the large specific surface area, the nanocatalyst is easier to agglomerate, resulting in an underutilized activity. Improving the dispersion of nanocatalysts also helps to exploit their activity during catalysis. Inspired by this, Kefeng Pan et al. synthesized porous FeS_2/C based on FeS_2–ethylenediamine nanowires in two steps. (**Scheme 4**) They put all the reactants ($FeCl_2$ and sulfur powder) in the stainless steel autoclave and reacted at high temperature to generate FeS_2–ethylenediamine nanocomposites.[61] After pyrolysis treatment, FeS_2/C nanowires owned a porous chain–like morphology were obtained.

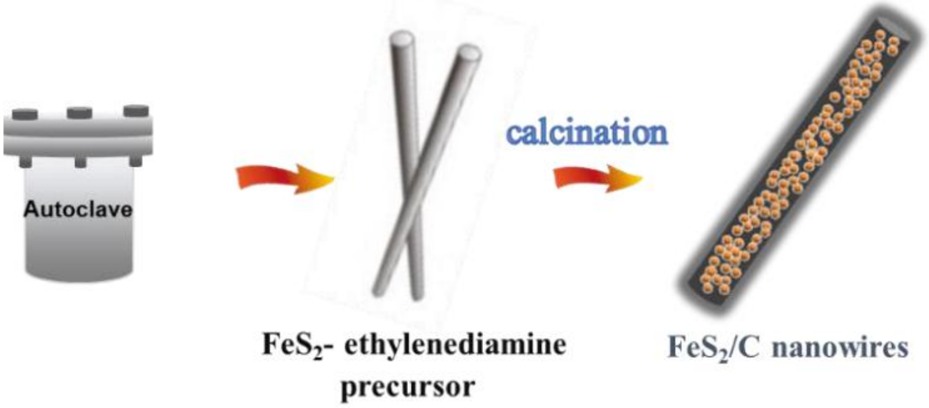

Scheme 4. Synthetic mechanism diagram of FeS_2/C nanowires. Taken from Ref. 61 and modified.

The porous chain–like FeS_2/C nanowires showed a diameter around 100 nm and a length in a micrometer scale (**Figure 5**).[61] Typically, the one–dimensional porous structure is conducive to the electrocatalytic application of materials, due to the large surface area and stable structure.

Especially, the initial FeS_2/C showed a worse OER performance than commercial IrO_2 tested in the KOH solution.[61] However, the OER activity of FeS_2/C dramatically increased to a high level after the activation of cyclings. The activated FeS_2/C catalyst delivered the overpotential of 291 mV and 338 mV under 10 mA/cm^{-2} and 50 mA/cm^{-2} in 1 M KOH for OER, respectively, which were significantly better than IrO_2.[61] Such a special reaction mechanism would greatly promote the development of highly active OER catalysts based on the PT–TMSs.

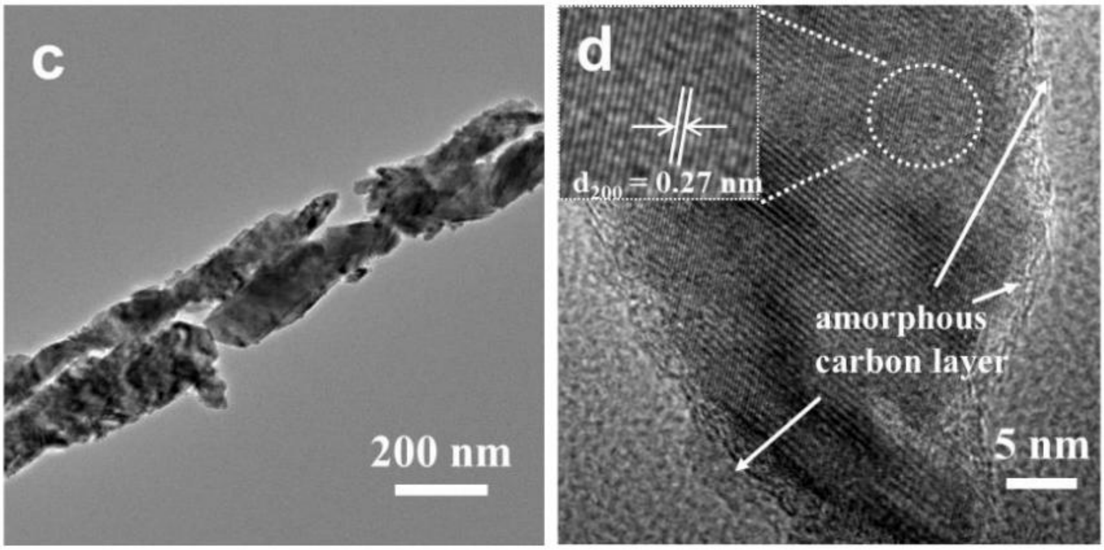

Figure 5 (a) TEM and (b) HRTEM images of prepared FeS_2/C nanowires. Taken from Ref. 61 and modified.

Another common type of sulfide, CoS_x also received numerous investigations. Ruijie Lin et al. fabricated hierarchical cobalt sulfide that the vertical Co_9S_8 nanosheets grew on horizontal $Co_{1-x}S$ nanoplates as shown in Figure 6.[62] There were many Co_9S_8 nanoflakes with an approximate diameter of ~70 nm scattered on the 2D $Co_{1-x}S$ substrate to form a hierarchical structure, which could effectively relieve the decrease of activity caused by the aggregation.[62] Moreover, the unique heterogeneous combination offered the structural stability of CoS_x–Co_9S_8. The obtained nanocomposite displayed the enhanced OER activity with only 275 mV overpotential at 10 mAcm^{-2}, much better than the overpotential of commercial RuO_2 (389 mV), due to the abundant exposed–edge active sites in this hierarchical structure.[62] Especially, the Tafel slope of CoS_x–Co_9S_8 was 30 mV/decade, much smaller than it of commercial RuO_2 (80 mV/decade), suggesting the fast OER kinetic reaction of CoS_x–Co_9S_8. It's worth noting that there were a larger number of defect sites in the CoS_x–Co_9S_8, as the hierarchical structure contains abundant edge atoms.[62]

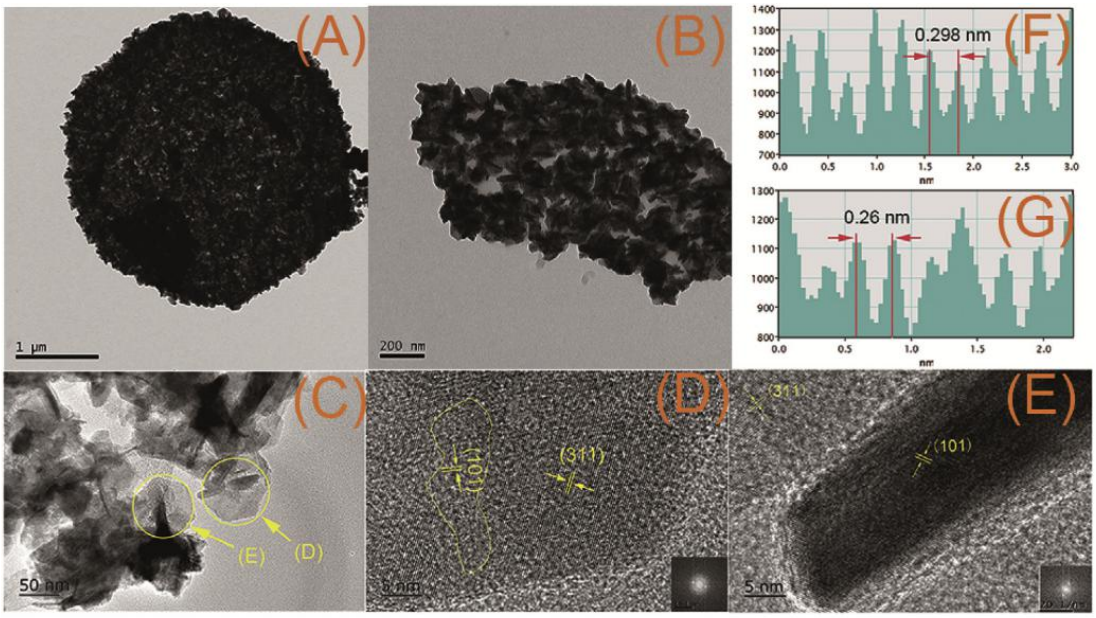

Figure 6. (A–E) The TEM images of the hierarchical cobalt sulfides. (E, F) The plane profile plot of the (311) and (101) facets. Taken from Ref. 62 and modified.

Besides, the CoS_x had an abundant redox pathway, driving various components of CoS_x to be applied in OER. Xiaoya Ma et al. synthesized Co_9S_8, Co_3S_4, and CoS_2 porous architecture through the simple hydrothermal approach using CS_2 as a template.[63] By changing the ratio of the sulfur and cobalt sources, different compositions of CoS_x formed in similar hollow nanospheres. Interestingly, as the proportion of sulfur sources increased, the products obtained gradually evolved from Co_9S_8 to Co_3S_4 and finally to CoS_2. The detailed synthesis process was shown in schematic 5.[63] Compared to the hollow Co_9S_8 spheres, the porous Co_3S_4 and CoS_2 owned larger surface area and rougher interface, which might be caused by the change of water/oil system. For the pyrite type CoS_x materials, the Co ions in the crystallographic structures were displayed in the form of CoS_6 octahedra. (Schematic 5b)[63] As reported by previous research, the special coordinated Co^{n+} in the CoS_x leads to excellent intrinsic OER performance.[63] Among all the Co^{n+} sites, the octahedrally coordinated Co^{n+} presents the better OER activity than tetrahedrally coordinated Co^{2+}, and more eminently, CoS_2 had the largest proportion of octahedrally coordinated Co^{n+} sites compared to Co_3S_4, Co_9S_8, CoS_4 and CoS_6 samples.[63] Veritably, the prepared CoS_2 achieved an overpotential of 290 mV at 10 mA cm–2, much lower than those of Co_9S_8 (342 mV), Co_3S_4 (307 mV) and commercial RuO_2 (295 mV).[63]

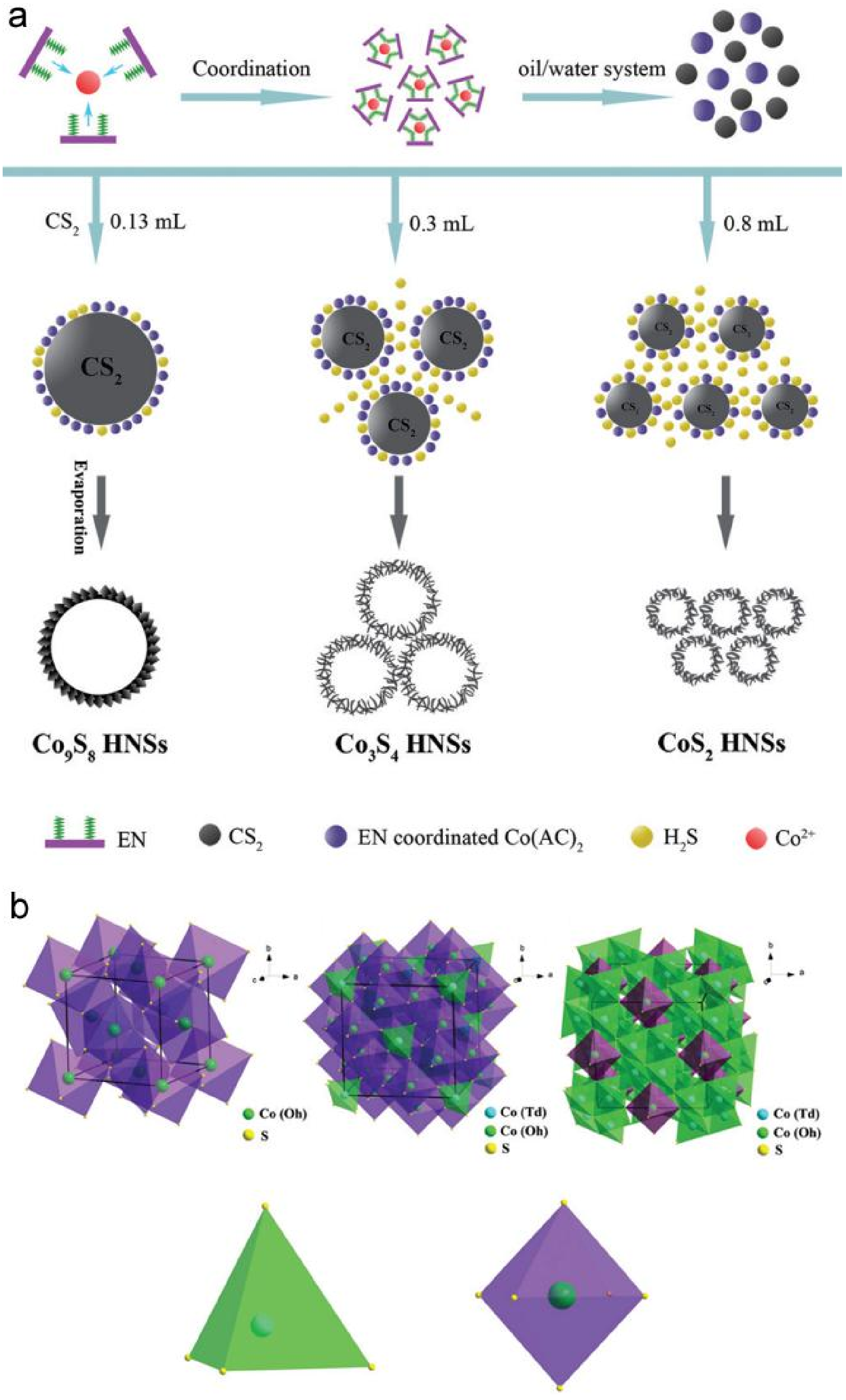

Schematic 5. (a) Synthetic procedures for Co_9S_8, Co_3S_4, and CoS_2 nanospheres, respectively. (b) Crystal structures of CoS_2, Co_3S_4, Co_9S_8, CoS_4, and CoS_6. Taken from Ref. 63 and modified.

To further make utilization of the CoS_2, one of the most effective ways is to disperse CoS_2 on the substrate to ensure sufficient contact between the material and the electrolyte. Tengyuan Dai et al. designed a hybrid material that used CeO_2 as a substrate to support $CoS_{1.97}$ nanosheets (CeO_2–$CoS_{1.97}$).[64] The SEM images in **Figure 7** showed the free–standing array morphology of the $CiS_{1.97}$–CeO_2, CeO_2–$CoS_{1.97}$ and $CoS_{1.97}$ samples. Each vertical growth nanosheet exhibited the 2D structure with width in the micron range, while the thickness in nanosize.[64] The special free–standing structure could make CeO_2–$CoS_{1.97}$ have a fully accessible surface of the electrolyte, thus improving the OER activity with the lowest overpotential of 264 mV under 10 $mAcm^{-2}$ in 1M KOH solution, which was much lower than that of $CoS_{1.97}$ (310 mV) or Ir/C catalyst (290 mV).[64] Furthermore, the DFT calculation results found the distinct electronic of CeO_2–$CoS_{1.97}$, with the electron–rich interfacial region, due to the strong reaction between CeO_2, and $CoS_{1.97}$.[64] The overlap of the s, p orbitals (S sites) and Fermi level could offer the material excellent conductivity. Such good electron transfer would facilitate the bonding process of *OH, thus further promoting the OER.[64]

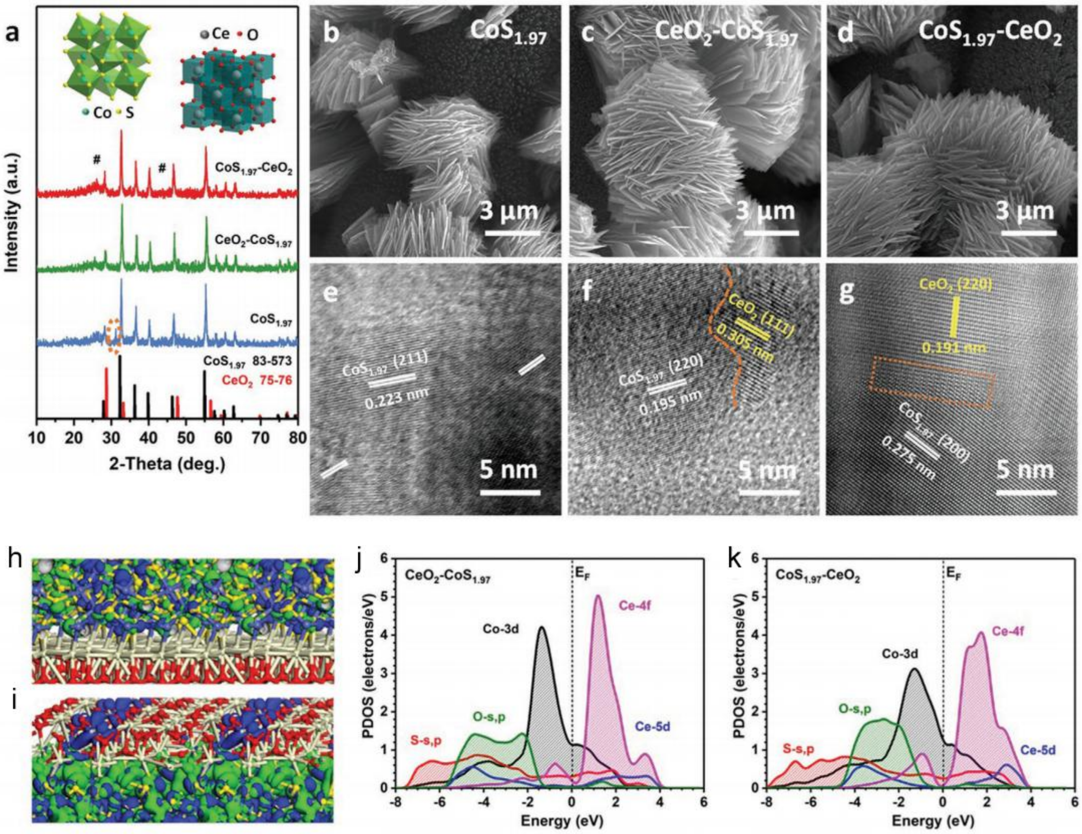

Figure 7. (a) The XRD patterns of the $CiS_{1.97}$–CeO_2, CeO_2–$CoS_{1.97}$ and $CoS_{1.97}$ samples. (b–d) The SEM images of three samples and (e–g) the corresponding HRTEM images. (h, i) The electronic distribution of CeO_2–$CoS_{1.97}$ and $CoS_{1.97}$–CeO_2 near to the Fermi level. (j, k) The projected partial density of states (PDOS) of CeO_2–$CoS_{1.97}$ and $CoS_{1.97}$–CeO_2. Taken from Ref. 64 and modified.

Apart from the conventional sulfides, manganese sulfide and noble metal sulfides, have also been extensively studied. Rahul B. Pujari et al. adopted a phase control technical route to synthesize manganese sulfide. Different manganese sulfide phases, including MnS_2, γ–MnS, and β–MnS were prepared from anion exchange via the hydrothermal method (See Figure 8a).[65] Before re–vulcanization, $MnCO_3$ thin films were firstly prepared in a Teflon liner on a flexible 304–type stainless steel. Sealing $MnCO_3$ and Na_2S into Teflon liner and heated to 303K for 24h, different phase of manganese sulfide was prepared *via* changing the proportion of raw materials.[65] The different phases of manganese sulfide, MnS_2, γ–MnS, and β–MnS showed superior OER with an overpotential of 301, 342 and 292 mV, respectively, better than the $MnCO_3$ (480 mV) in 1 M KOH at 10 mA cm^{-2}.[65,66] Yinlong Zhu et al. found a facile approach to synthesize the pyrite–type RuS_2 nanoparticles with abundant disorder units and defects in the crystal for water splitting application based on a low–temperature sulfuration process (Figure 8b).[66] Sulfuration temperature played a critical impact in the final products to create the special disorder structure, as well as the defects. To investigate the effect of reaction temperature, four different (400, 500, 600, and 700 ℃) steps were studied to analyze the relationship between the temperature and structure. The SEM images displayed the size range of the obtained RuS_2 nanoparticles located at 10–100 nm, however, there would be some big aggregates in the product. The HRTEM results revealed pyrite type crystalline structure of the RuS_2 crystal with a lattice spacing of 0.28 nm for (200) facet (Figure 8d).[66] For the cubic phase, Ru atoms are located at the fcc sublattice sites, in which every Ru atom is coordinated with six S atoms, and each S atom bonded with three Ru atoms (Figure 8c).[66] The OER performance of these catalysts was tested in 1 M KOH solution using the three–electrode system. The electrochemical double–layer capacitance measurements showed the low sulfuration temperature could be conducive to exposing more active sites.[66] Markedly, among the four samples, the RuS_2 nanoparticles reacted at 500 ℃ displayed the lowest overpotential of 282 mV at 10 mA cm^{-2}, which was also lower than that of commercial RuO_2 catalyst.[66] DFT calculations found the disordered structure could enhance the intrinsic conductivity of the materials and expose a large number of active sites, which would improve the charge transfer during the OER experiment together with the defect engineering during the preparation process.[66]

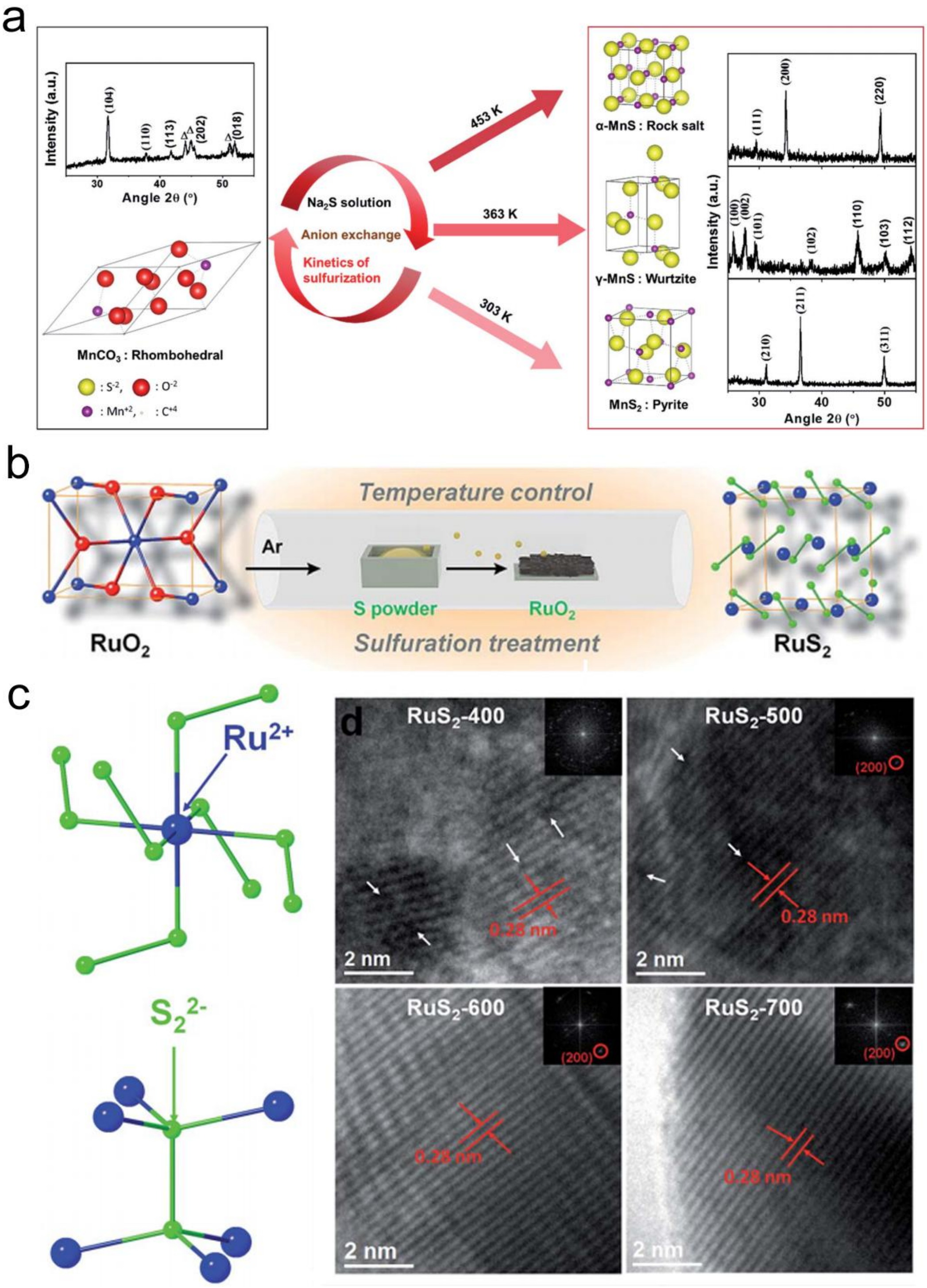

Figure 8. (a) Schematic of preparation about different phases of manganese sulfide from rhombohedral $MnCO_3$ *via* anion–exchange.[65] (b) Sulfuration process for the synthesis of RuS_2 nanoparticles used commercial RuO_2 as a precursor. (c) The coordination structure of the RuS_2. (d) HRTEM images of the RuS_2 nanoparticles under different reaction temperatures.[66] Taken from Ref. 65, 66 and modified.

Using a template to design and synthesize nanomaterials is also a very attractive method to form the target nanomaterials with different shapes or morphologies. Yujun Xu et al. adopted a template synthesis strategy to manufacture the well–dispersed RuS_2 nanoparticles on porous carbon spheres.[67] The whole reaction started from the uniform silicon dioxide nanospheres (SiO_2, with a diameter of ~500 nm) as the initial core template. After self–polymerization for 24 h, the SiO_2 was coated by an organic layer (dopamine hydrochloride).[67] The thickness of the organic layer could be adjusted by changing the reaction parameters. PDA on the surface of SiO_2 nanospheres would generate porous carbon after heated at 1000℃ treatment that called carbonization.[67] Then the SiO_2 could be etched by the HF/NH_4F solution, porous carbon shell would be lefted. Sealing $RuCl_3$, L–cysteine and carbon powder in Teflon–lined autoclave and reacted at 190℃ for 9h to obtain the amorphous RuS_x particles loaded on the porous carbon sheres.[67] Additionally, RuS_x/C nanocomposite was annealed in Ar environment at 800℃ to have the pyrite–type RuS_2 NPs. The detailed synthesis procedure of the crystals was illustrated in Figure 9.[67] As expected, the synthesized RuS_x/C material had superior electrocatalytic performance and structural stability.

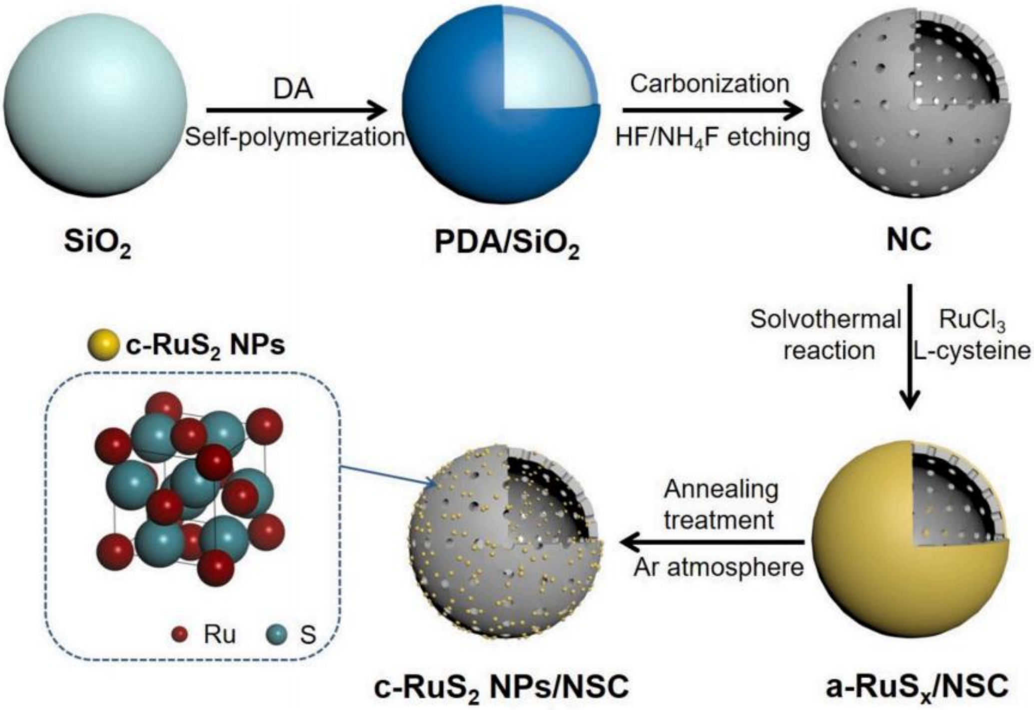

Figure 9. The synthesis procedure of RuS_2 nanoparticles on the porous carbon spheres. Taken from Ref. 67 and modified.

2.2.2 Synthesis of multimetallic PT–TMSs

Generally, the unique electrons in 3d orbitals of monometallic PT–TMSs are unsatisfactory for the overall electrochemical water splitting, considering the mechanism and intermediates adsorption and transfer process. The original electronic structure configuration of monometallic PT–TMSs could be adjusted by external metal doping. Additionally, metal doping or multi–metal alloys can bring abundant defects to the material and improve intrinsic conductivity. Hengjie Liu et al. explored the vanadium dopant NiS_2 to engineer heteroatom defects for enhanced overall water splitting.[37] Firstly, the NiV layered double hydroxides (LDH) were prepared through a hydrothermal reaction at 120 ℃ for 12 h. Then put the washed NiV–LDH powder into the furnace for sulfidation at 400 ℃ for 3.3 h, the V–NiS_2 material full of defects was obtained. The synthetic process was shown in Scheme 6.[37] Especially, the V–NiS_2 demonstrated enhanced overall water splitting activity with an overpotential of 110 mV at a current density of 10 mA cm^{-2} for HER and overpotential of 290 mV at current density of 10 mA cm^{-2} for OER in 1M KOH, which were much better than Pt/C (HER) and IrO_2 (OER).[37] The Density Functional Theory (DFT) calculation result displayed that the V–NiS_2 achieved metallic property based on the zero band gap, while the pristine NiS_2 exhibited a band gap of approximately 0.41 eV with the semiconductor feature.[37] The experimental characterization results further showed the lower resistivity of V–NiS_2 than pristine NiS_2. Such an interesting phase conversion phenomenon between semiconductor and metal might be an effective approach to adjust the OER activity of the PT–TMSs.[37] Qun Li et al. reported that cobalt doping in Cu_7S_4 nanodisks could modulate the electronic structure of the active centers to favor the OER catalytic process.[68] Pristine Cu_7S_4 nanoplates were prepared by a liquid phase synthesis process. The cuprous thiocyanate and oleylamine were added to the reaction bottle and kept at 240 ℃ for 0.5 h to generate Cu_7S_4 (Scheme 6e).[68] Then the collected

Cu_7S_4 nanoplates were dissolved into oleylamine together with cobalt(III) acetylacetonate for the next high temperature reaction. Through adjusting the amount of Cu_7S_4, series of Co_x–Cu_7S_4 nanocomposite were obtained. The corresponding XRD results of the Co_x–Cu_7S_4 were shown in Scheme 6 d. Co–dopant Cu_7S_4 nanoplates (Co:Cu=0.07) exhibited the lowest OER overpotential of 270 mV under the current density of 10 mAcm^{-2}, much better than it of pristine Cu_7S_4 (440 mV) and commercial IrO_2 (510 mV).[68] DFT calculations indicated the Co atoms in Cu_7S_4 nanosheet could enhance the electrotransfer between the Co and Cu sites, and reduce the energy barriers between the metal active sites and the intermediates. Moreover, the Co–engineered Cu_7S_4 displayed the larger density of states near the Fermi level, revealing the better conductivity.[68]

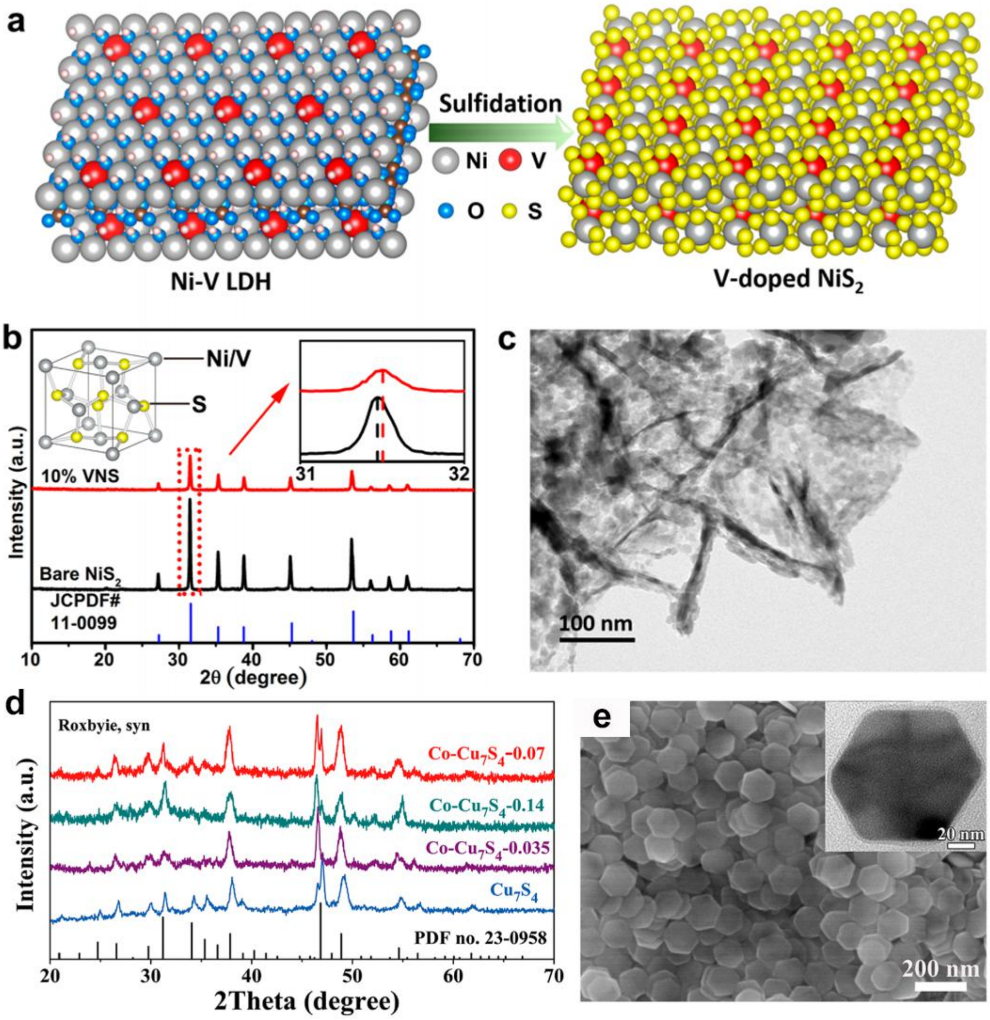

Scheme 6. (a) Synthetic process for V–doped NiS_2 nanocomposite. (b) The XRD patterns of the pristine NiS_2 and V–doped NiS_2.[37] (c) TEM image of V–doped NiS_2. (d) XRD results of the Co_x–

Cu_7S_4 materials. (e) SEM image of the Cu_7S_4 nanoplates.[68] Taken from Ref. 37, 68 and modified.

Similarly, pyrite–type ternary Ru doped NiS nanohybrids were synthesized through a mechanochemical–assisted pathway. Tian (Leo) Jin et al. mixed $NiCl_2$ (44 mg), $RuCl_3$ (70 mg) with thiourea in an agate reactor, which was placed in a planetary ball mill.[69] After being agitated at 800 rpm for 3 h, the as–prepared powder was transferred to the furnace and heated at 450 ℃ for 3 h. The synthesis diagram was shown in Figure 10. The well–dispersed single–phase pyrite–type ternary Ru–NiS nanoparticles on carbon (C) achieved exhilarated HER activity. Density functional theory (DFT) calculations indicated RuNiS–C could capture H_2O^* with faster kinetic and reduced the kinetic energy barrier by the Ru and Ni sites in this ternary sulfide, thereby boosting HER process.[69] In addition to the component control, it is also important to enhance the stability of the PT–TMSs. Loading the bimetallic sulfide on the substrate will effectively increase the dispersibility of the catalyst, and make the full utilization of the catalysts. Following this idea, pyrite–type Ni–doped CoS_2 (Ni–CoS_2) nanoneedle arrays were designed and supported on stainless steel (SS) to form the bimetallic $Ni_xCo_{1-x}S_2$/SS. Impressively, this $Ni_xCo_{1-x}S_2$/SS displays superior OER activity with an overpotential of 286 mV at 50 mA cm^{-2} and a corresponding Tafel value of 55 mV dec^{-1}.[46]

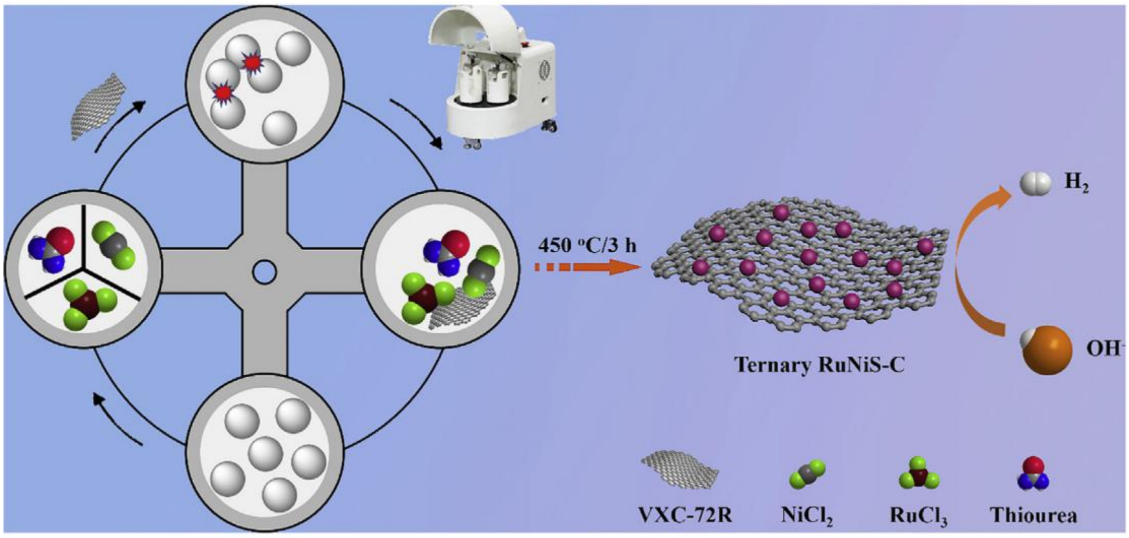

Figure 10. Synthesis diagram of RuNiS–C thorough the mechanochemical–assisted synergistic

strategy. Taken from Ref. 69 and modified.

As a widely studied combination, Ni/Fe bimetallic sulfide supported on substrate had a strong practical application potential. Ni/Fe bimetallic sulfide ($NiFeS_2$) nanoparticles grown on graphene were fabricated by a facile synthesis method. Chenyu Liu et al. fabricated NiFe LDH on graphene oxide (GO) to generate NiFe LDH–GO composites.[70] After solvothermal reaction in Teflon lined stainless steel autoclave and sulfidation process in a tube furnace, $NiFeS_2$–GN powder was obtained. $NiFeS_2$ nanoparticles evenly dispersed on graphene sheets and the detailed synthesis illustration was shown in Scheme 7.[70] The $(NiFe)S_2$ nanoflakes on the graphene gave the catalyst an effective substrate for the electrochemical water splitting application as the high conductivity property. The OER experiment of these materials was tested in the 1 M KOH solution by a three–electrode system at a scan rate of 2 mV/s. The as–prepared $NiFeS_2$–GN displayed a superior OER overpotential of 317 mV under 10 $mAcm^{-2}$.[70]

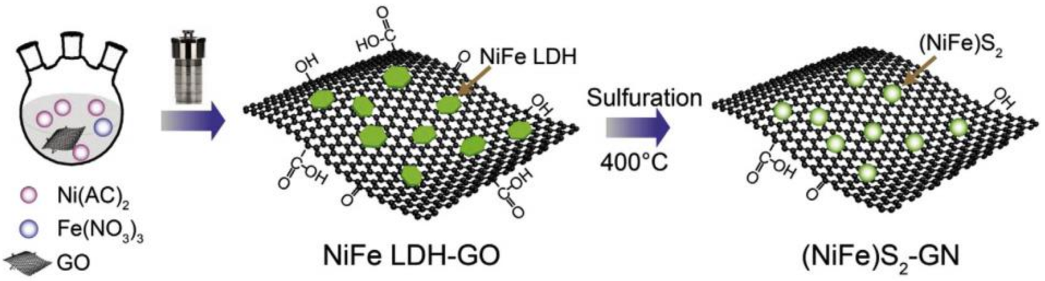

Scheme 7. The fabricating process of $(NiFe)S_2$–graphene. Taken from Ref. 70 and modified.

Carbon–based nanostructure, including graphene, carbon powder, and carbon tube, are widely applied in the electrocatalysis as the substrate. Interestingly, researchers found the combination of graphene and carbon tube could be favorable for building a hierarchical structure with a large electrocatalytic active area. Zhiliang Zhang and co–workers developed a polymerization reaction at 550 ℃ to prepare a hybrid material with Co–Fe species, C_3N_4, and graphene oxide. For the next step, this hybrid composite in–situ grew to $CoFeO_x$@CNTs/rGO in the N_2 atmosphere at the temperature above 800 ℃.[71] During this step, the carbon nanotube vertical grew on the surface of graphene, thus forming the brush–like architecture as shown in the Scheme 8.[71] The $CoFeO_x$ nanoparticles were encapsulated in the top edge of the carbon nanotube, driving the 3D mass transfer channels. After the sulfuration at 500 ℃ for 2h, the encapsulated CoFe oxide would generate CoFe sulfide.[71] Among the series $Co_xFe_{1-x}S_2$@N–CNTs/rGO (x = 0, 0.2, 0.4, 0.6, 0.8, and 1) catalysts, $Co_{0.6}Fe_{0.4}S_2$@N–CNTs afforded the lowest OER overpotential of 248 mV at 10 $mAcm^{-2}$, followed by $Co_{0.8}Fe_{0.2}S_2$@N–CNTs/rGO with an overpotential of 259 mV, revealing the high content of Fe in the material would benefit for the OER activity.[71]

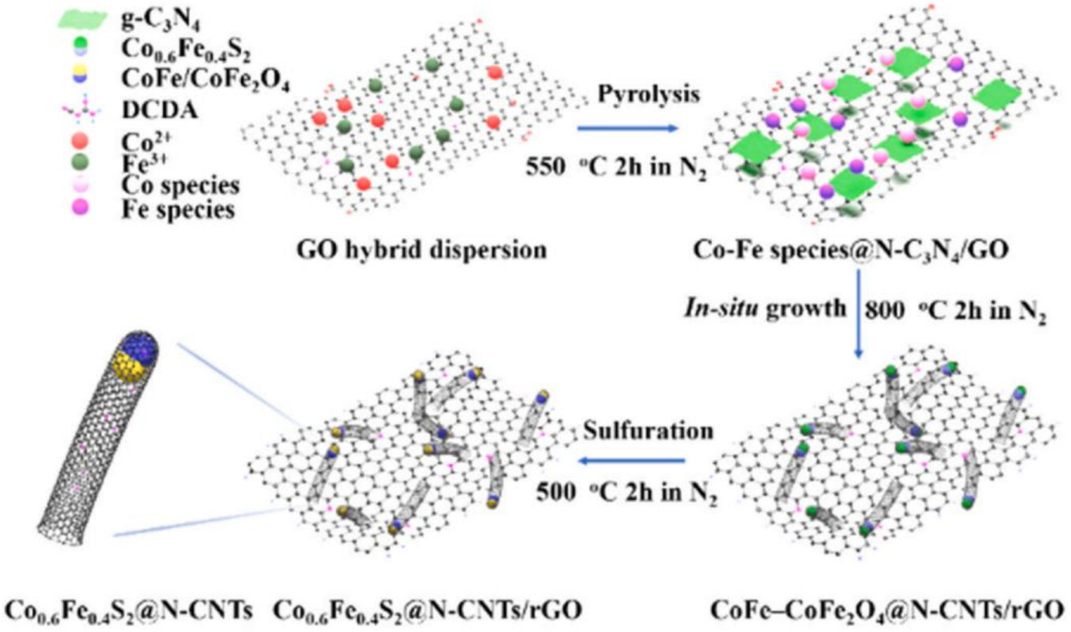

Scheme 8. The preparation of $Co_{0.6}Fe_{0.4}S_2$@N–CNTs/rGO. Taken from Ref. 71 and modified.

Different from the in–situ growth of carbon nanotube on the surface of carbon substrate, Di–Yan Wang et al. directly used carbon nanotubes to load CoFe sulfides for electrocatalysis.[72] The oxidized multi–walled carbon nanotubes dispersed into the anhydrous N,N–dimethylformamide (DMF) solution, followed by adding Fe and Co ions.[72] Physical adsorption allowed the hybrid to facilitate the acquisition of ultra–small FeCoS nanoparticles on the surface of nanotubes, consistent with the TEM results (Figure 11).[72] The X–ray diffraction pattern (XRD) indicated the

$Fe_{0.9}Co_{0.1}S_2$@CNTs had the similar pyrite pattern of FeS_2.[72] Furthermore, the X–ray absorption near–edge spectra (XANES) of the Fe K–edge and Co K–edge presented the positive divalent states of the Fe and Co in the final product. The Co doping in FeS_2 brought the lower kinetic energy barrier for H* adsorption.[72] The heteroatomic interactions between $Fe_{0.9}Co_{0.1}S_2$ and CNTs also played an important role in the catalytic activity.

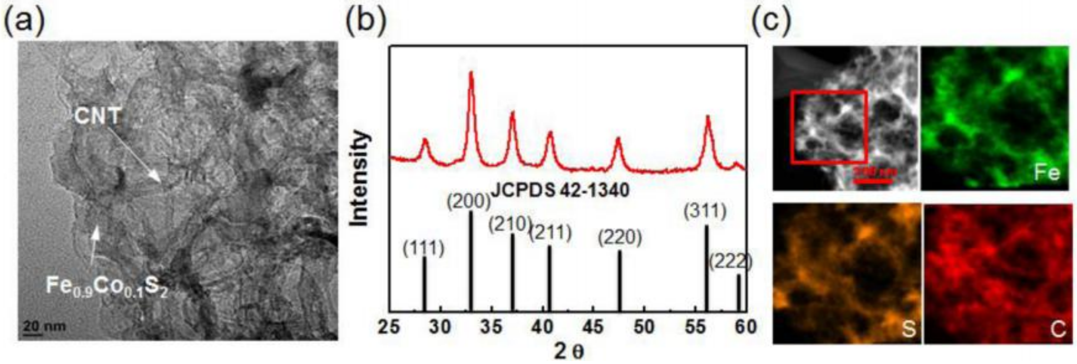

Figure 11. (a) The TEM and (b) XRD of $Fe_{0.9}Co_{0.1}S_2$@CNTs. (c) The EDS mapping results of the materials. Taken from Ref. 72 and modified.

The promoted synergistic effect between the ions in multimetal–doped sulfides can effectively improve the OER activity, due to the defects, charger transfer, or strain. To fully use the ascendancy of the hybrid material, Cu and Co–doped Ni_3S_2 grown on Ni foam were created for highly effective OER catalyst.[73–75] 3D Ni foam was selected as the substrate to mix with Co and Cu ions in the autoclave. After being reacted at 120 ℃ for 6 h, CuCo–precursors were coated on Ni foam to form the initial product. The CuCo–precursors continue to react with CH_3CSNH_2 and glutathione to synthesize CuCo–Ni_3S_2 on Ni foam through the liquid vulcanization method.[73] The typical synthetic route was shown in Scheme 9a. The CuCo doped Ni_3S_2 owned a dense layer on the surface of Ni foam with a lot of bulging structures.[73] The OER performance of all the samples was studied in the nitrogen saturated 1.0 M KOH electrolyte. The XPS analysis showed that Co, Cu and Ni atoms in CuCo–Ni_3S_2 exhibited rich valence states including Co^{2+}, Co^{3+}, Cu^{2+}, Ni^{3+} and Ni^{2+}.[73] Based on the previous literature, all the high valence metal sites could provide high OER activity. The CuCo–Ni_3S_2 possessed advantageous OER performance with a low overpotential of 400 mV vs. RHE at 100 mAcm^{-2}, which was much smaller than that of Co–Ni_3S_2 (425 mV), Cu–Ni_3S_2 (430 mV), Ni_3S_2 (438 mV) and RuO_2 (460 mV).[73] Stability and activity are the two biggest challenges for the practical application of the OER catalysts. Depositing an active amorphous layer on the nanostructure to form core–shell architecture is a practical approach to get high–performance catalyst. Guiding by this, Xiao Shang and co–workers developed an electrochemical method to deposit ultrathin amorphous Fe hydroxides layer on the V–NiS nanowire.[74] The V–NiS sample was prepared by a classic hydrothermal reaction which directly mixed the Ni foam, V and S sources in the reactor (Scheme 9c).[74] By adjusting the temperature of the electrochemical reaction, amorphous Fe layers with different deposition morphologies were developed and the products named eFe/NiVS/NF and uFe/NiVS/NF, respectively. In comparison, eFe/NiVS/NF displayed an overpotential of 225 mV at 100 mA cm^{-2}, which was smaller than it of uFe/NiVS/NF (240 mV), suggesting the Fe hydroxides could effectively promote the OER performance.[74]

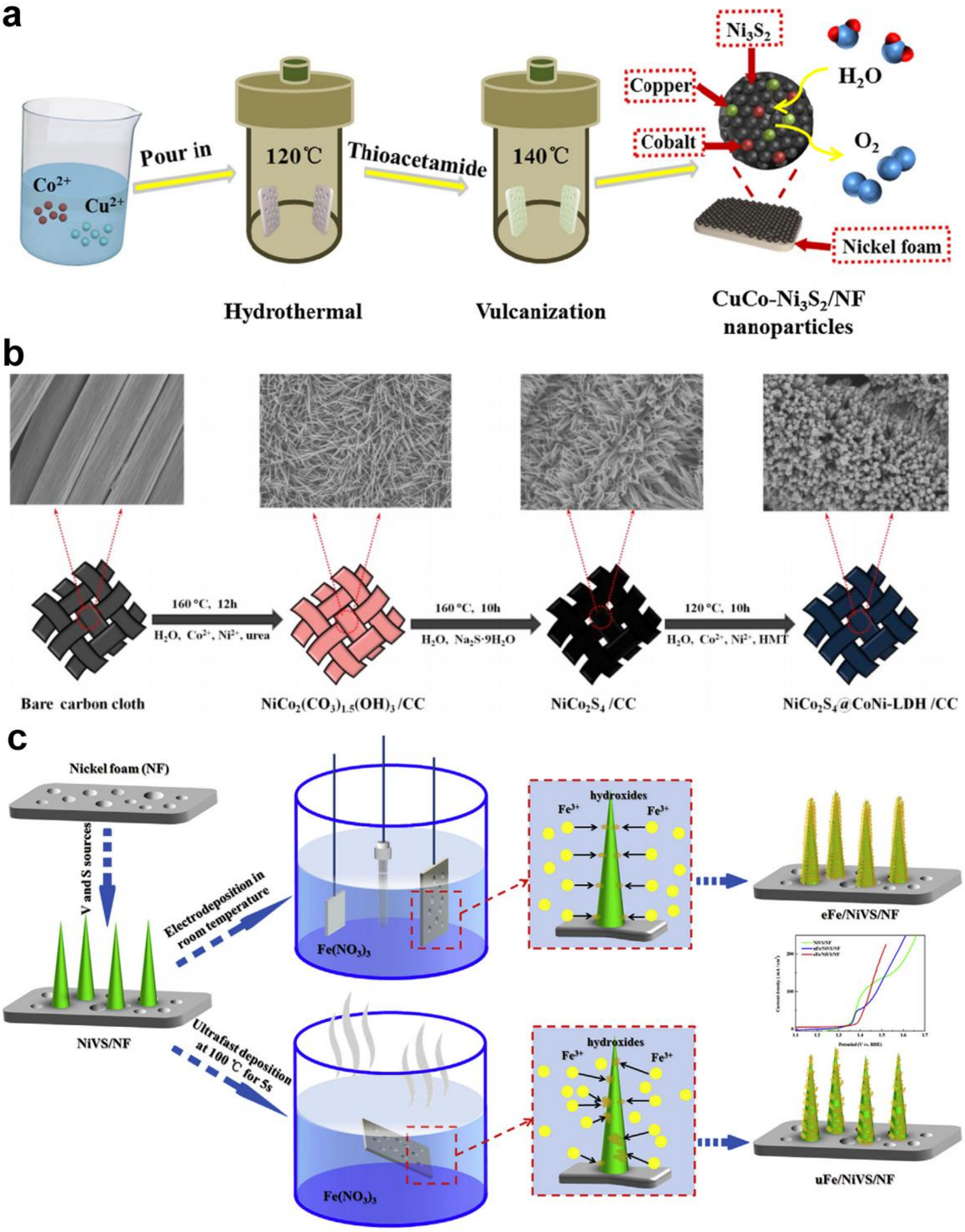

Scheme 9. Schematic diagram (a) for preparing $CuCo–Ni_3S_2$ on the Ni foam,[73] and (b) for synthesizing $NiCo_2S_4@CoNi–LDH/CC$.[75] (c) Electrodeposition amorphous Fe hydroxides on the V–doped NiS nanowires.[74] Taken from Ref. 73, 74, 75 and modified.

Feifei Yuan et al. prepared the hierarchical core–shell $NiCo_2S_4@CoNi–LDH$ hybrid supported on carbon cloth as the catalysts for the OER application.[75] A modified method was adopted to synthesize the carbon cloth–supported $NiCo_2(CO_3)_{1.5}(OH)_3$ by a facile hydrothermal reaction.[75] The Co and Ni ions and urea dissolved in a deionized water solution with a piece of carbon cloth (CC) in the steel autoclave. After high–temperature treatment, $NiCo_2(CO_3)_{1.5}(OH)_3$ nanoarrays loaded on the CC ($CC@NiCo_2(CO_3)_{1.5}(OH)_3$) were successfully obtained. Subsequently, $CC@NiCo_2(CO_3)_{1.5}(OH)_3$ would convert to CC–supported $NiCo_2S_4$ nanoarrays through liquid vulcanization reaction. Then the hexamethylenetetramine mixed with Ni and Co ions would generate CoNi–LDH on the surface of the $CC@NiCo_2S_4$ to produce $CC@NiCo_2S_4@CoNi$–LDH.[75] Scheme 9b displayed the synthesis process of the $CC@NiCo_2S_4@CoNi$–LDH electrocatalyst. This core–shell nanostructure demonstrated excellent OER performance with an overpotential of 337 mV at 100 $mAcm^{-2}$, much better than that of RuO_2/CC (379 mV) and $CC@NiCo_2(CO_3)_{1.5}(OH)_3$ (496 mV).[75] Further increasing the metal element species in the catalyst could enhance the interaction between the metal atoms, as well as the conductivity. High entropy materials (HEM) containing five or more elements which provide plenty of combinations for the OER experiment. HEM sulfides ($FeNiCoCrXS_2$, X=Mn, Cu, Zn, or Al) were synthesized through a two–step solvothermal method (Figure 12).[76] In the first step, the equimolar different kinds of metal ions were added in the autoclave together with the isopropanol and glycerol to obtain high entropy glycerate templates.[76] After solvothermal vulcanization under 160 ℃, various metal sulfides (FeS_x, NiS_x, CoS_x, CrS_x, and MnS_x, $FeNiCoCrS_2$, $FeNiS_x$, $FeNiCoS_x$, $FeNiCoCrXS_2$, where X is Cu, Zn, Mn or Al) were obtained. Typically, the obtained HEM $FeNiCoCrXS_2$ presented a spherical core–shell structure under micron–level size. The $FeNiCoCrMnS_2$ displayed the best OER activity with the overpotential of 199 mV at 10 $mAcm^{-2}$ among FeS_x, $FeNiS_x$, $FeNiCoS_x$, $FeNiCoCrS_2$.[76] The increasing of the metal species would gradually improve the OER activity. The HEM sulfides in this paper open can effectively expand the research of polymetallic atom sulfides for OER application.[76]

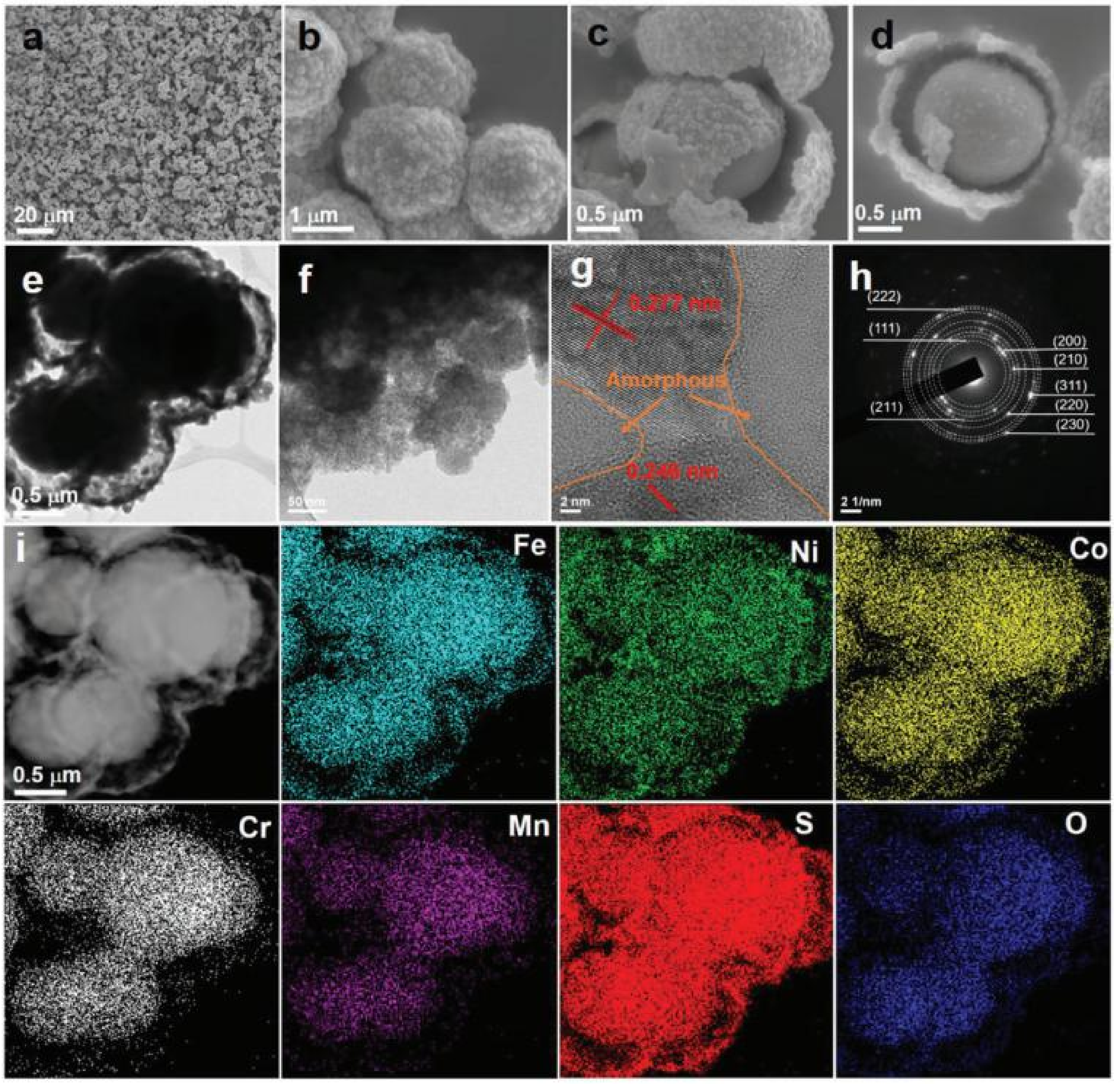

Figure 12. (a–d) SEM images, (e–g) TEM and HRTEM images of $FeNiCoCrMnS_2$. (h) SAED pattern of the material. (i) Typical HAADF image and the corresponding EDS mapping result of $FeNiCoCrMnS_2$. Taken from Ref. 76 and modified.

2.2.3 Synthesis of pyrite–type metallic bifunctional catalysts

An effective strategy to improve the electrocatalytic water splitting of PT–TMSs is introducing other non–metal elements, such as phosphorus (P) and boron (B), leading to the synergistic effect between S and P or B. Bifunctional PT–TMSs can make the electron configuration in d orbital more suitable for catalytic processes and facilitate the charge transfer during OER test. Bratati Roy et al. reported a solid–state reaction procedure to prepare pyrite–type CoPS nanoparticles.[77] The cobalt, phosphorous, and sulfur pellet was sealed in an evacuated (10^{-6} mbar) quartz ampoule and heated at 450 ℃ for 6 days, then heated up to 600 ℃ for more than 6 days. TEM characterization results showed the CoPS particles had an approximate size of 20 nm (See Figure 13 a,b) and the bifunctional CoPS presented good OER activity.[77] Jiayuan Li et al. found the strategy of element substitution could effectively control the electronic structure of the materials for their electrocatalytic application.[78] Pyrite–type Ni/P co–doped CoS_2 nanowires were manufactured with hydrothermal reaction using carbon cloth (CC) as substrate. The NiCoPS nanowires were dispersed onto CC with a uniform diameter of ~50 nm and length in micrometers (See Figure 13). The quaternary pyrite–structured NiCoSP/CC was efficient and durable electrode for OER with a low overpotential of 230 mV at 10 mA cm^{-2} in 1.0 M KOH. More importantly, NiCoSP/CC had great stability for overall water–splitting with an approximately ~100% Faradic efficiency over 100 h stability test in 1.0 M KOH.[78]

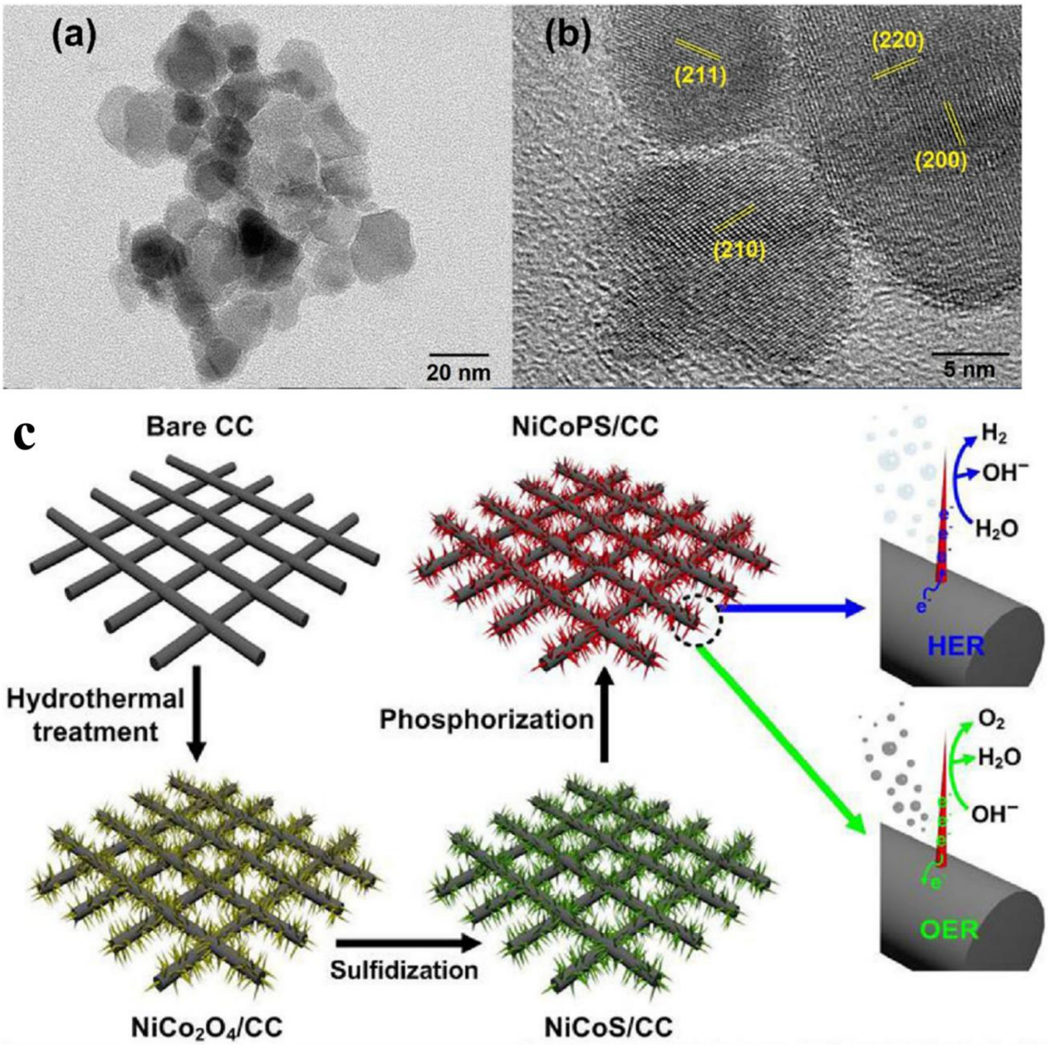

Figure 13. (a) TEM and (b) HRTEM of CoPS nanoparticles.[77] (c) The fabrication process of NiCoPS/CC.[78] Taken from Ref. 77,78 and modified.

Heterogeneous catalysis is a surface phenomenon, highly dependent on the surface composition. Biswanath Dutta et al. presented a partial surface selenization strategy for mesoporous CoSSe nanomaterials by the continuous introduction of anions through sulfuration and selenization.[79] Using this step–by–step synthesis method, the surface composition of CoSSe could effectively control in several atomic layers.[79] They synthesized mesoporous cobalt oxide (meso–Co_3O_4) mediated by processing the soft template. Followed by step and step reaction (Figure 14), sulfurization and selenization, the mesoporous CoSSe spheres with the size of ~2 μm were prepared.[79] In particular, the partial surface selenization strategy adopted in this system created a mesoporous CoSSe with more than 25 h operational stability during the electrocatalytic water splitting.[79] According to the same idea, various Se doped pyrites sulfides, including Se–CoS_2, Se–WS_2, and Se–MoS_2, were fabricated and applicated in electrocatalysis reaction with the superior activity.[79] Besides, the 2D ultrathin sulfides can significantly improve the catalytic properties because of the large surface area. Many studies found that the atoms at the edge of the 2D structure often acted as the active sites during the catalysis.[79] Thus synthesis of 2D heteroatom–doped sulfides would further promote the OER application. Jianpeng Sun et al. developed an economic–effective solvothermal method to prepare the atomically $NiSe_{1.2}S_{0.8}$ nanosheets with an average thickness of ~1.1 nm.[80] The thin $NiSe_{1.2}S_{0.8}$ nanosheets full of Ni–Se–S bonds and defects exhibited excellent water splitting activity.[80] As an important index for evaluating the catalytic activity of the catalysts, adsorption free energy of hydrogen (ΔG_{H*}) was adopted to analyze the interaction between the active sites and H*. The theoretical results indicated S–doping $NiSe_2$ had a smaller ΔG_{H*} value (−0.3 eV) than $NiSe_2$ (0.565 eV) and NiS_2 (−0.345 eV), consistent with experimental results.[80]

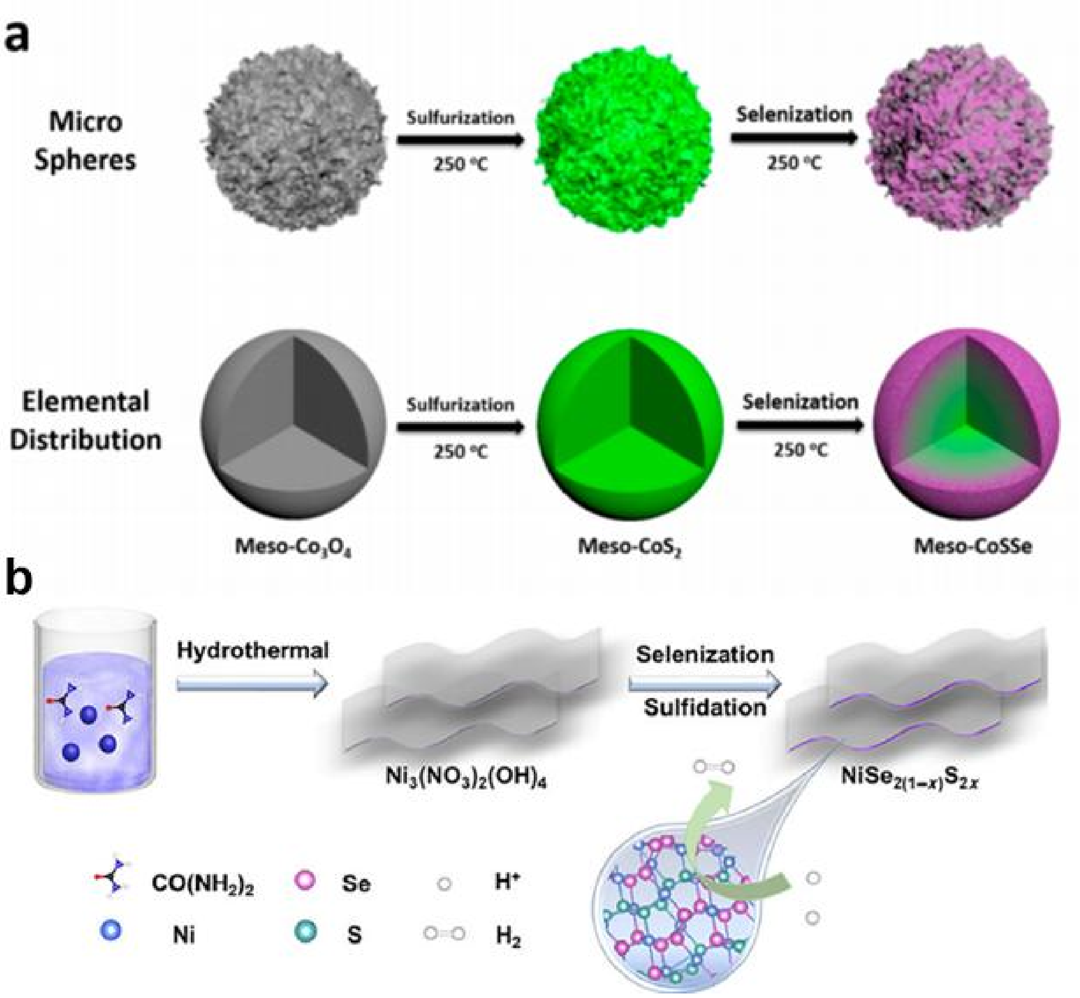

Figure 14. (a) Partial surface selenization strategy of the CoSSe synthesis.[79] (b) Two–step reactions to prepare $NiSe_{2(1-x)}S_{2x}$ nanosheets.[80] Taken from Ref. 79, 80 and modified.

Recently, numerous studies focused on nitrogen–doped carbon–based materials for water splitting due to the good conductivity and plentiful vacancies. Different biological matrices were selected for the synthesis of carbon–based compounds. Solid duck blood was chosen for pyrolysis and subsequent vulcanization.[81] To increase the active sites of the material, $Fe(NO_3)_3$ and $Ni(NO_3)_2$ were added into the reaction solution (Figure 15). After freeze–drying under a vacuum, a homogeneous intermediate was formed. Biological matrix samples would generate a large number of hollow units during the pyrolysis as the carbonization of organic macromolecules and gas release. The porous $Fe–C–N_x$ foam would generate after reacting at 850 ℃ under Ar atmosphere.[81] Subsequently, the 3D network carbon matrix structure loaded uniform dispersed

$Fe_xNi_{1-x}S_2$–C nanoparticles were obtained. The electrocatalytic OER performance of the cost–effective $Fe_xNi_{1-x}S_2$–C composite was investigated in the 1M KOH solution. Particularly, this hybrid material exhibited remarkably enhanced OER activity with an overpotential of 296 mV at current density of 10 mA cm^{-2}.[81] The fast reaction kinetics of $Fe_xNi_{1-x}S_2$–C was further evidenced by Tafel slopes (43 mV dec^{-1}). This strategy could be further extended to design other metal dopant sulfides and explore low–cost and high–activity catalysts for energy conversion.[81]

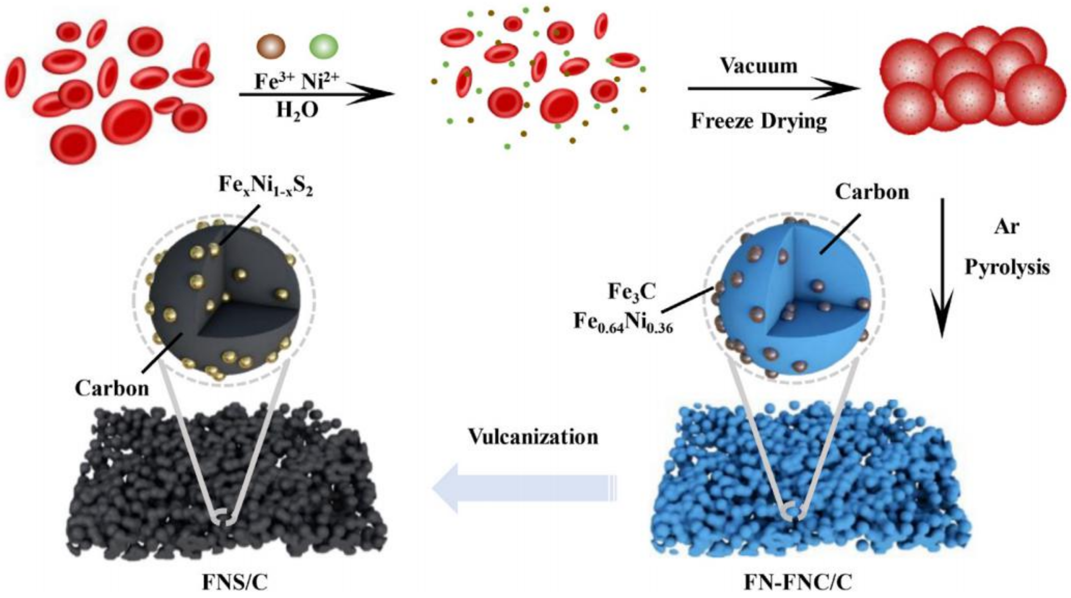

Figure 15. The fabrication process of $Fe_xNi_{1-x}S_2$–C material. Taken from Ref. 81 and modified.

Similarly, HyukSu Han and co–workers developed a one–step hydrothermal process to prepare $Co_{1-x}Ni_xS_2$−C composite (Figure 16). The graphene oxide was synthesized through the modified Hummer method.[82] As shown in Figure 16a, the as–prepared graphene powder, deionized water, $CoCl_2$, $NiCl_2$, and CH_4N_2S were transferred to stainless steel autoclave and reacted at 200 ℃ for 24h. Then the porous $Co_{1-x}Ni_xS_2$−C composite would be obtained for electrocatalytic OER reaction.[82] Figure 16b showed the centimeter–level dried $Co_{1-x}Ni_xS_2$−C solid with the black color. SEM images in Figure 16c, d showed the 3D porous composite contained typical 2D graphene and $Co_{1-x}Ni_xS_2$ nanoparticles.[82] The TEM images presented the $Co_{1-x}Ni_xS_2$ nanoparticles with the size of 300−500 nm which loaded on the graphene, revealing the large surface area for OER. The

$Co_{1-x}Ni_xS_2$–C hybrid material showed remarkable OER activity with an overpotential of 330 mV at 10 mAcm^{-2}, significantly better than commercial RuO_2 (350 mV).[82] In addition, $Co_{1-x}Ni_xS_2$–C also showed excellent catalytic stability after 1000 cycles. According to DFT calculation results, all the elements in the $Co_{1-x}Ni_xS_2$ had different functions during the OER. The Co elements tended to generate Co–N bonds, while S sites in $Co_{1-x}Ni_xS_2$–C would be attributed to the oxygen adsorption by losing an electron. The metal sites (Co and Ni) played important roles for OOH* generation on the Co–Ni bridge, Co–N, and Ni sites.[82] The detailed description of the OER mechanism was explained in Figure 16h, i. The combined synergy effect of active sites leads to the final superior OER activity.

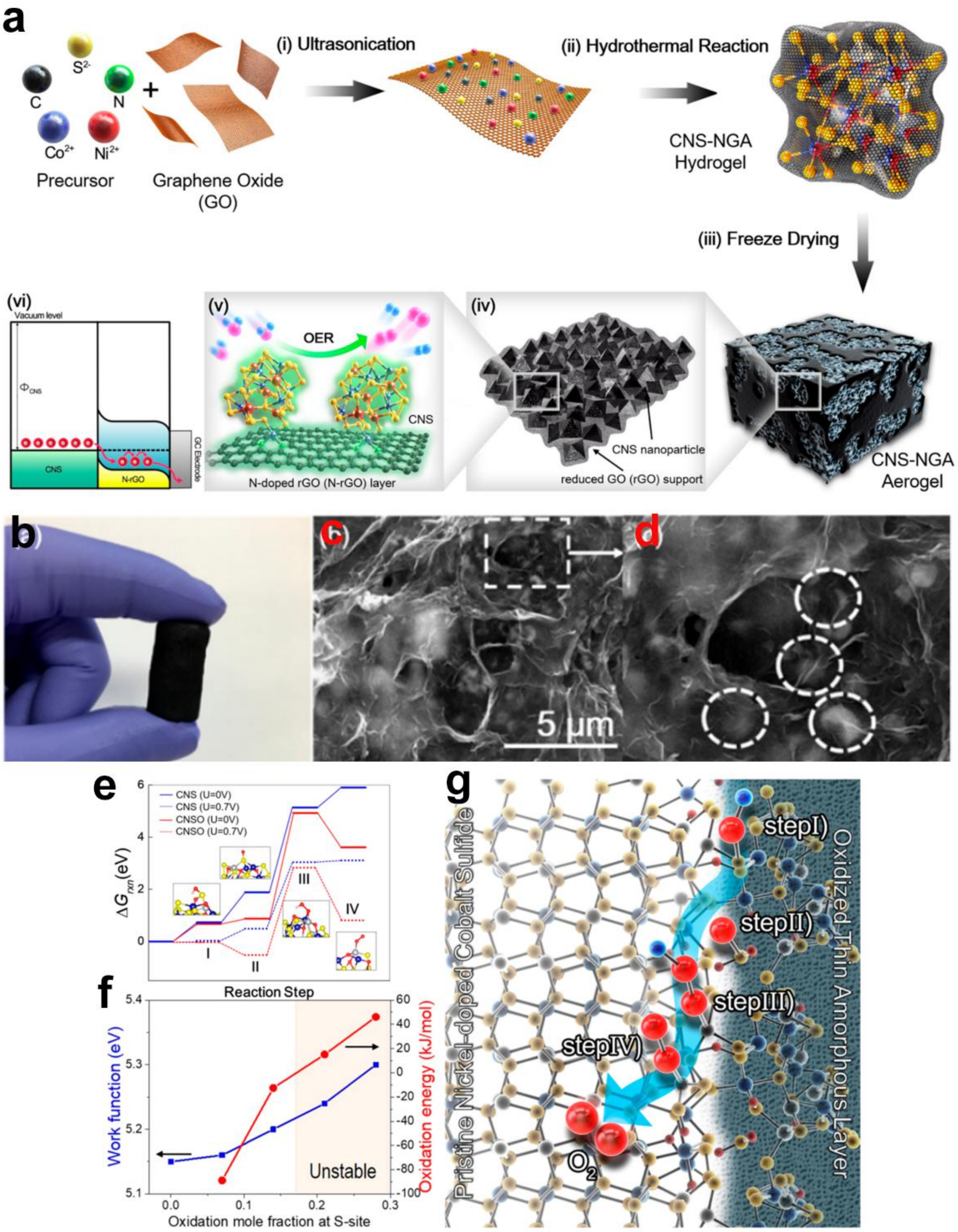

Figure 16. (a) (b) Digital photo image, (c–d) SEM images of CNS−NGA composite. (e, f) DFT calculated energy results for NS–C, graphene oxide aerogel and $Co_{1-x}Ni_xS_2$−C. (g) OER reaction on the boundaries between NS–C and $Co_{1-x}Ni_xS_2$−C. Taken from Ref. 82 and modified.

Apart from regulating the composition, including alloying/doping, controlling the morphology also plays an important role for the high activity OER catalysts. The research focused on the evolution of the structural shape combined with composition by the template approach has received extensive research. Yizhuo Song et al. used hollow Co–Fe prussian blue analogues (PBAs) as the initial template for sulfurization and Se doping step by step.[83] The hollow Co–Fe PBAs nanobox was prepared through liquid phase reaction by mixing $Co(NO_3)_2$ and trisodium citrate, and H_2O, then followed by adding $K_3[Fe(CN)_6]$ to form precipitation (see Figure 17). After sulfuration and selenization reaction, the well–defined hollow Se–$(CoFe)S_2$ nanobox with a size of ~230 nm were generated.[83] The uniform Se–$(CoFe)S_2$ nanobox contains five elements, including Co, Fe, Se, C and S, while the S atoms occupied the highest content based on the EDS line scan. Enlarged TEM images in Figure 17 clearly showed the hollow structure of Se–$(CoFe)S_2$ with CoS_2 and FeS_2 components.[83] The TEM–EDS results displayed the uniform distribution of the five elements over the entire material. Electrocatalytic OER activities of the Se–$(CoFe)S_2$ were investigated in 1 M KOH, as well as the related similar morphology samples such as $(CoFe)Se_2$, $(CoFe)S_2$, and commercial Ir/C. Among these materials, the Se–$(CoFe)S_2$ exhibited the best OER performance with an overpotential of 281 mV at 10 mA cm^{-2}. Besides, the Se–$(CoFe)S_2$ kept slightly changing after 1000 cycles stability test.[83] With a similar idea, Hongchao Yang and co–workers prepared hybrid composite materials with N, S co–doped hollow carbon nanospheres embed by nickel sulfides (Ni_9S_8–NSCs).[84] The samples with different chemical valence states (Ni_9S_8, Ni_9S_8–$NiS_{1.03}$ alloy and $NiS_{1.03}$) were systematically studied to know the chemical valence–activity relationship.[84] The Ni_9S_8–NSCs had a good crystallinity with a typical XRD pattern (Figure 17i) consisting of the Ni_9S_8 and carbon. The SEM and STEM images of the samples revealed the porous core–shell structure of the Ni_9S_8–NSCs (Figure 14j, k). Particularly, the $NiS_{1.03}$–NSCs with the highest–valence Ni species in the sample showed the lowest overpotential of ≈270 mV at 10 mA cm^{-2} in 1 M KOH solution.[84] Moreover, the $NiS_{1.03}$–NSCs kept their catalytic performance during the continuous testing for at least 10 h, significantly surpassing the commercial RuO_2, and other Ni–based electrocatalysts with low–valence Ni species. Valence engineering could construct high–valence metal centers in the pyrite–type sulfides, which can effectively improve and increase the number of active sites for the catalytic application.

Multiple metals in the samples could also contribute to the conductivity of the pyrite–type sulfides.[84] All these phases and morphological techniques would prove the rational design of effective electrocatalysts, especially the pyrite–type sulfides, for electrocatalytic water splitting application in acid or alkaline solution, thus greatly promoting the commercialization of pyrite sulfides.[84]

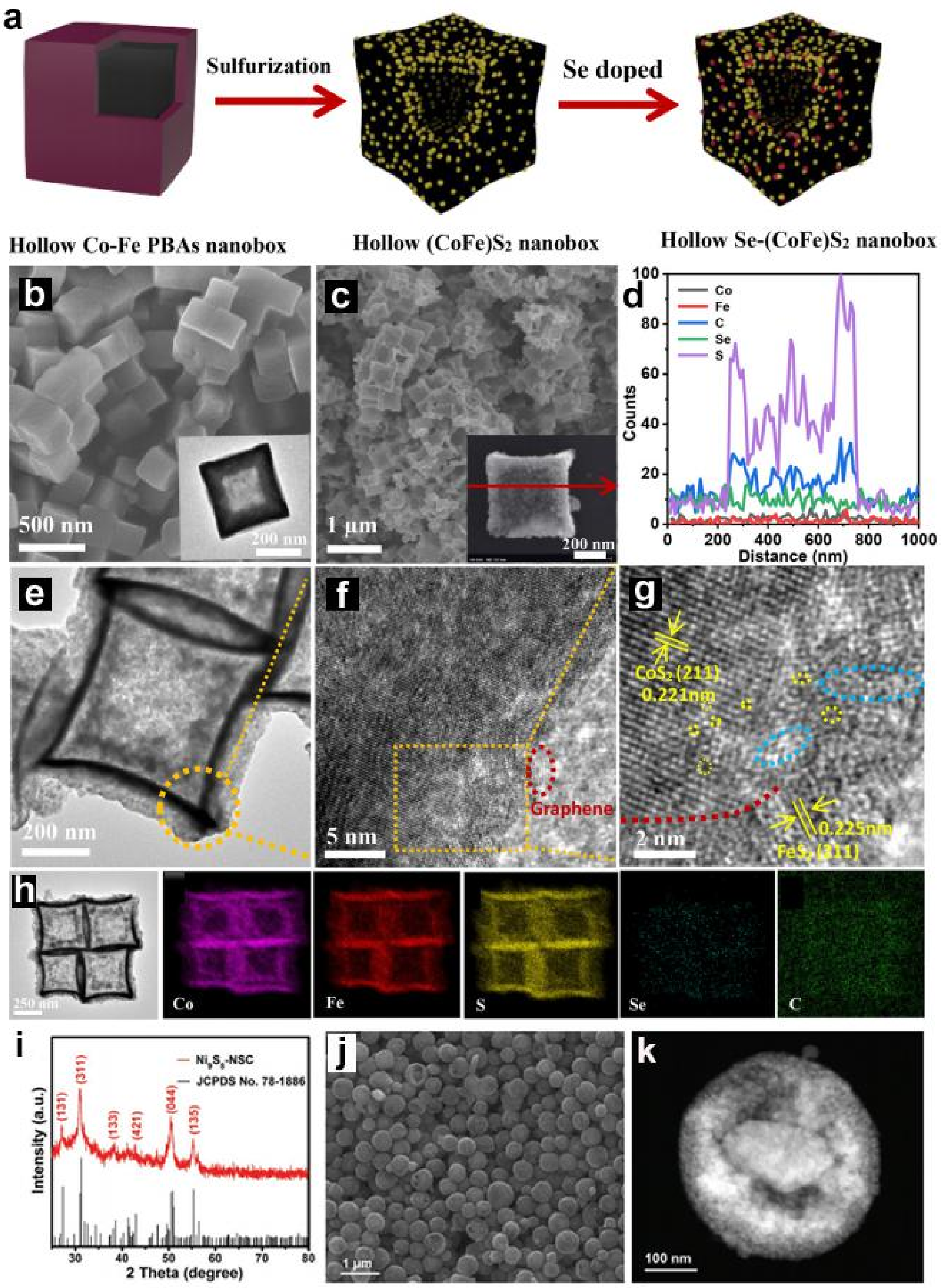

Figure 17. (a) The fabrication procedure of Se–(CoFe)S_2 nanobox. (b, c, d) The SEM and the corresponding EDS line scan results. (e, f, g) Magnified TEM images of a typical Se–(CoFe)S_2 nanobox. (h) STEM image of Se–(CoFe)S_2 and the EDS element mapping images.[83] (i) The XRD of Ni_9S_8–NSCs. (j) SEM and (k) STEM image of the Ni_9S_8–NSCs.[84] Taken from Ref. 83, 84 and modified.

To further aggravate the structural changes of electron property of the core–shell N–doping sulfide nanospheres, Xuefeng Lu and co–workers prepared the N–doped pyrite CoS_2 yolk–shell nanospheres (N–CoS_2 YSs) by a two–step procedure, hydrothermal and vulcanization reaction.[85] The Co ions, glycerol, and isopropanol were added into a steel autoclave and reacted at 180 ℃ for 6 h to obtain Co–glycerate precursors. After the vulcanization reaction, the solid Co–glycerate spheres converted into the yolk–shell N–CoS2 YSs.[85] This illustration diagram of the synthesis procedure is presented in Figure 18a. The SEM images in Figure 18b, d, f clearly showed the Co–glycerate kept the uniform spheres morphology during the generation of N–CoS_2 YSs. The corresponding TEM images (Figure 18 c, e, g) of N–CoS_2 YSs indicated the N–CoS_2 YSs had a uniform size of about ~ 400 nm with the typical yolk–shell characteristic. Benefiting from the hollow structure and unique electron state, the N–CoS_2 YSs exhibited excellent property for long–life Zn–air batteries application.[85] Functional sulfides have great potential for catalysis and energy storage, due to the adjustable complex electronic configuration.

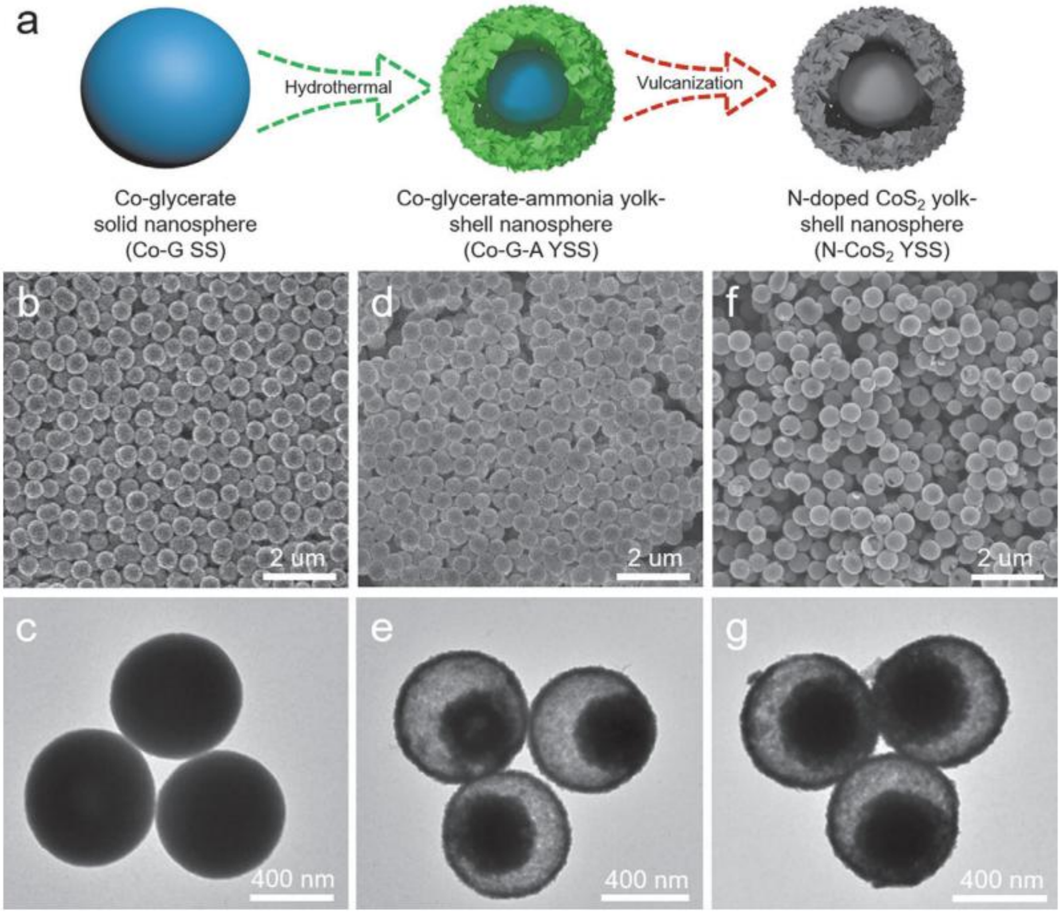

Figure 18. (a) The synthesis process of N–CoS$_2$ YSs. (b, d, f) SEM and (c, e, g) TEM images of Co–glycerate, Co–glycerate–ammonia yolk–shell nanospheres, and N–CoS$_2$ YSs. Taken from Ref. 85 and modified.

In this part, we have summarized the different synthetic methods with various reaction precursors for multifunctional pyrite sulfides, which might greatly promote the development of transition metal sulfides and contribute to the commercialization process for electrocatalytic water splitting. To better understand the methods and formulations to construct transition metal sulfide catalysts, we have summarized the approaches reported in the literature recently. Table 1 displayed the detailed information.

Table 1. The summarization of the methods with different precursors for synthesizing metal

sulfides.

Precursor	Solvents	Reaction temperature (°C)	Catalysts	Reference
Ni $(CH_3COO)_2$ sulfur powder	N,N–Dimethylformamide (DMF) Ethanol	180	NiS_2 Microspheres	56
$NiCl_2$ VCl_3 Urea	Deionized water	120	V–doped NiS_2 Nanosheets	37
Cobalt Phosphorou Sulphur	No	450/600	CoPS Nanoparticles	77
$FeCl_3$ Thiourea	1,2–propanediol	180	FeS_2 Nanoparticles	60
Carbon cloth (CC) $Ni(NO_3)_2$ $Co(NO_3)_2$ Urea Sulfur $NaH_2PO_2\cdot H_2O$	Deionized water	300/400	NiCoPS/CC	78
$MnSO_4$ Na_2SO_4 CH_4N_2O	Deionized water	90	MnS_2 γ–MnS α–MnS	65
$FeCl_2$ Polyvinylpyrrolidone (PVP, M=40000) Sulfur powder	Deionized water Ethylene glycol Ethylenediamine	200	FeS_2/C Nanowires	61
Anhydrous ruthenium chloride VXC–72R Thiourea Anhydrous nickel chloride	No	450	RuNiS Nanoparticles	69
Urea $Ni(NO_3)_2$ $Co(NO_3)_2$ Stainless steel	Deionized water	120	$Ni_xCo_{1-x}S_2$ Nanowires	46

$Ni(OAc)_2$ $Fe(NO_3)_3$ Graphene oxide	DMF Deionized water	120	$(NiFe)S_2$ Nanoparticles	70
$Ni(NO_3)_2$ DHT Thiourea	Methanol Deionized water	200	Nickel sulfide (Ni_7S_6)	58
Nickel(Ⅱ) chloride Anhydrous	Deionized water Ethylenediamine Carbon disulfide	180	NiS Ni_3S_4 NiS_2	59
RuO_2 Sulfur powder		400 500 600 700	RuS_2	65
$Co(CH_3CO_2)_2$ Ethylenediamine	CS_2 Deionized water	200	Co_9S_8 Co_3S_4 CoS_2	63
SiO_2 Dopamine Hydrochloride $RuCl_3$ L–cysteine	Deionized water	800	RuS_2 Nanoparticles Carbon spheres	67
$FeCl_3$ $CoCl_2$ Sulfur powder g–C_3N_4 Graphene oxide	Dicyandiamide	500	$Co_xFe_{1-x}S_2$@N–CNTs/rGO	71
Multiwalled carbon nanotubes $Fe(NO_3)_3$ Cobalt acetate	Anhydrous N,N–dimethylformamide (DMF),	180	$Fe_{1-x}Co_xS_2$/CNT	72
Cobalt(III) acetylacetonate Cuprous thiocyanate	Oleylamine	240	Co_x–Cu_7S_4 Nanodisks	68
$Fe(NO_3)_3$			FeS_x NiS_x CoS_x CrS_x	

$Ni(NO_3)_3$ $Co(NO_3)_2$ $Cr(NO_3)_2$ $Mn(NO_3)_2$	Isopropanol Glycerol	160	MnS_x $FeNiCoCrS_2$ $FeNiS_x$ $FeNiCoS_x$ $FeNiCoCrXS_2$ (where X is Cu, Zn, or Al)	76
$Co(NO_3)_2$ Sulfur powder Selenium powder	1-Butanol 2-Pluronic P123 Nitric acid	250	Meso–CoS_2 Meso–CoSSe	79
Fe $(NO_3)_3$ Ni $(NO_3)_2$ Solid duck blood, S powder	Deionized water	600	$Fe_xNi_{1-x}S_2$–C	81
$Ni(NO_3)_2$ $CO(NH_2)_2$ S powder Se powder $NaBH_4$	Deionized water Glycol	180	$NiSe_{1.2}S_{0.8}$	80
Graphene oxide $CoCl_2$ $NiCl_2$ CH_4N_2S	Deionized water	200	$Co_{1-x}Ni_xS_2$–C	82
$Co(NO_3)_2$ Trisodium citrate $K_3[Fe(CN)_6]$ Sulfur powder Selenium powder	Deionized water	350/250	Se–$(CoFe)S_2$	83
NiSO4 $N_2H_4•H_2O$ L-Cysteine M-Carbon cloth	Deionized water	600	Ni_9S_8–$NiS_{1.03}$–NSCs	84
$CoCl_2$ $NiCl_2$ Urea Na_2S $Co(NO_3)_2$ $Ni(NO_3)_2$	Deionized water	120	$NiCo_2S_4$@CoNi–LDH	75
$Co(NO_3)_2$ Glycerol Isopropanol Ammonia Sulfur powder	Deionized water	300	N–CoS_2 yolk–shell spheres	85

2.3 Synthesis of pyrite–type transition metal selenide (PT–TMS)

The earth–abundant 3d transition metal dichalcogenides are considered as the great promising catalysts for electrocatalytic water splitting to facilitate H_2 production in both basic and acidic mediums. Among them, the pyrite–structure selenides MSe_2 (M=Fe, Co, Ni) with optimal e_g occupancy regarded as alternative catalysts show great potential for the commercial application due to the superior intrinsic electrical conductivity than oxides and sulfides in HER and OER electrolysis appealing. Nevertheless, their electrocatalytic activity compared with noble metal electrocatalyst still needs to be further improved. In recent years, various approaches, such as heterostructure, incorporating dopants and vacancies engineering have developed efficient strategies to design cost–effective electrocatalysts with excellent activity and stability.

2.3.1 Single metal selenides

As one of the most common selenides, different morphology and size of $NiSe_2$ were well prepared and used for OER application. Xiao Li and co–workers prepared $NiSe_2$ by a solvothermal selenization method using nickel/oxidized foam (NF/NF(O_x)) as substrate.[86] Two kinds of Ni selenides were developed in this report with different phases of hexagonal and cubic (Figure 16a, b). According to the SEM images in Figure 16c, d, the $NiSe_2$ showed a pyramid shape when using NF(O_x) as support, while a nanorod structure was obtained when taking NF as substrate, revealing that the composition of the substrate had a great influence on the final structure of the materials. The electrochemical measurements suggested pyramid $NiSe_2$/NF (O_x) electrocatalyst showed an improvement OER activity with a smaller onset potential of 1.54 V compared to the NiSe/NF with the shape of the nanorod.[86]

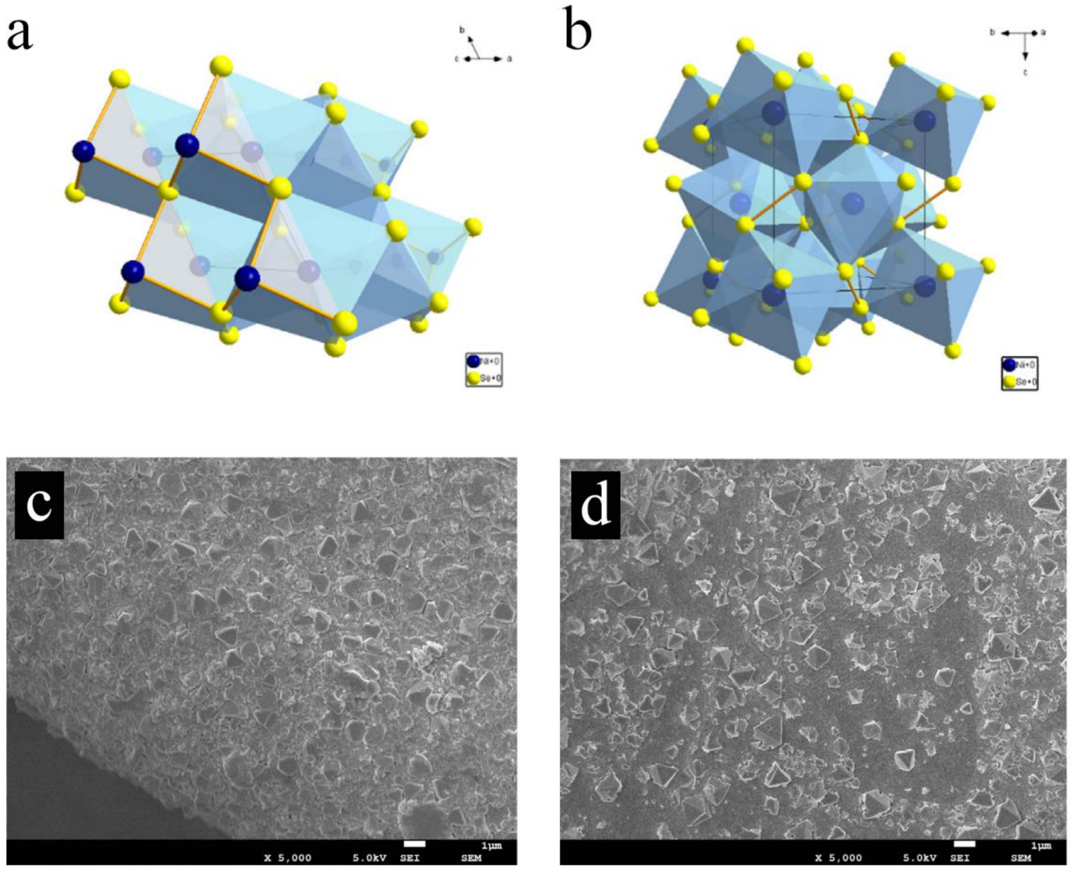

Figure 19. Crystal structure of (a) NiSe and (b) $NiSe_2$. The former is the hexagonal phase and the latter is the cubic phase. SEM images of (c) NiSe and (d) $NiSe_2$. Taken from Ref. 86 and modified.

As a complement, Lingling Zhai et al. found that the phase of the Ni selenide might change from cubic $NiSe_2$ to hexagonal NiSe in an alkaline medium during the electrocatalytic water splitting.[87] The cubic phase $NiSe_2$ materials were prepared through the thermal selenization approach. To observe the structural evolution, *Operando* Raman spectroscopy, and synchrotron X–ray powder diffraction (XRD) techniques were adopted to characterize the phase changes.[87] Both the XRD and Raman spectres indicated the Ni selenides transferred from the cubic to hexagonal phase together with the enhanced HER catalysis. The schematic diagram of the in–situ self–evolution process was recorded in Figure 20. The change of the phase of Ni–based selenides also might further drive the surface active sites to be more suitable for the catalytic system. Theoretical calculations discovered that the generated NiSe could act as the real active sites to possess an excellent conductivity and higher d–band center, thus benefiting for boosted catalytic activity.[87]

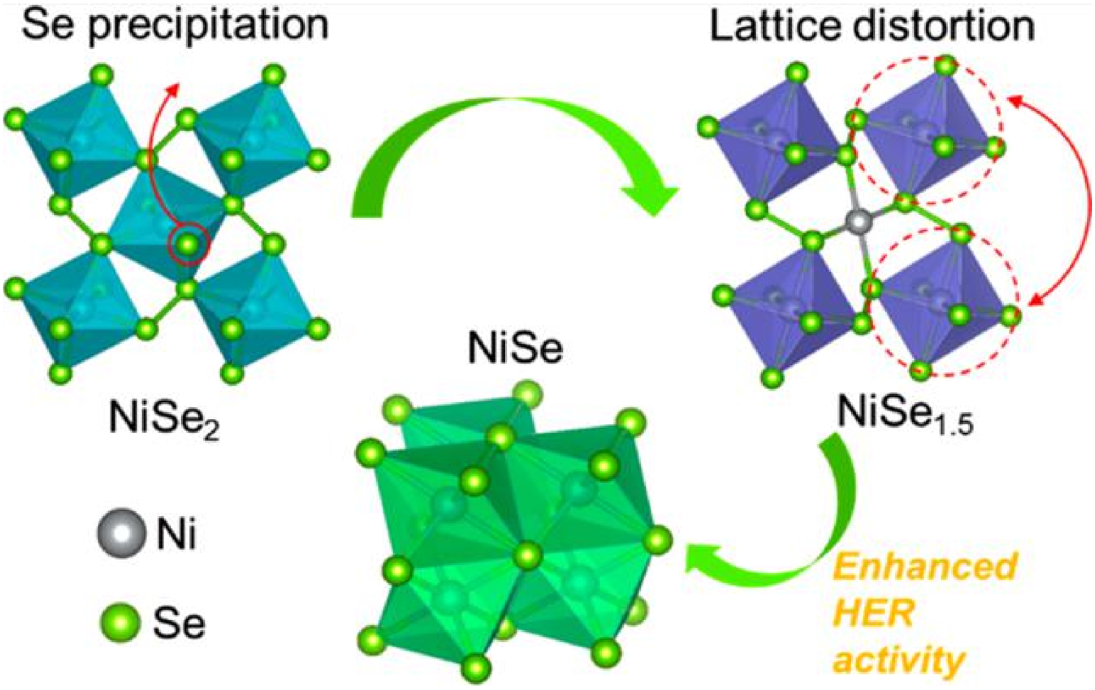

Figure 20. The phase evolution process of Ni–based selenides from the cubic to hexagonal phase. Taken from Ref. 87 and modified.

To further unleash the property of the pyrite–type $NiSe_2$ catalysts, a multilevel structure was fabricated by Fengmei Wang et al.[88] The reported pyrite–type $NiSe_2$ nanosheets were supported on the carbon fibers converted from $Ni(OH)_2$ nanosheets to Se–enriched $NiSe_2$ catalysts via chemical vapor deposition method. There were abundant particles scattered on the $NiSe_2$ nanosheet as shown in the TEM images in Figure 21. The EDS mapping images indicated the uniform distribution of Ni and Se elements of the $NiSe_2$ nanosheet. Additionally, the XRD and Raman spectres further confirmed the phase of pyrite–type $NiSe_2$. The Se–enriched $NiSe_2$ nanosheets played a prominent role in accelerating the adsorption of hydrogen intermediates. DFT calculation illustrated the H* adsorption free energy on the Se site was 0.13 eV, much lower than it on the Ni sites (0.87 eV), revealing the better desorption capacity of H*.[88] As expected, the $NiSe_2$ nanosheets showed an outstanding intrinsic HER activity with a lower overpotential of 117mV at a current density of 10 mA cm^{-2} and a low Tafel slope of 32 mV dec^{-1}.

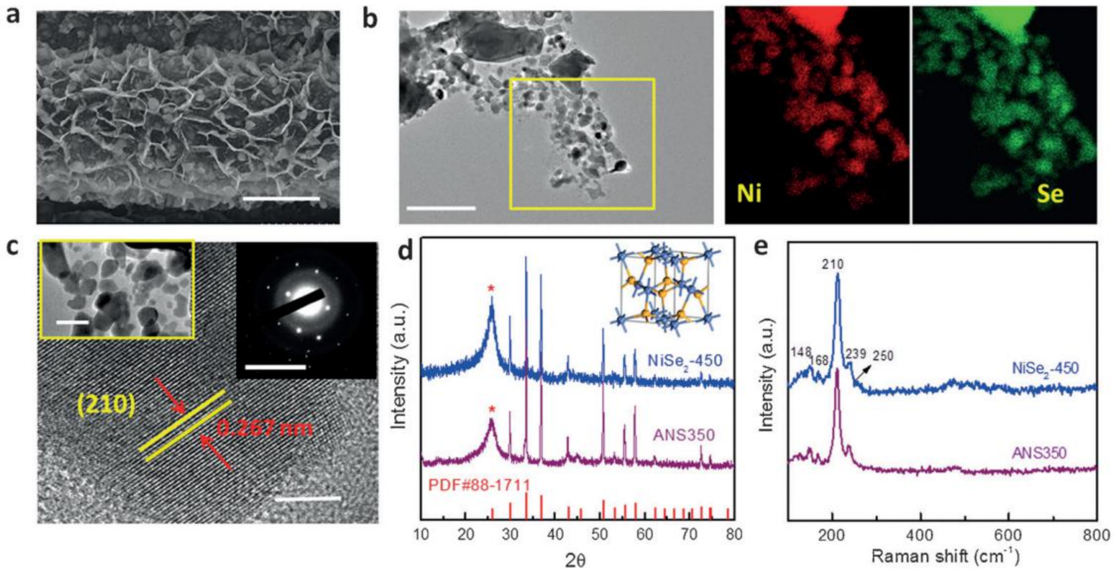

Figure 21. (a–c) The TEM characterization. (d) XRD and (e) Raman results of the $NiSe_2$. Taken from Ref. 88 and modified.

Similar to the Ni–based selenides, Co–based selenides were also received widely studied. Xiaobin Liu et al. synthesized the pyrite–type $CoSe_2$ microspheres by a MOF–assisted method.[89] At the beginning, the Co–MOF nanoparticles were designed first, then after annealing above 400 ℃, the highly selenized and dispersed $CoSe_2$ powder was obtained and the process was displayed in Figure 22.[89] Because of the porosity of Co–MOF, the as–prepared $CoSe_2$ microspheres also inherited the porous property, providing the large surface area which was benefiting for the OER catalysis application.[89] The hollow structure of $CoSe_2$ microspheres could offer more active sites due to the large number of edge atoms, which might facilitate mass transfer and electronic transportation. The pyrite–type $CoSe_2$ microspheres exhibited excellent OER performance compared to commercial IrO_2 catalyst, achieving an overpotential of 330 mV at 10 mA cm^{-2} and superior stability with negligible decay after 1000 cycles of voltammetry.[89]

Figure 22. Schematic illustration of the synthetic strategy of the $CoSe_2$ Microspheres. Taken from Ref. 89 and modified.

Recently, transition metal–based electrocatalysts phosphides and selenides have emerged as multifunctional OER electrocatalysts, due to their cost–effective and excellent conductivity.[90] Anion doping is an effective strategy to improve the intrinsic activity of the catalysts to meet the scalable OER application.[91,92] Ling Huang and co–workers reported a ternary Co–P–Se material prepared by a one–step method combined phosphorization and selenization process.[93] The initial CoO_x/CNTs were used as precursors. The special crystalline–amorphous heterostructure was constructed by the doping of Se atoms in CoP crystal to form the amorphous cobalt selenide ($CoSe_2$) as illustrated in Figure 23a. Using carbon nanotubes as a skeleton to support CoPSe–$CoSe_2$ could increase the specific surface area of the catalyst, and increase the accessible space between the materials and the electrolyte. With the increasing amount of Se, the coated P–$CoSe_2$ on CNTs appeared denser layer than the CoP/CNTs as shown in Figure 23 b–d. The CoPSe–$CoSe_2$/CNTs exhibited an improved OER activity with the amorphous $CoSe_2$, which afforded an overpotential of 268 mV at the current density of 10 mA cm^{-2}, as well as the good catalytic stability.[93]

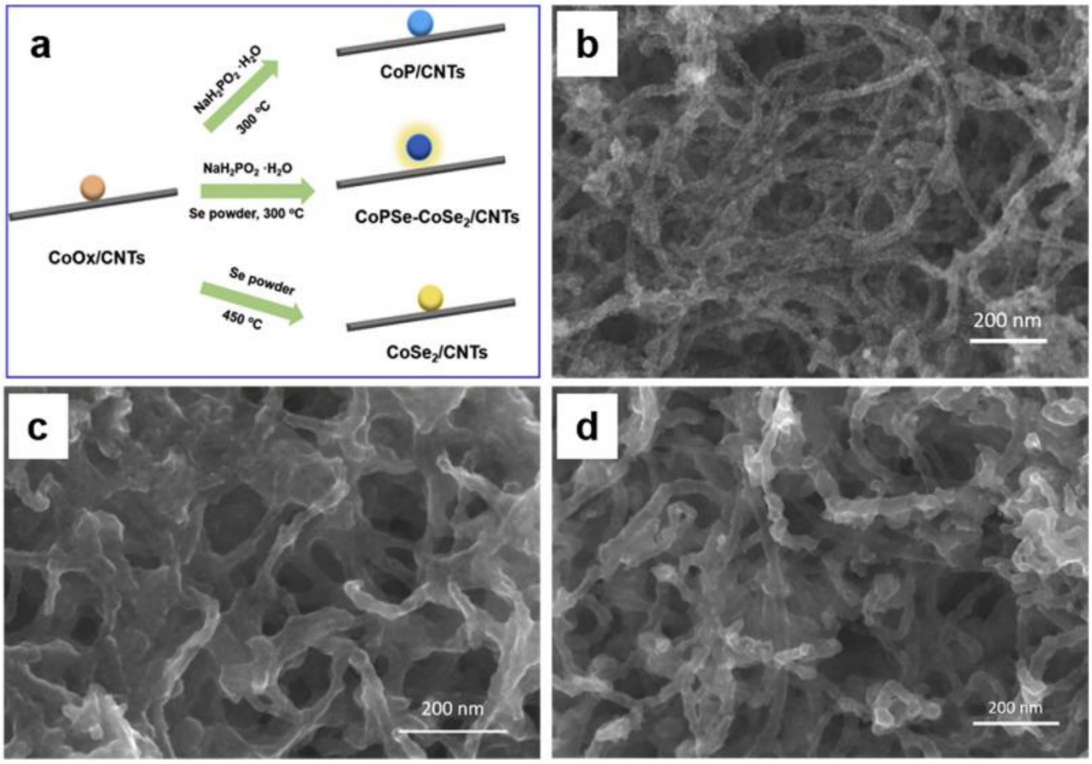

Figure 23. (a) The preparation process of CoP/CNTs, $CoSe_2$/CNTs, and CoPSe–$CoSe_2$/CNTs. (b–d) SEM images of the CoP/CNTs, $CoSe_2$/CNTs, and CoPSe–$CoSe_2$/CNTs. Taken from Ref. 93 and modified.

Hui Liu and co–workers introduced P into pyrite $NiSe_2$ nanosheets which were supported on carbon cloth (CC) through the thermal selenization and phosphorization method.[94] Firstly, the $Ni(OH)_2$ nanosheets were supported on CC by a simple hydrothermal process, immediately afterward, phosphorization and selenization were gradually carried out step by step to obtain the P doped $NiSe_2$/CC composite (Figure 24a).[94] The P–$NiSe_2$/CC sample presented excellent water splitting catalytic performance and ultra–long durability compared to $NiSe_2$.[94] Apart from the anion doping, the cation doped Ni/Co selenides have received special attention due to the suitable electronic configuration.[95–96] Shun Zhang et al. reported a substantive method to introduce the Ga atoms and the defects in pyrite $CoSe_2$ material. Layered Ga–$CoSe_2$ loaded on stainless steel mesh (Ga–$CoSe_2$/SSM), layered $CoSe_2$ nanosheets and $CoSe_2$ nanoparticles on SSM were systematically studied.[97] Among the three samples, Ga–$CoSe_2$ nanosheets with abundant oxygen vacancies were prepared by a multi–step method. The Co element was sputtered on the SSM to form a thin Co layer, and then painted by Ga element on the surface. After annealing, the Co and Ga layers would generate $CoGa_3$ alloy on the SSM. Interestingly, different concentrations and amounts of NaOH had a great influence on the final products of $CoSe_2$. When the concentration of NaOH increased, the products trended to be $CoSe_2$ nanoparticles, while the less amount and low concentration NaOH solution (50 mL, 0.5 M NaOH) was benefit for Ga–$CoSe_2$ nanosheets. It's noted that the low concentration NaOH solution could remove the Ga element in the $CoGa_3$ alloy by increasing the volume of NaOH (250 mL, 0.5 M NaOH).[97] The dealloying and selenization strategy mediated Ga–$CoSe_2$/SSM showed the outstanding OER activity with a small overpotential of 227 mV under 10 $mAcm^{-2}$ and long stability over 25 h.[97]

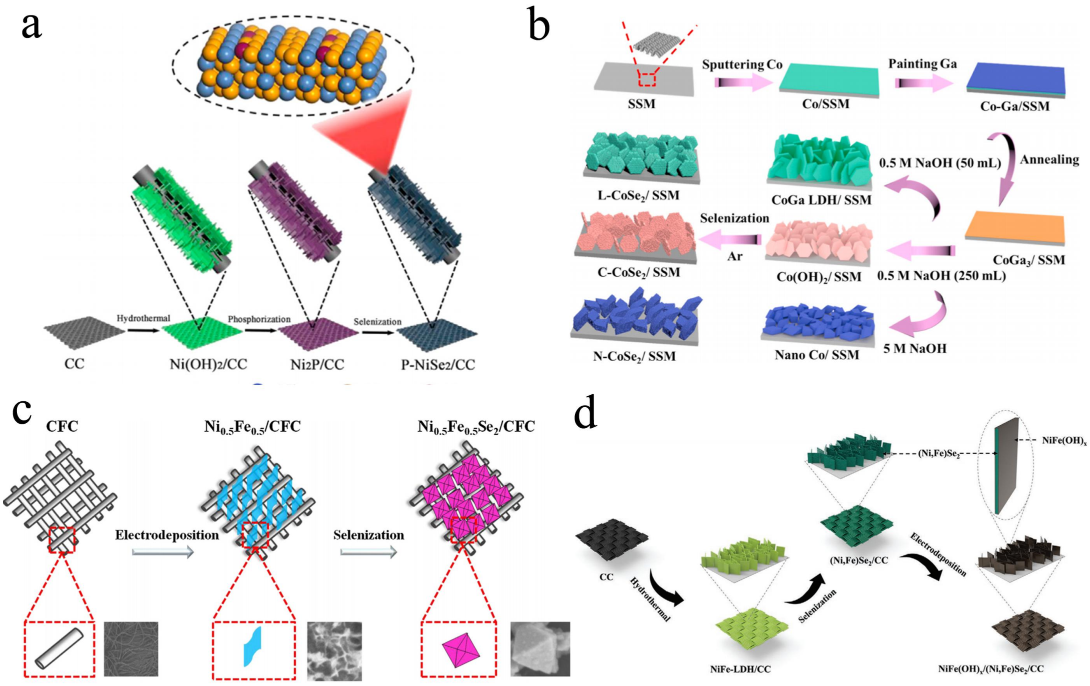

Figure 24. (a) The fabrication procedure of P–$NiSe_2$/CC.[94] (b) The preparation of layered Ga–$CoSe_2$/SSM, layered $CoSe_2$/SSM and $CoSe_2$ nanoparticles on SSM.[97] (c) The illustration of synthesis process for pyrite–type $Ni_{0.5}Fe_{0.5}Se_2$ on carbon fiber cloth.[98] (d) The preparation of $NiFe(OH)_x$/(Ni, Fe)Se_2 on carbon cloth.[99] Taken from Ref. 94, 97–99 and modified.

2.3.2 Polymetallic Selenides

Jing–Qi Chi et al. synthesized a pyrite–type binary diselenides ($Ni_{0.5}Fe_{0.5}Se_2$) supported on carbon fiber cloth (CFC) by a facile two–step process.[98] $Ni_{0.5}Fe_{0.5}$ hydroxide nanosheets were electrodeposited on the CFC and followed by solvothermal selenization, $Ni_{0.5}Fe_{0.5}Se_2$/CFC catalyst with octahedral morphology and uniform size was obtained (Figure 24c).[98] The systematic investigation about the effect of the different ratios of Ni/Fe ($Ni_xFe_{1-x}Se_{2x}$ = 0, 0.2, 0.5, 0.8, 1) revealed the ratio of Ni/Fe had a significant effect on OER activity. The $Ni_{0.5}Fe_{0.5}Se_2$/CFC had the best OER activity than other samples. Jing–Qi Chi et al. prepared the $Fe_{0.5}Co_{0.5}Se_2$ spheres as an effective electrocatalyst for enhanced OER application. The $Fe_{0.5}Co_{0.5}Se_2$ spheres were synthesized on CFC through a two–step method, including electrodeposition and solvothermal selenization. SEM images indicated that the $Fe_{0.5}Co_{0.5}Se_2$ had good–dispersion and uniform size of about 100 nm, which exposed large number of active sites. The $Fe_{0.5}Co_{0.5}Se_2$ displayed the excellent OER property than other samples, with a lower overpotential, smaller Tafel slope and better stability.[99]

Caichi Liu et al. reported a heterostructure consisting of amorphous NiFe–based (oxy)hydroxides and crystalline pyrite (Ni, Fe)Se_2 nanosheets for boosted OER performance.[100] The crystalline pyrite (Ni, Fe)Se_2 nanosheets showed great potential in contributing to the stability together with the amorphous NiFe–based (oxy)hydroxides, suggesting a strong synergistic effect between the two components. Profiting from the interface coupling effect, the $NiFe(OH)_x$/(Ni, Fe)Se_2 possessed splendid electrical conductivity and optimized adsorption energy of O–intermediates, thus realizing the outperforming OER performance with an overpotential of 180 mV at 10 mA cm^{-2} and a small Tafel slope of 42 mV dec^{-1}.[100]

Constructing the heterojunction is another facile way to control the electronic structure of the materials.[102,103] Generally, connecting two structures of different components in one material is the most common heterostructure. Developing different ways to synthesize heterostructures of pyrite–type TMDs are as important as the preparation of heteroatom doping or morphology controlling of these catalysts.[104–106] Shan Ni *et al.* reported an interfacial engineering strategy to construct $NiSe_2/FeSe_2$ p–p heterojunction by a thermal selenization method.[107] The TEM images in Figure 25 clearly showed the stacked particle morphology of the as–prepared $NiSe_2/FeSe_2$ p–p heterojunction with particle size more than 100 nm. There were abundant grain boundaries in the $NiSe_2/FeSe_2$ material based on the high–resolution TEM image. The heterostructure was beneficial to promote charge transfer and redistribution at heterointerface, which would facilitate the adsorption ability of the OH^- intermediate, thus improving the OER activity. Surprisingly, the $NiSe_2/FeSe_2$ p–p heterojunction showed an overpotential of 256 mV under 10 $mAcm^{-2}$, and even surpassed the benchmark RuO_2 noble–catalyst.[107]

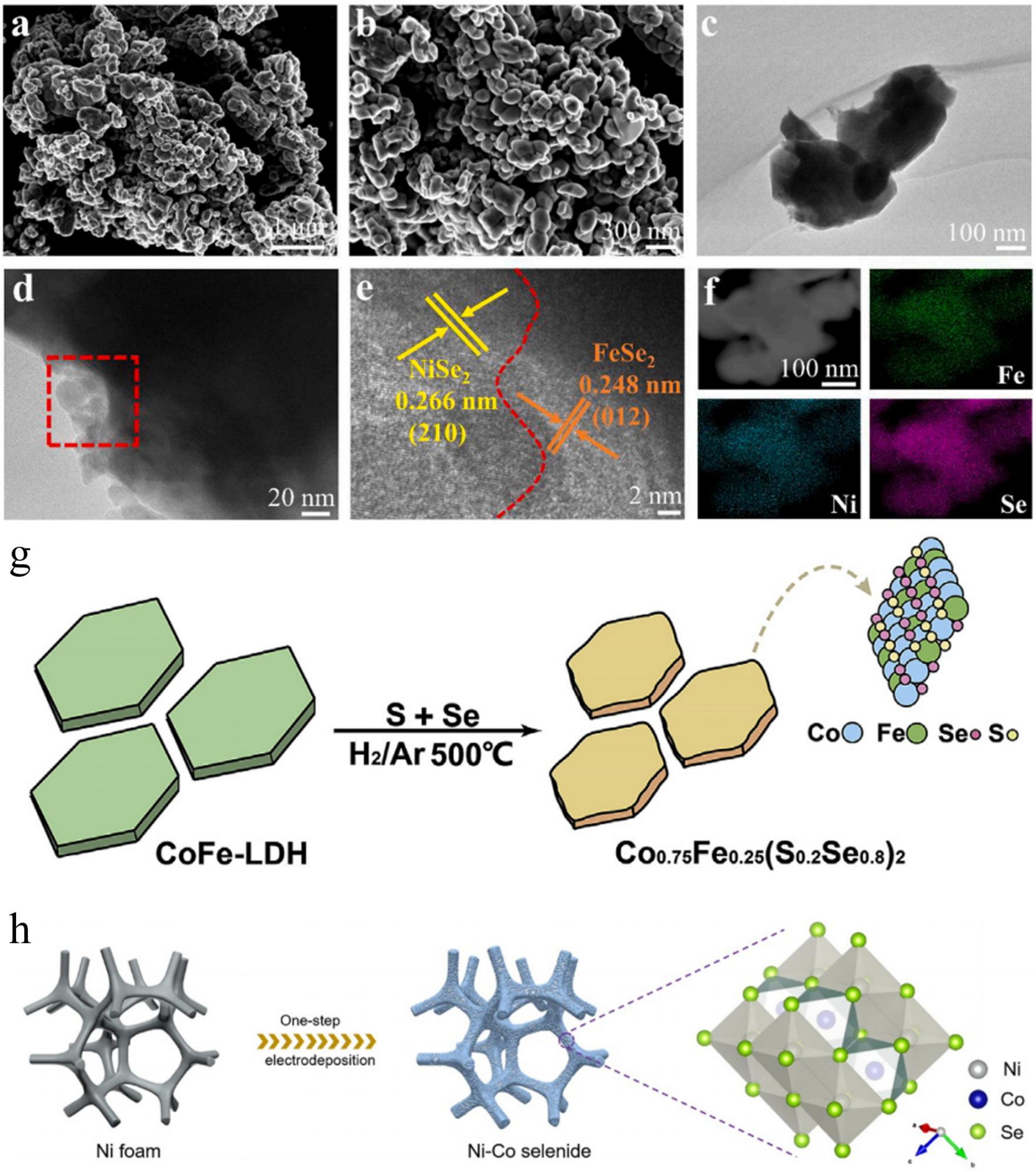

Figure 25. (a, b) SEM, (c–e) TEM and (f) EDS element mapping images of $NiSe_2/FeSe_2$ catalysts.[106] (g) Evolution process from CoFe–LDH precursor to $Co_{0.75}Fe_{0.25}(S_{0.2}Se_{0.8})_2$.[107] (h) The synthesis process of NiCo selenides.[108] Taken from Ref. 106–108 and modified.

An anion doped bimetallic selenide $Co_{0.75}Fe_{0.25}(S_{0.2}Se_{0.8})_2$ was developed by Huiying Kang et al. through simultaneous sulfuration and selenylation.[108] The scalably produced CoFe–layered double hydroxides (CoFe–LDHs) were used as a precursor to react with S and Se sources (Figure 25g). The irregular nanoplatelet–like $Co_{0.75}Fe_{0.25}(S_{0.2}Se_{0.8})_2$ demonstrated a highly porous structure that possessed excellent OER activity than those of $Co_{0.75}Fe_{0.25}S_2$ and $Co_{0.75}Fe_{0.2}Se_2$ materials.[108] The target $Co_{0.75}Fe_{0.25}(S_{0.2}Se_{0.8})_2$ catalyst owned the lowest OER overpotential of 293 mV under 10 mA cm^{-2} in 1M KOH, much better than it of commercial IrO_2 powder.[108] The facile and effective approach in this process could provide a strategy to prepare the highly efficient sulfides and selenides for water splitting. Different from the multi–step strategy, Lin Lv and co–workers constructed a yolk–shell structure based on nickel–cobalt diselenides ($NiCoSe_2$) to boost OER properties.[109] The $NiCoSe_2$/Ni catalysts were directly electrodeposited on the Ni foam under nanoscale and the yolk–shell structure was formed by the Kirkendall effect (Figure 25h). In addition, the e_g filling of Ni could be modulated by altering the atomic ratio of Ni/Co for enhanced OER performance. To reach the current density of 10 mA cm^{-2}, the overpotential of $NiCoSe_2$/Ni was only 249 mV, and Tafel slope of 43 mV dec^{-1}. Surprisingly, the $NiCoSe_2$/Ni showed good stability of 20 h electrolysis with only a slight increment of 23 mV.[109] Based on the similar Kirkendall effect mechanism, Jianwei Nai et al. prepared the Ni–Fe mixed diselenide nanocages with a uniform size of ~100 nm.[110] A self–templating strategy from original prussian–blue nanocubes used ammonia as an etchant to obtain hollow Ni–Fe mixed diselenide nanocages. The SEM and TEM images in Figure 26 reflected the etching process of the hollow structure from the corner to the internal position. The three–dimensional (3D) accessible open nanocubes offered more active sites in the catalysts for the OER application. Due to the 3D hollow structure in nanoscale, the Ni–Fe mixed diselenide nanocages presented the OER overpotential as low as 240 and 270 mV under the current density of 10 and 100 mA cm^{-2} in alkaline medium, respectively.[110] The Fourier transform infrared (FTIR) spectra indicated the etching process mainly occurred on the $Ni^{II}–N≡C–Fe^{III}$ sites as the ammonia molecule etched the atoms.[110]

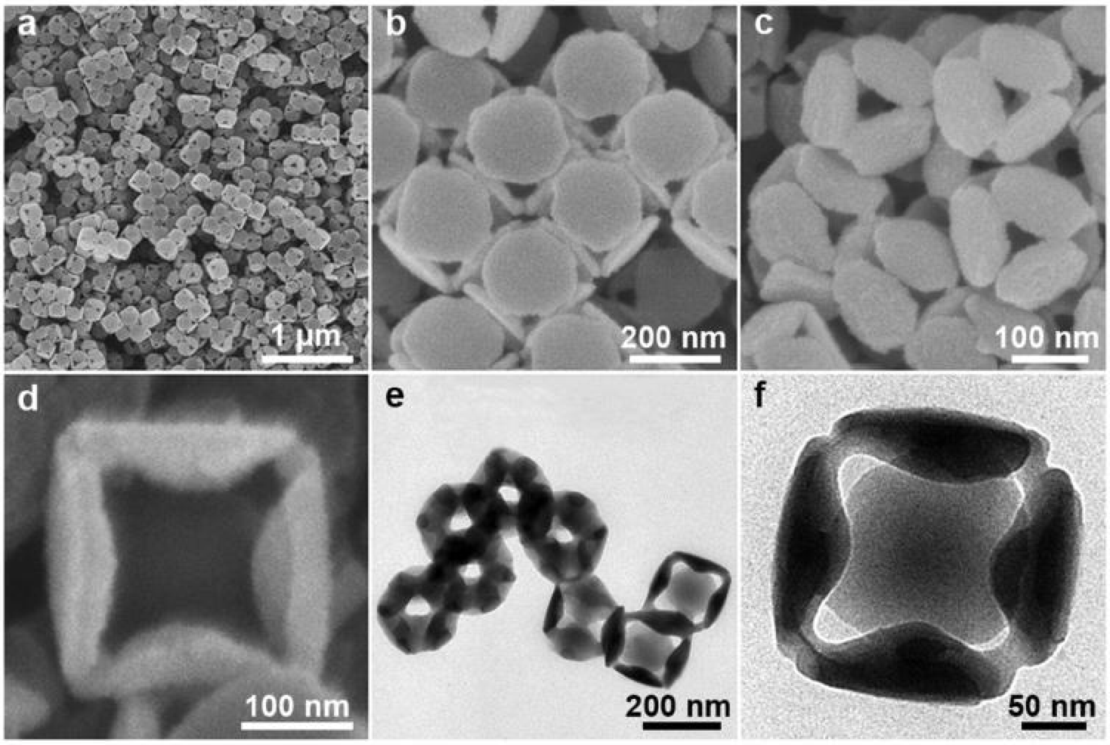

Figure 26. (a–d) SEM and (e, f) TEM images of the Ni–Fe PBA nanocages. Taken from Ref. 110 and modified.

Jun Zhou *et al*. reported an efficient electrocatalyst toward OER by a facile chemical bath method to prepare Fe–doped marcasite–type $NiSe_2$ (m–$Ni_{1-x}Fe_xSe_2$).[111] Unlike pyrite structure, the catalyst was designed via incorporating phase engineering and heteroatom doping, which could effectively modify the electronic structure and expose more active sites.[111] Firstly, the phase tuned from pyrite $NiSe_2$ to marcasite $NiSe_2$, then the Fe–doping method was adopted to further modify the conductivity of the catalysts (Figure 27a).[111] During the OER process, the *in-situ* formed amorphous Fe–doped NiOOH/$Ni(OH)_2$ shells were conducive to improving the catalytic activity and exhibited a surprising overpotential of 279 mV at 10 mA cm^{-2} with low Tafel slope and long stability.[111] Yunxiao Li and co–workers reported a simple strategy to improve the OER catalytic property of Ni–based catalysts by Fe–doping.[112] The porous $Ni_xFe_{1-x}Se_2$ nano–microspheres were prepared by solvothermal approach, which was conducive to improving the intrinsic activity of the materials. The aggregates of NiFe LDH offered the initial porous template for the liquid–phase selenization (Figure 27b). The porous $Ni_xFe_{1-x}Se_2$ nano–microspheres exhibited superior OER activity with the overpotential of 285 mV under 10 mA cm^{-2}.[112]

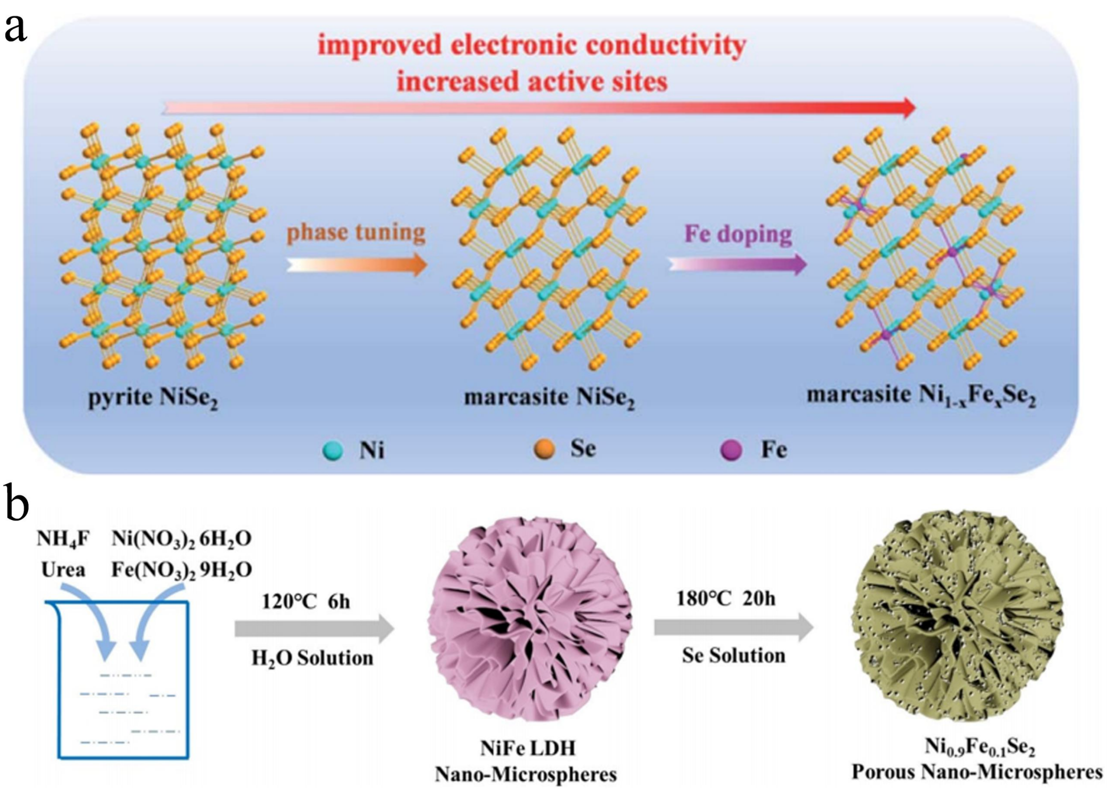

Figure 27. (a) Synthesis process of m–$Ni_{1-x}Fe_xSe_2$.[111] (b) The preparation of porous $Ni_xFe_{1-x}Se_2$ nano–microspheres.[112] Taken from Ref. 111, 112 and modified.

Gui Mei *et al.* synthesized a series of Mn–Co based yolk–shell catalysts as active species toward water splitting by annealing MnCo glycolate precursor (Figure 28a).[113] The SEM images of Mn–Co spheres in Figure 28b–d displayed micron–level size with the porous structure. Moreover, the HRTEM image in Figure 28e–h indicated the Mn–Co–based yolk–shell spheres owned typical $CoSe_2$ and $MnSe_2$ phases with the corresponding SAED and lattice arrangements.[113] In comparison with Mn–Co–based oxide and hydroxide, the selenide showed better OER catalytic activity among those compounds, which was attributed to the intrinsic conductivity and abundant active sites in selenides. In addition, the Mn and Co could play a synergy role in optimizing the adsorption energy of O–intermediates to reduce overpotential. Excellent catalytic performance with a cell voltage of 1.66 V under the current density of 50 mA cm^{-2} was obtained, better than most of the transition metal catalysts.[113]

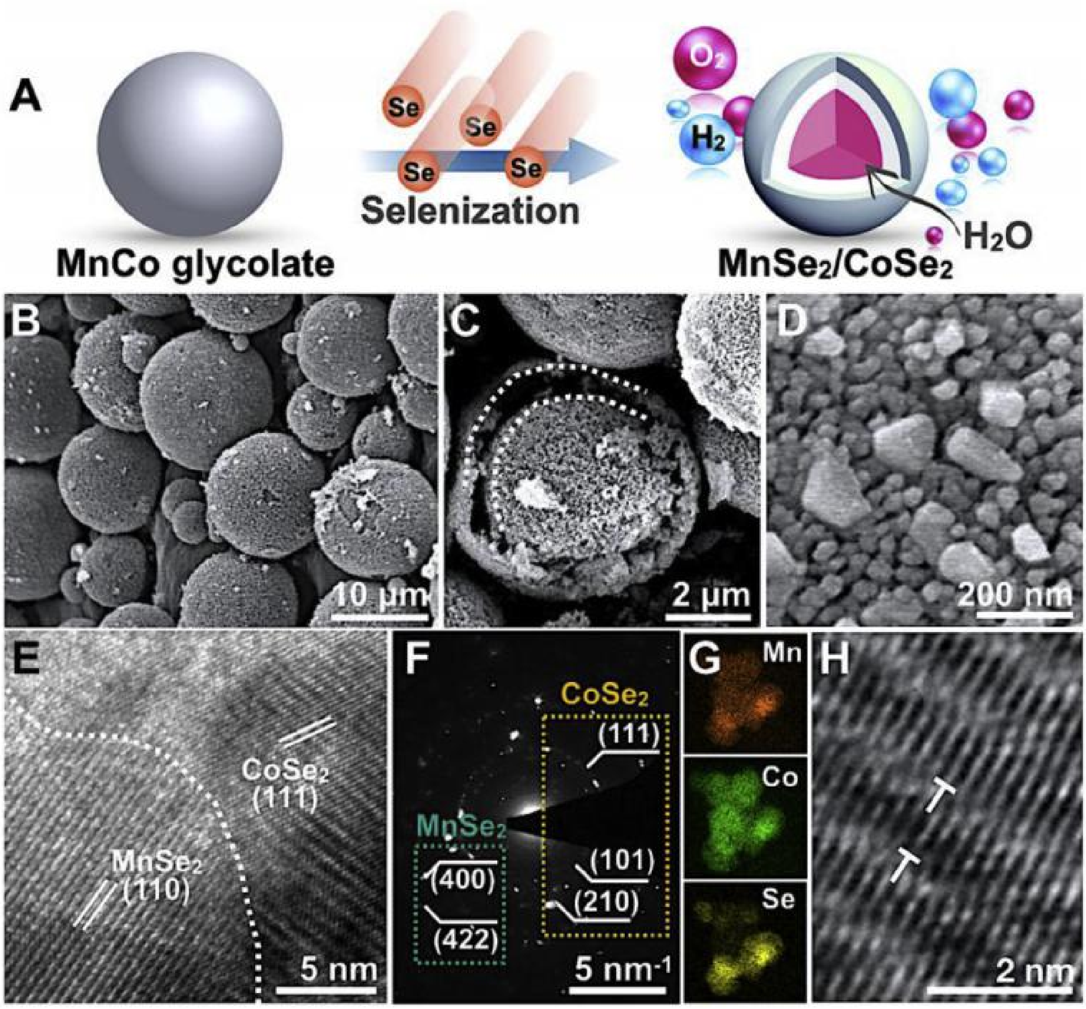

Figure 28. (a) The synthesis process of Mn–Co–Se yolk shell structure. (b–d) SEM and (e, h) HRTEM images, (f) the corresponding SAED pattern, (g) EDS results of Mn–Co–Se.[113] Taken from Ref. 113 and modified.

Similarly, Guoxing Zhu et al. reported $FeSe_2@CoSe_2$ core–shell particles loaded on reduced graphene oxide (rGO) acted as efficient electrocatalysts for OER, which was successfully prepared by a two–step solvothermal method (Figure 29).[114] The metal precursor was mixed with the rGO first to generate suspension, followed by adding $Se–N_2H_4$ solution for liquid selenization. The prepared $FeSe_2$/rGO composite further reacted with $CoCl_2$ solution under 180℃ to load a layer of Co–based compound. After annealing in Ar, $FeSe_2$@$CoSe_2$/rGO composite was finally generated.[114] Because of the large number of active sites induced by heterointerfaces, the charge interaction was further enhancement better than those of $CoSe_2$/rGO, $FeSe_2$/rGO, resulting in boosted OER performance. The $FeSe_2$@$CoSe_2$/rGO showed a lower overpotential of only 260 mV under 10 mA cm^{-2} and excellent durability compared with other catalysts.[114]

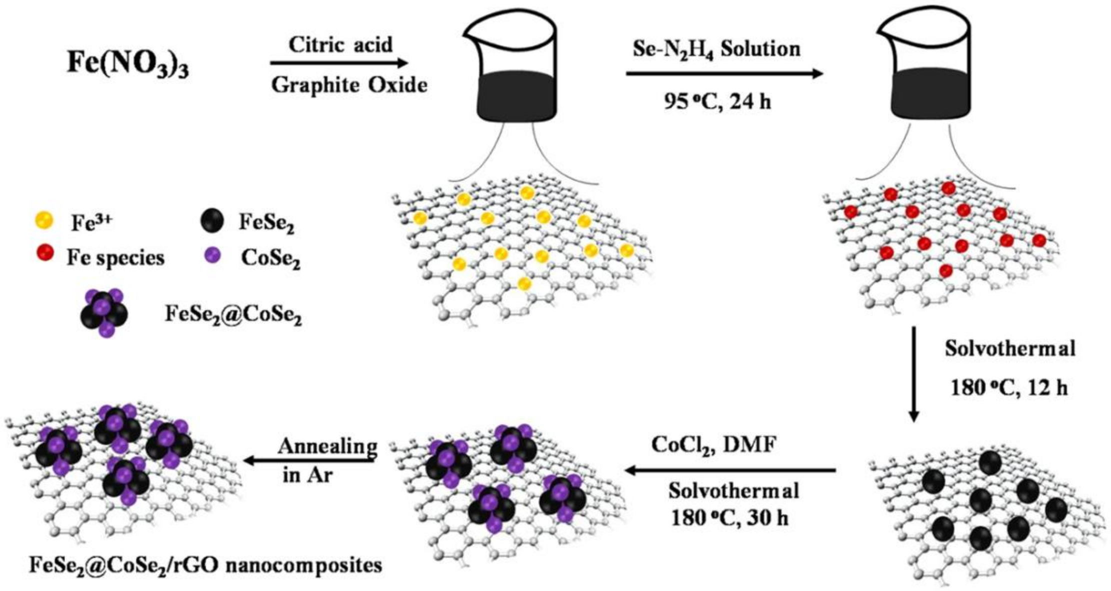

Figure 29. Schematic Illustration of the Preparation of the $FeSe_2$@$CoSe_2$/rGO Composite by Two Solvothermal Steps.[114] Taken from Ref. 114 and modified.

Zhi–Mei Luo et al. developed a self–template approach to prepare a hierarchical Co−Se−S−O ($CoSe_xS_{2-x}$@$Co(OH)_2$) nanotubes on CC for promoting OER catalysis in alkaline and neutral conditions.[115] The self–standing catalyst was prepared by a facile strategy consisting of selenization and sulfurization process, using Co(OH)F as precursor through anion–exchange. The in situ preparation process was shown in Figure 30, including the in situ conversion from the corresponding oxides to $CoSe_xS_{2-x}$@$Co(OH)_2$.[115] The two stepwise Kirkendall effects represented the large surface area and good conductivity of the $CoSe_xS_{2-x}$@$Co(OH)_2$ materials. As expected, the $CoSe_xS_{2-x}$@$Co(OH)_2$ exhibited an overpotential of 230 mV at 10 mA cm^{-2}, which was much superior to its monochalcogenide and counterparts, as well as commercial IrO_2.[115]

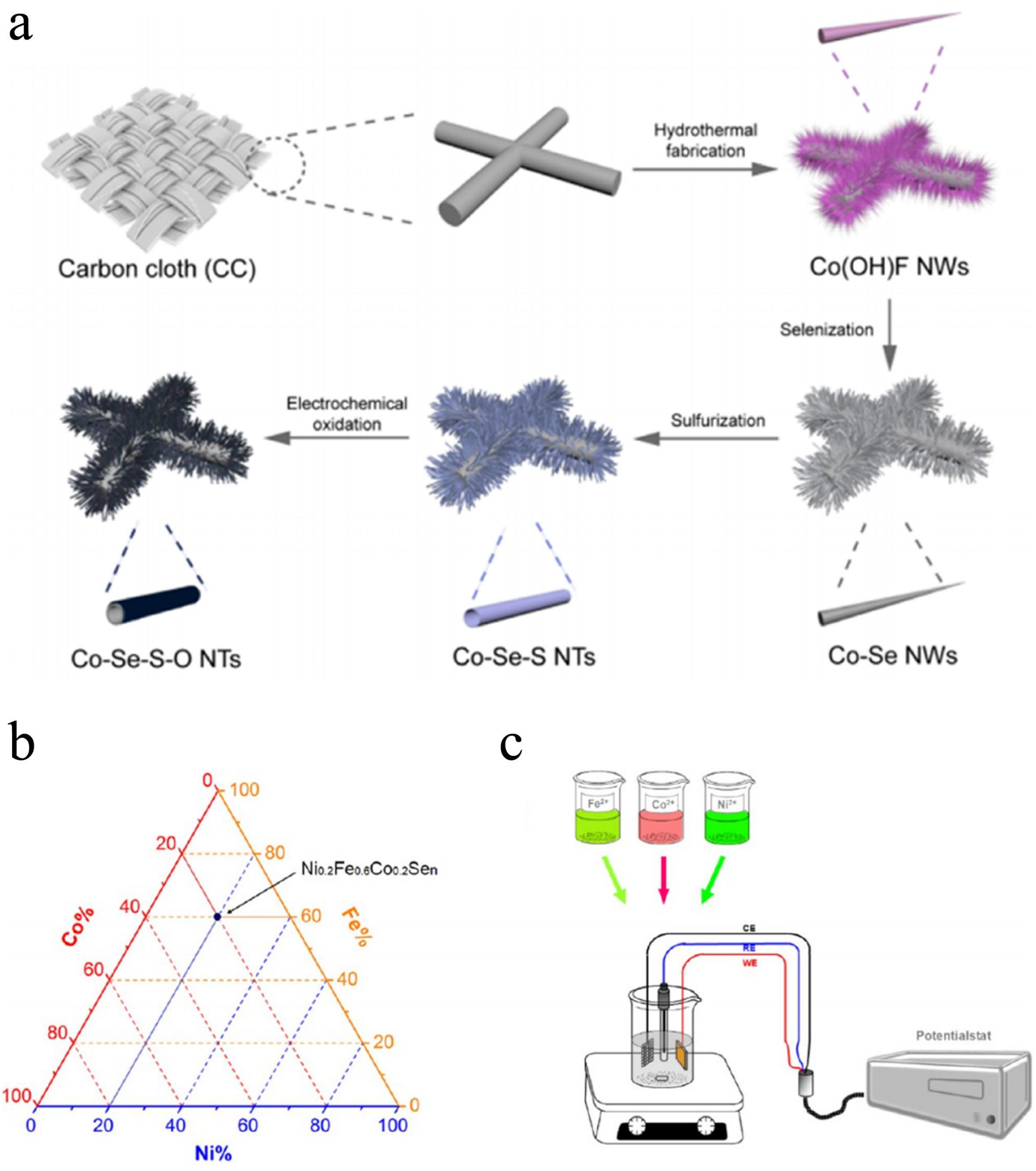

Figure 30. (a) Conversion process of $CoSe_xS_{2-x}@Co(OH)_2$.[115] (b) Ternary phase diagram for preparation of $Ni_{0.2}Fe_{0.6}Co_{0.2}Se_n$ and (c) The experimental set–up for electrodeposition.[116] Taken from Ref. 115, 116 and modified.

Quaternary mixed–metal selenides were investigated by Xi Cao and co–workers by combinatorial electrodeposition method based on the ternary phase diagram.[116] The binary, ternary and quaternary selenides were synthesized to identify the relationship between the OER activity and compositions.[116] The $(Ni_{0.25}Fe_{0.68}Co_{0.07})_3Se_4$ had the best OER activity than binary and ternary selenides with an overpotential of 230 mV at 10 mA cm^{-2}.[116] The first–principle density functional theory (DFT) was employed to calculate the hydroxyl adsorption energy on the catalyst, the $(Ni_{0.25}Fe_{0.68}Co_{0.07})_3Se_4$ was conductive to adsorb hydroxyl, resulting in a small onset potential, consisted with the experimental data.[116] Guojing Wang et al. prepared a series of metal–doped nickel–based selenide nanowires ($Ni_{1-x}M_xSe_2$ NWs) supported on the carbon fiber paper (CFP). The $Ni_{1-x}M_xSe_2$ NWs were applied as electrocatalyst for ammonia–borane electrooxidation. Based on the electrochemical results, the Cu substitution ($Ni_{1-x}Cu_xSe_2$) achieved superior catalytic activity than $Ni_{1-x}Co_xSe_2$ and $Ni_{1-x}Fe_xSe_2$. The $Ni_{1-x}M_xSe_2$ NWs have been modulated into a surface layer of $Ni_{1-x}M_xSe_{2-y}$–OOH NSs after the ammonia–borane electrooxidation. This *in–situ* conversion process offered the unique nanoarchitecture and electronic structure that contributed to the higher OER activity due to the superior intrinsic activity and a large amount of accessible active sites.[117] There were many other novel methods developed to synthesize selenides for different electrocatalytic applications. Jiajun Wang et al. reported a novel polyol solution reduction method to synthesize $CoIn_2Se_4$ electrocatalyst.[118] The Se powder dissolved in poly(vinylpyrrolidone), triethylene tetramine, and triethylene glycol mixture solution, then reacted with $Co(NO_3)_2$ and $InCl_3$ to form the $CoIn_2Se_4$ nanosheets (Figure 31a).[118] The $CoIn_2Se_4$ nanosheets showed Co^{2+} occupied tetrahedral sites while In^{3+} in the octahedral sites, which was consistent with spinel structure. After the incorporation of indium into $CoSe_2$ crystal, the reaction energy barrier was significantly reduced compared to $CoSe_2$ and In_2Se_3.[118] The catalytic activity for OER was drastically promoted, achieved a low overpotential of 315 mV under 10 $mAcm^{-2}$. In addition, the $CoIn_2Se_4$ nanosheets displayed high efficiency and long–stability of overall water–splitting.[118]

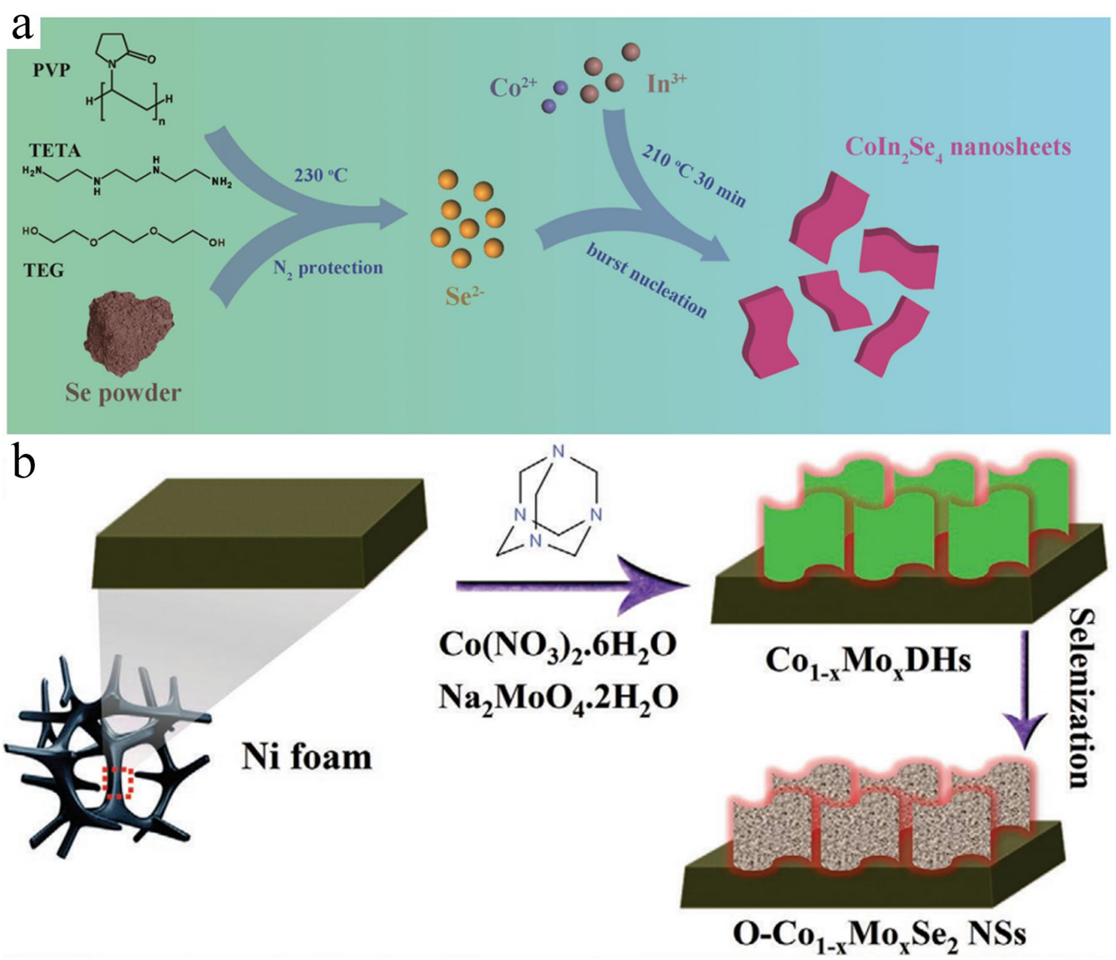

Figure 31. (a) The preparation process of $CoIn_2Se_4$.[118] (b) The fabrication process of the O–$Co_{1-x}Mo_xSe_2$ ($0 \leq x \leq 1$) self–standing nanosheets.[119] Taken from Ref. 118, 119 and modified.

Sampath Prabhakaran et al. reported a 3D hierarchical O–$Co_{1-x}Mo_xSe_2$ ($0 \leq x \leq 1$) nanosheets based on Mo–dopant $CoSe_2$ by a two–step simple hydrothermal method to construct attractive nanostructure as shown in Figure 31b. [119] The intermediate $Co_{1-x}Mo_x$DHs supported the final sheets structure of O–$Co_{1-x}Mo_xSe_2$ ($0 \leq x \leq 1$). Due to the large surface area and optimal electrochemical active sites of the catalyst, the electrocatalyst demonstrated improved OER catalytic performance with an overpotential of 189 mV at 10 mA cm^{-2}. Moreover, the O–$Co_{1-x}Mo_xSe_2$ ($0 \leq x \leq 1$) achieved attractive voltage (1.5 V) for overall water splitting, which was superior to that of the state–of–the–art Pt/C||RuO_2 catalyst.[119] Kang Jiang *et al.* found an electrochemical method to construct single platinum atoms supported on nanoporous $Co_{0.85}Se$

(Pt/np–$Co_{0.85}Se$) to facilitate the HER catalysis.[120] The electrochemically selective etching mediated Co vacancies in the np–$Co_{0.85}Se$ could anchor the Pt atoms and offer a suitable coordination environment to stabilize Pt atoms. The Pt/np–$Co_{0.85}Se$ demonstrated excellent activity with near–zero onset overpotential and a low Tafel slope of 35 mV dec^{-1}, due to the modulation of surface active centers toward the near–optimal adsorption/desorption behaviors.[120]

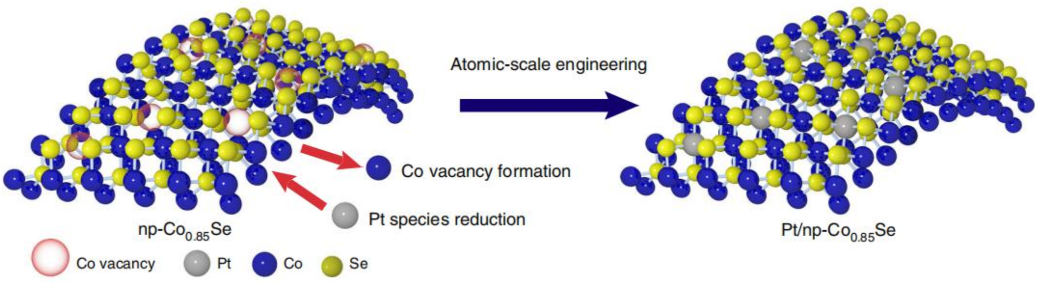

Figure 32. The fabrication procedure of Pt/np–$Co_{0.85}Se$. Taken from Ref. 120 and modified.

Sustainable energy is used for electrocatalytic water splitting to produce hydrogen, which acts as alternative energy to replace fossil fuels for low–carbon economy. Pyrite–type selenides had received extensively studied in recent years as effective catalysts for electrocatalytic water splitting. Numerous methods have been developed to synthesize catalysts of various morphologies, sizes and components, including heterostructure, and anion/cation doping. In this part, we had summarized many related results reported by the recent papers. Table 2 presents these methods in detail.

Table 2. The summarization of the methods with different precursors for synthesizing metal selenides.

Precursors	Solvents	Reaction temperature (°C)	Catalysts	Reference

NaOH $(NH_4)_2S_2O_8$, Se powder, NaHB4	Deionized water	140	$NiSe_2$ particles NiSe	86
Carbon fibers $Ni(NO_3)_2$ Hexamethylenetetramine Se powder	Deionized water	400 450 500	$NiSe_2$ nanosheets	88
$Co(NO_3)_2$ 1,3,5–benzenetricarboxylic acid selenium powder	Glycol Ethanol	400 450 550	$CoSe_2$ microspheres	89
Carbon nanotubes $NH_3 \cdot H_2O$ $NaH_2PO_2 \cdot H_2O$ Se powder Cobalt acetate	Ethanol	300/400	CoPSe–$CoSe_2$/CNTs	93
$Ni(NO_3)_2$ NH_4F NaH_2PO_2 Se powder	Deionized water	350/450	P–$NiSe_2$/CC	94
Co target Ga (99.99 wt%) Stainless steel mesh (SSM) NaOH Selenium powder	Deionized water	450	Ga–$CoSe_2$/SSM	97
Carbon fiber cloth $Ni(NO_3)_2$ $Fe(NO_3)_3$ Se powder $NaHB_4$	Deionized water	60	$Ni_{0.5}Fe_{0.5}Se_2$/CFC	98

N, N–dimethylformamide				
$Ni(NO_3)_2$ $Fe(NO_3)_3$ NH_4F Urea $NaBH_4$ Se powder Carbon cloths	Deionized water	60	$NiFe(OH)_x/(Ni, Fe)Se_2/CC$	100
$CoCl_2$ $C_6H_5O_7Na_3$ $K_3Co(CN)_6$ $K_2Ni(CN)_4$ $FeCl_2$ $NiCl_2$ Prussian blue Se powder	Deionized water	500	$NiSe_2/FeSe_2$	107
$Fe(NO_3)_2$ $Co(NO_3)_2$ Se powder S powder	Deionized water	500	$Co_{0.75}Fe_{0.25}(S_{0.2}Se_{0.8})_2$	108
$NiCl_2$ $CoCl_2$ LiCl Ni foams SeO_2	Deionized water	150	$NiCoSe_2$	109
Nickel(II) acetate tetrahydrate, Trisodium citrate dihydrate, Potassium hexacyanoferrate(III), $NH_3 \cdot H_2O$ Ethanol Se powder	Methanol Deionized water	350	Ni–Fe Mixed Diselenide Nanocages	110

$Co(NO_3)_2$ $Fe(NO_3)_3$ Se powder $NaHB_4$ DMF	Deionized water	60	$Fe_{0.5}Co_{0.5}Se_2$ spheres	98
$NiCl_2$ $FeCl_3$ Se Powder Oleylamine	Oleylamine	180	m–$Ni_{1-x}Fe_xSe_2$	111
$Co(CH_3CO_2)_2$ $Ni(NO_3)_2$ $Fe(NO_3)_3$ Urea NH_4F	Deionized water	120	$Ni_xFe_{1-x}Se_2$ Porous nano–microspheres	112
$Mn(CH_3COO)_2$ $Co(NO_3)_2$ Urea ethylene glycol Se powder NaOH	No	450	MnCo selenide yolk shell structures	113
$Fe(NO_3)_3$ Se powder Citric acid $N_2H_4·H_2O$ Graphene oxide $CoCl_2$ Polyvinylpyrrolidone	Distilled water N,N–dimethyl formamide (DMF)	180	$FeSe_2$@$CoSe_2$/rGO Composite	114
$Co(NO_3)_2$ IrO_2 Carbon cloth NH_4F $NaBH_4$ Se powder	Deionized water	140	$CoSe_xS_{2-x}$@$Co(OH)_2$	115
$NiSO_4$ $CoSO_4$ $FeSO_4$ selenium dioxide	Deionized water	Room temperature	$(Ni_{0.25}Fe_{0.68}Co_{0.07})_3Se_4$	116

$(NH_4)_2SO_4$ KOH				
$Co(NO_3)_2$ $Ni(NO_3)_2$ Urea $CuCl_2$ $NiCl_2$ $NaBH_4$ Carbon fiber paper	Deionized water	400	$Ni_{1-x}M_xSe_{2-y}$–OOH	117
$Co(NO_3)_2$ Indium chloride Poly(vinylpyrrolidone)	Triethylene glycol Triethylene tetramine	210	$CoIn_2Se_4$ nanosheets	118
$Co(NO_3)_2$ Na_2MoO_4 $C_6H_{12}N_4$ Selenium powder $NaBH_4$ Ni foam	Deionized water	180	O–$Co_{1-x}Mo_xSe_2$	119
Co poeder CoSe powder	No	High temperature	np–$Co_{0.85}Se$	120

3. Reaction mechanism analysis

Electrocatalytic water splitting based on renewable energy to produce hydrogen gas is an attractive strategy for the sustained development of society. Recently, numerous studies found various materials for highly effective OER activity, including transition metal oxides, transition metal sulfides, transition metal selenides, transition metal oxyhydroxides, etc.[121–123] Systematic understanding of the mechanism of electrocatalytic water splitting will effectively promote the development of advanced electrocatalysts. During the HER and OER reactions, H^+ or OH^- in the electrolyte will be involved in the catalytic process, resulting in the pH–related catalytic mechanism.[124–128] For water decomposition, it contains anodic and cathodic reactions. In acidic solution, the anodic reaction is $H_2O = 1/2O_2 + 2H^+ + 2e^-$, but in the alkaline medium, the anodic reaction is $2OH^- = 1/2O_2 + H_2O + 2e^-$.[124] Similarly, the cathodic reaction is $2H^+ + 2e^- = H_2$ (acidic) and $2H_2O + 2e^- = 2OH^- + H_2$ (alkaline).[124] Figure 33 displayed the reaction process in the water electrolysis system under different pH conditions. However, the active sites from different materials are dissimilar, resulting in the specific reaction mechanism which needs more exploration.

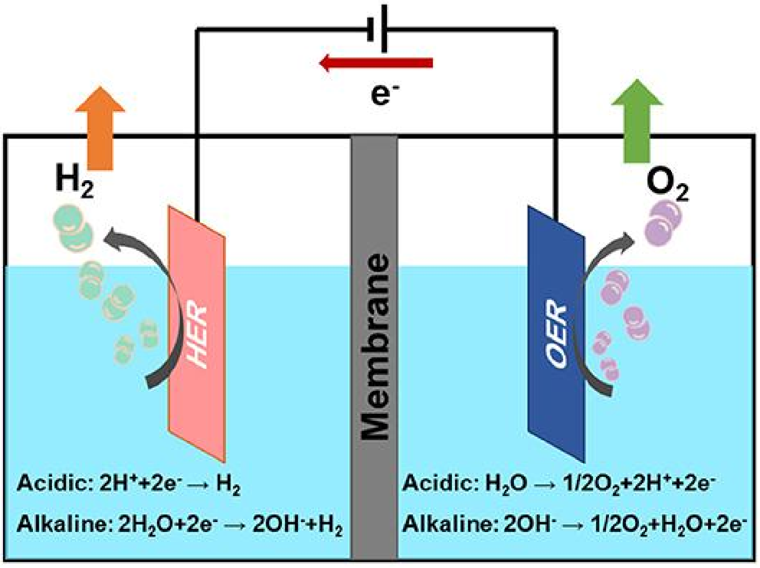

Figure 33. Water electrolysis system. Taken from Ref. 124 and modified.

4. Aims of the thesis

The principal goal of this thesis is to establish a facile method for control synthesis of pyrite–type transition metal dichalcogenides as effective catalysts for OER. Particular aims are as follows:

4.1 Synthesis of boron–doped pyrite–type ternary sulfide coated by amorphous boride

The first aim of the thesis is to design pyrite type sulfides as highly active catalysts for OER application. Our previous results found that amorphous polymetallic borides could be efficiently synthesized by liquid–phase–reduction. Moreover, the amorphous polymetallic borides could be scaled up according to the demand. We applied a two–step method, liquid–phase reduction and high–temperature reaction, to fabricate the boron–doped ternary pyrite–type sulfide catalyst. Various characterization instruments and computational simulations were used to analyze the structure of materials and elemental valence analysis. The obtained materials were subjected to OER testing under alkaline conditions.

4.2 Preparation of boron–doped ternary pyrite selenide

Numerous studies had shown that selenides could effectively promote the OER reaction. Meanwhile, valence–engineering could adjust the local electronic structure of the catalysts, further improving their activity and stability. Combining the synthesized amorphous polymetallic borides, we adopted a high–temperature gasification–strategy to synthesize polymetallic selenide. Polymetallic could effectively optimize the electronic structure, due to the difference in atomic radius. In addition, boron doping could also improve the electronic properties of selenides, as the electron-deficient properties. AC–TEM and DFT+U were used to analyze the atomic structure of the pyrite–type selenide.

5. Experimental part – Materials and methods

5.1 Experimental section

5.1.1 Chemicals

Cobalt nitrate ($Co(NO_3)_2·6H_2O$), Nickel nitrate ($Ni(NO_3)_2·6H_2O$), Anhydrous iron chloride ($FeCl_3·6H_2O$), Sodium borohydride ($NaBH_4$), Selenium powder, Sulfur powder were purchased from Sigma–Aldrich. The potassium hydroxide (KOH) and ethanol (absolute) were purchased from Penta. The distilled water (DIW, 18.2 MU) was the solvent for synthesis. All reagents were used without further purification.

5.1.2 Synthesis of pyrite–type B–FeCoNiS$_x$ crystal coated by amorphous FeCoNiB$_x$

A typical redox reaction was used to synthesize a series of amorphous borides (NiB, CoNiB, FeNiB and FeCoNiB). For the synthesis, 0.16 g $Co(NO_3)_2{\cdot}6H_2O$, 0.29 g $FeCl_3{\cdot}6H_2O$, and 1.16g $Ni(NO_3)_2{\cdot}6H_2O$ were added in a reaction flask and dissolved in DI water. After excess $NaBH_4$ solution was added into the flask, a large amount of black precipitation would generate. The precipitation was successively washed with DI water and ethanol to remove the reactants. Then the black precipitation was dried under 60 ℃ for overnight to obtain the black powder of the amorphous borides. Afterward, 0.48 g FeCoNiB and 0.4 g S powder were mixed and added into a quartz boat and transferred to a tube furnace. The mixture was heated to 400 ℃ (heating rate of 5 ℃/min) and reacted for 120 min under N_2 flow. After cooled to room temperature, boron–doped ternary pyrite type sulfide coated by amorphous boride was formed. Similarly, the boron–doped Ni, CoNi and FeNi–based sulfides were synthesized by the same reaction conditions but with the corresponding precursors.

5.1.3 Synthesis of pyrite–type FeCoNiSeB$_x$ catalyst

A two simple steps method was applied to synthesize the series of boron–doped selenides. Similar to the fabrication of sulfides, amorphous borides need to be synthesized in advance. Firstly, the amorphous NiB, FeNiB, CoNiB, FeCoNiB precursors were prepared by the wet chemical approach. 1 mmol amount of $Co(NO_3)_2$, $Ni(NO_3)_2$, and $FeCl_3$ was dissolved in DI water. Subsequently, a moderate amount of $NaBH_4$ solution was added into the mixture of the metal ions solution to generate the black amorphous boride. After repeated washing to remove the reactants, the as–prepared materials dried at 60 °C in an oven overnight. The obtained FeCoNiB and Se powder were placed in the quartz boat with the selenium located on the upstream side. Subsequently, the quartz boat was heated at 450 °C for 2 h under the Ar flow and finally cooled to room temperature to obtain $Fe_5Co_4Ni_{20}Se_{36}B_x$ powder. Similarly, the $NiSe_2B_x$, $FeNi_3Se_8B_x$, and $CoNi_3Se_8B_x$ catalysts were prepared under similar reaction conditions.

5.2 Structural Characterizations.

The transmission electron microscopy images (TEM), high–resolution transmission electron microscopy (HRTEM), selected area (electron) diffraction (SAED), electron energy loss spectroscopy (EELS) and Energy–dispersive X–ray spectroscopy were collected from JEOL model JEM–ARM–200F microscope operated at 200 kV. X–ray Powder Diffraction (XRD) data were recorded from Rigaku SmartLab using Cu Kα (γ =1.54178 A) radiation. The X–ray photoelectron spectroscopy (XPS) was recorded by an ESCALAB 250Xi XPS system using Mg as the excitation source.

5. 3 Electrochemical measurements

The electrochemical tests were carried out in the typical three–electrode system using Autolab electrochemical workstation and CHI 660E workstation in 1M KOH solution. To prepare the electrode, 5 mg of materials were dispersed in the mixture of DI water (750 μL), isopropanol (210 μL), and Nafion solution (40 μL, 5 wt %). After being sonicated for 30 min, homogeneous ink was formed. Then 10 μL ink gradually dripped onto the glassy carbon electrode and dried at room temperature. The saturated calomel electrode (SCE) was used as a reference, while the graphite rod was employed as the counter electrode. Based on the Nernst equation E(RHE)=E(SCE) + 0.242 + 0.059pH, the potential of SCE was converted to reversible hydrogen electrode (RHE). The polarization curves were recorded at a scan rate of 1.0 mV s^{-1}. Electrochemical impedance spectroscopy tests were recorded at Autolab electrochemical workstation and Solartron electrochemical workstation (German) with a frequency ranging from 0.01 to 105 Hz.

5. 4 Density functional theory calculation

Vienna ab initio simulation package (VASP) was applied for the density functional theory (DFT) calculations.[125] The projected augmented wave (PAW) combined Perdew–Burke–Ernzerhof (PBE) in the generalized gradient approximation (GGA) to analyze the ion–electron interaction.[126] For the boron–doped ternary pyrite type sulfide system, the cut–off energy for the function was 500 eV while the convergence criteria was 10^{-5} eV in energy and 10^{-2} eV $Å^{-1}$ in force.

The DFT+D3 method was used for describing spin–polarization and van der Waals interactions for the pyrite–type selenide system.[127] Moreover, the GGA + U approach was adopted to correct the coulombic interactions of Ni, Co and Fe, with the corresponding Ueff of 3.4, 3.4, and 3.3 eV, respectively. Similar to the boron–doped ternary pyrite type sulfide system, the cut–off energy and convergence criteria kept the same parameters.

6. Results

6. 1 Synthesis of pyrite selenide for highly efficient oxygen evolution

In this work, $Fe_5Co_4Ni_{20}Se_{36}B_x$ selenide particles were successfully prepared on the amorphous $FeCoNiB_x$ to generate the heterostructure ($FeCoNiB_x$@$Fe_5Co_4Ni_{20}Se_{36}B_x$). To analyze the crystal structure, the XRD Rietveld refinement method was applied to learn the atomic arrangement information.[128] The XRD curve in Figure 34a showed several obvious peaks that belonged to (210), (200), (211), (311), and (321) for the $Fe_5Co_4Ni_{20}Se_{36}B_x$ crystals (JCPDS:88–1711),[129] respectively. The XRD refinement results indicated metal atoms (Fe, Co, Ni) had similar positions while the B atoms mainly existed in the lattice spacing. Some of the B atoms bonded with some metals to form B–M bonds, and other B bonded with Se atoms as shown in Figure 34 B–D. Such a special atomic arrangement structure would promote the modulation of electronic structure.

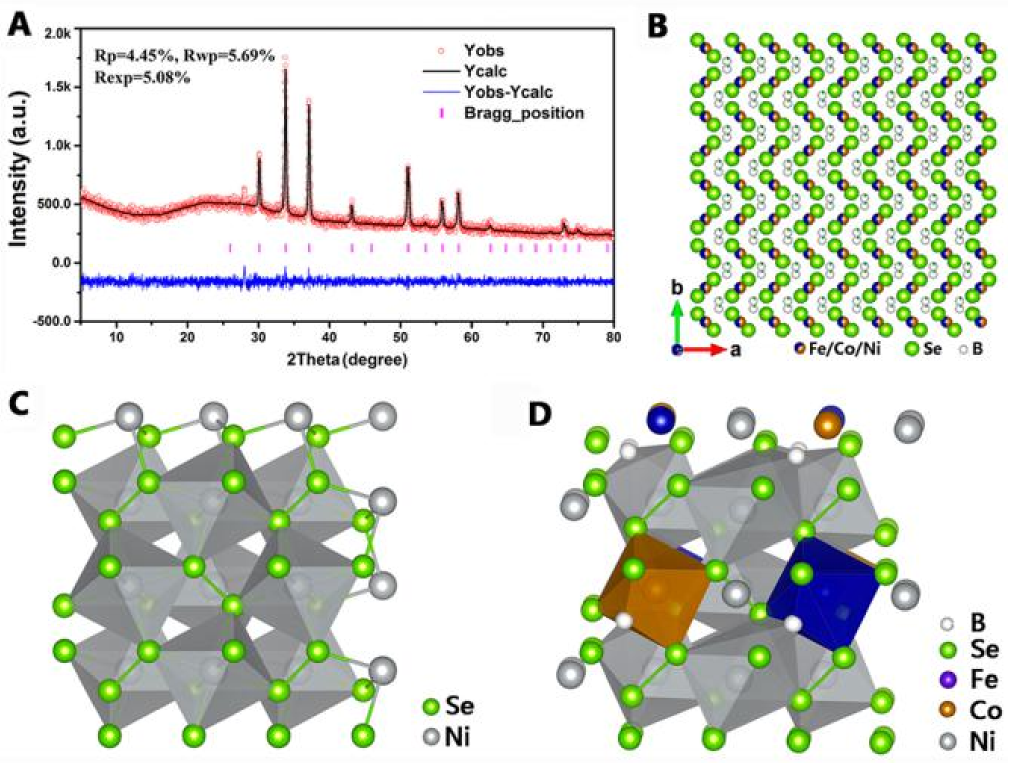

Figure 34. (A) XRD Rietveld refinement and (B) the atomistic model of $Fe_5Co_4Ni_{20}Se_{36}B_x$ crystal. (C, D) Crystal structures of $NiSe_2$ and $Fe_5Co_4Ni_{20}Se_{36}B_x$.

AC–TEM images in Figure 35 clearly showed the crystalline–amorphous structure of the $FeCoNiB_x@Fe_5Co_4Ni_{20}Se_{36}B_x$ materials. The $Fe_5Co_4Ni_{20}Se_{36}B_x$ nanoparticles with the size of ~ 50 nm were randomly loaded onto the amorphous $FeCoNiB_x$. SAED pattern in Figure 32B showed the good crystallinity of the $Fe_5Co_4Ni_{20}Se_{36}B_x$, consistent with the XRD curve, while the no diffraction lattice in FFT revealed the typical amorphous structure of the $FeCoNiB_x$. The HAADF–STEM and the corresponding EELS images in Figure 32 D, E presented the $Fe_5Co_4Ni_{20}Se_{36}B_x$ particle contained five elements (Fe, Co, Ni, Se, B) and the amorphous $FeCoNiB_x$ had four elements (Fe, Co, Ni, B). Notably, the crystalline–amorphous structure could effectively block the agglomeration of $Fe_5Co_4Ni_{20}Se_{36}B_x$ and provide a 3D accessible structure for the electrolyte, thus facilitating the electrochemical performance.

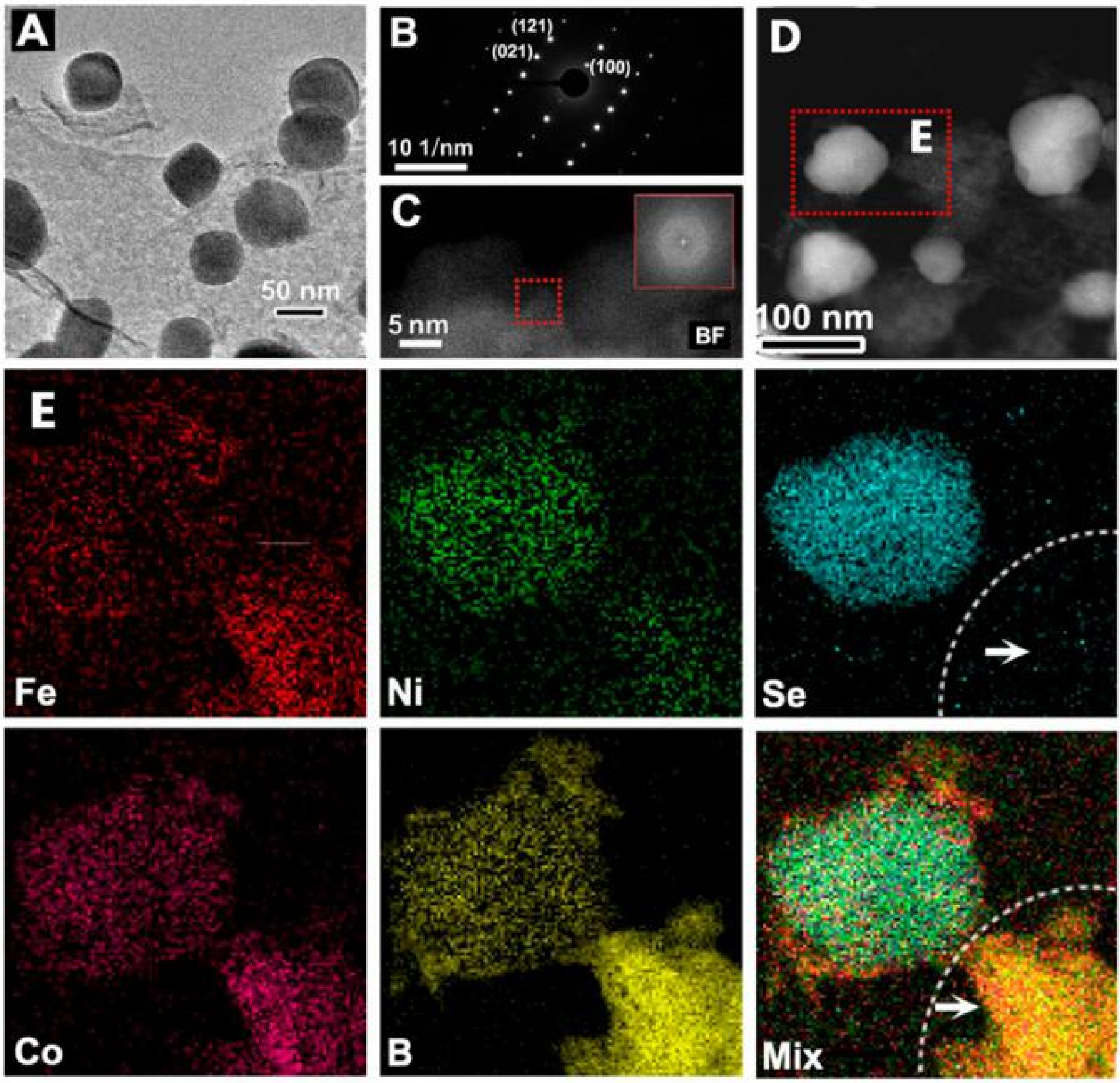

Figure 35. (A) HRTEM and (B) the corresponding SAED pattern of the $Fe_5Co_4Ni_{20}Se_{36}B_x$. (C, D) STEM images of $FeCoNiB_x$ and $FeCoNiB_x@Fe_5Co_4Ni_{20}Se_{36}B_x$. The inserted image in (C) was the FFT. (E) EELS mapping results of the $FeCoNiB_x@Fe_5Co_4Ni_{20}Se_{36}B_x$.

XPS was performed to further analyze the valence state of $FeCoNiB_x@Fe_5Co_4Ni_{20}Se_{36}B_x$. Based on the XPS spectra, the metals in $Fe_5Co_4Ni_{20}Se_{36}B_x$ mainly existed as oxidation states. The peaks at 711.79, 715.26, 725.49, and 729.35 eV (Figure 36A) corresponded to Fe–B, Fe^{3+} $2p_{3/2}$, Fe^{2+} $_{2p1/2}$, and Fe^{3+} $_{2p1/2}$, respectively.[129] The Co 2p spectrum could split into three peaks located at 776.39, 781.68, and 786.75 eV, associated with Co–B, Co^{2+}, and a satellite peak as shown in Figure 36B.[130] The three peaks at 851.6, 856.2, 859.9, and 862.7 eV in Ni $_{2p3/2}$ could be assigned to Ni–B,

Ni^{2+}, Ni^{3+} (Figure 36C).[131] The B 1s spectrum result showed two peaks at 185.68 eV and 192.15 eV, which could be assigned as M−B (M = Fe, Co, Ni) and trivalent oxidation states (Figure 36D).[130] The Se 3d XPS spectrum had two peaks at 54.74 eV and 55.73 eV, assigned to Se^{2-} and oxidation state of Se species in the surface of the $FeCoNiB_x@Fe_5Co_4Ni_{20}Se_{36}B_x$ (Figure 36E).[132] These results indicated the electrons could be transferred from the metals to boron and Se atoms. The projected density of states (PDOS) calculated by density functional theory (DFT) found the p orbital of B was overlapped with the orbitals of atoms around B, including the Se, Fe, Co, and Ni, revealing the B atoms bond with surrounding atoms.

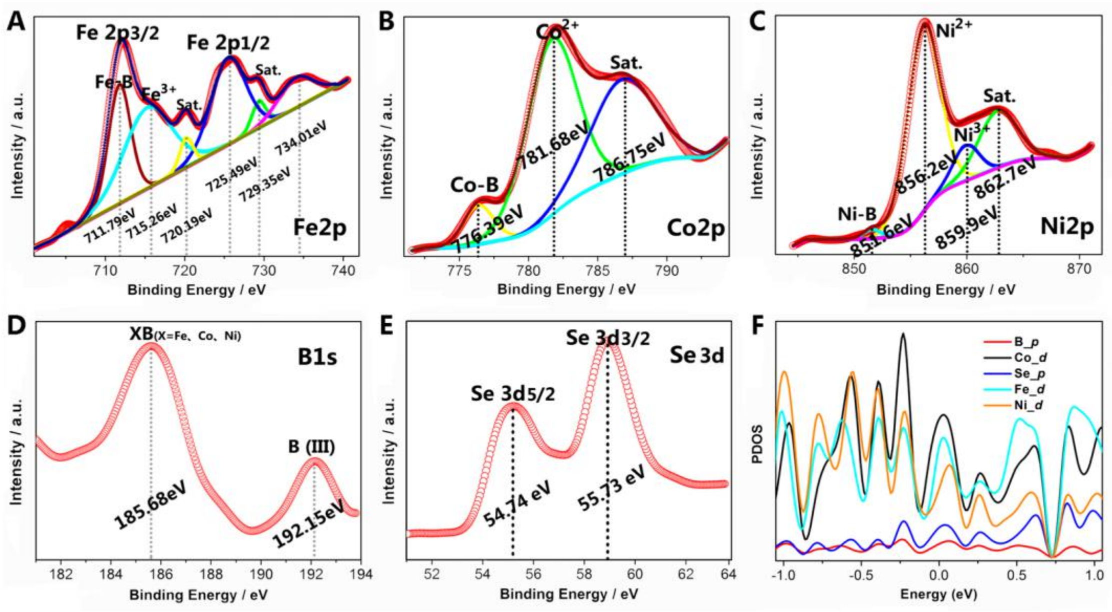

Figure 36. (A–E) XPS spectra of Fe 2p, Co 2p, Ni 2p, B1s, and Se2d. (F) PDOS of $Fe_{0.125}Co_{0.125}Ni_{0.75}Se_2B_{0.2}$.

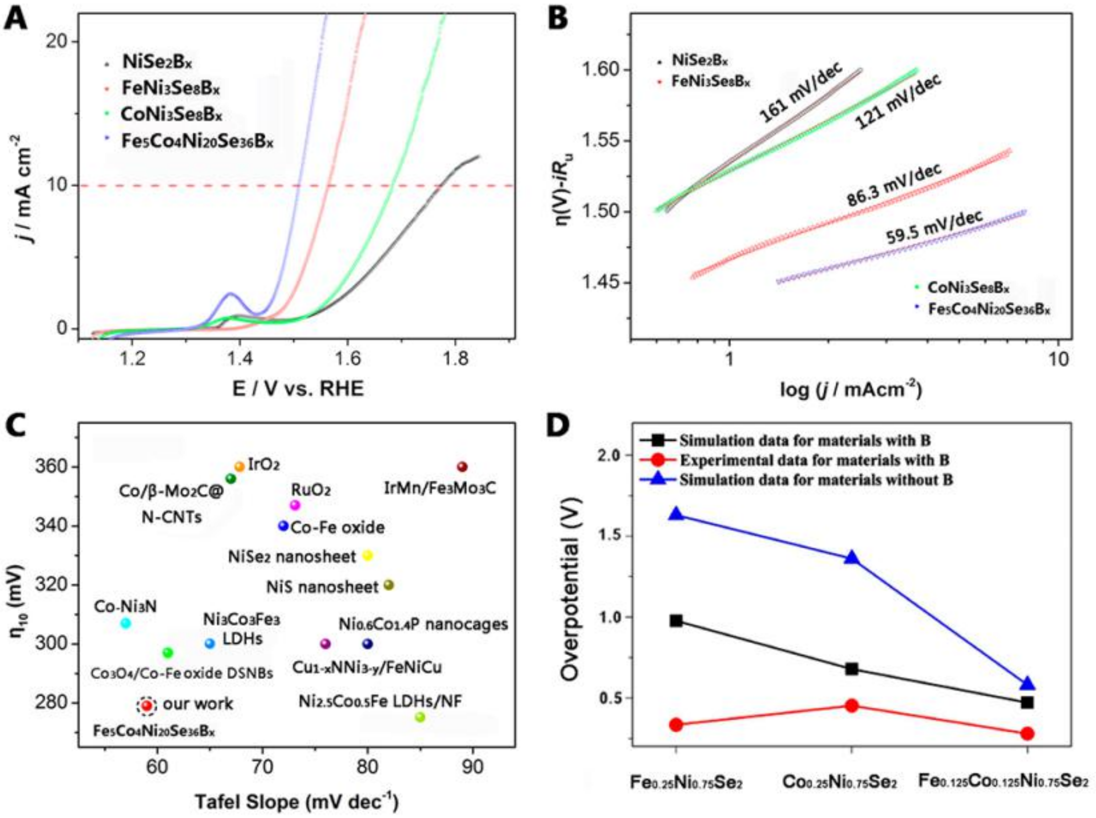

Figure 37. (A) Linear cyclic voltammetry curves of the $NiSe_2B_x$, $FeNi_3Se_8B_x$, $CoNi_3Se_8B_x$, and $Fe_5Co_4Ni_{20}Se_{36}B_x$ samples in 1.0 M KOH under the scan rate of 2 mV s_{-1}. (B) Tafel plots. (C) Comparison the Tafel slopes and overpotentials of targeted catalyst and other OER catalysts. (D) Comparison of theoretical and experimental results.

The OER performance of the prepared catalysts was tested by a standard three–electrode system in 1.0 M KOH solution. Figure 37A showed that the $Fe_5Co_4Ni_{20}Se_{36}B_x$ exhibited the best OER performance with the overpotential of 279.8 mV under 10 mA cm^{-2}, better than those of $NiSe_2B_x$ (543 eV), $FeNi_3Se_8B_x$ (335 eV), and $CoNi_3Se_8B_x$ (453 mV), respectively. The Tafel slopes in Figure 37B of $Fe_5Co_4Ni_{20}Se_{36}B_x$ was 59.5 mV dec^{-1}, much smaller than those of $FeNi_3Se_8B_x$ (86.3 mV dec^{-1}), $CoNi_3Se_8B_x$ (121 mV dec^{-1}), and $NiSe_2B_x$ (161mV dec^{-1}), respectively, indicating the fast kinetics process. Notably, the $Fe_5Co_4Ni_{20}Se_{36}B_x$ showed excellent OER property among the other catalysts reported recently (Figure 37C). Based on the DFT calculation (Figure 37D), with the increase of metal species, the overpotential of the materials would gradually decrease, and the boron doping could also benefit from reducing the overpotential.

6. 2 Synthesis of ternary pyrite¬type boron–sulfide coated by amorphous boride for highly efficient oxygen evolution

In this part, boron–doped ternary pyrite–type sulfides coated by amorphous boride ($Ni_{0.8}Fe_{0.1}Co_{0.1}S_2B_x$@$FeCoNiB_x$, B–TS–H@T–B) was prepared through sulfidation reaction. XRD was performed to analyze the structural information of the obtained crystal. The diffraction results contained several typical peaks which could be assigned as (111), (002), (113) facets of the $Ni_{0.8}Fe_{0.1}Co_{0.1}S_2B_x$ catalyst (Figure 38a).[133] XRD Rietveld refinement further conformed the main phase of the nanocomposite was $Ni_{0.8}Fe_{0.1}Co_{0.1}S_2B_x$ crystal and the corresponding atomic information. Similar to boron–doped polymetallic selenides, the B atoms in $Ni_{0.8}Fe_{0.1}Co_{0.1}S_2B_x$ were mainly embedded in the interstitial site in the lattice as illustrated in the Figure 38b.

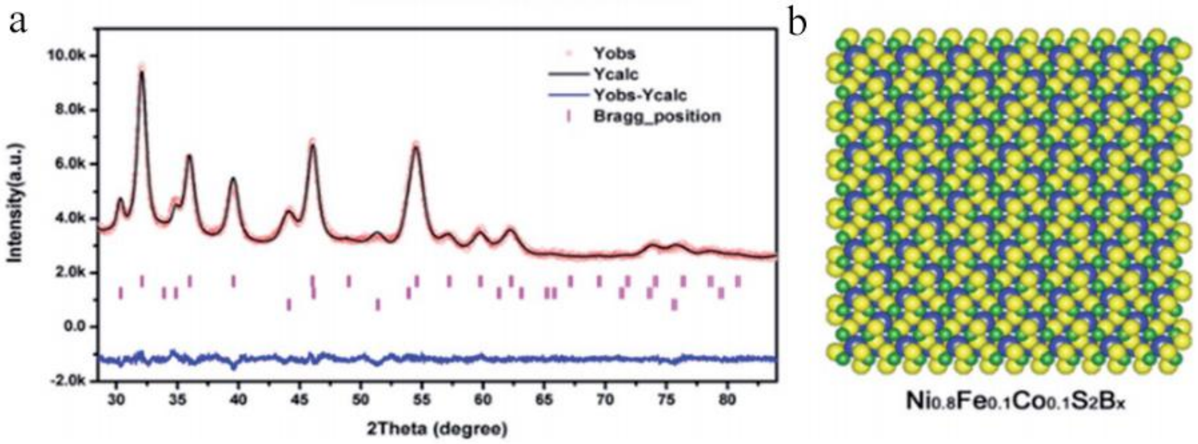

Figure 38. (a) The XRD Rietveld refinement of B–TS–H@T–B. (b) Structural model of the $Ni_{0.8}Fe_{0.1}Co_{0.1}S_2B_x$ catalyst with the S atoms of yellow color, metal atoms (Fe, Co, Ni) of blue color, and the B atoms of green color.

The morphology and atomic arrangement information were collected by AC–TEM and the results were displayed in Figure 39. Enlarged TEM images in Figure 39a–d presented that the amorphous thin layer coated on the surface of the $Ni_{0.8}Fe_{0.1}Co_{0.1}S_2B_x$. HRTEM image in Figure 39e showed the as–prepared boron–sulfide contained different phases of the crystals as the verification of FFT patterns (Figure 39e_1–e_3), which was consistent with the selected area in Figure 39e, corresponding with the XRD refinement results.

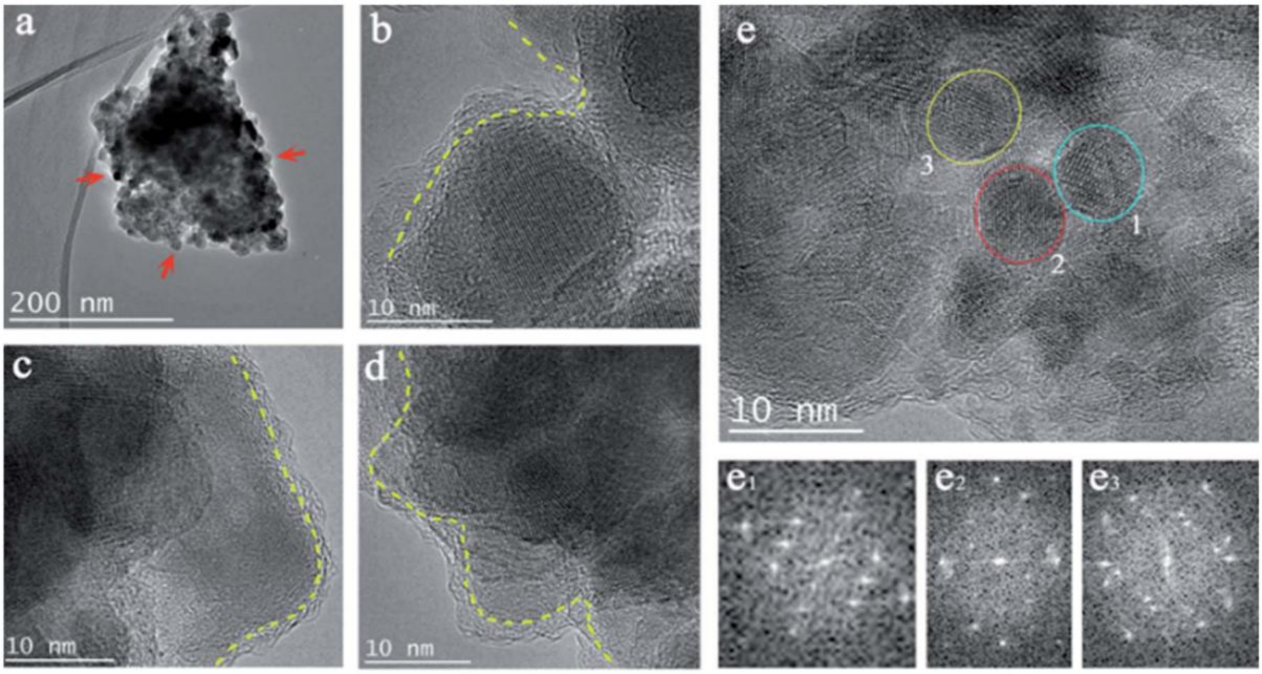

Figure 39. (a–d) Enlarged TEM images of B–TS–H@T–B. (e and $e_{1–3}$) HRTEM of the material and the corresponding FFT patterns of the selected area in (e).

The STEM image in Figure 40a displayed the morphology of B–TS–H@T–B. This nanocomposite contained numerous particles on the surface. For the crystalline particles, gradually magnified STEM images in Figure 40b, c clearly showed the lattice spacing of ~ 0.27 nm and ~ 0.32 nm, which was consistent with the (002) and (111) planes of $Ni_{0.8}Fe_{0.1}Co_{0.1}S_2B_x$.[134] The lattice angle of (002) and (111) planes was 55°, further explaining the structure of the boron–doped polymetallic sulfides. It should be pointed out that there was a thin amorphous layer on the surface of $Ni_{0.8}Fe_{0.1}Co_{0.1}S_2B_x$, due to the significant difference of the FFT results in Figure 40d, e, exhibiting the crystalline and amorphous heterostructure.

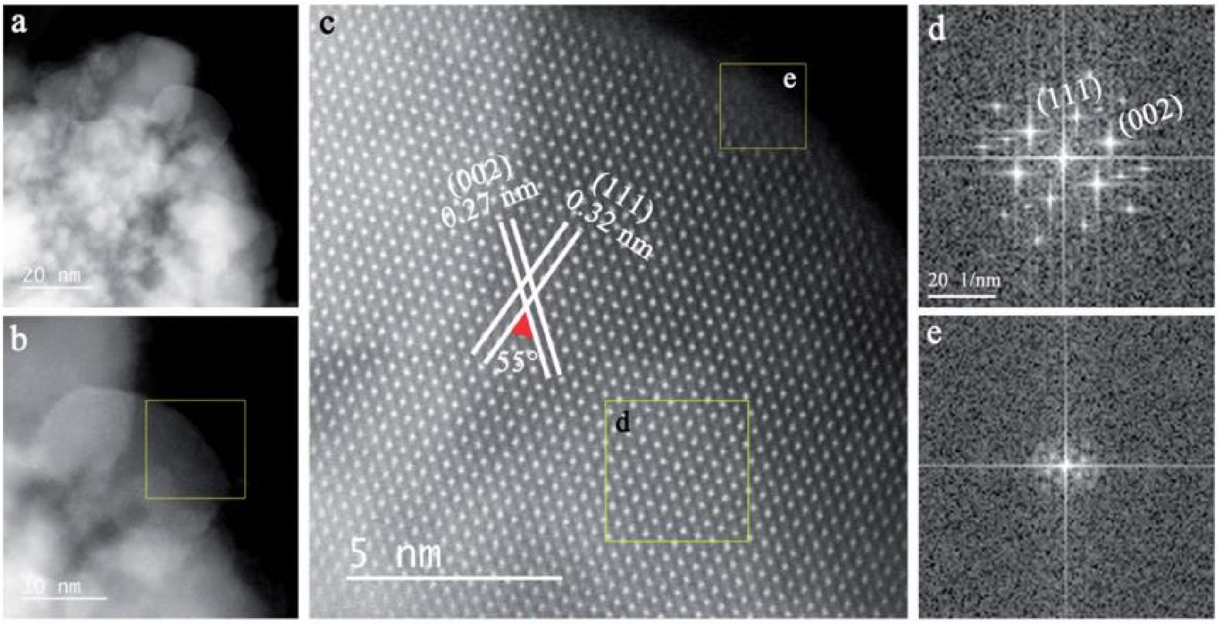

Figure 40. (a) STEM image of the B–TS–H@T–B. (b, c) Magnified STEM images to the atomic level. (d, e) FFT patterns of the selected area in (e).

The chemical valence state of the elements in B–TS–H@T–B was collected by XPS. Survey spectra in Figure 41a found the B2p, S2p, Fe2p, Co2p, and Ni2p elements in the material. The high–resolution XPS spectrum of Fe 2p in Figure 41b were deconvoluted into three peaks at 707.46 eV, 712.78 eV, and 720.38 eV, which would be recognized as Fe^{2+} 2p3/2, Fe^{3+} 2p3/2 and Fe^{2+} 2p1/2, respectively.[129] Additionally, the peaks at 704.92 eV and 708.65 eV were assigned as Fe–B bond and satellite peak. The binding energy positions of the Fe 2p demonstrated the Fe element mainly existed in the oxidation state.[129] Co 2p spectrum in Figure 41c could be fitted into four peaks at 778.99 eV, 780.84 eV, 784.07 eV and 793.99 eV, which could be appointed as Co–B, Co^{2+} 2p3/2, Co^{3+} 2p3/2, and Co^{2+} 2p1/2, respectively.[130] Similarly, the Ni 2p XPS spectrum had four fitted peaks at 853.68 eV, 855.35 eV, 859.6 eV and 870.93 eV, which could be assigned as Ni–B, Ni^{2+} 2p3/2, Ni^{3+} 2p3/2 and Ni^{2+} 2p1/2.[131] According to these results, the reduced binding energy represented the loss of electrons from the metals, and partial electrons transferred from the metals to B atoms. The B1s XPS (Figure 41f) had two peaks at 187.22 eV and 192.82 eV, the former was B–M bonds and the latter was contributed of the trivalent state as the adsorbed oxygen.[132] The S 2p spectrum in Figure 41e displayed four peaks at 161.03 eV, 161.97 eV, 163.08 eV, and 163.63 eV, successively belonging to S^{2-}, S 2p3/2, S 2p1/2 and SO_x species.[135] The air environment could result in the surface oxidation of the S atoms on the external positions. Based on the XPS results of the elements, the electrons would transfer from the metallic elements to B and S elements, thus forming abundant high–valence metal atomic sites which were conducive to improving the electrochemical performance of the catalysts.

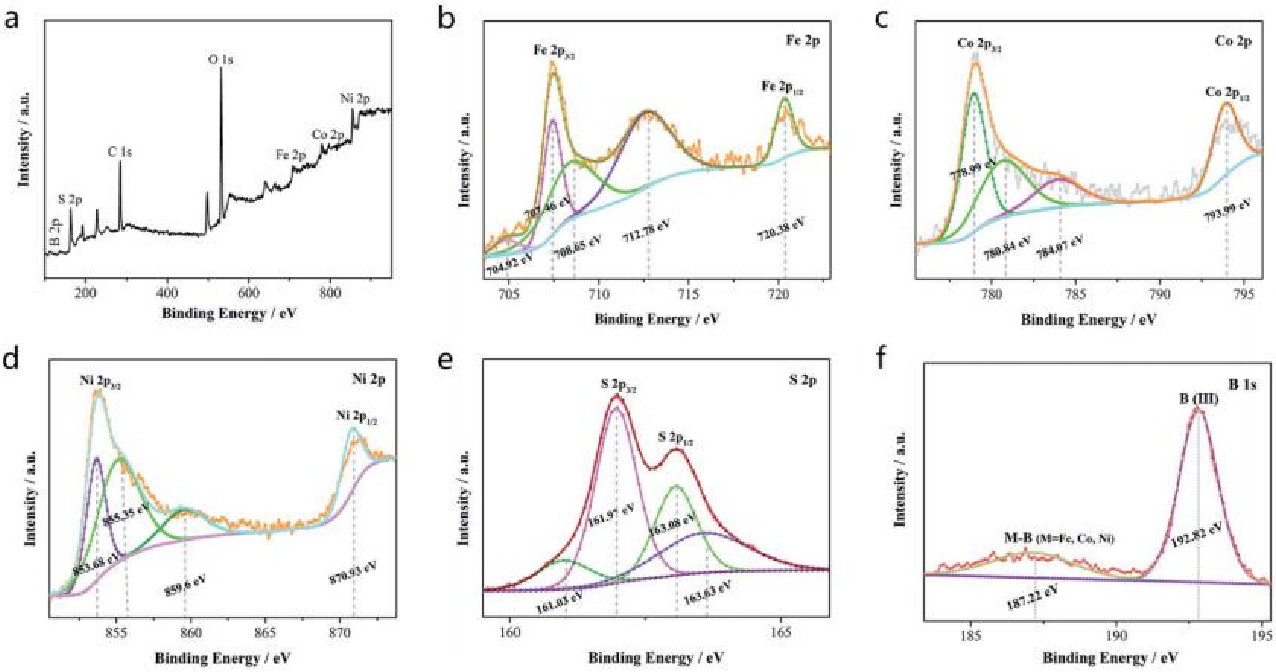

Figure 41. (a) XPS spectrum of B–TS–H@T–B. (b–f) XPS spectrums of Fe 2p, Co 2p, Ni2p, B 1s and S 2p.

The electrochemical performance was tested in 1 M KOH solution with the typical three–electrode system. A linear voltammetry curve was used to record the polarization curve of the samples. As expected, the B–TS–H@T–B presented the best OER activity with the overpotential of 392.4 mV at 50 mA cm^{-2}, which was much lower than that of boron–doped $CoNiS_x$ (459.4 mV, 50 mA cm^{-2}), boron–doped $FeNiS_x$ and boron–doped NiS_x as shown in Figure 42a. Moreover, the target catalyst displayed smaller overpotential even under the higher current density as displayed in Figure 42b. (100 mA cm^{-2} and 150 mA cm^{-2}). The B–TS–H@T–B also had the smallest Tafel slope (64 mV dec^{-1}), while the other samples all had the larger tafel slope (Figure 42c) revealing the faster OER kinetics over the B–TS–H@T–B surface. Furthermore, the B–TS–H@T–B exhibited excellent stability with a retention rate of 76.94% after the 10 h stability test, revealing the metal doping would contribute to the improvement of activity and stability.

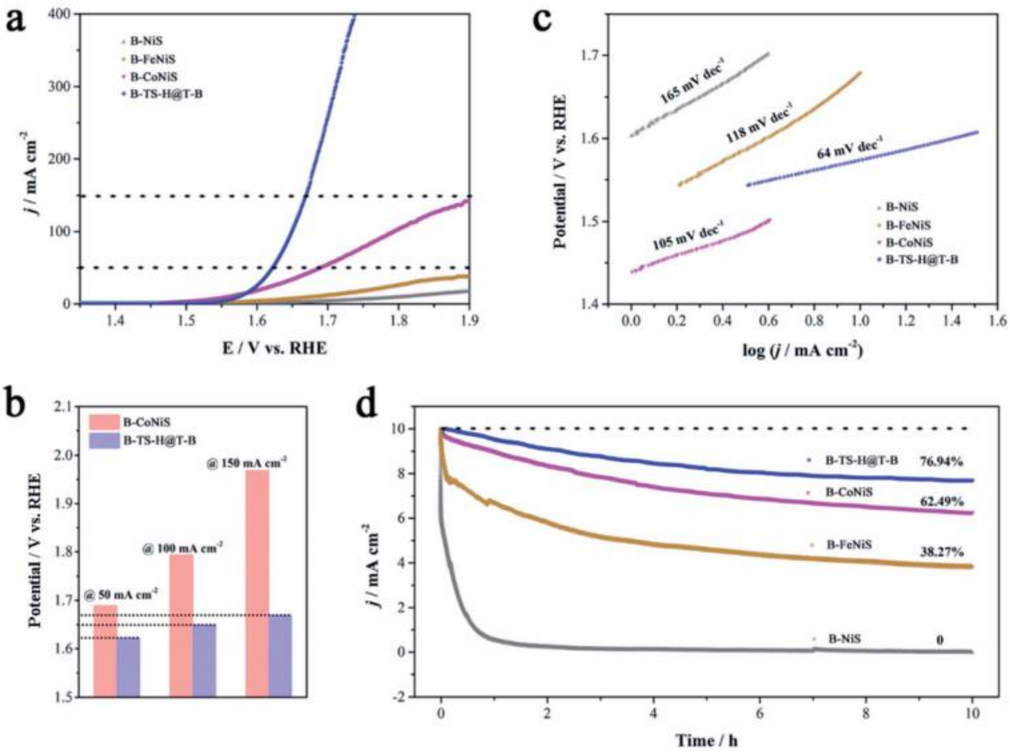

Figure 42. (a) Linear cyclic voltammetry curves of the B–TS–H@T–B, B–NiS, B–FeNiS, and B–CoNiS samples. (b) Overpotentials of the samples under 50 mAcm^{-2}, 100 mAcm^{-2} and 150 mAcm^{-2}, respectively. (c) Tafel slope curves of the four samples. (d) Long–time stability of the as–prepared electrocatalysts.

7. Summary

In this thesis, We focused on designing a facile method to prepare the pyrite–type polymetallic sulfides and selenides for electrocatalytic water splitting. The amorphous membrane coated on the catalysts could enhance the activity of the materials and simultaneously further consolidated the stability of the catalyst. Meanwhile, boron doping could effectively improve the intrinsic electronic structure of the catalyst for the electrocatalytic application. A two–step synthesis process was adopted to obtain the target materials, including the preparation of amorphous borides, and selenization/sulfuration step under megathermal conditions. The presented dissertation successfully establish a facile method to control the synthesis of polymetallic selenides and sulfides with the coating of the amorphous boride layer.

The first goal of the current thesis focused on finding the appropriate preparation methods to from high–quality amorphous borides. We used the wet chemical approach to synthesize the amorphous borides which contained NiB_x, $FeNiB_x$, $CoNiB_x$, and $FeCoNiB_x$ through the reaction between sodium borohydride and metal ion precursors. We used TEM and XRD techniques to analyze the composition and structure of the amorphous borides. Even more, the SAED was also applied to characterize the structure. The synthesized amorphous borides displayed the stacked in layers with a large number of corner and side atoms.

The selenization and sulfuration reaction were carried out in a tubular furnace under the flow of Ar or N_2 gas at above 300 ℃. During the selenization or sulfuration reaction, the vaporized Se or S atoms reacted with the amorphous boride, forming the clusters and then growth to particles. However, the atoms in amorphous boride involved in the reaction would generate the new bond which would drive the surrounding amorphous boride to coat on the surface of the obtained selenide or sulfide particles, finally forming the B–$FeCoNiS_x$@$FeCoNiB_x$ and $FeCoNiSeB_x$@$Fe_5Co_4Ni_{20}Se_{36}B_x$.

B–$FeCoNiS_x$@$FeCoNiB_x$ presented excellent OER activity than B–$FeCoNiS_x$ and $FeCoNiB_x$ with an overpotential of 419 mV vs. RHE under 100 mA cm^{-2} in KOH solution. Additionally, after 10 h stability test, the current density of B–FeCoNiS$_x$@FeCoNiB$_x$ catalyst only dropped 23.06%, much better than B–CoNiS (37.51%) and B–FeNiS (61.73%). The projected density of states (PDOS) results based on the DFT calculation indicated the redistribution of electrons on the metal sites in the B–FeCoNiS$_x$@FeCoNiB$_x$ were conducive to water decomposition.

Additionally, the valence engineered FeCoNiSeB$_x$@Fe$_5$Co$_4$Ni$_{20}$Se$_{36}$B$_x$ via boron doping exhibited highly efficient OER property. This heterostructure provided a physically anchored structure that could block the aggregation of the Fe$_5$Co$_4$Ni$_{20}$Se$_{36}$B$_x$ nanoparticles. Moreover, the special heterostructure offered 3D accessible units for the electrolyte during the catalysis. XRD Rietveld refinement result found the boron atoms mainly existed in the interstitial sites of Fe$_5$Co$_4$Ni$_{20}$Se$_{36}$B$_x$, while the Fe, Co, and Ni atoms co–occupied the same sites. DFT calculation results revealed the boron dopant and binary atomic substitution together contributed to weakening the reaction between the active sites and O intermediates during OER. FeCoNiSeB$_x$@Fe$_5$Co$_4$Ni$_{20}$Se$_{36}$B$_x$ showed the lowest overpotential of 279.8 mV at 10 mA cm^{-2}, compared to those of NiSe$_2$B$_x$ (543 mV), FeNi$_3$Se$_8$B$_x$ (335 mV), and CoNi$_3$Se$_8$B$_x$ (453 mV), respectively.

The work in this thesis illustrated that the pyrite–type sulfides and selenides with boron doping and amorphous layer coating had big potential for energy conversion, due to the special electronic configuration, which may provide a rationally approach for preparing novel electrocatalysts for clean energy application.

References

1. Hu, C.; Zhang L.; Gong, J., Recent Progress Made in the mechanism comprehension and design of electrocatalysts for alkaline water splitting. Energy Environ Sci 2019, 12, 2620.

2. You, B.; Sun, Y., Innovative strategies for electrocatalytic water splitting. Acc Chem Res 2018, 51, 1571.

3. Chu, S.; Majumdar, A., Opportunities and challenges for a sustainable energy future. Nature 2012, 488, 294–303.

4. Roger, I.; Shipman, M.; Symes, M., Earth–abundant catalysts for electrochemical and photoelectrochemical water splitting. Nat Rev Chem 2017, 1, 0003.

5. Suen, N.; Hung, S.; Quan, Q.; Zhang, N.; Xu, Y.; Chen, H., Electrocatalysis for the oxygen evolution reaction: recent development and future perspectives. Chem Soc Rev 2017, 46, 337−365.

6. Chu, S.; Majumdar, A., Opportunities and challenges for a sustainable energy future. Nature 2012, 488, 294−303.

7. Zou, X.; Zhang, Y., Noble metal–free hydrogen evolution catalysts for water splitting. Chem Soc Rev 2015, 44 , 5148−5180.

8. Hu, C.; Zhang, L.; Gong, J., Recent progress made in the mechanism comprehension and design of electrocatalysts for alkaline water splitting. Energy Environ Sci 2019, 12, 2620.

9. Shi, Y.; Zhang, B., Recent advances in transition metal phosphide nanomaterials: synthesis and applications in hydrogen evolution reaction. Chem Soc Rev 2016, 45, 1529.

10. Jeon, D.; Park, J.; Shin, C.; Kim, H.; Jang, J. W.; Lee, D. W.; Ryu, J., Superaerophobic hydrogels for enhanced electrochemical and photoelectrochemical hydrogen production. Sci Adv 2020, 6, 1.

11. Lu, H.; Tournet, J.; Dastafkan, K.; Liu, Y.; Ng, Y.; Karuturi, S.; Zhao, C.; Yin, Z., Noble–metal–free multicomponent nanointegration for sustainable energy conversion. Chem Rev 2021, 121, 10271–10366.

12. Reza Gholipour, M.; Dinh, C. T.; Beland, F.; Do, T. O., Nanocomposite heterojunctions as sunlight–driven photocatalysts for hydrogen production from water splitting. Nanoscale 2015, 7, 8187−8208.

13. Uddin, N.; Zhang, H.; Du, Y.; Jia, G.; Wang, S.; Yin, Z., Structural–phase catalytic redox reactions in energy and environmental applications. Adv Mater 2020, 32, 1905739.

14. Li, S.; Gao, Y.; Li, N.; Ge, L.; Bu, X.; Feng, P., Transition metal based bimetallic MOFs and MOF–derived catalysts for electrochemical oxygen evolution reaction. Energy Environ Sci 2021, 14, 1897−1927.

15. Tahir, M.; Pan, L.; Idrees, F.; Zhang, X.; Wang, L.; Zou, J.–J.; Wang, Z., Electrocatalytic oxygen evolution reaction for energy conversion and storage: A comprehensive review. Nano Energy 2017, 37, 136−157.

16. Pan, Q.; Wang, L., Recent perspectives on the structure and oxygen evolution activity for non–noble metal–based catalysts. J Power Sources 2021, 485, 229335.

17. Burke, M.; Enman, L.; Batchellor, A.; Zou, S.; Boettcher, S., Oxygen evolution reaction electrocatalysis on transition metal oxides and (Oxy)hydroxides: activity trends and design principles. Chem Mater 2015, 27, 7549−7558.

18. Peng, L.; Ahmad–Shah, S.; Wei, Z., Recent developments in metal phosphide and sulfide electrocatalysts for oxygen evolution reaction. Chinese J Catal 2018, 39, 1575–1593.

18. Du, J.; Li, F.; Sun, L., Metal–organic frameworks and their derivatives as electrocatalysts for the oxygen evolution reaction. Chem Soc Rev 2021, 50, 2663−2695.

19. Anantharaj, S.; Rao–Ede, S.; Sakthikumar, K.; Karthick, K.; Mishra, S.; Kundu, S., Recent trends and perspectives in electrochemical water splitting with an emphasis on sulfide, selenide, and phosphide catalysts of Fe, Co, and Ni: A review. ACS Catal 2016, 6, 8069−8097.

20. Hunter, B.; Gray, H.; Müller, A., Earth–abundant heterogeneous water oxidation catalysts. Chem Rev 2016, 116, 14120−14136.

21. Siahrostami, S.; Villegas, S.; Mostaghimi, A.; Back, S.; Farimani, A.; Wang, H.; Persson, K.; Montoya, J., A review on challenges and successes in atomic–scale design of catalysts for electrochemical synthesis of hydrogen peroxide. ACS Catal 2020, 10, 7495−7511.

22. Zhang, Y.; Han, C.; Gao, J.; Pan, L.; Wu, J.; Zhu, X.; Zou, J., NiCo–based electrocatalysts for the alkaline oxygen evolution reaction: a review. ACS Catal 2021, 11, 12485−12509.

23. Guo, Y.; Park, T.; Yi, J.; Henzie, J.; Kim, J.; Wang, Z.; Jiang, B.; Bando, Y.; Sugahara, Y.; Tang, J.; Yamauchi, Y., Nanoarchitectonics for transition–metal–sulfide–based electrocatalysts for water splitting. Adv Mater 2019, 31, 1807134.

24. Gao, M.; Zheng, Y.; Jiang, J.; Yu, S., Pyrite–type nanomaterials for advanced electrocatalysis. Acc Chem Res 2017, 50, 2194–2204.

25. Ogawa, S., Magnetic properties of 3d transition‐metal dichalcogenides with the pyrite structure. J Appl Phys 1979, 50, 2308.

26. Jiang, H.; He, Q.; Zhang, Y.; Song, L, Structural self–reconstruction of catalysts in electrocatalysis. Acc Chem Res 2018, 51, 2968–2977.

27. He, Z.; Yu, S.; Zhou, Y.; Li, X.; Qu, J., Magnetic field–induced phase–selective synthesis of ferrosulfide microrods by a hydrothermal process: microstructure control and magnetic properties. Adv Funct Mater 2006, 16, 1105−1111.

28. Craig, J.; Vokes, F.; Solberg, T., Pyrite: physical and chemical textures. Miner. Deposita 1998, 34, 82−101.

29. Jin, S., Are metal chalcogenides, nitrides, and phosphides oxygen evolution catalysts or bifunctional catalysts? ACS Energy Lett 2017, 8, 1937.

30. Joo, J.; Kim, T.; Lee, J.; Choi S.; Lee, K., Morphology−controlled metal sulfides and phosphides for electrochemical water splitting. Adv Mater 2019, 31, 1806682.

31. Guo, Y.; Tang, J.; Henzie, J.; Jiang, B.; Xia, W.; Chen, T.; Bando, Y.; Kang, Y.–M.; Hossain, M. S. A.; Sugahara, Y.; Yamauchi, Y. Mesoporous iron–doped $MoS_2/CoMo_2S_4$ heterostructures through organic−metal cooperative interactions on spherical micelles for electrochemical water splitting. ACS Nano 2020, 14, 4141−4152.

32. Yin, J.; Jin, J.; Zhang, H.; Lu, M.; Peng, Y.; Huang, B.; Xi, P.; Yan., C., Atomic arrangement in metal–doped NiS_2 boosts the hydrogen evolution reaction in alkaline media. Angew Chem Int Ed 2019, 58, 18676.

33. Sun, J.; Hu, X.; Huang, Z.; Huang, T.; Wang, X.; Guo, H.; Dai, F.; Sun, D., Atomically thin defect–rich Ni–Se–S hybrid nanosheets as hydrogen evolution reaction electrocatalysts. Nano Research 2020, 13, 2056–2062.

34. Yang, H.; Wang, C.; Zhang, Y.; Wang. Q., Chemical valence–dependent electrocatalytic activity for oxygen evolution reaction: a case of nickel sulfides hybridized with N and S co–doped carbon nanoparticles. Small 2018, 14, 1703273.

35. Nguyen, T.; Su, Y.; Lin, C.; Ting, J., Self–reconstruction of sulfate–containing high entropy sulfide for exceptionally high–performance oxygen evolution reaction electrocatalyst. Adv Funct Mater 2021, 31, 2106229.

36. Liu, H.; He, Q.; Jiang, H.; Lin, Y.; Zhang, Y.; Habib, M.; Chen, S.; Song, L., Electronic structure reconfiguration toward pyrite NiS_2 via engineered heteroatom defect boosting overall water splitting. ACS Nano 2017, 11, 11574.

37. Ni, B.; He, T.; Wang, J.; Zhang, S.; Ouyang, C.; Long, Y.; Zhuang J.; Wang, X.; The formation of $(NiFe)S_2$ pyrite mesocrystals as efficient pre–catalysts for water oxidation. Chem Sci 2018, 9, 2762.

38. Song, Y.; Zhao, X.; Liu, Z., Surface selenium doped hollow heterostructure/defects Co–Fe sulfide nanoboxes for enhancing oxygen evolution reaction and supercapacitors. Electrochim Acta 2021, 374, 137962.

39. Yang, H.; Wang, C.; Zhang, Y.; Wang, Q., Chemical valence–dependent electrocatalytic activity for oxygen evolution reaction: a case of nickel sulfides hybridized with N and S co–doped carbon nanoparticles. Small 2018, 14, 1703273.

41. Chen, J., Li, S., Kumar, V., Lee, P., Carbon coated bimetallic sulfide hollow nanocubes as advanced sodium ion battery anode. Adv Energy Mater 2017, 7, 1700180.

42. Han, H.; Kim, K.; Choi, H.; Ali, G.; Chung, K.; Hong, Y.; Choi, J.; Kwon, J.; Lee, S.; Lee, J.; Ryu, J.; Song, T.; Mhin, S., ACS Catal 2018, 8, 4091.

43. He, D.; Zhang, L.; He, D.; Zhou, G.; Lin, Y.; Deng, Z.; Hong, X.; Wu, Y.; Chen, C.; Li, Y., Amorphous nickel boride membrane on a platinum–nickel alloy surface for enhanced oxygen reduction reaction. Nat Commun 2016, 7, 12362.

44. Li, T.; Zhu, C.; Yang, X.; Gao, Y.; He, W.; Yue, H.; Zhao, H., Co_3O_4 nanoneedle@electroactive nickel boride membrane core/shellarrays: A novel hybrid for enhanced capacity. Electrochim Acta 2017, 246 , 226–233.

45. Roy, B.; Shebin, K.; Sampath, S. Pyrite–type cobalt phosphosulphide bifunctional catalyst for aqueous and gel–based rechargeable zinc–air batteries. J Power Sources 2020, 450, 227661.

46. He, G.; Zhang, W.; Deng, Y.; Zhong, C.; Hu, W.; Han, X., Engineering pyrite–type bimetallic Ni–doped CoS_2 nanoneedle arrays over a wide compositional range for enhanced oxygen and hydrogen electrocatalysis with flexible property. Catalysts 2017, 7, 366.

47. Yang, Y.; Liu, J.; Wang, Z.; Liu, F.; Ding, J., CO_2–mediated sulfur evolution chemistry of pyrite oxidation during oxy–fuel combustion. Combust Flame 2020, 218, 75–83.

48. Wang, J.; Zeng, H., A hybrid electrocatalyst with a coordinatively unsaturated metal−organic framework shell and hollow Ni_3S_2/NiS core for oxygen evolution reaction applications. ACS Appl Mater Interfaces 2019, 11, 23180−23191.

49. Cruz, R.; Bertrand, V.; Monroy, M.; González, I., Effect of sulfide impurities on the reactivity of pyrite and pyritic concentrates: a multi–tool approach. J Appl Geochem 2001, 16, 803–819.

50. Jiang, P.; Qian, X.; Gu, X.; Yang, R.; Probing anisotropic thermal conductivity of transition metal dichalcogenides MX_2 (M = Mo, W and X = S, Se) using time–domain Thermoreflectance. Adv Mater 2017, 29, 1701068.

51. Zhao, X.; Zhang, H. T.; Yan, Y.; Cao, J. H.; Li, X. Q.; Zhou, S. M.; Peng, Z. M.; Zeng, J. Engineering the electrical conductivity of lamellar silver–doped cobalt(II) selenide nanobelts for enhanced oxygen evolution. Angew Chem Int Ed 2017, 56, 328−332.

52. Zhao, Y.; Lu, Y.; Chen, L.; Wei, X.; Zhu, J.; Zheng, Y., Redox dual–cocatalyst–modified CdS double–heterojunction photocatalysts for efficient hydrogen production. ACS Appl Mater Interfaces 2020, 12, 46073−46083.

53. Liu, Y.; Wu, J.; Hackenberg, K.; Zhang, J.; Wang, Y.; Yang, Y.; Keyshar, K.; Gu, J.; Ogitsu, T.; Vajtai, R.; Lou, J.; Ajayan, P.; Wood, B.; Yakobson, B. Self–optimizing, highly surface active layered metal dichalcogenide catalysts for hydrogen evolution. Nat. Energy 2017, 2, 17127.

54. De Luna, P.; Quintero–Bermudez, R.; Dinh, C.–T.; Ross, M.; Bushuyev, O.; Todorovic, P.; Regier, T.; Kelley, S.; Yang, P.; Sargent, E., Catalyst electro–redeposition controls morphology and oxidation state for selective carbon dioxide reduction. Nat Catal 2018, 1, 103−110.

55. Xiang, W.; Tian, Q.; Zhong, C.; Deng, Y.; Han, X.; Hu, W., Atomic vacancies control of Pd–based catalysts for enhanced electrochemical performance. Adv Mater 2018, 30, 1704171.

56. Xiang, W.; Tian, Q.; Zhong, C.; Deng, Y.; Han, X.; Hu. W., A solution–based method for synthesizing pyrite–type ferrous metal sulfide microspheres with efficient OER activity. Chem Asian J 2020, 15, 2231–2238.

57. Jayaramulu, K.; Masa, J.; Tomanec, O.; Peeters, D.; Ranc, V.; Schneemann, A.; Zboril, R.; Schuhmann, W.; Fischer, R., Nanoporous nitrogen–doped graphene oxide/nickel sulfide composite sheets derived from a metal–organic framework as an efficient electrocatalyst for hydrogen and oxygen evolution. Adv Funct Mater 2017, 27, 1700451.

58. Yang, H.; Wang, C.; Zhang, Y.; Wang, Q., Chemical valence–dependent electrocatalytic activity for oxygen evolution reaction: A case of nickel sulfides hybridized with N and S co–doped carbon nanoparticles. Small 2018, 14, 1703273.

59. Shi, X.; Ling, X.; Li, L.; Zhong, C.; Deng, Y.; Han, X.; Hu, W., Nanosheets assembled into nickel sulfide nanospheres with enriched Ni^{3+} active sites for efficient water–splitting and zinc–air batteries. J Mater Chem A, 2019, 7, 23787.

60. Villalbaa, M.; Peronb, J.; Giraudb, M.; Tard. C., pH–dependence on HER electrocatalytic activity of iron sulfide pyrite nanoparticles. Electrochem. Commun. 2018, 91, 10–14.

61. Pan, K.; Zhai, Y.; Zhang, J.; Yu, K., FeS_2/C nanowires as an effective catalyst for oxygen evolution reaction by electrolytic water splitting. Materials 2019, 12, 3364.

62. Lin, R.; Lin, T.; Huang, J.; Huang, X.; Liu. Y., Hierarchical cobalt sulfide with vertical in–plane edge structure for enhanced electrocatalytic oxygen evolution reaction. Electrochim Acta 2018, 281, 348–356.

63. Ma, X.; Zhang, W.; Deng, Y.; Zhong, C.; Hu, W.; Han. X., Phase and composition controlled synthesis of cobalt sulfide hollow nanospheres for electrocatalytic water splitting. Nanoscale 2018, 10, 4816.

64. Dai, T.; Zhang, X.; Sun, M.; Huang, B.; Zhang, N.; Da, P.; Yang, R.; He, Z.; Wang, W.; Xi, P.; Yan. C., Uncovering the promotion of $CeO_2/CoS_{1.97}$ heterostructure with specific spatial architectures on oxygen evolution reaction. Adv Mater 2021, 33, 2102593.

65. Rahul B. Pujari, Girish S. Gund, Swati J. Patil, Ho Seok Park and Dong–Weon Lee, Anion–exchange phase control of manganese sulfide for oxygen evolution reaction. J Mater Chem A, 2020, 8, 3901.

66. Zhu, Y.; Tahini, H.; Wang, Y.; Lin, Q.; Liang, Y.; Doherty, C.; Liu, Y.; Li, X.; Lu, J.; Smith, S.; Selomulya, C.; Zhang, X.; Shao, Z.; Wang. H., Pyrite–type ruthenium disulfide with tunable disorder and defects enables ultra–efficient overall water splitting. J Mater Chem A, 2019, 7, 14222.

67. Xu, Y.; Du, C.; Shen, Q.; Huang, J.; Zhang, X.; Chen, J., Well–dispersed pyrite–type RuS_2 nanocrystals anchored on porous nitrogen and sulfur co–doped hollow carbon spheres for enhanced alkaline hydrogen evolution. Chem Eng J 2021, 417, 129318.

68. Li, Q.; Wang, X.; Tang, K.; Wang, M.; Wang, C.; Yan, C., Electronic modulation of electrocatalytically active center of Cu_7S_4 nanodisks by cobaltdoping for highly efficient oxygen evolution reaction. ACS Nano 2017, 11, 12230−12239.

69. Jin, T.; Liu, X.; Wang, H.; Wu, X.; Zhang, Y., Mechanochemical–assisted synthesis of ternary Ru–Ni–S pyrite analogue for enhanced hydrogen evolution performance. Carbon 2020, 162, 172−180.

70. Liu, C.; Ma, H.; Yuan, M.; Yu, Z.; Li, J.; Shi, K.; Liang, Z., Yang, Y.; Zhu, T.; Sun, G.; Li, H.; Ma, S. $(NiFe)S_2$ nanoparticles grown on graphene as an efficient electrocatalyst for oxygen evolution reaction. Electrochim Acta 2018, 286, 195–204.

71. Zhang, Z.; Xu, D.; Li, J.; Liu, J.; Long, X.; Su, K.; Guo, J.; Tong, H.; Liu, Z.; Qian, D., Highly electrocatalytic performance of bimetallic Co–Fe sulfide nanoparticles encapsulated in N–doped carbon nanotubes on reduced graphene oxide for oxygen evolution. J Alloys Compd 2021, 881, 160667.

72. Wang, D.; Gong, M.; Chou, H.; Pan, C.; Chen, H.; Wu, Y.; Lin, M.; Guan, M.; Yang, J.; Chen, C.; Wang, Y.; Hwang, B.; Chen, C.; Dai, H., Highly active and stable hybrid catalyst of cobalt–doped FeS_2 nanosheets−carbon nanotubes for hydrogen evolution reaction. J. Am Chem Soc 2015, 137, 1587−1592.

73. Qin, J.; Yang, M.; Hou, S.; Dong, B.; Chen, T.; Ma, X.; Xie, J.; Zhou, Y.; Nan, J.; Chai, Y., Copper and cobalt co–doped Ni_3S_2 grown on nickel foam for highly efficient oxygen evolution reaction. Appl Surf Sci 2020, 502, 144172.

74. Shang, X.; Yan, K.; Lu, S.; Dong, B.; Gao, W.; Chi, J.; Liu, Z.; Chai, Y.; Liu C., Controlling electrodeposited ultrathin amorphous Fe hydroxides film on V–doped nickel sulfide nanowires as efficient electrocatalyst for water oxidation.

75. Yuan, F.; Wei, J.; Qin, G.; Ni, Y., Carbon cloth supported hierarchical core–shell $NiCo_2S_4$@CoNi–LDH nanoarrays as catalysts for efficient oxygen evolution reaction in alkaline solution. J Alloys Compd 2020, 830, 154658.

76. Nguyen, T.; Su, Y.; Lin, C.; Ting, J., Self–reconstruction of sulfate–containing high entropy sulfide for exceptionally high–performance oxygen evolution reaction electrocatalyst. Adv Funct Mater 2021, 31, 2106229.

77. Roy, B.; Shebin, K.; Sampath, S. Pyrite–type cobalt phosphosulphide bifunctional catalyst for aqueous and gel–based rechargeable zinc–air batteries. J. Power Sources 2020, 450, 227661.

78. Li, J.; Xia, Z.; Zhou, X.; Qin, Y.; Ma, Y.; Qu, Y., Quaternary pyrite–structured nickel/cobalt phosphosulfide nanowires on carbon cloth as efficient and robust electrodes for water electrolysis. Nano Research 2017, 10, 814–825.

79. Dutta, B.; Wu, Y.; Chen, J.; Wang, J.; He, J.; Sharafeldin, M.; Kerns, P.; Jin, L.; Dongare, A.; Rusling, J.; Suib, S., Partial surface selenization of cobalt sulfide microspheres for enhancing the hydrogen evolution reaction. ACS Catal 2019, 9, 456−465.

80. Sun, J.; Hu, X.; Huang, Z.; Huang, T.; Wang, X.; Guo, H.; Dai, F.; Sun, D., Atomically thin defect–rich Ni–Se–S hybrid nanosheets as hydrogen evolution reaction electrocatalysts. Nano Research 2020, 13, 2056–2062.

81. Yang, X.; Xie, H.; Zou, Y.; Huang, Y.; Jiang, L.; Wang, X.; Tang, D.; Si, C.; Wang, J., Cost–effective and efficient plum–pudding–like $Fe_xNi_{1-x}S_2$/C composite electrocatalysts for oxygen evolution reaction. Renewable Energy 2021,168, 416–423.

82. Han, H.; Kim, K.; Choi, H.; Ali, G.; Chung, K.; Hong, Y.; Choi, J.; Kwon, J.; Lee, S.; Lee, J.; Ryu, J.; Song, T.; Mhin, S., Parallelized reaction pathway and stronger internal band bending by partial oxidation of metal sulfide−graphene composites: important factors of synergistic oxygen evolution reaction enhancement. ACS Catal 2018, 8, 4091−4102.

83. Song, Y.; Zhao, X.; Liu, Z., Surface selenium doped hollow heterostructure/defects Co–Fe sulfide nanoboxes for enhancing oxygen evolution reaction and supercapacitors. Electrochim Acta 2021, 374, 137962.

84. Yang, H.; Wang, C.; Zhang, Y.; Wang, Q., Chemical valence–dependent electrocatalytic activity for oxygen evolution reaction: A case of nickel sulfides hybridized with N and S co–doped carbon nanoparticles. Small 2018, 14, 1703273.

85. Lu, X.; Zhang, S.; Shangguan, E.; Zhang, P.; Gao, S.; Lou, X., Nitrogen–doped cobalt pyrite yolk–shell hollow spheres for long–life rechargeable Zn–air batteries. Adv Sci 2020, 7, 2001178.

86. Lia, X.; Han, G.; Liu, Y.; Dong, B.; Shang, X.; Hua, W.; Chai, Y.; Liu, Y.; Liu, C., In situ grown pyramid structures of nickel diselenides dependent on oxidized nickel foam as efficient electrocatalyst for oxygen evolution reaction. Electrochim Acta 2016, 205, 77–84.

87. Zhai, L.; Lo, T.; Xu, Z.; Potter, J.; Mo, J.; Guo, X.; Tang, C.; Tsang, S.; Lau, S., In situ phase transformation on nickel–based selenides for enhanced hydrogen evolution reaction in alkaline medium. ACS Energy Lett 2020, 5, 2483−2491.

88. Wang, F.; Li, Y.; Shifa, T.; Liu, K.; Wang, F.; Wang, Z.; Xu, P.; Wang, Q.; He, J., Selenium–enriched nickel selenide nanosheets as a robust electrocatalyst for hydrogen generation. Angew Chem Int Ed 2016, 55, 6919–6924.

89. Liu, X.; Liu, Y.; Fan, L., MOF–derived CoSe$_2$ microspheres with hollow interiors as high–performance electrocatalysts for the enhanced oxygen evolution reaction. J Mater Chem A, 2017, 5, 15310.

90. Niu, S.; Jiang, W.; Wei, Z.; Tang, T.; Ma, J.; Hu, J.; Wan, L., Se–doping activates FeOOH for cost–effective and efficient electrochemical water oxidation, J Am Chem Soc 2019, 141, 7005–7013.

91. Luo, J.; Wang, H.; Su, G.; Tang, Y.; Liu, H.; Tian, F.; Li, D., Self–supported nickel phosphosulphide nanosheets for highly efficient and stable overall water splitting, J Mater Chem A 2017, 5, 14865–14872.

92. Song, H.; Yoon, H.; Ju, B.; Lee, G.; Kim, D., 3D architectures of quaternary CoNi–S–P/graphene hybrids as highly active and stable bifunctional electrocatalysts for overall water splitting, Adv Energy Mater 2018, 8, 2319–2329.

93. Huang, L.; Wu, H.; Zhang, Y., One–step synthesis of CoPSe–$CoSe_2$/CNTs as efficient electrocatalyst for oxygen evolution reaction. Electrochim Acta 2020, 331,135362.

94. Liu, H.; Wang, K.; He, W.; Zheng, X.; Gong, T.; Li, Y.; Zhao, J.; Zhang, J.; Liang, L., Phosphorus–doped nickel selenides nanosheet arrays as highly efficient electrocatalysts for alkaline hydrogen evolution. Int J Hydrog Energy 2021, 46, 1967–1975.

95. Zhou, J.; Yuan, L.; Wang, J.; Song, L.; You, Y.; Zhou, R.; Zhang, J.; Xu, J., Combinational modulations of $NiSe_2$ nanodendrites by phase engineering and iron–doping towards an efficient oxygen evolution reaction, J Mater Chem A 2020, 8, 8113–8120.

96. Zheng, X.; Han, X.; Cao, Y.; Zhang, Y.; Nordlund, D.; Wang, J.; Chou, S.; Liu, H.; Li, L.; Zhong, C.; Deng, Y.; Hu, W., Identifying dense $NiSe_2$/$CoSe_2$ heterointerfaces coupled with surface high–valence bimetallic sites for synergistically enhanced oxygen electrocatalysis, Adv Mater 2020, 32, 2000607.

97. Zhang, S.; Zhang, J.; Liang, P.; Zhang, C.; Kou, T.; Zhang, Z., Corrosion engineering derived Ga doped $CoSe_2$ nanosheets intrinsically active for oxygen evolution reaction. J Power Sources 2021, 497, 229895.

98. Chi, J.; Shang, X.; Liang, F.; Dong, B.; Li, X.; Liu, Y.; Yan, K.; Gao, W.; Chai, Y.; Liu, C., Facile synthesis of pyrite–type binary nickel iron diselenides as efficient electrocatalyst for oxygen evolution reaction. Appl Surf Sci 2017, 401, 17–24.

99. Binary metal $Fe_{0.5}Co_{0.5}Se_2$ spheres supported on carbon fiber cloth for efficient oxygen evolution reaction. Int. J Hydrog Energy 2017, 42, 15189 –15195.

100. Liu, C.; Han, Y.; Yao, L.; Liang, L.; He, J.; Hao, Q.; Zhang, J.; Li, Y.; Liu, H., Engineering bimetallic NiFe–based hydroxides/selenides heterostructure nanosheet arrays for highly–efficient oxygen evolution reaction. Small 2021, 17, 2007334.

101. Wu, Z.; Lu, X.; Zang, S.; Lou, X, Non–noble–metal–based electrocatalysts toward the oxygen evolution reaction, Adv Funct Mater 2020, 30, 1910274.

102. Wang, J.; Gao, Y.; Kong, H.; Kim, J.; Choi, S.; Ciucci, F.; Hao, Y.; Yang, S.; Shao, Z.; Lim, J., Non–precious–metal catalysts for alkaline water electrolysis: operando characterizations, theoretical calculations, and recent advances. Chem Soc Rev 2020, 49, 9154–9196.

103. Chen, C.; Tuo, Y.; Lu, Q.; Lu, H.; Zhang, S.; Zhou, Y.; Zhang, J.; Liu, Z.; Kang, Z.; Feng, X.; Chen, D., Hierarchical trimetallic Co–Ni–Fe oxides derived from core–shell structured metal–organic frameworks for highly efficient oxygen evolution reaction. Appl Catal B: Environ 2021, 287, 119953.

104. Yang, Y.; Kang, Y.; Zhao, H.; Dai, X.; Cui, M.; Luan, X.; Zhang, X.; Nie, F.; Ren, Z.; Song, W., An interfacial electron transfer on tetrahedral $NiS_2/NiSe_2$ heterocages with dual–phase synergy for efficiently triggering the oxygen evolution reaction. Small 2020, 16, 1905083.

105. Wang, B.; Srinivas, K.; Wang, X.; Su, Z.; Yu, B.; Zhang, X.; Liu, Y.; Ma, F.; Yang, D.; Chen, Y., Self–assembled $CoSe_2$–$FeSe_2$ heteronanoparticles along the carbon nanotube network for boosted oxygen evolution reaction. Nanoscale 2021, 13, 9651–9658.

106. Ma, D.; Hu, B.; Wu, W.; Liu, X.; Zai, J.; Shu, C.; Tsega, T.; Chen, L.; Qian, X.; Liu, T., Highly active nanostructured CoS_2/CoS heterojunction electrocatalysts for aqueous polysulfide/iodide redox flow batteries. Nat Commun 2019, 10, 3367.

107. Ni, S.; Qu, H.; Xu, Z.; Zhu, X.; Xing, H.; Wang, L.; Yu, J.; Liu, H.; Chen, C.; Yang, L., Interfacial engineering of the $NiSe_2/FeSe_2$ p–p heterojunction for promoting oxygen evolution reaction and electrocatalytic urea oxidation. Appl Catal B 2021, 299, 120638.

108. Kang, H.; Li, H.; Zhao, X.; Yang, L.; Xu, S., Anion doped bimetallic selenide as efficient electrocatalysts for oxygen evolution reaction. Ceram Int 2020, 46, 2792–2797.

109. Lv, L.; Gan, Y.; Wan, H.; Li, Z.; Wang, C.; Wang, H., Electronic coupling regulation in yolk–shell nanostructured nickel–cobalt diselenides with octahedral coordination for boosted oxygen evolution reaction. Int. J Hydrog Energy 2021, 46, 28387–28396.

110. Nai, J.; Lu, Y.; Yu, L.; Wang, X.; Lou, X., Formation of Ni–Fe mixed diselenide nanocages as a superior oxygen evolution electrocatalyst. Adv Mater 2017, 29, 1703870.

111. Zhou, J.; Yuan, L.; Wang, J.; Song, L.; You, Y.; Zhou, R.; Zhang, J.; Xu, J., Combinational modulations of $NiSe_2$ nanodendrites by phase engineering and irondoping towards an efficient oxygen evolution reaction. J Mater Chem A, 2020, 8, 8113.

112. Li, Y.; Chen, R.; Yan, D.; Wang, S., Regulation of morphology and electronic structure of $NiSe_2$ by Fe for high effective oxygen evolution reaction. Chem Asian J 2020, 15, 3845–3852.

113. Mei, G.; Liang, H.; Wei, B.; Shi, H.; Ming, F.; Xu, X.; Wang, Z., Bimetallic MnCo selenide yolk shell structures for efficient overall water splitting. Electrochim Acta 2018, 290, 82–89.

114. Zhu, G.; Xie, X.; Li, X.; Liu, Y.; Shen, X.; Xu, K.; Chen, S., Nanocomposites based on $CoSe_2$- decorated $FeSe_2$ nanoparticles supported on reduced graphene oxide as high–performance electrocatalysts toward oxygen evolution reaction. ACS Appl Mater Interfaces 2018, 10, 19258−19270.

115. Luo, Z.; Wang, J.; Tan, J.; Zhang, M.; Lu, T., Self–template synthesis of Co−Se−S−O hierarchical nanotubes as efficient electrocatalysts for oxygen evolution under alkaline and neutral conditions. ACS Appl Mater Interfaces 2018, 10, 8231−8237.

116. Cao, X.; Hong, Y.; Zhang, N.; Chen, Q.; Masud, J.; Zaeem, M.; and Nath, M., Phase exploration and identification of multinary transition–metal selenides as high–efficiency oxygen evolution electrocatalysts through combinatorial electrodeposition. ACS Catal 2018, 8, 8273−8289.

117. Wang, G.; Wang, H.; Chen T.; Tan, Y., $Ni_{1-x}M_xSe_2$ (M=Fe, Co, Cu) nanowires as anodes for ammonia–borane electrooxidation and the derived $Ni_{1-x}M_xSe_{2-y}$–OOH ultrathin nanosheets as efficient electrocatalysts for oxygen evolution. J Mater Chem A, 2019, 7, 16372.

118. Wang, J.; Zheng, X.; Cao, Y.; Li, L.; Zhong, C.; Deng, Y.; Han, X.; Hu, W., Developing indium–based ternary spinel selenides for efficient solid flexible Zn–air batteries and water splitting. ACS Appl Mater Interfaces 2020, 12, 8115−8123.

119. Prabhakaran, S.; Balamurugan, J.; Kim, N.; Lee, J., Hierarchical 3D oxygenated cobalt molybdenum selenide nanosheets as robust trifunctional catalyst for water splitting and zinc–air batteries. Small 2020, 16, 2000797.

120. Jiang, K.; Liu, B.; Luo, M.; Ning, S.; Peng, M.; Zhao, Y.; Lu, Y.; Chan, T.; Groot, F.; Tan, Y., Single platinum atoms embedded in nanoporous cobalt selenide as electrocatalyst for accelerating hydrogen evolution reaction. Nat Commun 2019, 10, 1743.

121. Chen, W.; Wang, H.; Li, Y.; Liu, Y.; Sun, J.; Lee, S.; Lee, J.; Cui, Y. In situ electrochemical oxidation tuning of transition metal disulfides to oxides for enhanced water oxidation. ACS Cent Sci 2015, 1, 244−251.

122. Burke, M.; Enman, L.; Batchellor, A.; Zou, S.; Boettcher, S., Oxygen evolution reaction electrocatalysis on transition metal oxides and (oxy)hydroxides: activity trends and design principles. Chem Mater 2015, 27, 7549−7558.

123. Jin S., Are metal chalcogenides, nitrides, and phosphides oxygen evolution catalysts or bifunctional catalysts ? ACS Energy Lett 2017, 2, 1937−1938.

124. Han, W.; Li, M.; Ma, Y.; Yang, J., Cobalt–based metal–organic frameworks and their derivatives for hydrogen evolution reaction. Front Chem 2020, 8, 592915.

125. Kresse, G.; Furthmuller, J., Efficient iterative schemes for Ab initio total–energy calculations using a plane–wave basis set. Phys Rev B Condens Matter Mater Phys 1996, 54, 11169−11186.

126. Blöchl, P. E., Projector augmented–wave method. Phys Rev B Condens Matter Mater Phys 1994, 50, 17953−17979.

127. Grimme, S.; Antony, J.; Ehrlich, S.; Krieg, S., A consistent and accurate Ab initio parametrization of density functional dispersion correction (DFT–D) for the 94 elements H–Pu. J Chem Phys 2010, 132, 154104.

128. Lin, C.; Tsai, Y.; Johnston, H. E.; Fang, M.; Yu, F.; Zhou, W.; Whitfifield, P.; Li, Y.; Wang, J.; Liu, R.; Attfifield, J.–P., Enhanced photoluminescence emission and thermal stability from introduced cation disorder in phosphors. J Am Chem Soc 2017, 139, 11766−11770.

129. Qiu, B.; Cai, L.; Wang, Y.; Lin, Z.; Zuo, Y.; Wang, M.; Chai, Y., Fabrication of nickel−cobalt bimetal phosphide nanocages for enhanced oxygen evolution catalysis. Adv Funct Mater 2018, 28, 1706008.

130. Kim, J.; Kim, B.; Kim, H.; Kang, K., Recent progress on multimetal oxide catalysts for the oxygen evolution reaction. Adv Energy Mater 2018, 8, 1702774.

131. Zhou, P.; He, J.; Zou, Y.; Wang, Y.; Xie, C.; Chen, R.; Zang, S.; Wang, S. Single–crystalline layered double hydroxides with rich defects and hierarchical structure by mild reduction for enhancing the oxygen evolution reaction. Sci China Chem 2019, 62, 1365–1370.

132. Zuo, Y.; Rao, D.; Li, S.; Li, T.; Zhu, G.; Chen, S.; Song, L.; Chai, Y.; Han, H., Atomic vacancies control of Pd–based catalysts for enhanced electrochemical performance. Adv Mater 2018, 30, 1704171.

133. Sun, Y.; Xu, K.; Wei, Z.; Li, H.; Zhang, T.; Li, X.; Cai, W.; Ma, J.; Fan, H.; Li, Y., Strong electronic interaction in dual–cation incorporated $NiSe_2$ nanosheets with lattice distortion for highly efficient overall water splitting. Adv Mater 2018, 30, 1802121.

134. Sun, R.; Liu, S.; Wei, Q.; Sheng, J.; Zhu, S.; An, Q.; Mai, L., Mesoporous NiS_2 nanospheres anode with pseudocapacitance for high–rate and long–life sodium–ion battery. Small 2017, 13, 1701744.

135. Zhang, G.; Feng, Y.–S.; Lu, W.–T.; He, D.; Wang, C.–Y.; Li, Y.–K.; Wang, X.–Y.; Cao, F., Enhanced catalysis of electrochemical overall water splitting in alkaline media by Fe doping in Ni_3S_2 nanosheet arrays. ACS Catal, 2018, 8, 5431.

Original papers

1 In situ coating amorphous boride on ternary pyritetype boron sulfide for highly efficient oxygen evolution
(Appendix I)

2 Valence engineering via dual–cation and boron doping in pyrite selenide for highly efficient oxygen evolution
(Appendix II)

3 Spatially confined formation of single atoms in highly porous carbon nitride nanoreactors
(Appendix III)

1. Valence engineering via dual–cation and boron doping in pyrite selenide for highly efficient oxygen evolution

Yunpeng Zuo, Dewei Rao, Sainan Ma, Tingting Li, Yuen Hong Tsang, Štěpán Kment, and Yang Chai

ACS Nano, 2019, doi:10.1021/acsnano.9b04956

IF: 15.88

Abstract:

Valence engineering has been proved an effective approach to modify the electronic property of a catalyst and boost its oxygen evolution reaction (OER) activity, while the limited number of elements restricts the structural diversity and the active sites. Also, the catalyst performance and stability are greatly limited by cationic dissolution, ripening, or crystal migration in a catalytic system. Here we employed a widely used technique to fabricate heteroepitaxial pyrite selenide through dual–cation substitution and a boron dopant to achieve better activity and stability. The overpotential of Ni–pyrite selenide catalyst is decreased from 543 mV to 279.8 mV at 10 mA cm^{-2} with a Tafel slope from 161 to 59.5 mV dec^{-1}. Our theoretical calculations suggest both cation and boron doping can effectively optimize adsorption energy of OER intermediates, promote the charge transfer among the heteroatoms, and improve their OER property. This work underscores the importance of modulating surface electronic structure with the use of multiple elements and provides a general guidance on the minimization of activity loss with valence engineering.

2. In situ coating amorphous boride on ternary pyritetype boron sulfide for highly efficient oxygen evolution

Tingting Li, Tianyun Jing, Dewei Rao, Xiaotian Jia, Yunpeng Zuo, Štěpán Kment and
Radek Zbořil

Journal of Materials Chemistry A, 2021, doi: 10.1039/d0ta10633j
IF: 12.732

Abstract:

Multimetallic pyrite–type sulfides have been promising electrocatalytic materials for the electrochemical oxygen evolution reaction (OER), but sulfides still require further improvement due to the easy oxidization of surface atoms and the intrinsically low activity. Herein, we synthesized the ternary pyritetype boron sulfide in situ coated by amorphous $FeCoNiB_x$ as an efficient and durable heterogeneous catalyst for OER. The spherical aberration–corrected transmission electron microscopy clearly shows that the adjacent crystals exhibit different phases with an approximately 2 nm amorphous layer on the external surface of the catalysts. This hybrid catalyst exhibits the superior OER activity with an attractive overpotential of 419.4 mV vs. RHE at 100 mA cm^{-2} in 1 M KOH solution and excellent stability over 10 h. Density functional theory calculations reveal that the B atoms can attract the electrons from metals, resulting in the expansion of the unoccupied *d* orbitals of metals, which is beneficial to attract the electrons from OH groups, thus improving the OER performance of the catalyst combined with its special heterostructure. This study provides an advantageous method for engineering the electrical structure of pyrite–type sulfides for high OER activity and long durability.

3. Spatially confined formation of single atoms in highly porous carbon nitride nanoreactors

Yunpeng Zuo, Tingting Li, Ning Zhang, Tianyun Jing, Dewei Rao, Patrik Schmuki, Štěpán Kment, Radek Zboril, and Yang Chai

ACS Nano, 2021, doi.org/10.1021/acsnano.1c01872

IF: 15.88

Abstract:

Reducing the size of a catalyst to a single atom (SA) level can dramatically change its physicochemical properties and significantly boost its catalytic activity. However, the massive synthesis of SA catalysts still remains a grand challenge mainly because of the aggregation and nucleation of the generated atoms during the reaction. Here, we design and implement a spatially confined synthetic strategy based on a poroushollow carbon nitride (*p*–CN) coordinated with 1–butyl–3–methylimidazole hexafluorophosphate, which can act as a nanoreactor and allow us to obtain metal SA catalysts (*p*–CN@M SAs). This relatively easy and highly effective method provides a way to massively synthesize single/multiple atoms (*p*–CN@M SAs, M = Pt, Pd, Cu, Fe, etc.). Moreover, the amorphous NiB–coated *p*–CN@Pt SAs can further increase the loading amount of Pt SAs to 3.7 wt %. The synthesized *p*–CN@Pt&NiB electrocatalyst exhibits an extraordinary hydrogen evolution reaction activity with the overpotential of 40.6 mV@10 mA/cm^{-2} and the Tofel slope of 29.26 mV/dec.

Conference presentations

1. Self–reconstruction mediates isolated Pt tailored nanoframes for highly efficient catalysis

(poster presentation; Appendix Ⅳ)

2. Valence engineering in pyrite selenide for highly efficient oxygen evolution

(oral presentation)

List of abbreviations

TEM	transmission electron microscopes
HRTEM	high–resolution transmission electron microscopy
EELS	electron energy loss spectroscopy
EDS	energy–dispersive X–ray spectroscopy
LDH	layered Double Hydroxides
3D	three–dimensional
CV	cyclic voltammetry
MOFs	metal–organic frameworks
SAED	selected area diffraction
TMDs	transition metal dichalcogenides
XPS	X–ray photoelectron spectroscopy
XRD	X–ray powder diffraction
SEM	scanning electron microscope
TMDs	Transition–metal dichalcogenide
EIS	electrochemical impedance spectroscopy
HAADF–STEM	high–angular dark–field scanning transmission electron microscopy
LSV	linear sweep voltammetry
PT	pyrite–type
HER	hydrogen evolution reaction
OER	oxygen evolution reaction
GSAS	general structure analysis system
AC–TEM	spherical aberration corrected transmission electron microscopy
PDOS	Projected density of states

List of appendices

1. Original papers

Appendix I: *In situ* coating amorphous boride on ternary pyritetype boron sulfide for highly efficient oxygen evolution

Appendix II: Valence engineering *via* dual–cation and boron doping in pyrite selenide for highly efficient oxygen evolution

Appendix III: Spatially confined formation of single atoms in highly porous carbon nitride nanoreactors

2. Published posters

Appendix IV: Self–reconstruction mediates isolated Pt tailored nanoframes for highly efficient catalysis

Journal of
Materials Chemistry A

ROYAL SOCIETY
OF CHEMISTRY

PAPER

View Article Online
View Journal | View Issue

Cite this: *J. Mater. Chem. A*, 2021, **9**, 12283

In situ coating amorphous boride on ternary pyrite-type boron sulfide for highly efficient oxygen evolution†

Tingting Li, ‡[a] Tianyun Jing,‡[b] Dewei Rao, *[bd] Xiaotian Jia,[a] Yunpeng Zuo, *[c] Štěpán Kment[c] and Radek Zbořil [c]

Multimetallic pyrite-type sulfides have been promising electrocatalytic materials for the electrochemical oxygen evolution reaction (OER), but sulfides still require further improvement due to the easy oxidization of surface atoms and the intrinsically low activity. Herein, we synthesized the ternary pyrite-type boron sulfide *in situ* coated by amorphous $FeCoNiB_x$ as an efficient and durable heterogeneous catalyst for OER. The spherical aberration-corrected transmission electron microscopy clearly shows that the adjacent crystals exhibit different phases with an approximately 2 nm amorphous layer on the external surface of the catalysts. This hybrid catalyst exhibits the superior OER activity with an attractive overpotential of 419.4 mV *vs.* RHE at 100 mA cm^{-2} in 1 M KOH solution and excellent stability over 10 h. Density functional theory calculations reveal that the B atoms can attract the electrons from metals, resulting in the expansion of the unoccupied d orbitals of metals, which is beneficial to attract the electrons from OH^- groups, thus improving the OER performance of the catalyst combined with its special heterostructure. This study provides an advantageous method for engineering the electrical structure of pyrite-type sulfides for high OER activity and long durability.

Received 1st November 2020
Accepted 2nd May 2021

DOI: 10.1039/d0ta10633j

rsc.li/materials-a

Introduction

Hydrogen is one of the clean and sustainable energy sources, which is most likely to replace fossil fuels in the future.[1,2] Electrocatalytic water splitting has been extensively studied for hydrogen generation that involves two half reactions: hydrogen evolution reaction (HER) and oxygen evolution reaction (OER).[3,4] OER is the kinetic bottleneck of water splitting, which requires a high standard overpotential ($\eta \approx 1.23$ V *versus* reversible hydrogen electrode) with the four-electron–proton coupled processes; thus, it is particularly important to develop OER catalysts.[5–8] To date, most of the commercial catalysts of OER are noble metal oxides (*e.g.*, IrO_2, RuO_2), possessing small reserves, high cost and challenging large-scale application.[9,10] As a part of promising economically energy-conversion catalysts, pyrite-type sulfides (PTSs) have been adopted as one of the most efficient OER catalysts.[11,12] PTSs are typical semiconductors with the crystal system of isometric, representative of dianion units and cations in octahedral coordination.[12,13] Although such structure has favorable electronic modulation, the intrinsic performance of PTS still suffers from the easy oxidization of surface atoms, generally lower charge transfer and conductivity.[14,15]

The electronic structure and conductivity of PTSs can be effectively enhanced through doping 3d metals for improving the OER properties.[16–19] A series of binary metal pyrites have been developed to boost the OER activity of these catalysts compared to monometal sulfides.[20–22] Liu *et al.* synthesized the vanadium-doped pyrite NiS_2 nanosheets that exhibited extraordinary OER activity since the electronic property of NiS_2 reconfigured from the semiconductive to metallic characteristics after vanadium doping.[23] Ni *et al.* fabricated Fe-doped pyrite NiS_2 mesocrystals that effectively enhanced the OER property with the overpotential from 351 mV to 252 mV *vs.* RHE at 10 mA cm^{-2}.[24] Moreover, introducing boron atoms into the PTS catalysts can effectively modify the electronic property since the B 2p orbitals can be hybridized with 3d orbitals of metals, resulting in the easy delocalization of B-metals electrons, which is beneficial for OER.[25] In addition, constructing heterogeneous structures in PTSs is also a typical valence engineering to enhance the OER properties.[26,27] Nonetheless, PTSs suffer from the unsatisfied durability because of the cationic dissolution

---

[a] *Key Laboratory of Micro-Nano Materials for Energy Storage and Conversion of Henan Province, Institute of Surface Micro and Nano Materials, College of Chemical and Materials Engineering, Xuchang University, Henan 461000, People's Republic of China*

[b] *School of Materials Science and Engineering, Jiangsu University, Zhenjiang 212013, People's Republic of China. E-mail: dewei@ujs.edu.cn*

[c] *Regional Center of Advanced Technologies and Materials, Olomouc 78371, Czech Republic. E-mail: ypzuo01@gmail.com*

[d] *Department of Chemistry and Biochemistry, University of California Santa Cruz, 1156 High Street, Santa Cruz, California, 95064, USA*

† Electronic supplementary information (ESI) available. See DOI: 10.1039/d0ta10633j

‡ These authors contributed equally to this work.

and the easy oxidation of external sulfur species.[28–33] Thus, an appropriate synthesis route for the preparation a specific PTS simultaneously to improve the OER activity and stability will effectively expand the profitable applications of PTSs.

Coating the catalysts with a thin conductive layer, such as amorphous active materials or carbon based materials, are effective strategies to bring about remarkable catalytic durability, preventing the catalysts from aggregation and dissolution.[34–38] For the amorphous boride, it allows B in $FeCoNiB_x$ to be coordinatively unsaturated even after sulfuration. The B atoms lack electrons, which theoretically have a strong attraction towards the O species.[25,37] Accordingly, herein, we synthesized boron-doped ternary heterogeneous PTS coated by amorphous boride ($FeCoNiB_x$) following a two-step method. First, amorphous $FeCoNiB_x$ was synthesized according to the wet chemical method, in which sodium borohydride was used to react with metal salt precursors. Then, the boron-doped ternary PTS coated by amorphous boride (B-TS-H@T-B) can be prepared after sulfidation in a tube furnace. The spherical aberration correction transmission electron microscope (AC-TEM) clearly shows the special heterogeneous structures with the external amorphous coating. B-TS-H@T-B exhibited superior OER activity with a low overpotential of about 419.4 mV at 100 mA cm^{-2} in the 1 M KOH solution. Significantly, the current density of B-TS-H@T-B only dropped 23.06% after 10 h long-term reaction, which was better than B-NiS (∼100%), B-CoNiS (37.51%) and B-FeNiS (61.73%). Also, theoretical studies suggest that the electronic structure of B-TS-H@T-B was favorable redistribution for water splitting.

Experimental section

Chemicals

Nafion and sodium borohydride ($NaBH_4$) were obtained from Sigma–Aldrich. Other chemicals were purchased from Sinopharm Reagent Co., Ltd without further purification. The distilled water (DIW, 18.2 MΩ) was the solvent for synthesis.

Materials synthesis

The B-NiS, B-CoNiS, B-FeNiS and B-TS-H@T-B powers were obtained by the typical chemical reduction and annealing treatment. First, NiB, CoNiB, FeNiB, FeCoNiB precursors were synthesized by a redox reaction, respectively. A mixture of 1.16 g $Ni(NO_3)_2 \cdot 6H_2O$, 0.29 g $FeCl_3 \cdot 6H_2O$ and 0.16 g $Co(NO_3)_2 \cdot 6H_2O$ (the mole ratio of 4 : 1 : 1) was dissolved in deionized water under vigorous stirring. Then, the $NaBH_4$ aqueous solution was added and large amounts of black precipitation formed.

The products were washed in deionized water three times and dried overnight at 60 °C. Subsequently, 0.48 g FeCoNiB precursors and 0.4 g sulfur powders were mixed together and placed in a quartz boat, and then heated to 400 °C for 2 h at a heating rate of 5 °C min^{-1} in a nitrogen atmosphere. After cooling to room temperature naturally, B-TS-H@T-B was obtained. Similarly, B-NiS, B-CoNiS, B-FeNiS were obtained only by adding the corresponding precursors, while the sulfidation conditions and parameters were consistent with B-TS-H@T-B.

Materials characterization

The transmission electron microscopy images (TEM), high resolution TEM and EDX elemental mapping images were collected by a JEM-ARM-200F microscope operated at 200 kV. An X-ray diffractometer (Rigaku Smart Lab) using Cu Kα (γ = 1.54178 A) radiation was used to obtain X-ray powder diffraction (XRD) data. The X-ray photoelectron spectroscopy (XPS) was collected by an ESCALAB 250Xi XPS system using Mg as the excitation source.

Electrochemical measurements

All electrochemical measurements were performed in a typical three-electrode system at room temperature using a CHI electrochemical workstation (660E). 5 mg of the catalyst was dispersed in 1 mL of the mixed solution ($V_{\text{water}} : V_{\text{isopropyl alcohol}} = 10 : 7$) with 150 μL Nafion (5 wt%) under 30 min ultrasonication to form a homogeneous ink. 10 μL ink was dripped onto the glassy carbon electrode (GCE, with a diameter of 5 mm) and dried at room temperature. A saturated calomel electrode (SCE, with saturated KCl) and graphite rod were used as reference and counter electrodes, respectively. The electrolyte is 1 M KOH. According to the Nernst equation $E(\text{RHE}) = E(\text{SCE}) + 0.242 + 0.059\text{pH}$, the tested potentials were converted to the reversible hydrogen electrode (RHE). For the linear sweep voltammetry polarization curves, the scanning range was conducted from 1.3 V to 1.9 V *vs.* RHE at a scan rate of 5 mV s^{-1}.

Density functional theory calculation

In this present study, all density functional theory (DFT) calculations were performed by the Vienna *ab initio* simulation package (VASP).[39,40] To describe the ion-electron interactions, the projected augmented wave (PAW) method combined with the exchange-correlation functional of Perdew–Burke–Ernzerhof (PBE) in the generalized gradient approximation (GGA)[41,42] were employed. For each job of simulations, the cutoff energy for function is 500 eV, and the convergence criteria are 10^{-5} eV in energy and 10^{-2} eV Å^{-1} in force, respectively. Based on the XRD data of the as-synthesized samples, Ni, $FeCoS_2$ and FeCoNiS crystal structures were selected as the primary model, and then optimized *via* the above-mentioned method. Also, B-doping in the holes of these structures were also optimized.

Results and discussion

B-TS-H@T-B was synthesized through the redox and sulfidation process. Scheme S1† shows the growth process of B-FeCoNiS-H crystals coated by the thin amorphous $FeCoNiB_x$ layer. The $FeCoNiB_x$ powder was obtained by the redox reaction between sodium borohydride and metal salt precursors. After grinding with sulfur powder, the $FeCoNiB_x$ mixture was preloaded in a tube furnace under N_2 flow for the sulfidation step, as depicted in Scheme S1.† The formation process of B-TS-H@T-B contains nucleation and growth steps. The amorphous $FeCoNiB_x$ can act as the reactive substrate agent and the vaporized sulfur atoms will gradually react with $FeCoNiB_x$ to generate metal sulfide clusters randomly distributed in

$FeCoNiB_x$. Notably, sulfide has no intrinsic driving force for the growth of anisotropic structures when the metal sulfide clusters are surrounded by $FeCoNiB_x$ under the high temperature conditions. Based on the Wulff's theorem, the generated metal sulfide clusters gradually grew into bigger crystals to minimize the total interfacial free energy of the system.[43–45] Simultaneously, due to the coordinatively unsaturated bonds, the unreacted atoms in the amorphous $FeCoNiB_x$ tend to migrate and coat on the particle to bond with the surface atoms of the crystal. The detailed experimental process is in the experimental section. AC-TEM was adopted to analyze the crystal information of the as-synthesized catalysts. As shown in Fig. 1a, B-TS-H@T-B consists of abundant nano-particles scattered on the surface. The yellow-dotted lines in Fig. 1b–d clearly show the amorphous layer, which may effectively prevent the aggregation and leaching of the catalysts.[35,37] Fig. 1e presents the different fast Fourier transform (FFT) patterns of the crystals in B-TS-H@T-B, suggesting the heterogeneous structures.[25] The inhomogeneous division of elements in the TEM-EDX mapping results (Fig. S1a–d†) can further demonstrate the multiphase structure for B-TS-H@T-B. Besides, the elliptical circle areas in Fig. S1a–d† show that the amorphous layer is mainly boride. The XRD and Rietveld refinement analyses were used to further investigate the crystal structure of B-TS-H@T-B. The diffraction peaks in Fig. 1f are consistent with the (111), (002) and (113) planes of B-TS-H@T-B nanocatalysts.[38] The Rietveld refinement of B-TS-H@T-B was obtained using the FullProf Suite, indicating the main crystal phase of $Ni_{0.8}Fe_{0.1}Co_{0.1}S_2B_x$ combined with $CoFeS_2B_x$ and NiB_x.[39] Fig. 1g and S2† show the consistent atomistic model with the typical isometric structure. The XRD refinement results of B-TS-H@T-B reveal that the cation atoms in $Ni_{0.8}Fe_{0.1}Co_{0.1}S_2B_x$ have the same sites and B atoms mainly embedded in the interstitial site.

The STEM image in Fig. 2a displays the morphology of B-TS-H@T-B, which contains numerous nanoparticles. The typical high resolution STEM image in Fig. 2b and c clearly illustrate the lattice fringes with the *d* spacings of 0.27 nm and 0.32 nm, which are consistent with the (002) and (111) facets of B-TS-

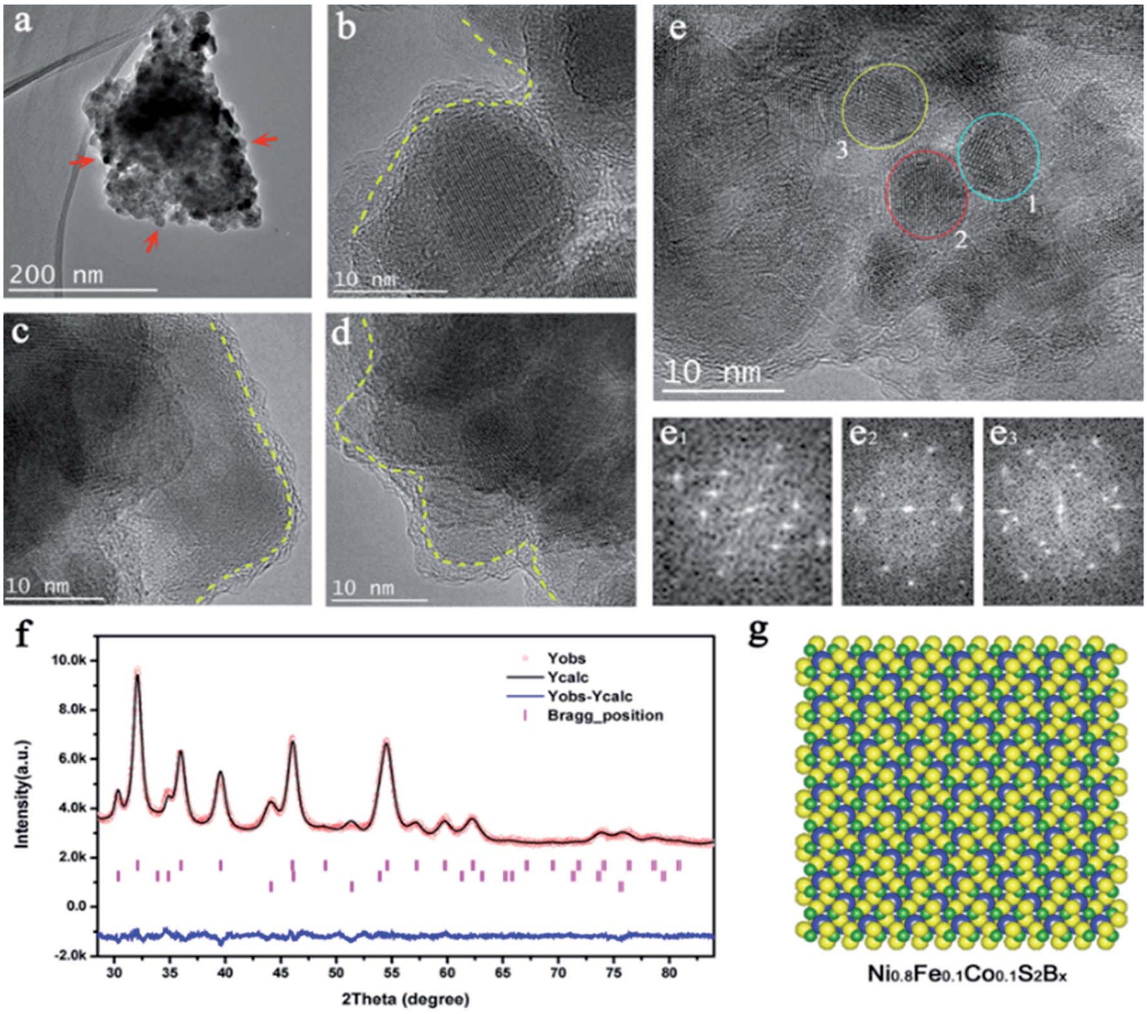

Fig. 1 Morphology and structure characterization of B-TS-H@T-B. (a) The TEM and (b, c, d) the corresponding magnified HRTEM images as pointed by red arrows. The yellow dotted lines marked the thin amorphous layer on the surface of the catalysts. (e) The HRTEM image of B-TS-H@T-B and the corresponding FFT patterns. (f) XRD Rietveld refinement of the B-TS-H@T-B hybrid materials. (g) The atomistic model of $Ni_{0.8}Fe_{0.1}Co_{0.1}S_2B_x$ with the green spheres (B atoms), yellow spheres (S atoms) and blue spheres (metal atoms).

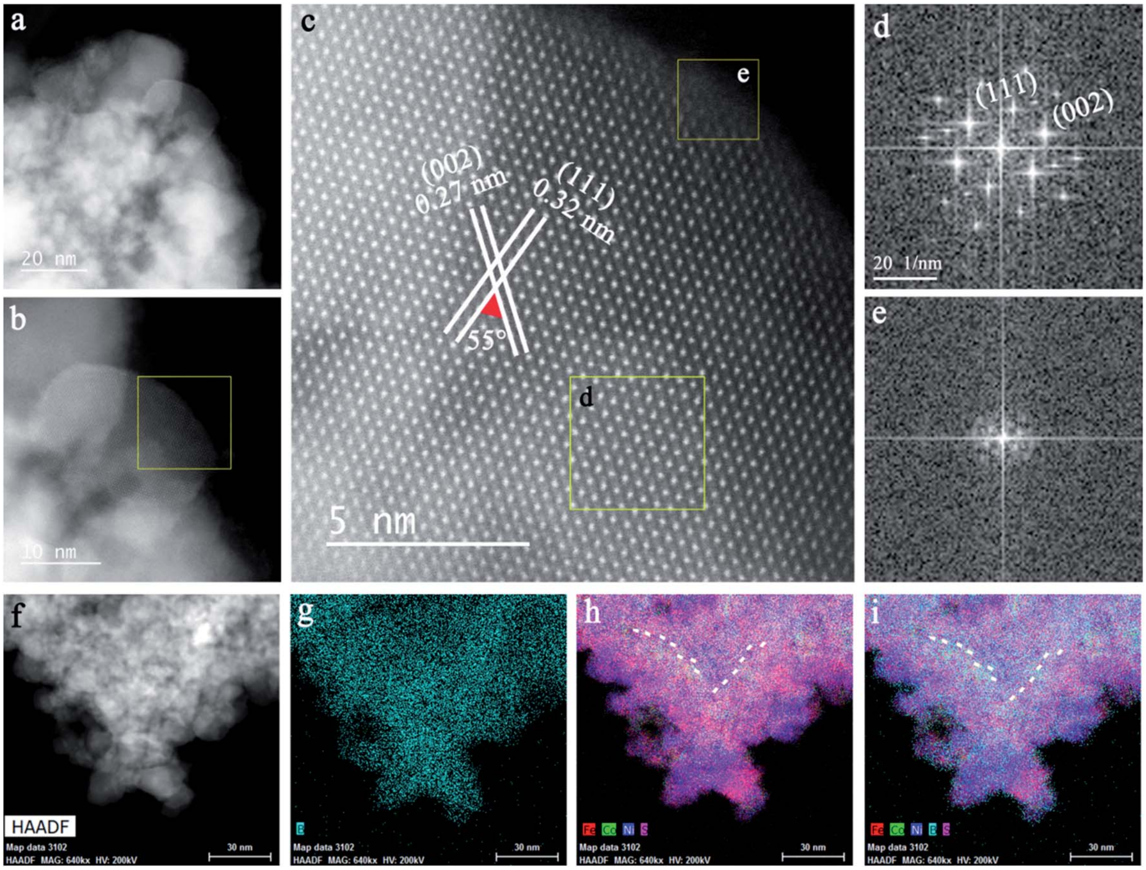

Fig. 2 Structural analysis of B-TS-H@T-B. (a) STEM image of B-TS-H@T-B and (b, c) the enlarged STEM images of the selected box of B-TS-H@T-B. (d and e) Corresponding FFT images of the marked boxes in (c). (f–i) EDX elemental mapping of B-TS-H@T-B.

H@T-B.[16,38] The angle between the two crystal planes is 55°, which further proves the structure is boron-doped ternary PTSs based on the crystal parameters. The enclosed area by the yellow dots in Fig. 2c shows the amorphous layer on the surface of the boron-doped ternary PTS, corresponding to the FFT diffraction result in Fig. 2d and e. Similarly, the typical EDX mapping images of B-TS-H@T-B show that the crystal phase contains B, S and metal elements, highlighted by the dashed dots.

The surface chemical states of B-NiS, B-CoNiS, B-FeNiS and B-TS-H@T-B were determined by X-ray photoelectron spectroscopy (XPS), as shown in Fig. S3, S4† and 3. It can be directly observed that the survey spectra of B-TS-H@T-B contains signals corresponding Fe, Co, Ni, B and S elements in Fig. 3a. The high-resolution XPS spectra of Fe, Co and Ni in Fig. 3b–d demonstrate that the three metal elements mainly exist in the form of oxidation states, respectively. For the Fe 2p spectrum (Fig. 3b), the core level can be deconvoluted into three peaks at 707.46 eV, 712.78 eV, and 720.38 eV, indicating the presence of Fe^{2+} and Fe^{3+} species, which are recognized as Fe^{2+} $2p_{3/2}$, Fe^{3+} $2p_{3/2}$ and Fe^{2+} $2p_{1/2}$, respectively.[10,25] In addition, there are two small peaks at 704.92 eV and 708.65 eV recognized as Fe–B and satellite peak, such peaks with reduced binding energy represent the loss of electrons from Fe, respectively.[25] The Co 2p XPS spectrum in Fig. 3c is fitted to four peaks at 778.99 eV, 780.84 eV, 784.07 eV and 793.99 eV, along with a spin–orbit splitting of 15 eV, which are assigned to Co-B, Co^{2+} $2p_{3/2}$, Co^{3+} $2p_{3/2}$, and Co^{2+} $2p_{1/2}$, respectively.[10,25] Similarly, as shown in Fig. 3d, the Ni 2p peaks are composed of Ni–B, Ni^{2+} $2p_{3/2}$, Ni^{3+} $2p_{3/2}$ and Ni^{2+} $2p_{1/2}$, which are recorded at 853.68 eV, 855.35 eV, 859.6 eV and 870.93 eV, respectively.[10] According to the XPS spectra of Fe, Co and Ni, partial electrons transfer from metals to B atoms, indicating the formation of B–M bonds. The peak at 192.82 eV in B 1s XPS reveal the existence of trivalent state.[25] The high-resolution S 2p spectrum in Fig. 3e clearly shows four peaks for S^{2-}, S $2p_{3/2}$, S $2p_{1/2}$ and SO_x at 161.03 eV, 161.97 eV, 163.08 eV, and 163.63 eV, respectively. The surface oxidation of S arises from the direct exposure to the air environment.[9,16] In addition, according to the analysis of the XPS results of B-NiS, B-CoNiS, B-FeNiS and B-TS-H@T-B in Fig. S3 and S4,† metal active sites in B-TS-H@T-B will increase with the doping of Co and Fe, which is conducive to the catalytic process.

As widely recognized, the surface atom arrangement of the catalysts has a crucial impact on the OER property.[15,25] It is essential to understand the external atomic structure of the $Ni_{0.8}Fe_{0.1}Co_{0.1}S_2B_x$ catalyst. Atomic resolution STEM images in Fig. 4a and b clearly display the atomic perspective of $Ni_{0.8}Fe_{0.1}Co_{0.1}S_2B_x$, revealing the uniform thickness layer (2–3 nm) coated on the crystal surface. The live FFT results taken from the yellow arrow pointed direction (Fig. 4c) indicate the subtle change of the atomic arrangement. The typical diffraction spots

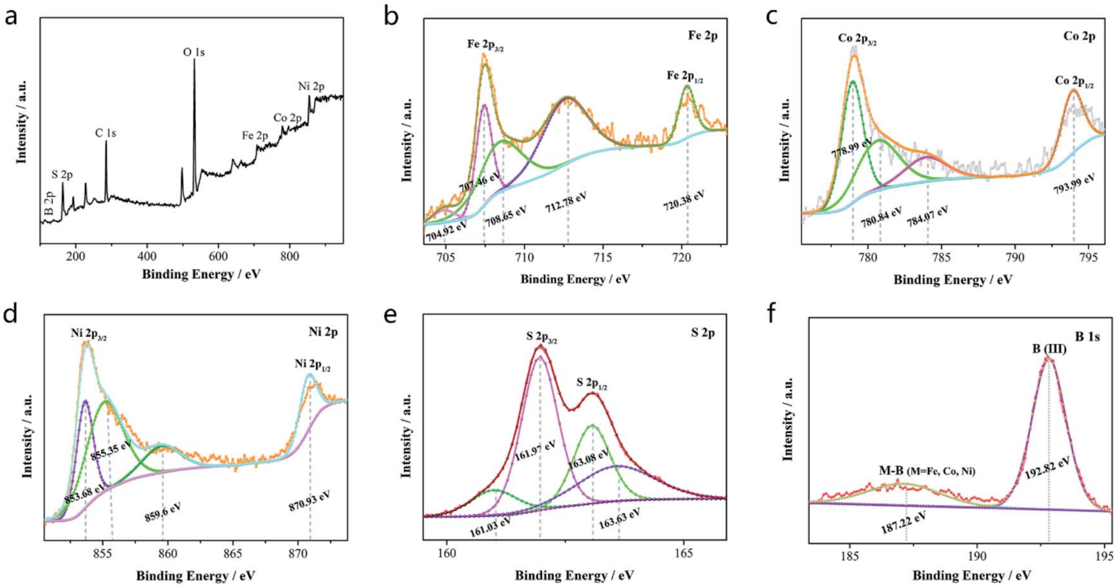

Fig. 3 Surface chemical states characterization of B-TS-H@T-B. (a) XPS spectrum of B-TS-H@T-B. (b–f) High-resolution XPS of Fe 2p, Co 2p, Ni 2p, B 1s and S 2p.

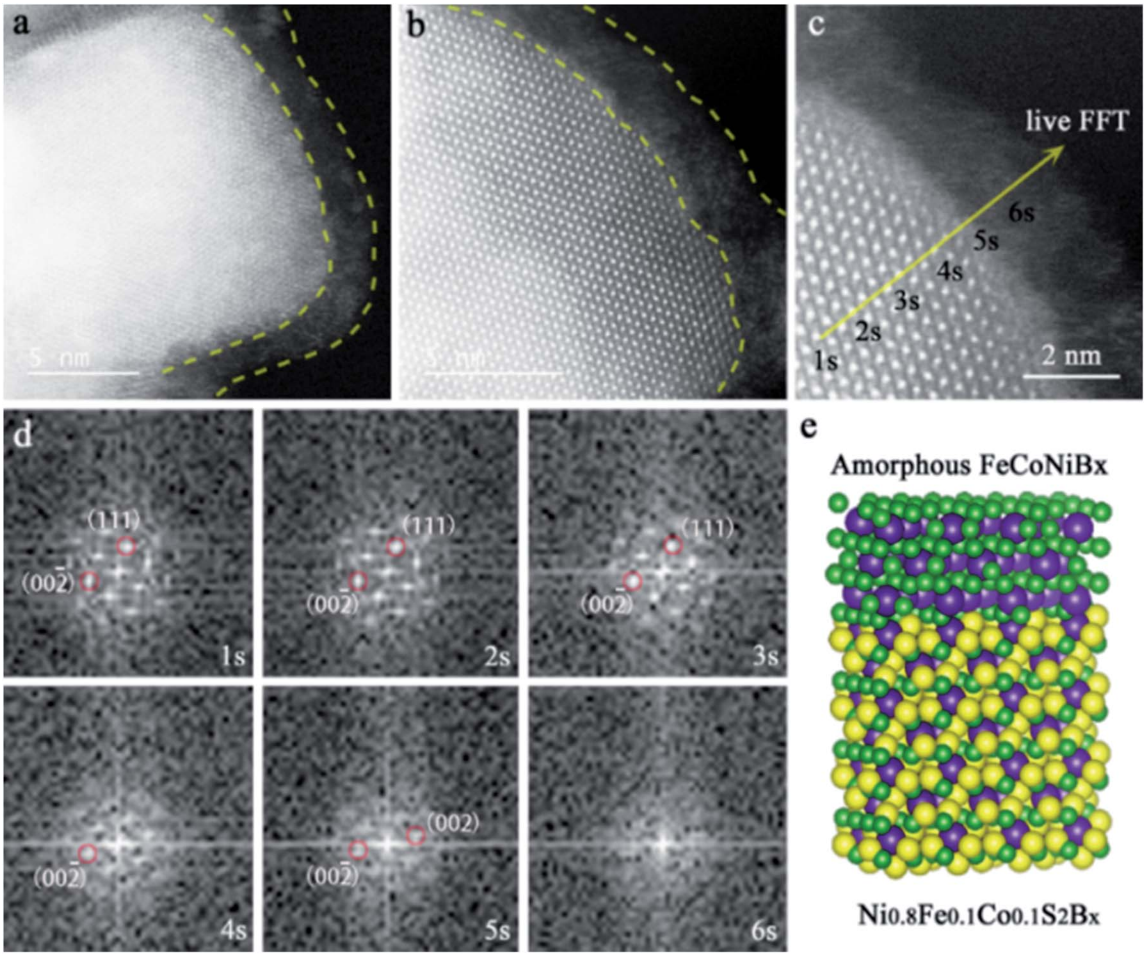

Fig. 4 Structure analysis of B-TS-H@T-B. (a–c) Enlarged STEM images of B-TS-H@T-B. (d) Corresponding live FFT results. (e) Schematic of the atomic arrangement model. The yellow balls represent S atoms, the purple balls represent Fe/Co/Ni atoms and the green balls represent B atoms.

in Fig. 4d, corresponding to the exposed (111) and (002) planes along the [−110] zone axis, exhibit the gradually weakened intensity. The metal atoms have a similar arrangement between the crystal and amorphous layer, as shown the schematic in Fig. 4e.

The electrochemical OER activity of the PTS was measured in a standard test system in the 1 M KOH electrolyte at room temperature. The electrochemically active surface areas (ECSAs) of these electrocatalysts were measured from the double-layer capacitance (C_{dl}) (Fig. S5†). As shown in Fig. 5a and b, the polarization curves of B-TS-H@T-B displays a potential of 392.4 mV at the current density of 50 mA cm^{-2}, which is much lower than that of bimetallic sulfides (B-CoNiS, 459.4 mV). With the increase in the current density, B-TS-H@T-B has a minor overpotential change compared to the bimetallic sulfides B-CoNiS, exhibiting the superior OER activity. The fitted Tafel slope of B-TS-H@T-B is 64 mV dec^{-1} (Fig. 5c), which is lower than B-CoNiS (105 mV dec^{-1}), B-FeNiS (118 mV dec^{-1}) and B-NiS (165 mV dec^{-1}), suggesting more favourable OER kinetics over the B-TS-H@T-B surface. Furthermore, the chronoamperometry curve was used to investigate the long-time stability of the as-prepared electrocatalysts. Fig. 5d presents the CA curves at the specific current density of 10 mA cm^{-2} in 1 M KOH. The retention rate is 76.94% for B-TS-H@T-B after the 10 h stability test that is much better than B-CoNiS (62.49%) and B-FeNiS (38.27%), suggesting the multimetallic doping and amorphous layer coating contributes the superior activity and stability of B-TS-H@T-B catalysts.

The TEM results of B-TS-H@T-B before and after the OER test were carried out to analyze the changes in the surface structure, which can intuitively reflect the surface condition of the electrocatalysts. The HRTEM and the corresponding EDS mapping images in Fig. S6† show the crystals in B-TS-H@T-B (after OER test) are coated by the amorphous layer with the thickness of 1.5–2 nm. The thickness of the amorphous layer gradually reduces during the OER process compared to the pristine (2–3 nm), which have significant effects on the stability of the B-TS-H@T-B catalyst. As reported, the multi-metals system can heavily influence the performance of OER for the regulated electronic properties.[40–42] Interestingly, in this present study, the prepared sample has higher OER performance than numerous other reported multi-metal systems (Tables S1 and S2†). Therefore, the influence of B doping needs to be deeply explored. Herein, based on the XRD results in Fig. 1f, $Ni_{0.8}Fe_{0.1}Co_{0.1}S_2$, $CoFeS_2$ and Ni structures, as well as the B-doped ones, were selected to explore the influence of B doping. The deformation charge density of B-doped ones has been calculated through DFT simulation. As shown in Fig. S7,† the doped B can attract some electrons from metals, which could regulate the electron distribution. Also, the expanded unoccupied

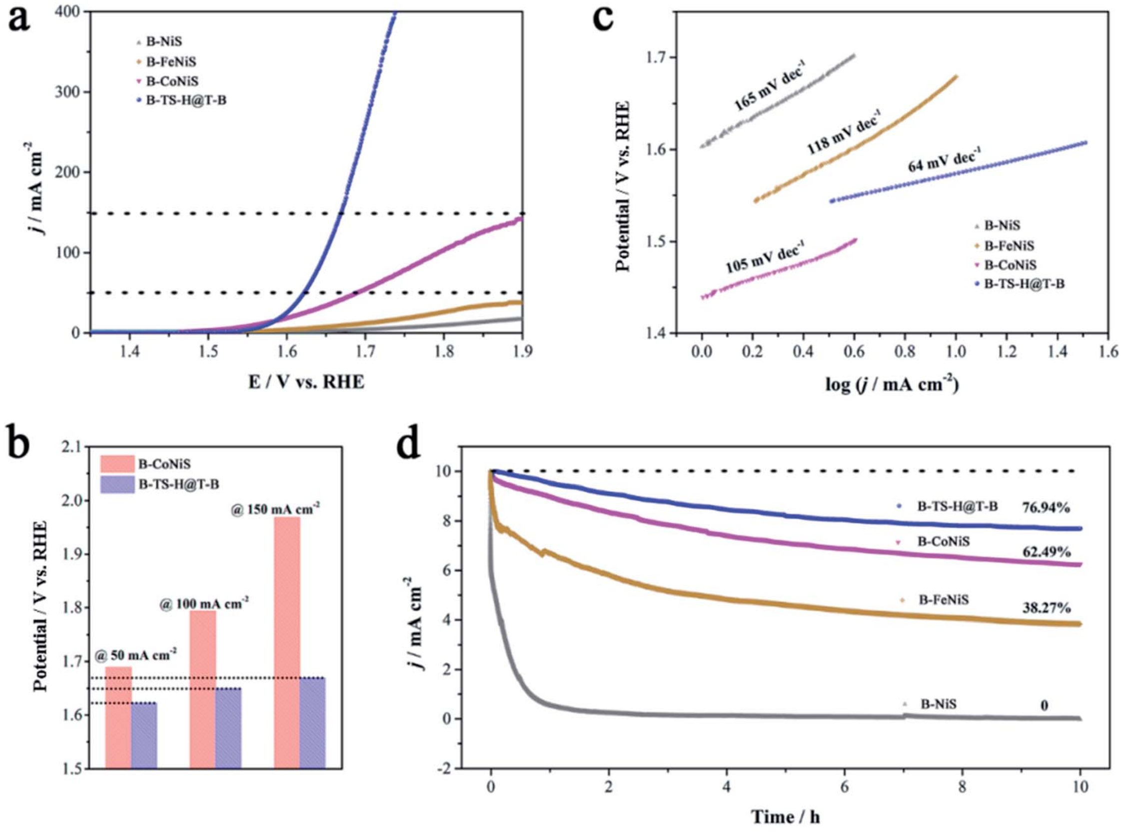

Fig. 5 Electrochemical OER activities of B-TS-H@T-B, B-FeNiS, B-CoNiS, B-NiS. (a) Polarization curves of bare B-TS-H@T-B, B-FeNiS, B-CoNiS, B-NiS. (b) The potential of B-CoNiS and B-TS-H@T-B catalysts at 50 mA cm^{-2}, 100 mA cm^{-2}, and 150 mA cm^{-2}. (c) Corresponding Tafel plots of the catalysts towards OER. (d) Chronoamperometry (CA) curves of B-TS-H@T-B, B-FeNiS, B-CoNiS, B-NiS at 10 mA cm^{-2}.

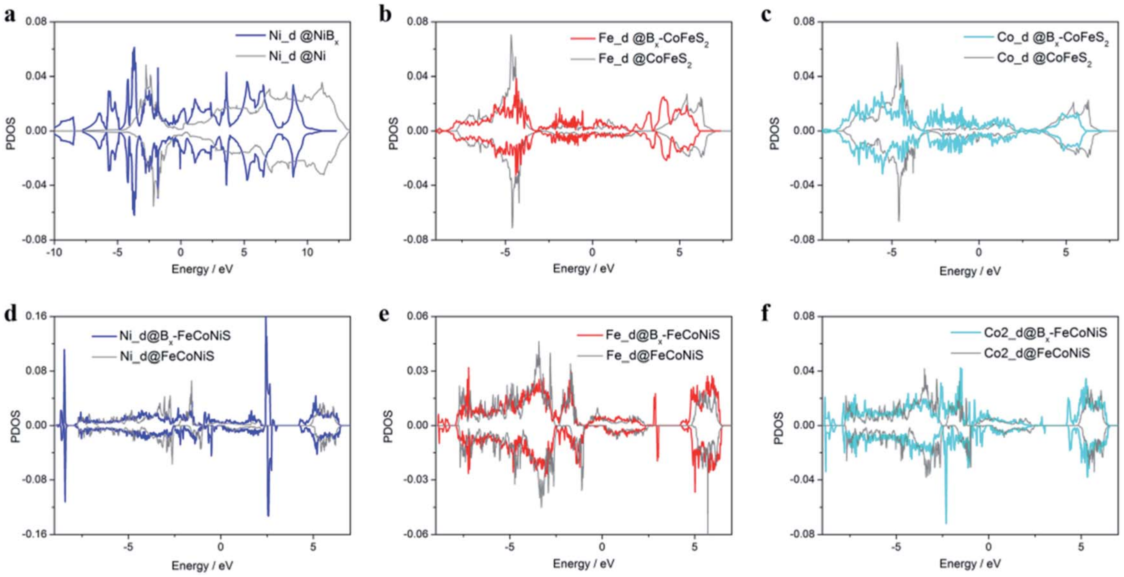

Fig. 6 The projected density of states (PDOS). (a) d orbitals of Ni in NiB_x and Ni crystals. (b) d orbitals of Fe in $CoFeS_2$ and $CoFeS_2B_x$. (c) d orbitals of Co in $CoFeS_2$ and $CoFeS_2B_x$. (d) d orbitals of Ni in FeCoNiS and $FeCoNiSB_x$. (e) d orbitals of Fe in FeCoNiS and $FeCoNiSB_x$. (f) d orbitals of Co in FeCoNiS and $FeCoNiSB_x$. Fermi level in this study is shifted to zero.

orbitals of metals are beneficial for OER processes since the electrons of the OH group would transfer to these empty orbitals more easily. To clear understand the influence of the redistribution of electrons, the projected density of states (PDOS) for metals have been simulated. Fig. 6 shows the d orbitals of metals with or without B. Clearly, the downshifted d orbitals for all metals are observed after B-doping, and such downshifted of the d band distribution should enhance the OER processes since it can optimize the interactions to O-intermediates and enhance the OER processes.[40–42] In addition, the reduced empty orbitals (higher than Fermi level of zero as in Fig. 6) can attract more electrons from O^- contained intermediates, which can accelerate the electron transfer. As shown in Fig. 6, some part electrons in metals are attracted by doped B atoms, indicating the charge transfer, which consisted with XPS data. Notably, the electron transfer will regulate the electron distribution and influence the OER processes. For metal sites, the loss of electrons would empty the expanded d orbitals, which can help to attract electrons during the reaction step (such as $* + OH^- \rightarrow *OH + e^-$), leading to increased OER reaction processes. Therefore, our suggested B-doped method can effectively regulate the electronic structures of metals, resulting in a high performance of OER.

Conclusions

In summary, a novel multimetallic pyrite-type sulfide coated by amorphous layer (B-TS-H@T-B) was successfully synthesized by a facile strategy. The multiple metallic atoms that replace the Ni positions in the pyrite NiS_2 can effectively improve its conductivity, thus having the metallic characteristics. B doping reconfigures the electronic structure of B-TS-H@T-B, which downshifts the d-band of the metals and enhances the binding ability of O-intermediates in OER processes. Notably, B-TS-H@T-B shows remarkable OER activity and durability than single metal and bimetal Ni-based sulfides under 100 mA cm^{-2}, making it a prospective candidate for the large-scale commercial OER catalyst. In addition, this study can inspire numerous studies about non-metallic element doping or multi-metal catalysts for designing efficient electrocatalysts for water splitting.

Conflicts of interest

There are no conflicts to declare.

Acknowledgements

This work was supported by the National Natural Science Foundation of China (No. 51801075, 51902281), the Scientific and Technological Projects of Henan Province (212102210293, 202102210022). Š. K. was supported by the Operational Programme Research, Development and Education-European Regional Development Fund, Project No. CZ.02.1.01/0.0/0.0/15_003/0000416 of the Ministry of Education, Youth and Sports of the Czech Republic. Theoretical work was carried out at LvLiang Cloud Computing Center of China, and the calculations were performed on TianHe-2. D. R. gratefully acknowledge the support of Jiangsu Overseas Visiting Scholar Program for University Prominent Young and Mid-aged Teachers and Presidents.

Notes and references

1 Y. Shi and B. Zhang, *Chem. Soc. Rev.*, 2016, **45**, 1529.

2 C. Hu, L. Zhang and J. Gong, *Energy Environ. Sci.*, 2019, **12**, 2620.
3 B. You and Y. Sun, *Acc. Chem. Res.*, 2018, **51**, 1571.
4 M. Gong, D.-Y. Wang, C.-C. Chen, B.-J. Hwang and H. Dai, *Nano Res.*, 2016, **9**, 28.
5 B. Konkena, J. Masa, A. J. R. Botz, I. Sinev, W. Xia, J. Koßmann, R. Drautz, M. Muhler and W. Schuhmann, *ACS Catal.*, 2016, **7**, 229.
6 R. Miao, J. He, S. Sahoo, Z. Luo, W. Zhong, S.-Y. Chen, C. Guild, T. Jafari, B. Dutta, S. A. Cetegen, M. Wang, S. P. Alpay and S. L. Suib, *ACS Catal.*, 2016, **7**, 819.
7 C. Wei, Y. Sun, G. G. Scherer, A. C. Fisher, M. Sherburne, J. W. Ager and Z. J. Xu, *J. Am. Chem. Soc.*, 2020, **142**, 7765–7775.
8 S. Niu, W. J. Jiang, T. Tang, L. P. Yuan, H. Luo and J. S. Hu, *Adv. Funct. Mater.*, 2019, **29**, 1902180.
9 G. Zhang, Y.-S. Feng, W.-T. Lu, D. He, C.-Y. Wang, Y.-K. Li, X.-Y. Wang and F.-F. Cao, *ACS Catal.*, 2018, **8**, 5431.
10 A.-L. Wang, H. Xu and G.-R. Li, *ACS Energy Lett.*, 2016, **1**, 445.
11 Y. Guo, T. Park, J. W. Yi, J. Henzie, J. Kim, Z. Wang, B. Jiang, Y. Bando, Y. Sugahara, J. Tang and Y. Yamauchi, *Adv. Mater.*, 2019, **31**, 1807134.
12 M.-R. Gao, Y.-R. Zheng, J. Jiang and S.-H. Yu, *Acc. Chem. Res.*, 2017, **50**, 2194.
13 S. Ogawa, *J. Appl. Phys.*, 1979, **50**, 2308.
14 S. Jin, *ACS Energy Lett.*, 2017, **8**, 1937.
15 J. Joo, T. Kim, J. Lee, S. I. Choi and K. Lee, *Adv. Mater.*, 2019, **31**, 1806682.
16 G. He, W. Zhang, Y. Deng, C. Zhong, W. Hu and X. Han, *Catalysts*, 2017, **7**, 366.
17 Y. Guo, J. Tang, J. Henzie, B. Jiang, W. Xia, T. Chen, Y. Bando, Y. M. Kang, M. S. A. Hossain, Y. Sugahara and Y. Yamauchi, *ACS Nano*, 2020, **14**, 4141.
18 Q. Li, X. Wang, K. Tang, M. Wang, C. Wang and C. Yan, *ACS Nano*, 2017, **11**, 12230.
19 J. Yin, J. Jin, H. Zhang, M. Lu, Y. Peng, B. Huang, P. Xi and C. H. Yan, *Angew. Chem., Int. Ed.*, 2019, **58**, 18676.
20 Z. Peng, D. Jia, A. M. Al-Enizi, A. A. Elzatahry and G. Zheng, *Adv. Energy Mater.*, 2015, **5**, 1402031.
21 J. Yu, G. Cheng and W. Luo, *J. Mater. Chem. A*, 2017, **5**, 15838.
22 X. Ding, W. Li, H. Kuang, M. Qu, M. Cui, C. Zhao, D. Qi, F. Oropeza and K. Zhang, *Nanoscale*, 2019, **11**, 23217.
23 H. Liu, Q. He, H. Jiang, Y. Lin, Y. Zhang, M. Habib, S. Chen and L. Song, *ACS Nano*, 2017, **11**, 11574.
24 B. Ni, T. He, J. O. Wang, S. Zhang, C. Ouyang, Y. Long, J. Zhuang and X. Wang, *Chem. Sci.*, 2018, **9**, 2762.
25 Y. Zuo, D. Rao, S. Ma, T. Li, Y. H. Tsang, S. Kment and Y. Chai, *ACS Nano*, 2019, **13**, 11469.
26 X. Han, X. Wu, Y. Deng, J. Liu, J. Lu, C. Zhong and W. Hu, *Adv. Energy Mater.*, 2018, **8**, 1800935.
27 J. Li, Z. Xia, X. Zhou, Y. Qin, Y. Ma and Y. Qu, *Nano Res.*, 2017, **10**, 814.
28 J. Hou, B. Zhang, Z. Li, S. Cao, Y. Sun, Y. Wu, Z. Gao and L. Sun, *ACS Catal.*, 2018, **8**, 4612.
29 M. S. Faber, M. A. Lukowski, Q. Ding, N. S. Kaiser and S. Jin, *J. Phys. Chem. C*, 2014, **118**, 21347.
30 X. Zou and Y. Zhang, *Chem. Soc. Rev.*, 2015, **44**, 5148.
31 M. Cabán-Acevedo, M. Stone, J. Schmidt, J. Thomas, Q. Ding, H. Chang, M. Tsai, J. He and S. Jin, *Nat. Mater.*, 2015, **14**, 1245.
32 J. Staszak-Jirkovský, C. Malliakas, P. Lopes, N. Danilovic, S. Kota, K. Chang, B. Genorio, D. Strmcnik, V. Stamenkovic, M. Kanatzidis and N. Markovic, *Nat. Mater.*, 2016, **15**, 197.
33 M. Wang, W. Zhang, F. Zhang, Z. Zhang, B. Tang, J. Li and X. Wang, *ACS Catal.*, 2019, **9**, 1489.
34 T. Li, C. Zhu, X. Yang, Y. Gao, W. He, H. Yue and H. Zhao, *Electrochim. Acta*, 2017, **246**, 226.
35 J. Chen, S. Li, V. Kumar and P. Lee, *Adv. Energy Mater.*, 2017, **7**, 1700180.
36 H. Han, K. Kim, H. Choi, G. Ali, K. Chung, Y. Hong, J. Choi, J. Kwon, S. Lee, J. Lee, J. Ryu, T. Song and S. Mhin, *ACS Catal.*, 2018, **8**, 4091.
37 D. He, L. Zhang, D. He, G. Zhou, Y. Lin, Z. Deng, X. Hong, Y. Wu, C. Chen and Y. Li, *Nat. Commun.*, 2016, **7**, 12362.
38 R. Sun, S. Liu, Q. Wei, J. Sheng, S. Zhu, Q. An and L. Mai, *Small*, 2017, **13**, 1701744.
39 J. Rodriges-Carvajal, *Phys. B*, 1993, **192**, 55.
40 G. Kresse and J. Furthmuller, *Phys. Rev. B: Condens. Matter Mater. Phys.*, 1996, **54**, 11169.
41 P. E. Blöchl, *Phys. Rev. B: Condens. Matter Mater. Phys.*, 1994, **50**, 17953–17979.
42 G. kresse and D. Joubert, *Phys. Rev. B: Condens. Matter Mater. Phys.*, 1999, **59**, 1758–1775.
43 Y. Zuo, D. Rao, S. Li, T. Li, G. Zhu, S. Chen, L. Song, Y. Chai and H. Han, *Adv. Mater.*, 2018, **30**, 1704171.
44 Y. Xia, *Angew. Chem., Int. Ed.*, 2009, **48**, 60.
45 X. Xia, Y. Wang, A. Ruditskiy and Y. Xia, *Adv. Mater.*, 2013, **25**, 6313.

ACS NANO
Cite This: ACS Nano 2019, 13, 11469−11476
www.acsnano.org
ARTICLE

Valence Engineering *via* Dual-Cation and Boron Doping in Pyrite Selenide for Highly Efficient Oxygen Evolution

Yunpeng Zuo,[†,∥,#] Dewei Rao,[‡,#] Sainan Ma,[†,#] Tingting Li,[§] Yuen Hong Tsang,[†] Stepan Kment,[∥] and Yang Chai*,[†]

[†]Department of Applied Physics, The Hong Kong Polytechnic University, Hung Hom, Kowloon, Hong Kong, People's Republic of China

[‡]School of Materials Science and Engineering, Jiangsu University, Zhenjiang 212013, People's Republic of China

[§]Institute of Surface Micro and Nano Materials, Xuchang University, Xuchang, Henan 461002, People's Republic of China

[∥]Regional Center of Advanced Technologies and Materials, Olomouc 78371, Czech Republic

S *Supporting Information*

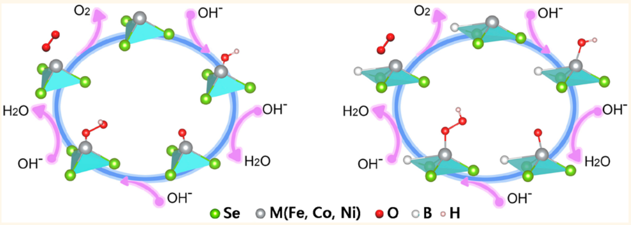

ABSTRACT: **Valence engineering has been proved an effective approach to modify the electronic property of a catalyst and boost its oxygen evolution reaction (OER) activity, while the limited number of elements restricts the structural diversity and the active sites. Also, the catalyst performance and stability are greatly limited by cationic dissolution, ripening, or crystal migration in a catalytic system. Here we employed a widely used technique to fabricate heteroepitaxial pyrite selenide through dual-cation substitution and a boron dopant to achieve better activity and stability. The overpotential of Ni-pyrite selenide catalyst is decreased from 543 mV to 279.8 mV at 10 mA cm^{-2} with a Tafel slope from 161 to 59.5 mV dec^{-1}. Our theoretical calculations suggest both cation and boron doping can effectively optimize adsorption energy of OER intermediates, promote the charge transfer among the heteroatoms, and improve their OER property. This work underscores the importance of modulating surface electronic structure with the use of multiple elements and provides a general guidance on the minimization of activity loss with valence engineering.**

KEYWORDS: *oxygen evolution reaction, valence engineering, pyrite selenide, multimetallic compound, boron doping*

Oxygen evolution reaction (OER) has been extensively studied for the development of sustainable and clean energy devices, such as hydrogen fuel cells, metal−air batteries, *etc.*[1−8] The OER is based on a four-electron−proton coupled reaction, requiring a high overpotential (η) with respect to the standard reduction potential $E \approx 1.23$ V.[3−6] To reduce the overpotential and the overall energy consumption of water electrolysis, researchers have developed various electrocatalytic systems to facilitate water splitting reactions.[9−25] Transition metal pyrite selenides have been demonstrated as a promising catalyst for OER, which can provide a high activity and high cost-effectiveness compared to commonly used noble metal or oxide catalysts.[8−12] However, their performances achieved so far are still rather low for practical applications.

Cation doping has been demonstrated to be an attractive approach to improve the OER activity of pyrite selenides, as it can improve the electrical conductivity and introduce more lattice vacancies working as active centers.[25−28] For example, Li *et al.* found out that an Fe, Co dual cation in $NiSe_2$ reduces the Tafel slope from 105 mV dec^{-1} to 63 mV dec^{-1} for OER due to the increase of the surface active sites.[26] Song *et al.* reported crystalline−amorphous phase F-Co_2B exhibiting a superior overpotential of ∼320 mV, which was better than Co_2B and RuO_2.[28] Although the interaction between the multiple element atoms can give rise to the changing geometries and/or surface electronic structures, the detrimental phenomena including cationic dissolution, ripening, or crystal migration still limit practical applications of multimetallic selenides.[10,25,26]

Modifying the local electronic structure of the multimetallic selenides by valence engineering is an effective method to improve both catalytic activity and stability. As a typical valence engineering route, the favorable heteroepitaxial structure has been extensively employed to suppress ripening

Received: June 24, 2019
Accepted: September 19, 2019
Published: September 23, 2019

DOI: 10.1021/acsnano.9b04956
ACS Nano 2019, 13, 11469−11476

or crystal migration compared to single-component metal and metallic alloys.[21−25] Additionally, the boron dopant within the multimetallic selenides can relieve the cationic dissolution.[16,19,20] Furthermore, the nanoscale selenides with multiple exposed sites enable the decrease of the kinetic energy barriers of the OER reaction.[20−25] The wet chemical approaches have been adopted to synthesize selenides with heterostructures at the nanoscale by undergoing nucleation growth based on preformed seed particles.[22,24,29−32] The alloy composition obtained by the wet chemical method is usually restricted by three elements, which greatly limits the structural diversity and the possibility of adjusting the composition.[2] Although some techniques such as printing methods, melt processing, and high-temperature thermal reduction combined with cold-rolling operation have been successfully used to prepare multimetal composites consisting of five or more elements,[31−36] these methods require sophisticated instruments and are especially inapplicable for mixing elements with varied physical and chemical properties.[29] In this work, we develop a facile method to produce boron-doped ternary pyrite selenide on an amorphous membrane. The crystalline−amorphous structure provides an intimate structure for the catalytic system, which blocks the physical aggregation of catalytic nanoparticles. On the other hand, this special crystalline−amorphous structure allows 3D accessibility for the electrolyte in the process of preparing the electrode. The resulting materials exhibit superior performance in terms of low overpotential and long electrochemical stability. Our theoretical studies suggest that the boron dopant and binary atomic substitution can weaken the interaction between catalyst and OER intermediates, which enable an efficient catalytic process.

RESULTS AND DISCUSSION

The boron-doped ternary pyrite selenide ($Fe_5Co_4Ni_{20}Se_{36}B_x$) was synthesized through a wet chemical method. Scheme S1 depicts the growth process of the $Fe_5Co_4Ni_{20}Se_{36}B_x$ nanocatalyst supported on an amorphous FeCoNi-B membrane. Figure S1 shows the preloaded amorphous multimetallic boride membrane (MBM) selenized in a tube furnace under a nitrogen flow. The Fe/Co/Ni/Se composition was determined to be 5:4:20:36 by using transmission electron microscopy energy-dispersive X-ray spectroscopy (TEM-EDX), and the corresponding elemental maps are displayed in Figure S2. The gaseous Se atoms react with the MBM and generate $Fe_5Co_4Ni_{20}Se_{36}B_x$ nuclei on the surface of the MBM during this initial stage. The nucleus grows into small $Fe_5Co_4Ni_{20}Se_{36}B_x$ clusters with the deposition of the newly formed selenide atoms. Finally, $Fe_5Co_4Ni_{20}Se_{36}B_x$ nanoparticles were synthesized on the MBM.

X-ray powder diffraction (XRD) was used to further understand the crystal structural of the $Fe_5Co_4Ni_{20}Se_{36}B_x$ nanoparticles. The diffraction peaks in the XRD spectrum (Figure S3) can be well identified to the (210), (200), (211), (311), and (321) for the $Fe_5Co_4Ni_{20}Se_{36}B_x$ nanomaterials compared to $NiSe_2$ with a JCPDS number 88-1711.[24−27] The Rietveld refinement analysis was carried out using the computer software General Structure Analysis System (GSAS), showing that Fe, Co, and Ni atoms co-occupy the same site with the composition ratios of 2:1 and 1:1 for Ni/(Fe+Co) and Fe/Co (Figure 1A), respectively.[37,38] These refined results reveal that B atoms are embedded in the interstitial sites of the crystal. Some of them form B−M (M = Fe, Co, Ni) bonds, as shown in Figure 1B−D, while other portions bond to Se.[11,14]

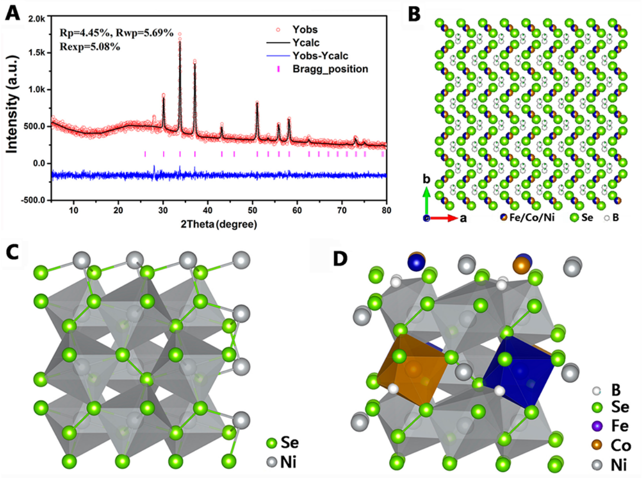

Figure 1. (A) XRD Rietveld refinement of $Fe_5Co_4Ni_{20}Se_{36}B_x$ and (B) the atomistic model. (C, D) Schematic illustration of $NiSe_2$ and $Fe_5Co_4Ni_{20}Se_{36}B_x$ crystal structures.

The structure of $Fe_5Co_4Ni_{20}Se_{36}B_x$ materials was characterized by spherical aberration corrected transmission electron microscopy (AC-TEM). The as-prepared $Fe_5Co_4Ni_{20}Se_{36}B_x$ nanoparticles are supported on the FeCoNiB membrane with good dispersion and narrow distribution of particle size (Figure 2A). The selected area electron diffraction (SAED) pattern of $Fe_5Co_4Ni_{20}Se_{36}B_x$ nanoparticles exhibits (Figure 2B) discrete and bright diffraction dots, indicating their good crystallinity.[23] The inset fast Fourier transformation (FFT) image in Figure 2C indicates the amorphous structure of the supporting membrane.[14,19] The HAADF-STEM-electron energy-loss spec-

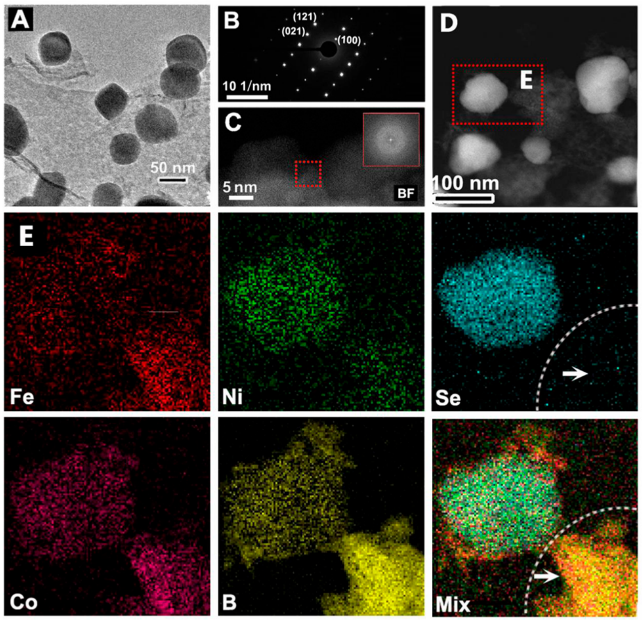

Figure 2. (A) HRTEM image and (B) SAED pattern of the $Fe_5Co_4Ni_{20}Se_{36}B_x$ nanoparticles. (C) STEM images of the supporting membrane. The inset is the fast Fourier transformation (FFT) image. (D) STEM image of the FeCoNiSeB_x catalyst and (E) the corresponding HAADF-STEM-electron energy-loss spectroscopy (EELS) mapping images.

troscopy (EELS) mapping was used to characterize the elemental distribution of $Fe_5Co_4Ni_{20}Se_{36}B_x$ nanoparticles (Figure 2D,E), in which the particular atoms are visualized as Fe (red), Ni (green), Co (pink), B (yellow), and Se (blue). The individual elemental maps and their combined distribution map confirm the presence of all five elements in the nanoparticles.

As widely accepted, the surface structure of catalysts plays a very important role in the catalytic reaction.[15,21] Therefore, the understanding the exterior structure of catalyst is indispensable for the OER catalytic mechanism.[34−36] The atomic-resolution TEM images of $Fe_5Co_4Ni_{20}Se_{36}B_x$ nanoparticles in Figure 3 show the exposed (210) and (111) facets (Figure 3A_1−A_3, Figure 3B_1−B_3, respectively) with the corresponding FFT images, revealing the uniformity of the crystal structure. Although it is difficult to observe the exact atomic structure through TEM images (Figure 3C,E), the corresponding simulated images in Figure 3D,F with the typical [210] and [111] zone axis reveal that the B atoms are located at interstitial sites, which is consistent with the Rietveld refinement analysis conclusions.

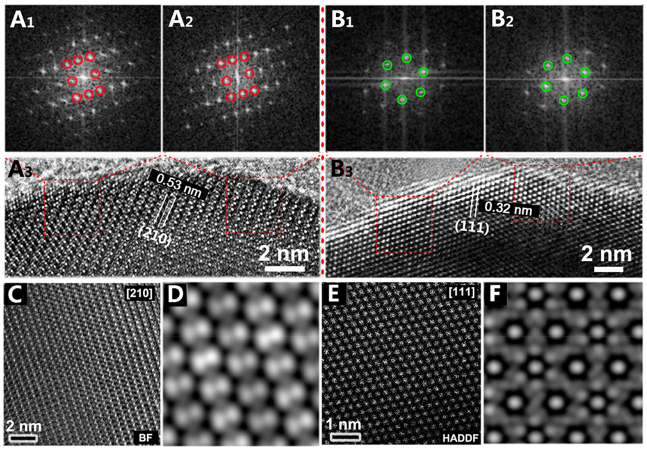

Figure 3. Corresponding FFT images of the exposed (210) ($A_{1,2,3}$) and (111) ($B_{1,2,3}$) facets for the $Fe_5Co_4Ni_{20}Se_{36}B_x$ particle. (C, D and E, F) HRTEM and simulated images of $Fe_5Co_4Ni_{20}Se_{36}B_x$ with the two typical zone axes [210] and [111].

In order to characterize the chemical states of the synthesized $Fe_5Co_4Ni_{20}Se_{36}B_x$ materials, we performed X-ray photoelectron spectroscopy (XPS). Figure 4A−E clearly show the Fe, Co, Ni, Se, and B signals in the XPS spectrum. Obviously, the elements Fe, Co, and Ni mainly exist as oxidation states in the $Fe_5Co_4Ni_{20}Se_{36}B_x$ materials. For the Fe 2p spectrum, the multiple peaks at 711.79, 715.26, 725.49, and 729.35 eV are assigned to Fe−B, Fe^{3+} $2p_{3/2}$, Fe^{2+} $2p_{1/2}$, and Fe^{3+} $2p_{1/2}$, respectively, along with the corresponding satellite peaks at 720.19 and 734.01 eV.[12,15] The $2p_{3/2}$ peaks of the Co 2p spectrum (Figure 4B) can be decomposed into three peaks at 776.39, 781.68, and 786.75 eV, which are associated with Co−B, Co^{2+}, and a satellite peak.[11] Similarly, the Ni $2p_{3/2}$ peaks can be assigned to Ni−B, Ni^{2+}, Ni^{3+}, and a satellite peak at 851.6, 856.2, 859.9, and 862.7 eV.[11,14] The corresponding XPS spectra of Fe, Co, and Ni indicate that the electrons are transferred from these transitional metals into boron atoms in the $Fe_5Co_4Ni_{20}Se_{36}B_x$ materials. The B 1s spectrum clearly shows two chemical forms, including M−B (M = Fe, Co, Ni) (185.68 eV) and trivalent oxidation states (192.15 eV).[11] The surface oxidation stems from the inevitable direct exposure to the ambient environment. The Se 3d XPS spectrum is fitted into two peaks at 54.74 (Se $3d_{5/2}$) and 55.73 eV (Se $3d_{3/2}$), which originate from the Se^{2-} of $Fe_5Co_4Ni_{20}Se_{36}B_x$.[7,17] In addition, a doublet peak (58.8 eV) assigned to the oxidation state of Se species can be attributed to the oxidation of Se at the $Fe_5Co_4Ni_{20}Se_{36}B_x$ surface.[7,17] The XPS spectra of $NiSe_x$, B-$NiSe_x$, and Ni 2p in Figure S4 further reveal that electrons are transferred from transitional metals into B atoms. Through density functional theory (DFT) calculations, we also found that the B atoms are bonded with surrounding atoms, which can be demonstrated by projected density of states (PDOS) of atoms in $Fe_{0.125}Co_{0.125}Ni_{0.75}Se_2B_{0.2}$, as displayed in Figure 4F. Clearly, the p orbital of B (red line) is overlapped with the outermost orbital of other atoms around B, including the p

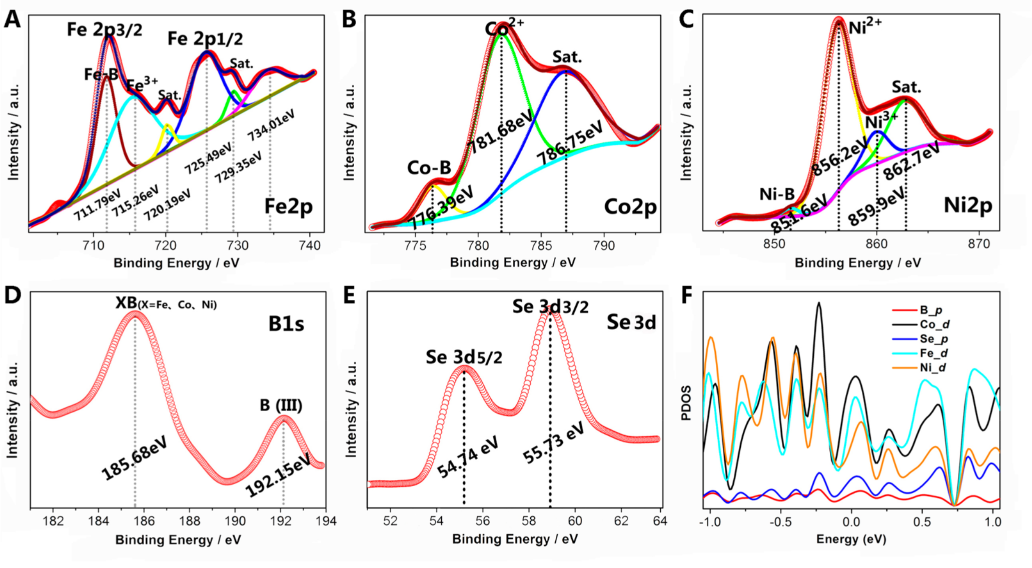

Figure 4. (A−E) X-ray photoelectron spectroscopy (XPS) spectra for the $Fe_5Co_4Ni_{20}Se_{36}B_x$. (F) Projected density of states (PDOS) of $Fe_{0.125}Co_{0.125}Ni_{0.75}Se_2B_{0.2}$.

DOI: 10.1021/acsnano.9b04956
ACS Nano 2019, 13, 11469−11476

orbital of Se and the d orbital of metal atoms. To accurately describe the bonding state of B to metal atoms, the negative crystal orbital Hamilton population (−COHP) between B and metals is calculated by the Lobster code,[39] which can describe detailed chemical interactions of bonding states between two atoms, as well as their bond states of the orbital (Figure S5). The positive −COHP values represent the bonding state, and the negative values represent the antibonding. Clearly, the −COHP curves below the Femi level almost lie in the region of positive values, which means that the B 2p orbitals are bonded with 3d orbitals of metals, and some of the electrons between the B−metals are easy to lose because of the existence of negative values under the Fermi level, which can be beneficial for catalysis processes. These results suggest that B atoms bond with surrounding atoms, which is consistent with our experimental results (Figure 4A−E).

The electrocatalytic OER activities of the prepared materials were investigated using a standard three-electrode half-cell and 1.0 M KOH as the electrolyte. The NiSeB, FeNiSeB, and CoNiSeB compounds were adopted as the control samples to understand the activity of the $Fe_5Co_4Ni_{20}Se_{36}B_x$ composite. The SEM images and the corresponding EDS analysis of $NiSe_2B_x$, $FeNi_3Se_8B_x$, and $CoNi_3Se_8B_x$ (Figure S6−S8) show their similar structure with a stable element composition. Based on the OER polarization curves (Figure 5A), the $Fe_5Co_4Ni_{20}Se_{36}B_x$ composite obviously exhibits the lowest overpotential (η) of 279.8 mV to reach a current density of 10 mA cm^{-2}, compared to those of $NiSe_2B_x$, $FeNi_3Se_8B_x$, and $CoNi_3Se_8B_x$ (543, 335, and 453 mV, respectively). The current density at η = 250 mV is 7.3 mA cm^{-2}, which is 4.6-, 4.4-, and 3.8-fold higher than those of $NiSe_2B_x$, $CoNi_3Se_8B_x$, and $FeNi_3Se_8B_x$, respectively (Figure S9). The Tafel slopes of these catalysts were further investigated to estimate their OER performance. As presented in Figure 5B, the Tafel slopes are 59.5, 86.3, 121, and 161 mV dec^{-1} for $Fe_5Co_4Ni_{20}Se_{36}B_x$, $FeNi_3Se_8B_x$, $CoNi_3Se_8B_x$, and $NiSe_2B_x$, respectively. The $Fe_5Co_4Ni_{20}Se_{36}B_x$ exhibited the smallest Tafel slope, which suggests more favorable OER kinetics than the other samples. The electrochemically active surface areas (ECSAs) of these catalysts were evaluated from the double-layer capacitance (Cdl) (Figure S10). The ECSA-normalized polarization curves presented in Figure S11 show that the current density of $Fe_5Co_4Ni_{20}Se_{36}B_x$ is still better than the other three catalysts. The OER kinetics of these catalysts were further investigated by electrochemical impedance spectroscopy (Figure S12), which showed similar results. This outstanding OER performance of $Fe_5Co_4Ni_{20}Se_{36}B_x$ is superior to most of the other selenides or Fe/Co/Ni-based OER catalysts in alkaline solution as well as the noble metal oxides IrO_x and RuO_2 in Figure 5C (see Tables S1 and S2 in the Supporting Information). We investigate the effect of metal doping on the overpotential through DFT calculations. Figure 5D shows the overpotentials for the catalysts with and without B dopants. These results indicate that the catalysts with FeCo co-doping exhibit lower overpotentials than that with Fe- or Co-doped surfaces. Meanwhile, the Fe or Co-doped surfaces without B also have higher overpotential than FeCo co-doping ones with B-doping. These results indicate that the co-doped metal atoms are also beneficial to OER processes, in good agreement with our experimental results.

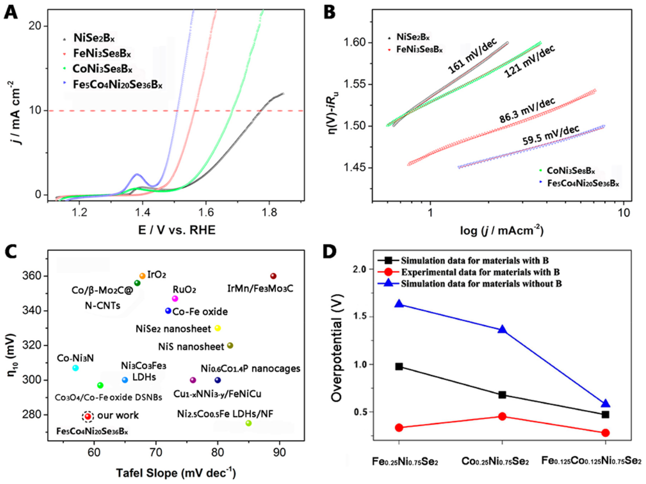

Figure 5. Electrochemical performances of $NiSe_2B_x$, $FeNi_3Se_8B_x$, $CoNi_3Se_8B_x$, and $Fe_5Co_4Ni_{20}Se_{36}B_x$ for OER. (A) *iR*-corrected polarization curves obtained in 1.0 M KOH at a scan rate of 2 mV s^{-1}. (B) Corresponding Tafel plots. (C) Tafel slopes and overpotentials of $Fe_5Co_4Ni_{20}Se_{36}B_x$ compared with other OER catalysts (Table S2). (D) Overpotentials from experimental and theoretical works.

Long-time stability of the catalysts is another critical factor for practical applications. As shown in Figure S13, $Fe_5Co_4Ni_{20}Se_{36}B_x$ maintains a current density of 10 mA cm^{-2} over a period of at least 10 h without obvious potential increase, suggesting the excellent durability of the synthesized $Fe_5Co_4Ni_{20}Se_{36}B_x$. Figure S14 shows the TEM image and the STEM elemental mapping images of $Fe_5Co_4Ni_{20}Se_{36}B_x$ after the durability test, respectively. During the durability test, the $Fe_5Co_4Ni_{20}Se_{36}B_x$ particles were slightly enlarged (Figure S14A) on the amorphous membrane. The distribution of elements for $Fe_5Co_4Ni_{20}Se_{36}B_x$ after the stability test demonstrates the excellent structural durability of the multimetallic selenide boride with maintaining stable elemental composition. The excellent stability is attributed to the presence of the support of a homogeneous membrane, which prevents the agglomeration of catalytic nanoparticles as a result of the strong interaction by the *in situ* growth.

To understand the effect of $Fe_5Co_4Ni_{20}Se_{36}B_x$ on the promotion of the activity of the oxygen evolving catalysts, we performed DFT calculations to evaluate the composition effect on the energetics of OER intermediates, including (111) surfaces of pristine structures and their corresponding ones with B dopants (namely, $Fe_{0.25}Ni_{0.75}Se_2$, $Fe_{0.25}Ni_{0.75}Se_2B_{0.2}$, $Co_{0.25}Ni_{0.75}Se_2$, $Co_{0.25}Ni_{0.75}Se_2B_{0.2}$, $Fe_{0.125}Co_{0.125}Ni_{0.75}Se_2$, $Fe_{0.125}Co_{0.125}Ni_{0.75}Se_2B_{0.2}$). Figure 6 shows the Gibbs free energy (ΔG) for each OER intermediate step, where the solid line indicates the computed free energies without external voltage (U = 0), and the dashed line represents the modified free energies under a theoretical reaction potential. For $Fe_{0.25}Ni_{0.75}Se_2$ (Figure 5A), the overpotential value for OER is 1.63 V. This large overpotential is mainly limited by the high desorption ΔG of 2.86 eV for the step of $^*OOH \rightarrow ^* + O_2 + H^+ + e$, where * represents the catalyst. In contrast, the B-doped $Fe_{0.25}Ni_{0.75}Se_2$ has a lower but still large overpotential of 0.977 V, which can be attributed to the stronger adsorption to the OOH-based intermediate (the corresponding ΔG for the limiting step is 2.207 eV). Details of the relationship between overpotential value and ΔG is described in the section Calculation Methods. Similarly, the other catalysts with B dopants exhibit a smaller overpotential than that of pristine

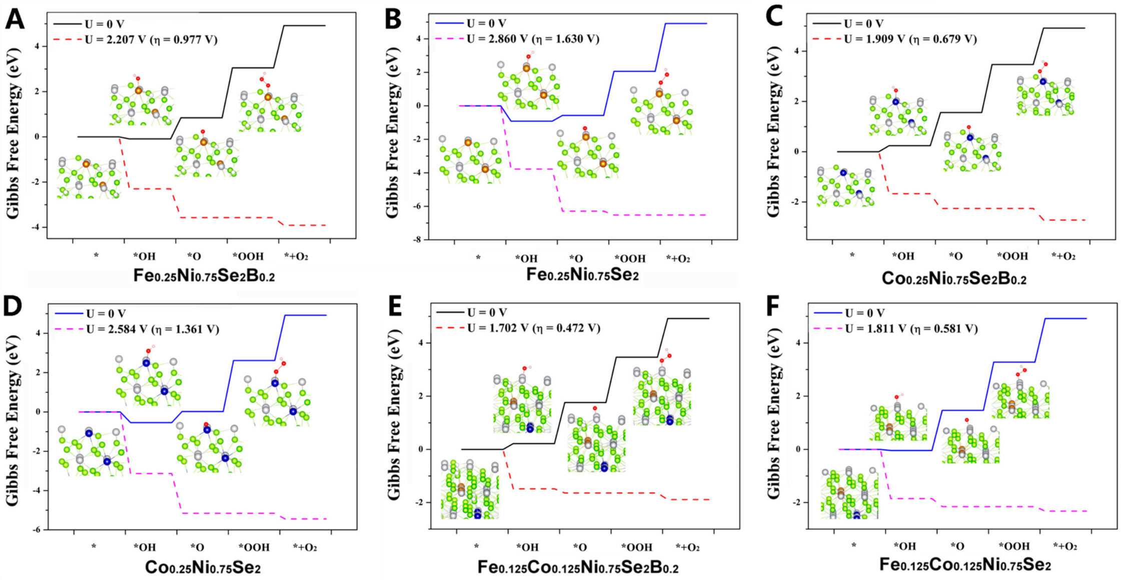

Figure 6. Activities of the OER intermediate process calculated with DFT+U. The processes of OER steps on (111) surfaces of different materials: (A) $Fe_{0.25}Ni_{0.75}Se_2$, (B) $Fe_{0.25}Ni_{0.75}Se_2B_{0.2}$, (C) $Co_{0.25}Ni_{0.75}Se_2$, (D) $Co_{0.25}Ni_{0.75}Se_2B_{0.2}$, (E) $Fe_{0.125}Co_{0.125}Ni_{0.75}Se_2$, and (F) $Fe_{0.125}Co_{0.125}Ni_{0.75}Se_2B_{0.2}$. Solid line: Computed free energies without external voltage (U = 0). Dashed line: modified free energies under theoretical reaction potential.

ones. Specifically, the overpotentials of $Co_{0.25}Ni_{0.75}Se_2$, $Co_{0.25}Ni_{0.75}Se_2B_{0.2}$, $Fe_{0.125}Co_{0.125}Ni_{0.75}Se_2$, and $Fe_{0.125}Co_{0.125}Ni_{0.75}Se_2B_{0.2}$ are 1.361, 0.679, 0.581, and 0.472 V, respectively.

We also investigated the deformation charge density for all surfaces and the PDOS at active sites to understand the effects of multimetal and B-doping on the activity of the OER catalysts. Figure S15 shows the deformation charge density of selected (111) facets. For the catalysts with B dopants, electrons (yellow area in Figure S15) are clearly accumulated around the B atom (white balls in Figure S15). These electrons are transferred from adjacent metals atoms, where the electron deletion areas (displayed as the cyan area in Figure S15) are only located on metal atoms. Such a polarized charge distribution strengthens the interaction between B and metal atoms and reduces the number of electrons in metal atoms, especially the outermost electrons in the d orbital, which heavily modifies the properties of metal sites. Taking $Co_{0.25}Ni_{0.75}Se_2$ (Figure 6C) and $Co_{0.25}Ni_{0.75}Se_2B_{0.2}$ (Figure 6D) as examples, the strong adsorption of the −OOH group limits the overpotential of $Co_{0.25}Ni_{0.75}Se_2$. The Gibbs free energy difference (ΔG) for the generation of an OOH-based intermedium (*OOH) is 2.584 eV, which is greatly reduced to 1.909 eV with the B dopants (Figure 6C). This reduction can be understood as a result of the loss of d electrons of metal atoms, as displayed in Figure S15, which reduces the possibility of the charge transfer from metal atoms to the −OOH group and gives rise to a weak interaction between the metal site and the −OOH group. As a result, the Gibbs energy ΔG is reduced for the OER process. Through Bader analysis,[40] the total number of electrons of the −OOH group on $Co_{0.25}Ni_{0.75}Se_2B_{0.2}$ is 13.489e, which means that the −OOH group accepts 0.489e from $Co_{0.25}Ni_{0.75}Se_2B_{0.2}$. In contrast, the electrons transferred from $Co_{0.25}Ni_{0.75}Se_2$ to the −OOH group are 0.527e. The proposed OER mechanisms for selenides before and after B dopant in Figure 7A,B clearly show that the B dopant weakens the interaction between the catalyst and the −OOH group as the result of ΔG. Similar phenomena are also observed for other multimetllic selenide borides. Figure 7C shows the PDOS of d orbitals of atoms at active sites, indicating that the d electrons of metal atoms are redistributed with the introduction of other metal atoms and B. We also calculated the number of d electrons of active metal sites. The B-doping can reduce the total d electrons around metals, where the electrons are transferred from the metal to B atoms, consistent with the data of deformation charge density. In addition, the transfer of d electrons from metals to B enhances the interactions between B and the metals, which can reasonably explain the presence of M−B bonds in the XPS data in Figure 4.

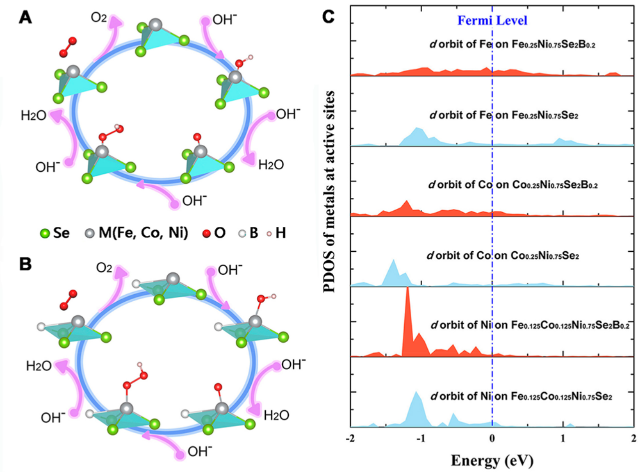

Figure 7. (A, B) Proposed OER mechanisms for pyrite selenides before and after B dopant. (C) PDOS of atoms at active sites.

CONCLUSIONS

In summary, the heteroepitaxial pyrite selenides by dual-cation substitution and boron dopant can effectively prevent corrosion benefiting from the *in situ* nucleation growth process

DOI: 10.1021/acsnano.9b04956
ACS Nano 2019, 13, 11469−11476

and exhibit superior OER activity and stability. In particular, boron in $Fe_5Co_4Ni_{20}Se_{36}B_x$ can effectively adjust the adsorption energy of OH intermediates and facilitates the charge transfer from the surface to the current collector. The synergistic effect between the embedded B, Se and Fe, Co, and Ni in the pyrite selenides can generate active sites that further improve the OER reaction kinetics. This work illustrates the potential of multimetallic selenide boride materials in energy conversion owing to the special atomic and electronic structures, which may contribute to rationally fabricating high-performance electrocatalysts.

EXPERIMENTAL METHODS

Material Synthesis. The $NiSe_2B_x$, $FeNi_3Se_8B_x$, $CoNi_3Se_8B_x$, and $Fe_5Co_4Ni_{20}Se_{36}B_x$ powders were synthesized by two simple steps. First, the Ni-, FeNi-, CoNi-, and FeCoNi-based precursors were synthesized by chemical methods. A 1 mmol amount of $Co(NO_3)_2 \cdot 6H_2O$ (Sigma-Aldrich), 1 mmol of $Ni(NO_3)_2 \cdot 6H_2O$ (Sigma-Aldrich), and 1 mmol of $FeCl_3 \cdot 6H_2O$ (Sigma-Aldrich) were dissolved in DI water to form a transparent solution, respectively. The FeCoNi-based precursor was prepared by adding a moderate amount of $NaBH_4$ (Sigma-Aldrich) solution into the $Ni(NO_3)_2 \cdot 6H_2O$ (1 mmol), $Co(NO_3)_2 \cdot 6H_2O$, and $FeCl_3 \cdot 6H_2O$ (1 mmol) mixed solution (mole ratio of 3:0.5:0.5); then a black precipitate was immediately produced. The precipitate was collected and dried at 60 °C in an oven overnight. Then a thermal selenization process was employed in the following step to obtain the $Fe_5Co_4Ni_{20}Se_{36}B_x$. The as-prepared precipitate and selenium powder were placed in a quartz boat. The selenium powder (Alfa Aesar) was put at the upstream side of the tube furnace with a distance of 10 cm to the precipitate. Subsequently, the precipitate was heated at 450 °C for 2 h with a heating rate of 5 °C min^{-1} under an argon atmosphere and finally cooled to ambient temperature naturally. For comparison, $NiSe_2B_x$, $FeNi_3Se_8B_x$, and $CoNi_3Se_8B_x$ were also prepared under similar conditions despite the differences in the metal irons.

Structural Characterizations. Powder XRD data were obtained through an X-ray diffractometer (Rigaku SmartLab) using Cu Kα (γ = 1.54178 A) radiation. SEM images were recorded in a field-emission scanning electron microscope (JSM-6490, JEOL) operating at 5 kV. TEM and HRTEM, SAED, EELS, and EDX elemental mapping were collected on a JEOL model JEM-ARM-200F microscope operated at 200 kV. XPS was acquired on an ESCALAB 250Xi XPS system using Mg as the excitation source.

Electrochemical Measurements. To prepare the working electrode, 5 mg of catalysts was dispersed in 750 μL of DI water, 210 μL of isopropanol, and 40 μL of 5 wt % Nafion solution followed by sonication to form a homogeneous ink. Then 10 μL of the ink was loaded onto a glassy carbon electrode of 5 mm in diameter. Then the electrode was dried naturally at room temperature. Electrochemical measurements were carried out on a CHI 660E electrochemical workstation (CH Instruments, Inc., Shanghai) in a standard three-electrode system at room temperature with an aqueous solution of 1.0 M KOH (pH = 14) used as the electrolyte. A Hg/HgO (1.0 M NaOH) electrode and a graphite rod were used as the reference electrode and counter electrode, respectively. All the measured potentials *vs* Hg/HgO were converted to reversible hydrogen electrode according to the equation $E(\text{RHE}) = E(\text{Hg/HgO}) + 0.098 + 0.059\,\text{pH}$. The polarization curves obtained from linear sweep voltammetry measurements were recorded at a scan rate of 1.0 mV s^{-1}. Electrochemical impedance spectroscopy measurements were performed in a Solartron electrochemical workstation (German) at a frequency ranging from 0.01 to 105 Hz with a small AC voltage amplitude, of which the data were fitted by Zview software. The ECSA was determined by the electrochemical Cdl from the scan-rate dependence of CVs.

Calculation Methods. The Vienna *ab Initio* Simulation Package code was employed to study the adsorption of OH groups on the potential catalysts.[41] The nuclei−electron interactions were described by the projector augmented wave pseudopotentials,[42] at the level of generalized gradient approximation (GGA) in the form of Perdew, Burke, and Ernzerhof.[43] The spin-polarization was considered in these calculations, as well as the van der Waals interaction, which was described by the DFT+D3 method developed by Grimme.[44,45] Further, the Coulombic interactions for transition metals are corrected by the GGA + U approach, in which the parameters of U_{eff} of 3.4, 3.4, and 3.3 eV were used for Ni, Co, and Fe, respectively. For all calculations, the cutoff energy was 500 eV, and the convergence criteria are 10^{-5} eV for energy and 10^{-2} eV/Å for force. Methods for the process of OER were described in more detail in our initial work.[46]

ASSOCIATED CONTENT

Supporting Information

The Supporting Information is available free of charge on the ACS Publications website at DOI: 10.1021/acsnano.9b04956.

Figures S1−S15 and Tables S1 and S2 (PDF)

AUTHOR INFORMATION

Corresponding Author

*E-mail: ychai@polyu.edu.hk.

ORCID

Dewei Rao: 0000-0003-0410-5259
Yuen Hong Tsang: 0000-0001-5632-5224
Yang Chai: 0000-0002-8943-0861

Author Contributions

#Y. Zuo, D. Rao, and S. Ma contributed equally to this work.

Notes

The authors declare no competing financial interest.

ACKNOWLEDGMENTS

This work was supported by the Research Grant Council of Hong Kong (N_PolyU540/17), the Hong Kong Polytechnic University (G-YBPS), the Scientific and Technological Projects of Henan Province (182102210502), Education Department of Henan Province (18A430003), and the National Natural Science Foundation of China (Nos. 51801075, 91750112). The calculation work was carried out at the National Supercomputer Center in LvLiang, China, and the calculations were performed on TianHe-2.

REFERENCES

(1) Suen, N.; Hung, S.; Quan, Q.; Zhang, N.; Xu, Y.; Chen, H. Electrocatalysis for the Oxygen Evolution Reaction: Recent Development and Future Perspectives. *Chem. Soc. Rev.* **2017**, *46*, 337−365.

(2) Yao, Y.; Huang, Z.; Xie, P.; Lacey, S. D.; Jacob, R.; Xie, H.; Chen, F.; Nie, A.; Pu, T.; Rehwoldt, M.; Yu, D.; Zachariah, M. R.; Wang, C.; Shahbazian-Yassar, R.; Li, J.; Hu, L. Carbothermal Shock Synthesis of High-Entropy-Alloy Nanoparticles. *Science* **2018**, *359*, 1489−1494.

(3) Chu, S.; Majumdar, A. Opportunities and Challenges for a Sustainable Energy Future. *Nature* **2012**, *488*, 294−303.

(4) Zhang, B.; Zheng, X.; Voznyy, O.; Comin, R.; Bajdich, M.; García-Melchor, M.; Han, L.; Xu, J.; Liu, M.; Zheng, L.; Arquer, F.; Dinh, C.; Fan, F.; Yuan, M.; Yassitepe, E.; Chen, N.; Regier, T.; Liu, P.; Li, Y.; Luna, P.; Janmohamed, A.; Xin, H.; Yang, H.; Vojvodic, A.; Sargent, E. H. Homogeneously Dispersed Multimetal Oxygen-Evolving Catalysts. *Science* **2016**, *352*, 333−337.

(5) Hu, F.; Zhu, S.; Chen, S.; Li, Y.; Ma, L.; Wu, T.; Zhang, Y.; Wang, C.; Liu, C.; Yang, X.; Song, L.; Yang, X.; Xiong, Y. Amorphous Metallic NiFeP: A Conductive Bulk Material Achieving High Activity for Oxygen Evolution Reaction in Both Alkaline and Acidic Media. *Adv. Mater.* **2017**, *29*, 1606570.

(6) McCrory, C.; Jung, S.; Peters, J.; Jaramillo, T. F. Benchmarking Heterogeneous Electrocatalysts for the Oxygen Evolution Reaction. *J. Am. Chem. Soc.* **2013**, *135*, 16977−16987.

(7) Anantharaj, V.; Ede, S. R.; Sakthikumar, K.; Karthick, K.; Mishra, S.; Kundu, S. Recent Trends and Perspectives in Electrochemical Water Splitting with An Emphasis on Sulfifide, Selenide, and Phosphide Catalysts of Fe, Co, and Ni: A Review. *ACS Catal.* **2016**, *6*, 8069−8097.

(8) Friebel, D.; Louie, M. W.; Bajdich, M.; Sanwald, K.; Cai, Y.; Wise, A. M.; Cheng, M.; Sokaras, D.; Weng, T.; Alonso-Mori, R.; Davis, R.; Bargar, J.; Nørskov, J.; Nilsson, A.; Bell, A. Identification of Highly Active Fe Sites in (Ni, Fe)OOH for Electrocatalytic Water Splitting. *J. Am. Chem. Soc.* **2015**, *137*, 1305−1313.

(9) Mendoza-Garcia, A.; Zhu, H.; Yu, Y.; Li, Q.; Zhou, L.; Su, D.; Kramer, M. J.; Sun, S. Controlled Anisotropic Growth of Co-Fe-P from Co-Fe-O Nanoparticles. *Angew. Chem., Int. Ed.* **2015**, *54*, 9642.

(10) Xia, C.; Jiang, Q.; Zhao, C.; Hedhili, M. N.; Alshareef, H. N. Selenide-Based Electrocatalysts and Scaffolds for Water Oxidation Applications. *Adv. Mater.* **2016**, *28*, 77−85.

(11) Kim, J.; Kim, B.; Kim, H.; Kang, K. Recent Progress on Multimetal Oxide Catalysts for the Oxygen Evolution Reaction. *Adv. Energy Mater.* **2018**, *8*, 1702774.

(12) Qiu, B.; Cai, L.; Wang, Y.; Lin, Z.; Zuo, Y.; Wang, M.; Chai, Y. Fabrication of Nickel−Cobalt Bimetal Phosphide Nanocages for Enhanced Oxygen Evolution Catalysis. *Adv. Funct. Mater.* **2018**, *28*, 1706008.

(13) Liu, Z.; Dong, C.; Huang, Y.; Cen, J.; Yang, H.; Chen, X.; Tong, X.; Su, D.; Wang, Y.; Wang, S. Modulating the Electronic Structure of Ultrathin Layered Double Hydroxide Nanosheets with Fluorine: An Efficient Electrocatalyst for the Oxygen Evolution Reaction. *J. Mater. Chem. A* **2019**, *7*, 14483−14488.

(14) Zhou, P.; He, J.; Zou, Y.; Wang, Y.; Xie, C.; Chen, R.; Zang, S.; Wang, S. Single-Crystalline Layered Double Hydroxides with Rich Defects and Hierarchical Structure by Mild Reduction for Enhancing the Oxygen Evolution Reaction. *Sci. China: Chem.* **2019**, *62*, DOI: 10.1007/s11426-019-9511-x.

(15) Jiang, J.; Sun, F.; Zhou, S.; Hu, W.; Zhang, H.; Dong, J.; Jiang, Z.; Zhao, J.; Li, J.; Yan, W.; Wang, M. Atomic-Level Insight into Super-Efficient Electrocatalytic Oxygen Evolution on Iron and Vanadium co-Doped Nickel (oxy)Hydroxide. *Nat. Commun.* **2018**, *9*, 2885.

(16) Liu, G.; He, D.; Yao, R.; Zhao, Y.; Li, J. Amorphous NiFeB Nanoparticles Realizing Highly Active and Stable Oxygen Evolving Reaction for Water Splitting. *Nano Res.* **2018**, *3*, 1664−1675.

(17) Zuo, Y.; Rao, D.; Li, S.; Li, T.; Zhu, G.; Chen, S.; Song, L.; Chai, Y.; Han, H. Atomic Vacancies Control of Pd-Based Catalysts for Enhanced Electrochemical Performance. *Adv. Mater.* **2018**, *30*, 1704171.

(18) Xu, K.; Chen, P. Z.; Li, X.; Tong, Y.; Ding, H.; Wu, X.; Chu, W.; Peng, Z.; Wu, C.; Xie, Y. Metallic Nickel Nitride Nanosheets Realizing Enhanced Electrochemical Water Oxidation. *J. Am. Chem. Soc.* **2015**, *137*, 4119−4125.

(19) Bediako, D. K.; Surendranath, Y.; Nocera, D. G. Mechanistic Studies of the Oxygen Evolution Reaction Mediated by a Nickel-Borate Thin Film Electrocatalyst. *J. Am. Chem. Soc.* **2013**, *135*, 3662−3674.

(20) Masa, J.; Weide, P.; Peeters, D.; Sinev, I.; Xia, W.; Sun, Z.; Somsen, C.; Muhler, M.; Schuhmann, W. Amorphous Cobalt Boride (Co2B) as A Highly Efficient Nonprecious Catalyst for Electrochemical Water Splitting: Oxygen and Hydrogen Evolution. *Adv. Energy Mater.* **2016**, *6*, 1502313.

(21) Chen, P.; Xu, K.; Zhou, T.; Tong, Y.; Wu, J.; Cheng, H.; Lu, X.; Ding, H.; Wu, C.; Xie, Y. Strong-Coupled Cobalt Borate Nanosheets/Graphene Hybrid as Electrocatalyst for Water Oxidation Under Both Alkaline and Neutral Conditions. *Angew. Chem., Int. Ed.* **2016**, *55*, 2488−2492.

(22) Zuo, Y.; Li, T.; Ren, H.; Zhu, G.; Han, K.; Zhuang, L.; Han, H. Self-Assembly of Pt-Based Truncated Octahedral Crystals into Metal-Frameworks Towards Enhanced Electrocatalytic Activity. *J. Mater. Chem. A* **2016**, *4*, 15169−15180.

(23) Mistry, H.; Varela, A.; Kühl, S.; Strasser, P.; Cuenya, B. R. Nanostructured Electrocatalysts with Tunable Activity and Selectivity. *Nat. Rev. Mater.* **2016**, *1*, 1−14.

(24) Zuo, Y.; Wu, L.; Cai, K.; Li, T.; Yin, W.; Li, D.; Li, N.; Liu, J.; Han, H. Platinum Dendritic-Flowers Prepared by Tellurium Nanowires Exhibit High Electrocatalytic Activity for Glycerol Oxidation. *ACS Appl. Mater. Interfaces* **2015**, *7*, 17725−17730.

(25) Xu, X.; Song, F.; Hu, X. A Nickel Iron Diselenide-Derived Efficient Oxygen-Evolution Catalyst. *Nat. Commun.* **2016**, *7*, 12324.

(26) Sun, Y.; Xu, K.; Wei, Z.; Li, H.; Zhang, T.; Li, X.; Cai, W.; Ma, J.; Fan, H.; Li, Y. Strong Electronic Interaction in Dual-Cation-Incorporated NiSe2 Nanosheets with Lattice Distortion for Highly Efficient Overall Water Splitting. *Adv. Mater.* **2018**, *30*, 1802121.

(27) Tang, C.; Zhang, R.; Lu, W.; He, L.; Jiang, X.; Asiri, A. M.; Sun, X. Fe-Doped CoP Nanoarray: A Monolithic Multifunctional Catalyst for Highly Efficient Hydrogen Generation. *Adv. Mater.* **2017**, *29*, 1602441.

(28) Han, H.; Choi, H.; Mhin, S.; Hong, Y.; Kim, K.; Kwon, J.; Ali, G.; Chung, K.; Je, M.; Umh, H.; Lim, D.; Davey, K.; Qiao, S.; Paik, U.; Song, T. Advantageous Crystalline-Amorphous Phase Boundary for Enhanced Electrochemical Water Oxidation. *Energy Environ. Sci.* **2019**, *12*, 2443−2454.

(29) Jiang, J.; Lu, S.; Gao, H.; Zhang, X.; Yu, H. Ternary FeNiS2 Ultrathin Nanosheets as An Electrocatalyst for Both Oxygen Evolution and Reduction Reactions. *Nano Energy* **2016**, *27*, 526−534.

(30) Gao, S.; Lin, Y.; Jiao, X.; Sun, Y.; Luo, Q.; Zhang, W.; Li, D.; Yang, J.; Xie, Y. Partially Oxidized Atomic Cobalt Layers for Carbon Dioxide Electroreduction to Liquid Fuel. *Nature* **2016**, *529*, 68.

(31) Chen, C.; Kang, Y.; Huo, Z.; Zhu, Z.; Huang, W.; Xin, H.; Snyder, J.; Li, D.; Herron, J.; Mavrikakis, M.; Chi, M.; More, K.-L.; Li, Y.-D.; Markovic, N.-M.; Somorjai, G.-A.; Yang, P.-D.; Stamenkovic, V.-R. Highly Crystalline Multimetallic Nanoframes with Three-Dimensional Electrocatalytic Surfaces. *Science* **2014**, *343*, 1339.

(32) George, C.; Genovese, A.; Casu, A.; Prato, M.; Povia, M.; Manna, L.; Montanari, T. CO Oxidation on Colloidal $Au_{0.8}Pd_{0.2}$−Fe_xO_y Dumbbell Nanocrystals. *Nano Lett.* **2013**, *13*, 752−757.

(33) Cortie, M. B.; McDonagh, A. M. Synthesis and Optical Properties of Hybrid and Alloy Plasmonic Nanoparticles. *Chem. Rev.* **2011**, *111*, 3713−3735.

(34) McCrory, C.; Jung, S.; Peters, J. C.; Jaramillo, T. F. Benchmarking Heterogeneous Electrocatalysts for the Oxygen Evolution Reaction. *J. Am. Chem. Soc.* **2013**, *135*, 16977−16987.

(35) Tung, C.; Hsu, Y.; Shen, Y.; Zheng, Y.; Chan, T.; Sheu, H.; Cheng, Y.; Chen, H. Reversible Adapting Layer Produces Robust Single-Crystal Electrocatalyst for Oxygen Evolution. *Nat. Commun.* **2015**, *6*, 8106.

(36) Liang, H.; Meng, F.; Cabán-Acevedo, M.; Li, L.; Forticaux, A.; Xiu, L.; Wang, Z.; Jin, S. Hydrothermal Continuous Flow Synthesis and Exfoliation of NiCo Layered Double Hydroxide Nanosheets for Enhanced Oxygen Evolution Catalysis. *Nano Lett.* **2015**, *15*, 1421.

(37) Lin, C.; Tsai, Y.; Johnston, H. E.; Fang, M.; Yu, F.; Zhou, W.; Whitfifield, P.; Li, Y.; Wang, J.; Liu, R.; Attfifield, J.-P. Enhanced Photoluminescence Emission and Thermal Stability from Introduced Cation Disorder in Phosphors. *J. Am. Chem. Soc.* **2017**, *139*, 11766−11770.

(38) Wang, B.; Lin, H.; Huang, F.; Xu, J.; Chen, H.; Lin, Z.; Wang, Y. Non-Rare-Earth $BaMgAl_{10-2x}O_{17}$:xMn^{4+}, xMg^{2+}: A Narrow-Band Red Phosphor for Use as A High-Power Warm w-LED. *Chem. Mater.* **2016**, *28*, 3515−3524.

(39) Maintz, S.; Deringer, V.; Tchougréeff, A.; Dronskowski, R. LOBSTER 2.0.0 and its Nuts and Bolts. *J. Comput. Chem.* **2016**, *37*, 1030−1035.

(40) Yu, M.; Trinkle, D. R. Accurate and Efficient Algorithm for Bader Charge Integration. *J. Chem. Phys.* **2011**, *134*, 064111.

(41) Kresse, G.; Furthmuller, J. Efficient Iterative Schemes for *Ab Initio* Total-Energy Calculations Using A Plane-Wave Basis Set. *Phys. Rev. B: Condens. Matter Mater. Phys.* **1996**, *54*, 11169−11186.

(42) Kresse, G.; Furthmüller, J. Efficiency of *Ab Initio* Total Energy Calculations for Metals and Semiconductors Using a Plane-Wave Basis Set. *Comput. Mater. Sci.* **1996**, *6*, 15−50.

(43) Blöchl, P. E. Projector Augmented-Wave Method. *Phys. Rev. B: Condens. Matter Mater. Phys.* **1994**, *50*, 17953−17979.

(44) Perdew, J. P.; Burke, K.; Ernzerhof, M. Generalized Gradient Approximation Made Simple. *Phys. Rev. Lett.* **1996**, *77*, 3865−3868.

(45) Grimme, S.; Antony, J.; Ehrlich, S.; Krieg, S. A Consistent and Accurate *Ab Initio* Parametrization of Density Functional Dispersion Correction (DFT-D) for the 94 Elements H-Pu. *J. Chem. Phys.* **2010**, *132*, 154104.

(46) Meng, L.; Rao, D.; Tian, W.; Cao, F.; Yan, X.; Li, L. Simultaneous Manipulation of O-Doping and Metal Vacancy in Atomically Thin $Zn_{10}In_{16}S_{34}$ Nanosheet Arrays toward Improved Photoelectrochemical Performance. *Angew. Chem.* **2018**, *130*, 17124−17129.

ACS NANO

www.acsnano.org

Spatially Confined Formation of Single Atoms in Highly Porous Carbon Nitride Nanoreactors

Yunpeng Zuo, Tingting Li, Ning Zhang, Tianyun Jing, Dewei Rao,* Patrik Schmuki, Štěpán Kment,* Radek Zbořil, and Yang Chai*

Cite This: *ACS Nano* 2021, 15, 7790−7798

ABSTRACT: **Reducing the size of a catalyst to a single atom (SA) level can dramatically change its physicochemical properties and significantly boost its catalytic activity. However, the massive synthesis of SA catalysts still remains a grand challenge mainly because of the aggregation and nucleation of the generated atoms during the reaction. Here, we design and implement a spatially confined synthetic strategy based on a porous-hollow carbon nitride (*p*-CN) coordinated with 1-butyl-3-methylimidazole hexafluorophosphate, which can act as a nanoreactor and allow us to obtain metal SA catalysts (*p*-CN@M SAs). This relatively easy and highly effective method provides a way to massively synthesize single/multiple atoms (*p*-CN@M SAs, M = Pt, Pd, Cu, Fe, *etc.*). Moreover, the amorphous NiB-coated *p*-CN@Pt SAs can further increase the loading amount of Pt SAs to 3.7 wt %. The synthesized *p*-CN@Pt&NiB electrocatalyst exhibits an extraordinary hydrogen evolution reaction activity with the overpotential of 40.6 mV@10 mA/cm^{-2} and the Tofel slope of 29.26 mV/dec.**

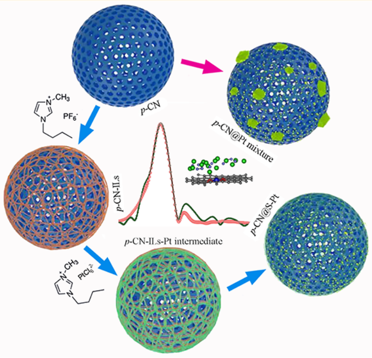

KEYWORDS: *single atom, spatially confined synthetic strategy, massive synthesis, ionic liquid, hydrogen evolution*

INTRODUCTION

Single-atom (SA) catalysis has been found as one of the most attractive research topics in heterogeneous catalysis owing to the superior atom utilization, such as selective hydrogenation, water splitting, and fuel cell.[1−4] The special coordination chemistry of SAs enables its distinctive physicochemical properties, in which the unsaturated SAs can bond with molecules in appropriate orientations with an optimized interaction.[5−8] In previous reports, researchers synthesized SA catalysts according to different methods, which usually suffer from harsh reaction conditions, including high temperature and complex gas reduction conditions.[9−14] Therefore, it requires us to develop the general and alternative ways for synthesizing SAs. The spatial limitation of the nanocontainer can theoretically provide a suitable reaction space to confine nanosized particles or even SAs. For instance, Mirkin and coworkers developed a funnel-type nanoreactor to synthesize metal nanoparticles.[15] However, the ultrafine particles or SAs always suffer from a thermodynamic aggregation to reduce their excess surface energy, which makes it extremely laborious to get SAs that rely solely on the technological progress. Porous carbon materials can act as similar reactors because of their abundant undulated structure on the surface and micro/mesopores throughout the materials.[16,17] To retard the agglomeration during the SAs preparation, heteroatoms (such as N, P) doped in the carbon materials with good coordination ability can securely *in situ* attach SAs and provide a greater stability.[18−20] Nevertheless, these approaches do not work well under fast and large amount reactions. Thus, it is quite necessary to develop an effective alternative method. It has been reported that ionic liquids (ILs) offer a wide range of uses, such as a structure-regulated synthesis of metal nanoparticles and special electrolyte, due to their special properties.[21−24] As the water content increases, the charge groups in ILs can be effectively separated within a certain range and can selectively adsorb or filter metal ions in aqueous solutions.[25] ILs also can tune the electronic state of the metal SAs, thus enhancing the interaction between SAs and the substrate and benefiting the stability of the SAs.[26]

The platinum group metal (PGM), such as Pt, Pd, and Ir, plays a crucial role for a hydrogen evolution reaction (HER), which is closely related to the rising demand for green energy for sustainable development.[4,25] Although PGMs show excellent HER activity, a large-scale production is not an economically viable option because of the high cost. Atomic utilization efficiency has emerged as an advanced indicator to

Received: March 3, 2021
Accepted: April 15, 2021
Published: April 19, 2021

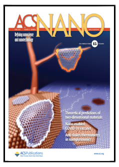

https://doi.org/10.1021/acsnano.1c01872

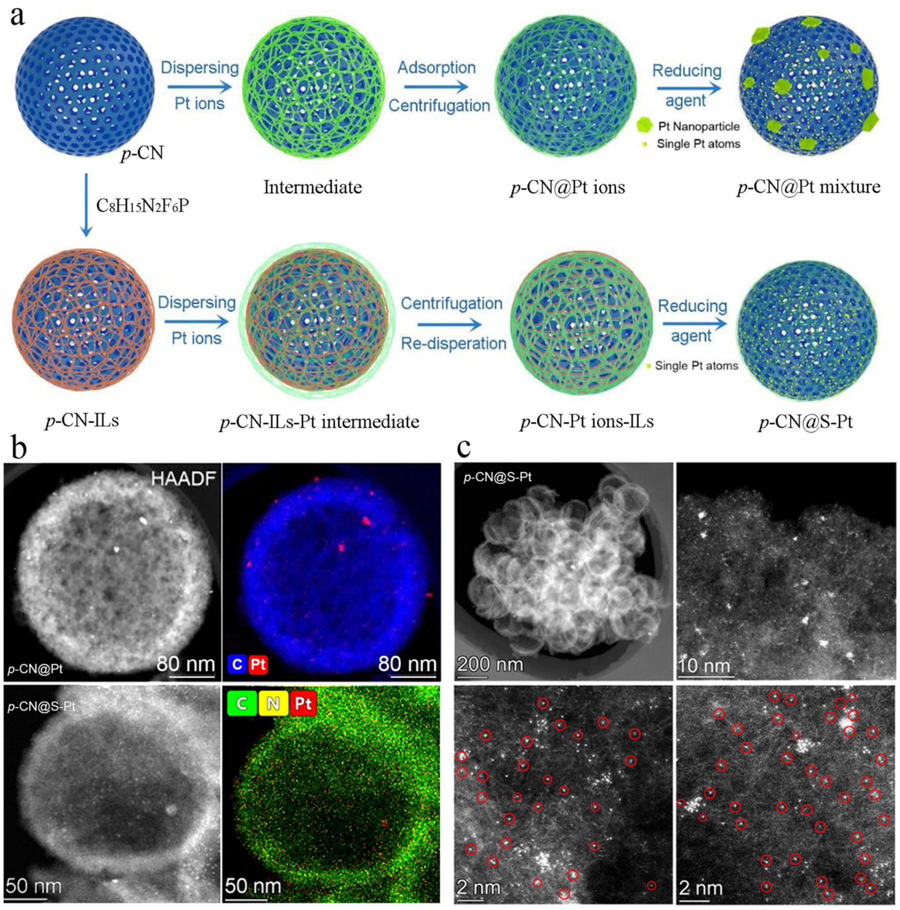

Figure 1. Synthesis and characterization of the *p*-CN@Pt and *p*-CN@S−Pt. (a) Schematic of the synthetic process of the Pt nanoparticles and SAs mixture on *p*-CN and the generated progress of *p*-CN@S−Pt with the $C_8H_{15}N_2F_6P$. (b) EDS mapping images of the *p*-CN@Pt and *p*-CN@S−Pt. (c) STEM image of the *p*-CN@S−Pt and the corresponding magnified images of the *p*-CN@S−Pt to the atomic-resolution. Some of the single Pt atoms are highlighted by the inset red circles.

evaluate the catalytic properties of catalysts, especially for PGM.[4] One of the strategies to improve the atomic utilization efficiency of PGM is based on reducing their size to isolated SAs.[27−31] Here, we synthesized a hollow porous carbon nitride (*p*-CN) nanosphere-enriched undulated structure and micropores as a nanoreactor, employing the 1-butyl-3-methylimidazole hexafluorophosphate ($C_8H_{15}N_2F_6P$) as a regulator to control the content of metal ions on the *p*-CN. The *p*-CN-supported Pt SAs (*p*-CN@S−Pt) catalysts were successfully prepared following a wet chemistry method. To further increase the loading amount of Pt SAs and enhance the stability of the *p*-CN@S−Pt, amorphous boron−nickel (NiB) with good electronic conductivity is introduced to coat *p*-CN@S−Pt. The Pt content in *p*-CN@S−Pt&NiB can reach to 3.7 wt %, larger than that of *p*-CN@S−Pt (2.56 wt %). Additionally, the *p*-CN@S−Pt&NiB exhibited a superior HER activity with the overpotential of 40.6 mV@10 mA/cm^{-2} and the Tofel slope of 29.26 mV/dec, much better than commercial Pt/C (50.7 mV, 46.45 mV/dec).

RESULTS AND DISCUSSION

Synthesis and Characterization of *p*-CN@S−Pt. The *p*-CN@S−Pt was prepared by a wet chemical method using *p*-CN hollow nanospheres as a support and $C_8H_{15}N_2F_6P$ as a regulator. High-resolution transmission electron microscopy (HRTEM) and scanning electron microscopy (SEM) were employed to investigate the morphology of such synthesized *p*-CN-based materials. The synthesized *p*-CN materials exhibit a relatively uniform nanosphere feature with the diameter of 250−330 nm (SEM images in Figure S1). TEM images in Figure S2 clearly show the porous structure of *p*-CN. There are plentiful sub-nanometer channels in the overall structure of the *p*-CN material, which can ideally serve as trap sites for the attachment of SAs. The specific surface areas of *p*-CN were determined by the Brunauer−Emmett−Teller (BET) method. The calculated BET surface areas reach 1005 m^2/g. Furthermore, the pore size distribution of *p*-CN (Figure S3) is majorly in the range between 4 and 6 nm, which is highly suitable for anchoring the SAs. The HRTEM and BET results simultaneously confirmed that the *p*-CN material can be used as a nanoreaction vessel.[32] The X-ray diffraction (XRD) pattern of *p*-CN (Figure S4) indicates the peaks at 27.7° and 50.75° are well-indexed to the (002) and (100) planes with standard XRD profiles of the CN crystal structure.[33] The characteristic diffraction peaks of the synthesized *p*-CN show good crystallinity, indicating a potential for good conductivity.[9,10,33,34] The Raman spectrum of the *p*-CN component (Figure S5) shows the typical peaks of D and G bands at ∼1320 and ∼1590 cm^{-1}. The intensity ratio of I_D/I_G is 1.18, which reveals that the *p*-CN is rather disordered with a large number of defects that can provide more sites for SA accommodation.[35]

As illustrated in the upper line of Figure 1a, the *p*-CN@Pt SAs were fabricated via a four-step process. Typically,

https://doi.org/10.1021/acsnano.1c01872
ACS Nano 2021, 15, 7790−7798

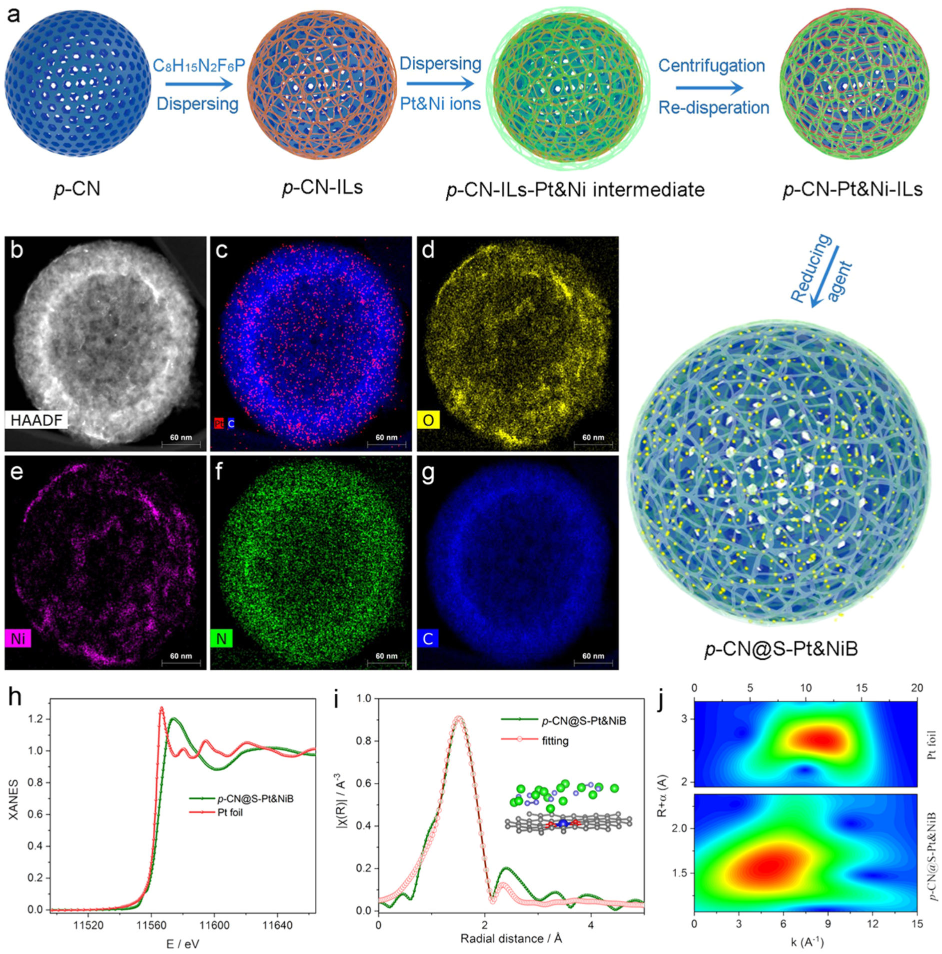

Figure 2. Synthesis and structure determination of *p*-CN@S−Pt&NiB by EDS-mapping and XAFS. (a) Illustration of the preparation process of *p*-CN@S−Pt&NiB. (b−g) The enlarged HAADF-STEM images and corresponding element maps (O: yellow, Ni: pink, N: green, C: blue, Pt: red). (h) The XANES spectra and (i) FT-EXAFS fitting curves of *p*-CN@S−Pt&NiB at Pt L_3 edge. (j) WT-EXAFS of *p*-CN@S−Pt&NiB.

$C_8H_{15}N_2F_6P$ was physically mixed with the *p*-CN powder and then sonicated for 20 min. Chloroplatinic acid and ethanol are gradually injected into the mixture, and then the solution is continuously sonicated for another 30 min. There is a portion of the chloroplatinic acid on the surface of the *p*-CN under physical adsorption. The sodium borohydride was added as the reducing agent, and the *p*-CN@Pt complex that contained Pt nanoparticles and Pt SAs was finally obtained. High-angle annular dark-field scanning transmission electron microscopy (HAADF-STEM) energy-dispersive X-ray spectroscopy (EDS) mapping images of the *p*-CN@Pt complex (Figure 1b) indicate the existence of small Pt particles, which is in line with HRTEM results of the *p*-CN@Pt complex (Figure S6), whereas, when the $C_8H_{15}N_2F_6P$ was mixed with the chloroplatinic acid, the negatively charged functional group F_6P could coordinate with Pt ions to generate $C_8H_{15}N_2F_6P$−Pt complexes, thus regulating the dispersion of Pt ions (Figure S7a,b). After centrifugation, a certain amount of Pt precursor together with $C_8H_{15}N_2F_6P$ was adsorbed on the surface of the *p*-CN as shown in Figure S7c. Then the *p*-CN@Pt complex was redispersed in ethanol/deionized water and reacted with the sodium borohydride to obtain *p*-CN@S−Pt catalysts. HAADF-STEM EDS-mapping images (Figure 1b and Figure S8) clearly show the uniform distribution of the Pt element in the *p*-CN@S−Pt catalysts as well as SEM images (Figure S9), indicating no particles on the surface of the *p*-CN and the generation of single Pt atoms. To demonstrate the distribution of SAs at the surface of *p*-CN materials, HRTEM images of the samples are collected by a spherical aberration-corrected transmission electron microscope (AC-TEM), as displayed in Figure 1c and Figure S10. It can be observed that the surface of *p*-CN materials is densely packed with single Pt atoms. The continuously enlarged STEM images directly display the homogeneously distributed Pt SAs within the *p*-CN matrix. Some Pt SAs are marked by red circles in Figure 1c for better observation.

Another grand challenge for monatomic catalysts is to prepare SAs in large amounts excluding their further migration and agglomeration during the catalytic process. On the basis of our previous studies,[36,37] the NiB with good electronic conductivity may further improve the corrosion resistance and stability of the *p*-CN@S−Pt. By changing the Pt solution to a Pt/Ni (Pt/Ni = 1:2) mixture precursor (Figure 2a), the *p*-CN@S−Pt&NiB can be synthesized under identical conditions. The content of Pt in the final *p*-CN@S−Pt&NiB catalyst was determined by inductively coupled plasma mass spectrometry (ICP-MS). The results in Figure S11 show the increased content of Pt SAs (3.7%) after the introduction of the NiB component. Figure S12 shows SEM images of the *p*-CN@S−Pt&NiB, indicating that the entire *p*-CN is fully coated with NiB&Pt SAs. Further investigation by HAADF-STEM showed that the amorphous NiB material was well-

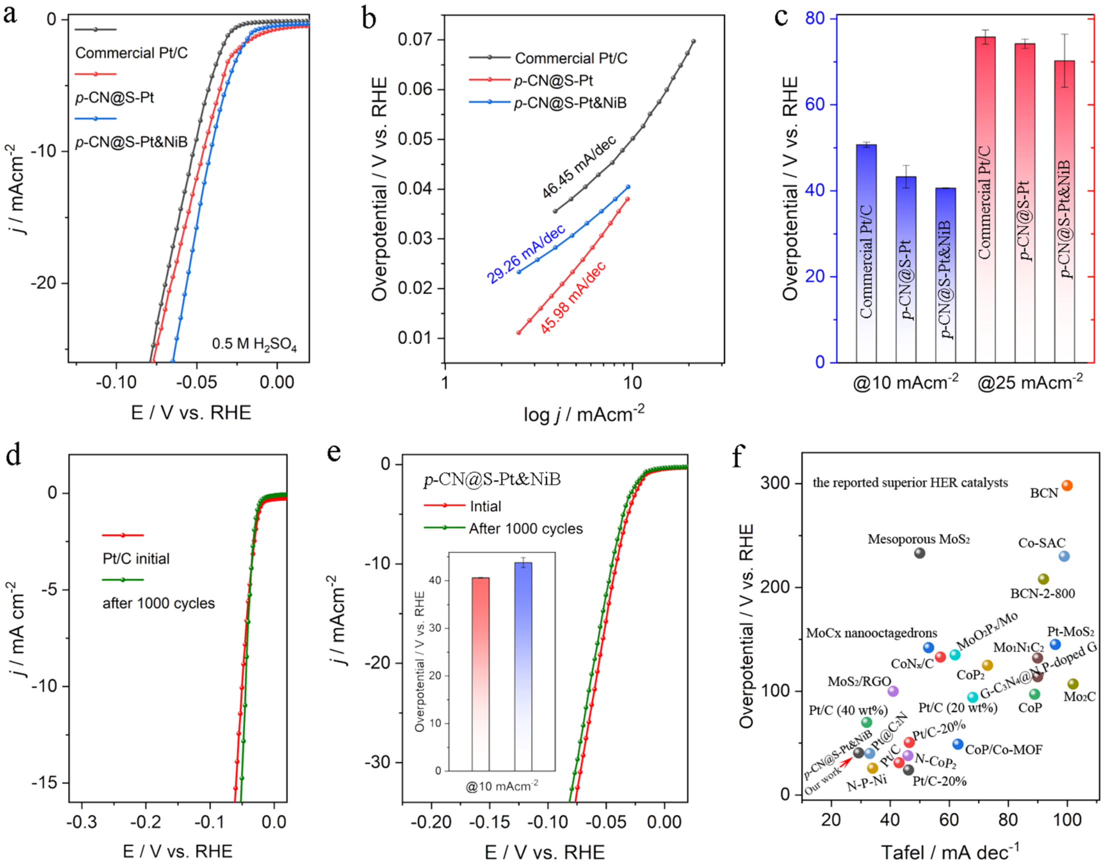

Figure 3. Electrocatalytic performance of the commercial Pt/C (20 wt % Pt), *p*-CN@S−Pt, and *p*-CN@S−Pt&NiB. (a) HER polarization curves for the three samples without IR compensation. (b) The Tafel plots for *p*-CN@S−Pt&NiB and the corresponding reference catalysts. (c) Comparison of overpotentials at 10 and 25 mA cm^{-2} of *p*-CN@S−Pt&NiB, Pt/C, and *p*-CN@S−Pt. (d) Durability test of Pt/C before and after 1000 cycles test. (e) Durability test of *p*-CN@S−Pt&NiB, the LSV curves measured before and after 1000 cycles test. The inset image in (e) is the overpotential under 10 mA cm^{-2} of *p*-CN@S−Pt&NiB before and after the stability test. (f) Comparison of overpotentials and Tafel plots for HER of other reported catalysts.

dispersed in the undulated structure and micropores. The corresponding EDS mapping images (Figure 2b−g) can also further point to the good dispersibility of the Pt, Ni, and B over the p-CN support. To further verify the applicability of this method, *p*-CN@S−Cu&NiB, *p*-CN@S−Fe&NiB, and *p*-CN@S−Pd&NiB were prepared under identical synthetic steps. The HRTEM and EDS results (Figure S13) clearly show the monodisperse metal atoms on the *p*-CN and the corresponding metal content.

The X-ray photoelectron spectroscopy (XPS) of *p*-CN@S−Pt&NiB was conducted to study the elemental composition and its chemical states. As shown in Figure S14, the *p*-CN@S−Pt&NiB is composed of Pt, Ni, B, O, C, and N. For the high-resolution C 1s spectrum, the subpeaks at 284.78, 285.58, 288.38, and 289.33 eV are associated with the C=C, C=N/C=O, C−N/C−O, and C−C=O chemical bonds, respectively.[10,26,27] In Figure S14c, the high resolution of the B 1s spectrum of the *p*-CN@S−Pt&NiB reveals the presence of Pt−B (198.53 eV) and Ni−B (200.08 eV), suggesting that part of the B atoms in *p*-CN@S−Pt&NiB hold a negative charge (δ^-).[36] The peak at the binding energy of 192.03 eV is attributed to a B−O signal, possibly from an oxidized B species during air exposure.[36] Moreover, the N 1s spectrum of the *p*-CN@S−Pt&NiB reveals the four types of nitrogen active sites—pyridinic-N (398.38 eV), pyrrolic-N (399.38 eV), graphitic-N (401.53 eV), and oxidized-N (404.63 eV).[10,17,26,27] As illustrated in Figure S14e,f, the metals (Ni and Pt) exist in *p*-CN@S−Pt&NiB as a mixture of two valence states: Ni^{2+} $2p_{3/2}$ (855.83 eV); Ni^{2+} $2p_{1/2}$ (873.58 eV); Pt^{2+} $4f_{7/2}$ (72.73 eV); Pt^{2+} $4f_{5/2}$ (75.33 eV); Ni−B (852.48 eV); and Pt−B (67.98 eV, 71.48 eV), indicating that they are positively charged (δ^+).[18,36] The coordination environment and electronic structure of *p*-CN@S−Pt&NiB were also confirmed by X-ray absorption fine spectroscopy (XAFS) measurements. The Pt L_3-edge X-ray absorption near edge structure (XANES) spectra of *p*-CN@S−Pt&NiB and Pt foil (Figure 2h) show the white line peak position of *p*-CN@S−Pt&NiB shifts to higher energy compared to that of Pt foil, and they reveal the positive valence state of Pt in *p*-CN@S−Pt&NiB, which agreed with the XPS results.[5,8,27,37] The extended XAFS (EXAFS) fitting curves at the R space of Pt foil and *p*-CN@S−Pt&NiB are shown in Figure S15 and Figure 2i. The structural parameters are summarized in Table S1. The EXAFS spectrum of the R space for *p*-CN@S−Pt&NiB exhibited a dominant Pt−N/Pt-Ni coordination (Figure 2i), indicating the surrounding atoms were adjacent to isolated Pt atoms. Compared with the fitting results of *p*-CN@S−Pt&NiB and Pt foil, the coordination numbers (CNs) of Pt−N and Pt−Ni are 4.3 and 0.6 with the corresponding band lengths of 2.02 and 2.07 Å, respectively. The resulting Pt−Ni scattering path indicates that Pt SA has a strong interaction with NiB. Additionally, a wavelet transform (WT) analysis was also used

https://doi.org/10.1021/acsnano.1c01872
ACS Nano 2021, 15, 7790−7798

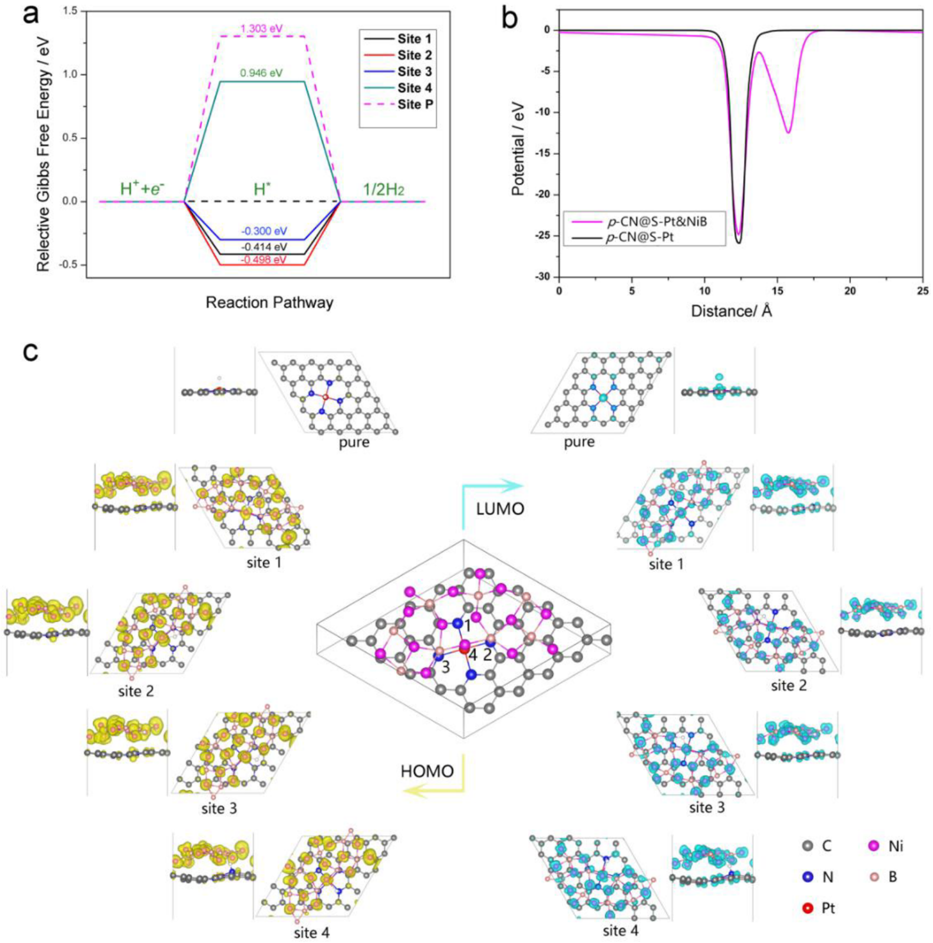

Figure 4. DFT calculations of the active sites in *p*-CN@S−Pt&NiB for HER activity. (a) HOMO and LUMO of the selected potential active sites. (b) Calculated free energy profiles of H adsorption on different positions at a potential *U* = 0 relative to the RHE at pH = 7. (c) The work function of the selected potential active sites. Site 1 is above the NiB film, sites 2 and 3 located at the side of NiB film, and site 4 is around Pt and N.

to reinforce the atomic information in both k and R spaces. The WT contour plot of *p*-CN@S−Pt&NiB (Figure 2j) exhibits the scattering peak at ∼5 $Å^{-1}$, further consolidating the argument of isolated single Pt atoms. According to the existing results, the content of Pt−N and Pt−Ni in the *p*-CN@S−Pt&NiB implies that the partially isolated Pt in *p*-CN@S−Pt&NiB is coordinated with Ni and that the other part is coordinated with N.

Electrocatalytic Properties of Such Synthesized Materials. To prove that the developed facile synthetic procedure is suitable for the preparation of highly active catalysts we compared the prepared materials in an electrocatalytic HER in an acidic electrolyte (0.5 M H_2SO_4). The polarization curves based on the linear sweep voltammetry (LSV) of these catalysts without *iR* corrections were measured. It can be seen that *p*-CN@S−Pt and *p*-CN@S−Pt&NiB gave a better HER performance than Pt/C (20 wt % Pt) with the overpotential (at 10 mA cm^{-2}) of 43.3, 40.6, and 50.7 mV, respectively. Meanwhile, *p*-CN@S−Pt&NiB showed the Tafel slope of 29.26 mV dec^{-1}, which was obviously lower than that of Pt/C (46.45 mV dec^{-1}) and *p*-CN@S−Pt (45.98 mV dec^{-1}). All the results in Figure 3a−c indicate that the *p*-CN@S−Pt&NiB showed a superior HER activity. The overpotential and Tafel slope of *p*-CN@S−Pt&NiB (40.6 mV@10 mA cm^{-2}, 29.26 mV dec^{-1}) were lower than those values for other reported superior catalysts, such as Pt-MoS_2 (145 mV@10 mA cm^{-2}, 96 mV dec^{-1}), Pt@C_2N (40 mV@10 mA cm^{-2}, 33 mV dec^{-1}), N−P−Ni (25.8 mV@10 mA cm^{-2}, 34 mV dec^{-1}), *etc.*, as shown in Figure 3f and Table S2. Besides, the stability of the catalysts was studied from LSV curves before and after 1000 cycles. The nearly identical LSV curves (Figure 3d,e) show that the *p*-CN@S−Pt&NiB has a similar stability to that of Pt/C. The durability of the Pt/C, *p*-CN@S−Pt, and *p*-CN@S−Pt&NiB were also verified by chronopotentiometric curves at the current density of 10 mA cm^{-2} (Figure S16). The *p*-CN@S−Pt&NiB showed better stability than *p*-CN@S−Pt, revealing the NiB can effectively protect the catalysts from aggregation and dissolution, thus enhancing the durability. To verify the underlying mechanism of *p*-CN@S−Pt&NiB that induced a good HER performance, we characterize the Pt/C, *p*-CN@S−Pt, and *p*-CN@S−Pt&NiB by using electrochemical impedance spectroscopy (EIS). As depicted in Figure S17, the *p*-CN@S−Pt&NiB showed a lower solution resistance than *p*-CN@S−Pt, which may be attributed to the good electrical conductivity of NiB and a large catalyst/electrolyte interface contact area.[36,38] Moreover, the low charge resistance of *p*-CN@S−Pt&NiB is also beneficial for HER.[39,40]

Theoretical Calculations. Density functional theory (DFT) calculations were performed to gain insight into the mechanism of the HER process. Four sites on the *p*-CN@S−

Pt&NiB surface, including the ones at the top of the NiB film (site 1), the ones at the side of the NiB film (sites 2 and 3), the one around Pt (site 4), and the one above the Pt of *p*-CN@S−Pt (site P), were regarded as the reaction sites for H species, enabling us to further understand the synergistic effect between *p*-CN, NiB, and Pt SAs. The hydrogen adsorption Gibbs free energy (ΔG_{*H}) of the P site in the *p*-CN@S−Pt model was calculated to be as high as 1.303 eV, indicating the unfavorable hydrogen adsorption. When interacting with NiB, the related ΔG_{*H} values are substantially decreased (Figure 4a) to promote the hydrogen adsorption and activation. Such a ΔG_{*H} decrease for the *p*-CN@S−Pt&NiB model can allow us to rationalize the enhanced HER activity with reduced overpotential. To deeply understand the mechanism and the influence of NiB, the potentials of *p*-CN@S−Pt&NiB and *p*-CN@S−Pt were also explored. From Figure 4b, it can be seen that the electrons are mainly concentrated near the CN plane with the position of ∼12.5 Å, at which the electrons have low energy levels, making the electron transfer process difficult to achieve. With the addition of NiB, a large number of electrons clearly appears at higher energy levels (at the position of ∼16 Å, where the NiB component is located). These electrons are more easily transferred to the adsorbed species, such as *H, which can quickly provide the required electrons for the electrochemical process to give a higher HER performance. To deeply explore the electron behavior, the highest occupied molecular orbital (HOMO) and lowest unoccupied molecular orbital (LUMO) for five adsorbed models were calculated, including H at sites 1−4 and pure site (P). As shown in Figure 4c, the HOMO of *p*-CN@S−Pt is located at the Pt atom, which means that Pt is the active site for providing electrons to accelerate the HER reaction.

The HOMOs of *p*-CN@S−Pt&NiB are mainly located at NiB, indicating that the electrons at NiB can come out easily and combine with H to produce H_2 under a small, external electric field. The LUMO can accept the electrons to meet the requirements of energy and electron for HER to accelerate the reactions. However, this was not observed with *p*-CN@S−Pt under the same isosurface level, suggesting the electron transfer from HOMO to LOMO at the P site is more difficult than the one on other selected sites. This conclusion can reasonably explain that the P site has a higher overpotential and the small electron charge transfer between *p*-CN@S−Pt and adsorbed *H(0.024 e) and the more electrons on H at other sites.

CONCLUSIONS

In summary, we have developed a massive single-atom synthesis process exploiting sub-nanometer pore channels in the structure of *p*-CN as nanoreactors and $C_8H_{15}N_2F_6P$ as an accelerant. To further enhance the loading amount and stability of Pt SAs, the amorphous NiB was *in situ* synthesized to coat the Pt SAs with a high Pt SA content (3.7 wt %). The *p*-CN@S−Pt&NiB displays superior HER activity in acid electrolytes. The overpotential of the *p*-CN@S−Pt&NiB at 10 mA cm^{-2} was 40.6 mV, which is better than that of the advanced commercial Pt/C. The DFT calculations confirmed that the synergistic effect of the *p*-CN-Pt and NiB-Pt made the electron transfer easier, thus accelerating the HER and lowering the overpotential. Our study reveals the predominant role of ILs and nanoreactors, which can provide a valuable guidance for the design of isolated atom catalysts for different reactions.

METHODS

Preparation of Hollow Porous Carbon Nitride (*p*-CN) Nanospheres. Author: Please verify that the changes made to improve the English still retain your original meaning.The *p*-CN was prepared according to a modified method.[41] Typically, 2 g of cetyltrimethylammonium bromide (CTAB) was dissolved in the mix solution with 100 mL of deionized water, 40 mL of ethanol, and 1.5 mL of aqueous ammonia. Then, 0.55 g of resorcinol, 0.74 mL of a 37 wt % formaldehyde solution, and 3 mL of ethyl orthosilicate (TEOS) were added into the flask step by step under magnetic stirring at 70 °C. Melamine (0.3 g) immediately added into the flask after the mixture solution became milky white and was kept for 24 h at 70 °C. Then, the solution was transferred to an autoclave for a hydrothermal reaction at 100 °C for 24 h. The obtained product was centrifuged and washed with ethanol three times. After it was dried in an oven at 100 °C, the powder was calcined at 800 °C for 3 h with the heating rate of 3 °C min^{-1} in a N_2 atmosphere. The template was etched using 2 mol L^{-1} NaOH solution by stirring at room temperature for 24 h to remove SiO_2, and the obtained black powder was washed with nitric acid/deionized water until its pH was neutral. To further remove the residual SiO_2 in the *p*-CN, the sample was soaked in concentrated hydrofluoric acid for 5 h, and the final powder was washed by deionized water several times. After they were dried, the hollow porous carbon nitride (*p*-CN) nanospheres were obtained. The dried powder was continually heated at 600 °C for a while to get clean *p*-CN for the next step.

Preparation of *p*-CN@Pt Nanoparticle with an Appropriate Amount of Single Atoms (*p*-CN@Pt). To prepare the *p*-CN@Pt complex, 20 mg of *p*-CN and 10 mg of (hydro)chloroplatinic acid ($H_2PtCl_6{\cdot}6H_2O$) were dispersed in a suitable amount of deionized water/ethanol and ultrasonicated for 30 min. Then the *p*-CN&H_2PtCl_6 complex was collected by centrifugation. Because of physical adsorption and weak bonding, part of the Pt ions in the solution would be adsorbed and fixed on the surface of the *p*-CN. After centrifugation, the precipitate was further dispersed in the aqueous solution, and then sodium borohydride ($NaBH_4$) was added to obtain *p*-CN@Pt nanoparticles mixed with an appropriate amount of single atoms.

Preparation of *p*-CN@Pt Single Atoms (*p*-CN@Pt-SAs). For the synthesis of *p*-CN-supported Pt monatomic catalysts, the *p*-CN material (20 mg) is first dispersed in the 1-butyl-3-methylimidazole hexafluorophosphate ($C_8H_{15}N_2F_6P$). Then 10 mg of $H_2PtCl_6{\cdot}6H_2O$ and a suitable amount of H_2O/ethanol is added and ultrasonicated for 40 min. The remaining experimental steps are similar to the *p*-CN@Pt.

Preparation of *p*-CN@S−Pt&NiB Catalyst. The synthesis process is similar to that of *p*-CN@Pt-SAs except for the substitution of the Pt precursor for the Pt/Ni precursor (Pt/Ni = 1:2).

Preparation of *p*-CN@S−Pd&NiB, *p*-CN@S−Cu&NiB, and *p*-CN@S−Fe&NiB Catalysts. For the synthesis of *p*-CN@S−Pd&NiB, the *p*-CN material (20 mg) is first dispersed in the 1-butyl-3-methylimidazole hexafluorophosphate ($C_8H_{15}N_2F_6P$). Then 6 mg of Na_2PdCl_4 and a suitable amount of H_2O/ethanol is added and ultrasonicated for 40 min. The remaining experimental steps are similar to those of the *p*-CN@Pt. For the synthesis of the *p*-CN@S−Cu&NiB and *p*-CN@S−Fe&NiB, 4 mg of $Cu(NO_3)_2$ and 2 mg of $Fe(NO_3)_3$ were added separately into the reaction with a similar synthesis process of *p*-CN@S−Pd&NiB to obtain *p*-CN@S−Cu&NiB and *p*-CN@S−Fe&NiB.

Structural Characterizations. Powder XRD data were obtained through an X-ray diffractometer (Rigaku SmartLab) using Cu Kα (γ = 1.541 78 A) radiation. Transmission electron microscopy (TEM), high-resolution TEM, and EDX elemental mapping were collected on a JEOL model JEM-ARM-200F microscope operated at 200 kV and an FEI Titan HRTEM microscope operated at 300 kV. The X-ray absorption spectra (XAS) were recorded at the XAS station (BL14W1) of the Shanghai Synchrotron Radiation Facility (SSRF). The Raman spectroscopy was tested by a DXR Raman microscope. The XPS was acquired on an ESCALAB 250Xi XPS system using Mg as the excitation source. The inductively coupled plasma masss pectrometry was tested by an Agilent-7900 ICP-MS system.

Electrochemical Measurements. All the electrochemical tests were recorded on an Autolab electrochemistry workstation at room temperature. All the electrochemical measurements were performed in 0.5 M H_2SO_4. The Ag/AgCl KCl-saturated CHI was used as a reference electrode, and all the potentials in the our paper were transformed to relative hydrogen electrode (RHE): $E(\text{RHE}) = E(\text{Ag/AgCl}) + 0.1976$ V. For the HER test, the graphite rod was used as a counter electrode. To prepare a suspension, the catalysts were dispersed in 1 mL of deionized water that contained 500 μL of isopropyl alcohol and 100 μL of Nafion solution (5 wt %) and sonicated for 40 min. The prepared catalyst inks of Pt/C, *p*-CN@S−Pt, and *p*-CN@S−Pt&NiB were dropped on the surface of the glassy carbon (GC) electrode with the Pt loading of 5 μg cm^{-2} for Pt/C and ~1.2 μg cm^{-2} for *p*-CN@S−Pt and *p*-CN@S−Pt&NiB. Notably, there will be some deviation when the ink is taken by pipet on the GC electrode. Before the LSV measurements, the catalysts were tested in the electrolyte by cyclic voltammetry (CV) for several cycles. All the electrochemical results are without IR correction.

Density Functional Theory Calculations. DFT calculations were performed by the Vienna *ab initio* simulation package (VASP),[42] by which the geometric structures as well as electronic properties were calculated. For all calculation jobs, the ion-electron interactions are described by the projected augmented wave (PAW) method combined with an exchange-correlation functional of Perdew−Burke−Ernzerhof (PBE) in the generalized gradient approximation.[43,44] The criteria of 10^{-5} eV in energy, 10^{-2} eV/Å in force, and 500 eV in cutoff energy were set for all numerical calculations. Additionally, to accurately describe the weak van der Waals interactions, the Grimme DFT-D3 dispersion correction method was employed.[45]

The total hydrogen evolution reaction can be written in eq 1.

$$e^- + H^+ \rightarrow {}^{1/2}H_2 \tag{1}$$

For each step, the reaction Gibbs free energy ΔG is defined by eq 2

$$\Delta G = \Delta E + \Delta \text{ZPE} - T\Delta S + \Delta G_U + \Delta G_{\text{pH}} \tag{2}$$

where ΔE is the electronic energy difference, ΔZPE is the change in zero-point energies, T is the temperature (T = 298.15 K), and ΔS is the entropy change. $\Delta G_U = -eU$, in which U is the potential related to the standard hydrogen electrode. ΔG_{pH} is the corrected Gibbs free energy of H^+ ions depending on the concentration, which can be determined as $\Delta G_{\text{pH}} = 0.059\text{pH}$, where the value of pH was set to zero. The entropy of adsorption of $^{1/2}H_2$ is $\Delta S_H \approx -\frac{1}{2}S^0{}_{H_2}$ where $S^0{}_{H_2}$ is the entropy of H_2 in the gas phase at standard conditions.

All calculations were assisted by the vaspkit code.[46]

ASSOCIATED CONTENT

Supporting Information

The Supporting Information is available free of charge at https://pubs.acs.org/doi/10.1021/acsnano.1c01872.

> SEM, XRD, Raman, BET, and TEM results of the *p*-CN. HRTEM images of the *p*-CN loaded PtNPs. EDS mapping images of the *p*-CN@Pt and *p*-CN@S−Pt. STEM images of *p*-CN@S−Pt. XPS survey pattern of *p*-CN@S−Pt&NiB. Enlarged SEM images of *p*-CN@S−Pt&NiB. HER stability test of the obtained catalysts (PDF)

AUTHOR INFORMATION

Corresponding Authors

Yang Chai − *Department of Applied Physics, The Hong Kong Polytechnic University, Kowloon, Hong Kong, People's Republic of China;* orcid.org/0000-0002-8943-0861; Email: ychai@polyu.edu.hk

Dewei Rao − *School of Materials Science and Engineering, Jiangsu University, 212013 Zhenjiang, People's Republic of China;* orcid.org/0000-0003-0410-5259; Email: dewei@ujs.edu.cn

Štěpán Kment − *Regional Centre of Advanced Technologies and Materials, Czech Advanced Technology and Research Institute, Palacký University, 779 00 Olomouc, Czech Republic; CEET, Nanotechnology Centre, Centre of Energy and Environmental Technologies, VŠB−Technical University of Ostrava, 708 00 Ostrava, Poruba, Czech Republic;* orcid.org/0000-0002-6381-5093; Email: stepan.kment@upol.cz

Authors

Yunpeng Zuo − *Department of Applied Physics, The Hong Kong Polytechnic University, Kowloon, Hong Kong, People's Republic of China;* orcid.org/0000-0002-3912-9704

Tingting Li − *Institute of Surface Micro and Nano Materials, Xuchang University, 461002 Xuchang, Henan, People's Republic of China*

Ning Zhang − *Department of Applied Physics, The Hong Kong Polytechnic University, Kowloon, Hong Kong, People's Republic of China;* orcid.org/0000-0002-0755-1708

Tianyun Jing − *School of Materials Science and Engineering, Jiangsu University, 212013 Zhenjiang, People's Republic of China*

Patrik Schmuki − *Department of Materials Science, University of Erlangen-Nuremberg, Institute for Surface Science and Corrosion WW4-LKO, D-91058 Erlangen, Germany; Regional Centre of Advanced Technologies and Materials, Czech Advanced Technology and Research Institute, Palacký University, 779 00 Olomouc, Czech Republic*

Radek Zbořil − *Regional Centre of Advanced Technologies and Materials, Czech Advanced Technology and Research Institute, Palacký University, 779 00 Olomouc, Czech Republic; CEET, Nanotechnology Centre, Centre of Energy and Environmental Technologies, VŠB−Technical University of Ostrava, 708 00 Ostrava, Poruba, Czech Republic;* orcid.org/0000-0002-3147-2196

Complete contact information is available at: https://pubs.acs.org/10.1021/acsnano.1c01872

Notes

The authors declare no competing financial interest.

ACKNOWLEDGMENTS

This research was funded by the Hong Kong Polytechnic University (Grant No. W144), Operational Programme Research, Development and Education—European Regional Development Fund, Project No. CZ.02.1.01/0.0/0.0/15_003/0000416 of the Ministry of Education, Youth and Sports of the Czech Republic. This work was also supported by the National Natural Science Foundation of China (Nos. 51801075 and 51902281). Theoretical work was carried out at LvLiang Cloud Computing Center of China, and the calculations were performed on TianHe-2.

REFERENCES

(1) Roger, I.; Shipman, M.-A.; Symes, M.-D. Earth-Abundant Catalysts for Electrochemical and Photoelectrochemical Water Splitting. *Nat. Rev. Chem.* **2017**, *1*, 0003.

(2) Wei, H.; Huang, K.; Wang, D.; Zhang, R.; Ge, B.; Ma, J.; Wen, B.; Zhang, S.; Li, Q.; Lei, M.; Zhang, C.; Irawan, J.; Liu, L.; Wu, H.

Iced Photochemical Reduction to Synthesize Atomically Dispersed Metals by Suppressing Nanocrystal Growth. *Nat. Commun.* **2017**, *8*, 1490.

(3) Jiao, Y.; Zheng, Y.; Davey, K.; Qiao, S.-Z. Activity Origin and Catalyst Design Principles for Electrocatalytic Hydrogen Evolution on Heteroatom-Doped Graphene. *Nat. Energy* **2016**, *1*, 16130.

(4) Wang, A.; Li, J.; Zhang, T. Heterogeneous Single-Atom Catalysis. *Nat. Rev. Chem.* **2018**, *2*, 65−81.

(5) Huang, K.; Zhang, L.; Xu, T.; Wei, H.; Zhang, R.; Zhang, X.; Ge, B.; Lei, M.; Ma, J.; Liu, L.; Wu, H. −60 °C Solution Synthesis of Atomically Dispersed Cobalt Electrocatalyst with Superior Performance. *Nat. Commun.* **2019**, *10*, 606.

(6) Yao, Y.; Huang, Z.; Xie, P.; Wu, L.; Ma, L.; Li, T.; Pang, Z.; Jiao, M.; Liang, Z.; Gao, J.; He, Y.; Kline, D. J.; Zachariah, M. R.; Wang, C.; Lu, J.; Wu, T.; Li, T.; Wang, C.; Shahbazian-Yassar, R.; Hu, L. High Temperature Shockwave Stabilized Single Atoms. *Nat. Nanotechnol.* **2019**, *14*, 851−857.

(7) Wei, S. J.; Li, A.; Liu, J. C.; Li, Z.; Chen, W. X.; Gong, Y.; Zhang, Q. H.; Cheong, W. C.; Wang, Y.; Zheng, L. R.; Xiao, H.; Chen, C.; Wang, D. S.; Peng, Q.; Gu, L.; Han, X. D.; Li, J.; Li, Y. Direct Observation of Noble Metal Nanoparticles Transforming to Thermally Stable Single Atoms. *Nat. Nanotechnol.* **2018**, *13*, 856−861.

(8) Zhang, L.; Doyle-Davis, K.; Sun, X. Pt-Based Electrocatalysts with High Atom Utilization Efficiency: From Nanostructures to Single Atoms. *Energy Environ. Sci.* **2019**, *12*, 492−517.

(9) Jiao, L.; Jiang, H. Metal-Organic-Framework-Based Single-Atom Catalysts for Energy Applications. *Chem.* **2019**, *5*, 1−19.

(10) Chen, Y.; Ji, S.; Zhao, S.; Chen, W.; Dong, J.; Cheong, W.-C.; Shen, R.; Wen, X.; Zheng, L.; Rykov, A. I.; Cai, S.; Tang, H.; Zhuang, Z.; Chen, C.; Peng, Q.; Wang, D.; Li, Y. Enhanced Oxygen Reduction with Single-Atomic-Site Iron Catalysts For a Zinc-Air Battery and Hydrogen Air Fuel Cell. *Nat. Commun.* **2018**, *9*, 5422.

(11) Zhao, D.; Chen, Z.; Yang, W.; Liu, S.; Zhang, X.; Yu, Y.; Cheong, W.-C.; Zheng, L.; Ren, F.; Ying, G.; Cao, X.; Wang, D.; Peng, Q.; Wang, G.; Chen, C. MXene (Ti_3C_2) Vacancy-Confined Single-Atom Catalyst for Efficient Functionalization of CO_2. *J. Am. Chem. Soc.* **2019**, *141*, 4086−4093.

(12) Zhu, Y.; Sun, W.; Luo, J.; Chen, W.; Cao, T.; Zheng, L.; Dong, J.; Zhang, J.; Zhang, M.; Han, Y.; Chen, C.; Peng, Q.; Wang, D.; Li, Y. A Cocoon Silk Chemistry Strategy to Ultrathin N-Doped Carbon Nanosheet with Metal Single-Site Catalysts. *Nat. Commun.* **2018**, *9*, 3861.

(13) Hossain, M. D.; Liu, Z.; Zhuang, M.; Yan, X.; Xu, G.; Gadre, C. A.; Tyagi, A.; Abidi, I. H.; Sun, C.; Wong, H.; Guda, A.; Hao, Y.; Pan, X.; Amine, K.; Luo, Z. Rational Design of Graphene-Supported Single Atom Catalysts for Hydrogen Evolution Reaction. *Adv. Energy Mater.* **2019**, *9*, 1803689.

(14) Wei, H.; Liu, X. Y.; Wang, A.; Zhang, L.; Qiao, B. T.; Yang, Y. F.; Huang, Y. Q.; Miao, S.; Liu, J.; Zhang, T. FeO_x-Supported Platinum Single-Atom and Pseudo-Single-Atom Catalysts for Chemoselective Hydrogenation of Functionalized Nitroarenes. *Nat. Commun.* **2014**, *5*, 5634.

(15) Jibril, L.; Chen, P.; Hu, J.; Odom, T.; Mirkin, C.−A. Massively Parallel Nanoparticle Synthesis in Anisotropic Nanoreactors. *ACS Nano* **2019**, *13*, 12408−12414.

(16) Li, Y.; Wang, H.; Xie, L.; Liang, Y.; Hong, G.; Dai, H. MoS_2 Nanoparticles Grown on Graphene: An Advanced Catalyst for the Hydrogen Evolution Reaction. *J. Am. Chem. Soc.* **2011**, *133*, 7296−7299.

(17) Chen, W.; Pei, J.; He, C. T.; Wan, J.; Ren, H.; Zhu, Y.; Wang, Y.; Dong, J.; Tian, S.; Cheong, W. C.; Lu, S.; Zheng, L.; Zheng, X.; Yan, W.; Zhuang, Z.; Chen, C.; Peng, Q.; Wang, D.; Li, Y. Rational Design of Single Molybdenum Atoms Anchored on N-Doped Carbon for Effective Hydrogen Evolution Reaction. *Angew. Chem., Int. Ed.* **2017**, *56*, 16086−16090.

(18) Jin, H.; Liu, X.; Chen, S.; Vasileff, A.; Li, L.; Jiao, Y.; Song, L.; Zheng, Y.; Qiao, S.-Z. Heteroatom-Doped Transition Metal Electrocatalysts for Hydrogen Evolution Reaction. *ACS Energy Lett.* **2019**, *4*, 805−810.

(19) Zhou, Y.; Che, F.; Liu, M.; Zou, C.; Liang, Z.; De Luna, P.; Yuan, H.; Li, J.; Wang, Z.; Xie, H.; Li, H.; Chen, P.; Bladt, E.; Quintero-Bermudez, R.; Sham, T. K.; Bals, S.; Hofkens, J.; Sinton, D.; Chen, G.; Sargent, E. H. Dopant-Induced Electron Localization Drives CO_2 Reduction to C_2 Hydrocarbons. *Nat. Chem.* **2018**, *10*, 974−980.

(20) Liu, T.; Li, P.; Yao, N.; Cheng, G.; Chen, S.; Luo, W.; Yin, Y. CoP-Doped MOF-Based Electrocatalyst for pH-Universal Hydrogen Evolution Reaction. *Angew. Chem., Int. Ed.* **2019**, *58*, 4679−4684.

(21) Dupont, J.; Scholten, J.-D. On the Structural and Surface Properties of Transition-Metal Nanoparticles in Ionic Liquids. *Chem. Soc. Rev.* **2010**, *39*, 1780−1804.

(22) Zhang, H.; Cui, H. Synthesis and Characterization of Functionalized Ionic Liquid-Stabilized Metal (Gold and Platinum) Nanoparticles and Metal Nanoparticle/Carbon Nanotube Hybrids. *Langmuir* **2009**, *25*, 2604−2612.

(23) Pensado, A.-S.; Pádua, A. Solvation and Stabilization of Metallic Nanoparticles in Ionic Liquids. *Angew. Chem., Int. Ed.* **2011**, *50*, 8683−8687.

(24) Chun, Y.; Shin, J.; Song, C.; Lee, S. Palladium Nanoparticles Supported Onto Ionic Carbon Nanotubes as Robust Recyclable Catalysts in an Ionic Liquid. *Chem. Commun.* **2008**, *8*, 942−944.

(25) Rodenbücher, C.; Wippermann, K.; Korte, C. Atomic Force Spectroscopy on Ionic Liquids. *Appl. Sci.* **2019**, *9*, 2207.

(26) Ding, S.; Guo, Y.; Hulsey, M. J.; Zhang, B.; Asakura, H.; Liu, L.; Han, Y.; Gao, M.; Hasegawa, J.-y.; Qiao, B.; Zhang, T.; Yan, N. Electrostatic Stabilization of Single-Atom Catalysts by Ionic Liquids. *Chem.* **2019**, *5*, 1−13.

(27) Zheng, T.; Jiang, K.; Ta, N.; Hu, Y.; Zeng, J.; Liu, J.; Wang, H. Large-Scale and Highly Selective CO_2 Electrocatalytic Reduction on Nickel Single-Atom Catalyst. *Joule* **2019**, *3*, 265−278.

(28) Han, A.; Chen, W.; Zhang, S.; Zhang, M.; Han, Y.; Zhang, J.; Ji, S.; Zheng, L.; Wang, Y.; Gu, L.; Chen, C.; Peng, Q.; Wang, D.; Li, Y. A Polymer Encapsulation Strategy to Synthesize Porous Nitrogen-Doped Carbon-Nanosphere-Supported Metal Isolated-Single-Atomic-Site Catalysts. *Adv. Mater.* **2018**, *30*, 1706508.

(29) Hülsey, M.; Zhang, J.; Yan, N. Harnessing the Wisdom in Colloidal Chemistry to Make Stable Single-Atom Catalysts. *Adv. Mater.* **2018**, *30*, 1802304.

(30) Zhu, C.; Fu, S.; Shi, Q.; Du, D.; Lin, Y. Single-Atom Electrocatalysts. *Angew. Chem., Int. Ed.* **2017**, *56*, 13944−13960.

(31) Zou, X.; Zhang, Y. Noble Metal-Free Hydrogen Evolution Catalysts for Water Splitting. *Chem. Soc. Rev.* **2015**, *44*, 5148−5180.

(32) Wang, J.; Xu, F.; Jin, H.; Chen, Y.; Wang, Y. Non-Noble Metal-Based Carbon Composites in Hydrogen Evolution Reaction: Fundamentals to Applications. *Adv. Mater.* **2017**, *29*, 1605838.

(33) Fina, F.; Callear, S.; Carins, G.; Irvine, J. Structural Investigation of Graphitic Carbon Nitride *via* XRD and Neutron Diffraction. *Chem. Mater.* **2015**, *27*, 2612−2618.

(34) Zhang, C. H.; Sha, J. W.; Fei, H. L.; Liu, M. J.; Yazdi, S.; Zhang, J. B.; Zhong, Q. F.; Zou, X. L.; Zhao, N. Q.; Yu, H. S.; Jiang, Z.; Ringe, E.; Yakobson, B. I.; Dong, J. C.; Chen, D. L.; Tour, J. M. Single-Atomic Ruthenium Catalytic Sites on Nitrogen-Doped Graphene for Oxygen Reduction Reaction in Acidic Medium. *ACS Nano* **2017**, *11*, 6930−6941.

(35) Ozkan, C.; Ozkan, U. *Handbook of Graphene, Vol. 5: Energy, Healthcare, and Environmental Applications;* Scrivener Publishing LLC, Wiley: Beverly, MA, 2019.

(36) Zuo, Y.; Rao, D.; Ma, S.; Li, T.; Tsang, Y.; Kment, S.; Chai, Y. Valence Engineering *via* Dual-Cation and Boron Doping in Pyrite Selenide for Highly Efficient Oxygen Evolution. *ACS Nano* **2019**, *13*, 11469−11476.

(37) Choy, J.-H.; Kim, D.-K.; Hwang, S.-H.; Demazeau, G.; Jung, D.-K. XANES and EXAFS Studies on the Ir—O Bond Covalency in Ionic Iridium Perovskites. *J. Am. Chem. Soc.* **1995**, *117*, 8557−8566.

(38) Li, T.; Zhu, C.; Yang, X.; Gao, Y.; He, W.; Yue, H.; Zhao, H. Co_3O_4 Nanoneedle@Electroactive Nickel Boride Membrane Core/Shell Arrays: A Novel Hybrid for Enhanced Capacity. *Electrochim. Acta* **2017**, *246*, 226−233.

(39) Tang, C.; Zhang, R.; Lu, W.; He, L.; Jiang, X.; Asiri, A. M.; Sun, X. Fe-Doped CoP Nanoarray: A Monolithic Multifunctional Catalyst for Highly Efficient Hydrogen Generation. *Adv. Mater.* **2017**, *29*, 1602441.

(40) Xie, Y.; Cai, J.; Wu, Y.; Zang, Y.; Zheng, X.; Ye, J.; Cui, P.; Niu, S.; Liu, Y.; Zhu, J.; Liu, X.; Wang, G.; Qian, Y. Boosting Water Dissociation Kinetics on Pt−Ni Nanowires by N-Induced Orbital Tuning. *Adv. Mater.* **2019**, *31*, 1807780.

(41) Shu, C.; Song, B.; Wei, X.; Liu, Y.; Tan, Q.; Chong, S.; Chen, Y.; Yang, X.-D.; Yang, W.-H.; Liu, Y. Mesoporous 3D Nitrogen-Doped Yolk-Shelled Carbon Spheres For Direct Methanol Fuel Cells with Polymer Fiber Membranes. *Carbon* **2018**, *129*, 613−620.

(42) Kresse, G.; Furthmuller, J. Efficient Iterative Schemes for *Ab Initio* Total-Energy Calculations Using a Plane-Wave Basis Set. *Phys. Rev. B: Condens. Matter Mater. Phys.* **1996**, *54*, 11169−11186.

(43) Blöchl, P.-E. Projector Augmented-Wave Method. *Phys. Rev. B: Condens. Matter Mater. Phys.* **1994**, *50*, 17953−17979.

(44) Kresse, G.; Joubert, D. From Ultrasoft Pseudopotentials to the Projector Augmented-Wave Method. *Phys. Rev. B: Condens. Matter Mater. Phys.* **1999**, *59*, 1758−1775.

(45) Grimme, S.; Antony, J.; Ehrlich, S.; Krieg, H. A Consistent and Accurate *Ab Initio* Parametrization of Density Functional Dispersion Correction (Dft-d) for the 94 Elements H-Pu. *J. Chem. Phys.* **2010**, *132*, 154104.

(46) Wang, V.; Xu, N.; Liu, J.; Tang, G.; Geng, W. Vaspkit: A User-Friendly Interface Facilitating High-Throughput Computing and Analysis Using Vasp Code. 2019, *arXiv*:1908.08269. e-Print archive. https://arxiv.org/abs/1908.08269 (accessed 2020-02-22).

https://doi.org/10.1021/acsnano.1c01872

APPENDIX Ⅳ

Self–reconstruction mediates isolated Pt tailored nanoframes for highly efficient catalysis

Yunpeng Zuo, Tianyun Jing, Tingting
Li, Štep̌án Kment

InfoSummit–International Conference on Information Technology Materials
In: Part 2: “Material Information
for Energy Conversion”.

Chengdu, China 2021

Palacký University Olomouc   Regional Centre of Advanced Technologies and Materials

Self-reconstruction mediate isolated Pt tailored nanoframes for highly efficient catalysis

Yunpeng Zuo, Tianyun Jing, Tingting Li, Štěpán Kment

Introduction

☆ Surface reconstruction of nanocatalysts is an inevitable process during heterogeneous catalysis, resulting in dynamic changes of active sites.

☆ It remains a grand challenge to identify the evolution of active sites due to the small size and complex surrounding systems.

☆ Ethylene glycol (EG) has great potential for alcohol fuel cells, due to its better security and higher energy density.

☆ Hydroxyl group in EG can act as capping agent for promoting morphologic change.

☆ The mismatch between the surface free energy and Gibbs free energy may drive the structure reconstruction of the catalysts during catalysis

Results

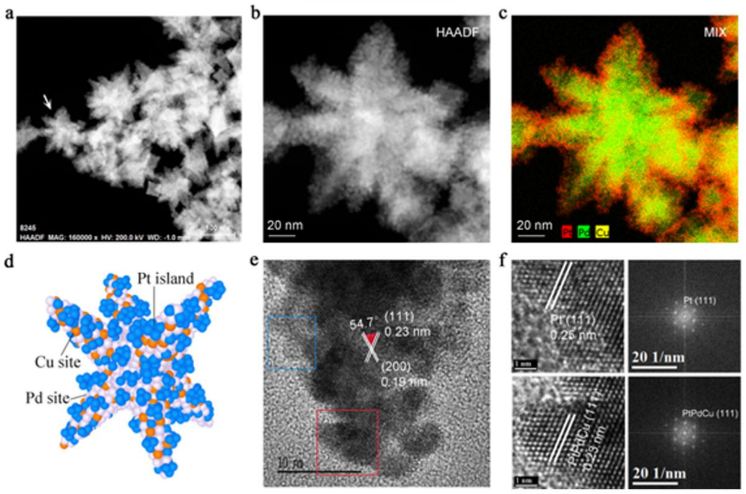

Figure 1. a) HAADF-STEM image of h-PdCu&Pt and b) the enlarged typical single h-PdCu&Pt marked by the white arrow in a). c) The corresponding EDS elemental mapping image. d) Illustration of the atomic model for h-PdCu&Pt. e) The representative HRTEM image for h-PdCu&Pt. f) HRTEM images and FFT patterns are consistent with selected area in the blue and red squares inserted in e).

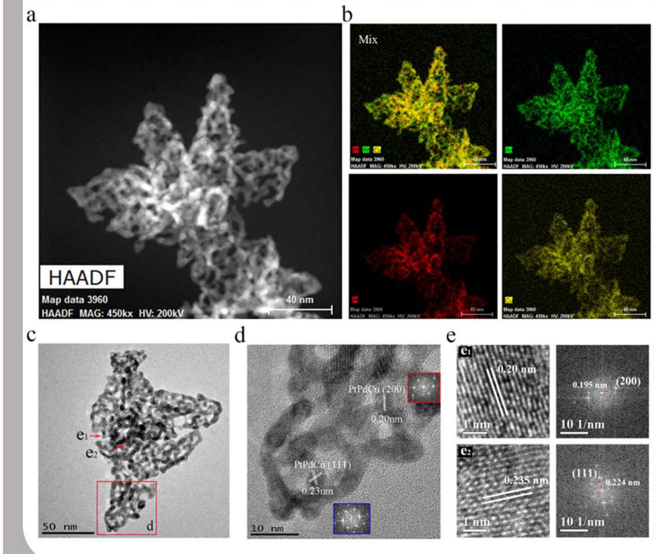

Fig.2 (a,b) STEM and EDS mapping images of the SAPt-PdCu NF. c) HRTEM images for SAPt-PdCu NF d) HRTEM image selected by red square in d), and the corresponding FFT patterns from the marked area of lattice spacing e) The magnified HRTEM images and corresponding FFT patterns of the selected area in c) indicated by the arrows.

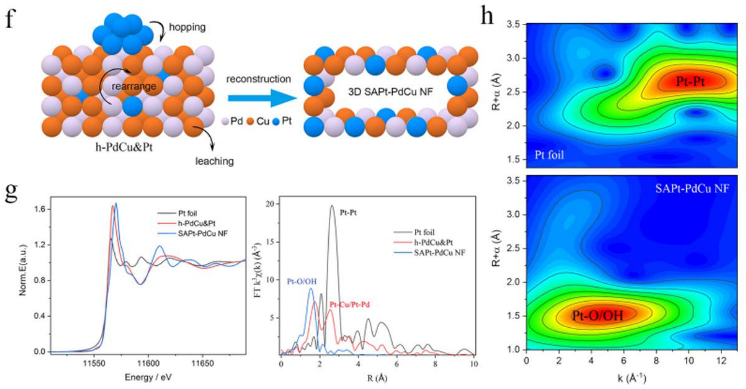

Fig 3. f) Schematic diagram of structural evolution from h-PdCu&Pt to SAPt-PdCu NF. g) XANES curves and FT-EXAFS curves of the Pt foil, h-PdCu&Pt and SAPt-PdCu NF at Pt L3 edge. h) WT-EXAFS of Pt foil and SAPt-PdCu NF.

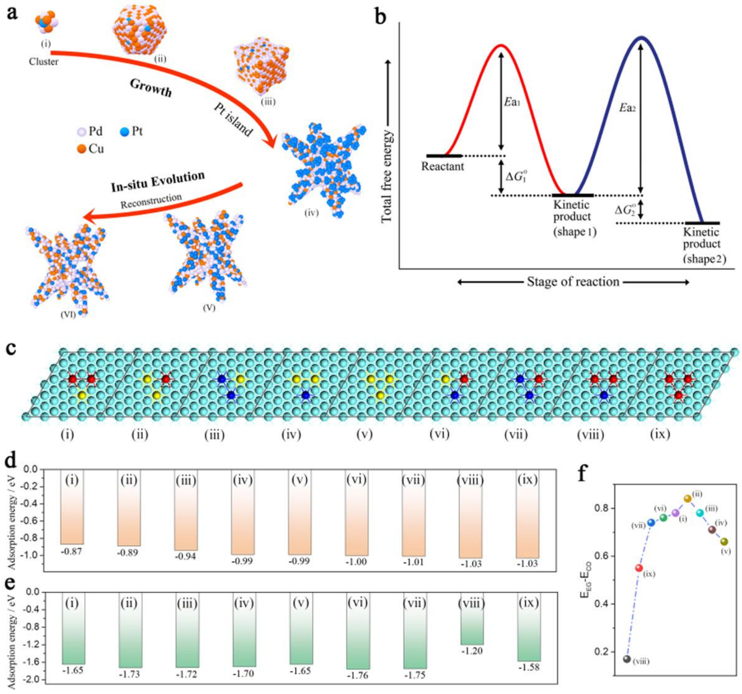

Fig. 4. a) Schematic illustrations of the formation process from h-PdCu&Pt to SAPt-PdCu NF. b) the total free energy of the Pt-based catalyst at different reaction stages. c) the models of SAPt-PdCu surfaces, and triangles are (i) PtCu$_2$, (ii) Pt$_2$Cu, (iii) PtPd$_2$, (iv) Pt$_2$Pd, (v) Pt$_3$, (vi) PtCuPd, (vii) CuPd$_2$, (viii) Cu$_2$Pd, (ix) Cu$_3$. d) the adsorption energy (unit: eV) of C$_2$H$_4$(OH)$_2$ on models of c). e) the adsorption energy (unit: eV) of CO on models of c). f) the difference of EEG-ECO of the models. Navy balls, Pd; Blue balls, Pd; red balls, Cu; yellow balls, Pt; gray balls, C; white balls, H; green balls, O.

Conclusion

☆ The mismatch between the surface free energy and Gibbs free energy drives the structure reconstruction from h-PdCu&Pt to single Pt active sites tailored PdPtCu nanoframes (SAPt-PdCu NF) during catalysis

☆ This discovery promotes the recognition of active sites and facilitate the design of stable catalysts with high activity for heterogeneous catalysis

Reference

1. Yunpeng Zuo, et al. *Adv. Mater.* 2018, 30, 1074171.
2. Yunpeng Zuo, et al. *J. Mater. Chem. A*, 2021, doi.org/10.1039/D1TA05411B

Department of Physical Chemistry
Faculty of Science
PALACKY UNIVERSITY, OLOMOUC

Pyrite type transition metal dichalcogenides for oxygen evolution

Doctoral dissertation

By

Yunpeng Zuo, MSc

Under
Study program: Chemistry, P1417
Field of study: Nanomaterial Chemistry, 1407V023

Supervisor: Ing. Kment Štěpán, PhD.

Olomouc 2022

Ph.D. thesis was carried out at the Department of Physical Chemistry, Faculty of Science, Palacký University Olomouc, in 2022.

Candidate: **M.Sc. Yunpeng Zuo**

Supervisor: **Ing. Kment Štěpán, Ph.D.**

Reviewers: ....

....

....

....

The evaluation of the Ph.D. thesis was written by ....

....

The summary of the Ph.D. thesis was sent for distribution on ....

The oral defence will take place on .... in front of the commission for the Ph.D. study of the program Chemistry in ....

The Ph.D. thesis is available in the Library of the Physical Chemistry department of the Faculty of Science of Palacký University Olomouc, Šlechtitelů 31, Olomouc-Holice.

Content

1. Introduction

Environmental problems based on the combustion of fossil fuel are the great challenges for the sustainable development of society that humans have to face for the next decades.[1,2] Developing a green pathway to replace fossil fuel and reducing the hazardous gases emission can effectively improve the existing problems.[3,4] Although the development and application of renewable energy, such as wind, tidal, solar, has been stimulating for a long time, the low energy delivery efficiency limited the large–scale application of sustainable energy.[5–8] Apart from the development of advanced energy conversion devices, converting renewable energy into chemical energy will be more conducive to the commercial application of sustainable energy. As the typical green energy source with the highest gravimetric energy, hydrogen is the ideal sustainable gas to replace fossil fuels in various industries.[9,10] Currently, electrocatalytic water splitting is an implementable method for hydrogen generation, and this electrolytic process has been widely studied that contains two half–reactions oxygen evolution reaction (OER) and hydrogen evolution reaction (HER).[11–13] Concerning HER and OER, the OER process undergoes four–electron−proton to form one O_2 molecular, which requires a large overpotential ($\eta \approx 1.23$ V vs standard reduction potential) for the whole water−splitting reaction. Thus, the OER is regarded as the rate–limiting step of electrocatalytic water splitting, compared to HER. Based on this mentioned reason, enormous studies devoted to the development of highly effective OER catalysts to relieve the sluggish kinetics and increase the energy conversion efficiency.[14,15] However, at present, the water−splitting reaction, especially the OER, still suffers from low efficiency and insufficient stability to meet the requirement of the practical application. So it is particularly important to develop highly active HER/OER catalysts.[16, 17]

A large number of researchers discovered the pH of the electrolyte is strongly related to the mechanism of OER. In an acidic solution, OER proceeds in four steps shown in the equations.[18,19] In an acidic environment, H_2O will form OH^* on the surface of the active sites (Equation 1), then further interact with water molecules to produce O^* and OOH^* intermediates (Equation 2 or Equation 3).[20,21] Different from the acid solution, OH^* will generate from the OH^- instead of H_2O in an alkaline environment (Equation 5–7).[22] Finally the oxygen gas will generate based on the OOH^* intermediates (Equation 4 and 8). It is worth noting that the $OH^* \rightarrow O^*$ and $O^* \rightarrow OOH^*$ processes are the rate–limiting steps with a higher energy barrier value of 3.2 eV.[20,21] Thus, if the catalysts can effectively reduce the energy barrier of these steps, they will be the advantageous candidates for the superior OER. To date, most of the commercial catalysts of OER are noble metal oxides (e.g., IrO_2, RuO_2), possessing small reserves, high cost, and challenging large–scale application.[20, 23]

In an acidic system,

$2H_2O \rightarrow OH^* + H_2O + H^+ + e^-$ (1)

$OH^* + H_2O \rightarrow O^* + H^+ + H_2O + e^-$ (2)

$O^* + H_2O \rightarrow OOH^* + H^+ + e^-$ (3)

$OOH^* \rightarrow O_2 + H^+ + e^-$ (4)

In an alkaline system,

$4OH^- \rightarrow OH^* + 3OH^- + e^-$ (1)

$OH^* + 3OH^- \rightarrow O^* + 2OH^- + H_2O + e^-$ (2)

$O^* + 2OH^- + H_2O \rightarrow OOH^* + OH^- + H_2O + e^-$ (3)

$OOH^* + OH^- + H_2O \rightarrow O_2 + 2H_2O + e^-$ (4)

* denotes the surface adsorption sites

Pyrite–type transition metal dichalcogenides (PT–TMDs) have emerged as one of the most valuable candidates for the highly effective OER catalysts.[24,25] It is worth noting that the PT–TMDs nanomaterials have special physical properties covered from conductor, semiconductor, and insulator, with a wide range of applications.[26,27,28] The PT–TMDs display a crystal system of isometric with the octahedral coordination which contains cations and dianion units.[25, 29] The intrinsic electronic configuration of the PT–TMDs nanocatalysts are favorable for the OER application, but the catalytic performance still suffers from the unstable surface composition (easy to be oxidized) and sluggish charge transfer.[30,31]

Valence engineering has been adopted as the regular strategy and easily implemented approach to alleviating the shortcomings. Especially, the 3d heteroatoms doping or alloying in the PT–TMDs can effectively modify its electronic modulation to be suitable for the OER process.[32–33] Considerable polymetal pyrites were developed as substantial materials during the past decades for the enhanced OER catalysts relative to the monometal sulfides.[34–36] As the most common PT–TMDs, the pyrite sulfides, and selenides with 3d transition metal atoms doping have been widely reported in OER application. V–doped pyrite NiS_2 nanosheets have been synthesized by the simple chemical method, and the physical property of this material changed from representative semiconductor to conductive material, which exhibited superior OER performance.[37] Similarly, the Fe–dopant mediated novel pyrite NiS_2 mesocrystals presented a boosted OER activity with an overpotential from 351 mV to 252 mV vs. RHE at 10 $mAcm^{-2}$ in alkaline solution.[38]

Additionally, non–metallic atom doping in the PT–TMDs can attract the electrons of the metal sites in the material, forming the high valence sites which would facilitate the adsorption of O–containing intermediates, thus improving catalytic activity.[39,40] Moreover, the structural stability of the PT–TMDs could be further modified by coating a carbon layer or amorphous membrane.[41,42] It had discovered the B–doping in the PT–TMDs significantly changed the d orbital electronic configuration of the transition metals science the electronic hybridized between the metal d orbitals and B 2p orbitals, resulting in the delocalization of the electrons on active sites.[43] This special electronic configuration was beneficial for OER process, especially the intermediate steps. As another big challenge, the dissolution of surface cations and oxidation of external species of PT–TMDs during the OER seriously affect the structural stability of the material. So it is very important to develop some methods or strategies to fabricate a stable surface structure for remarkable catalytic durability. Coating the PT–TMDs with the conductive active layers, such as amorphous borides and carbon membrane, could effectively prevent the ripening or aggregation of the material, and finally enhance the stability and activity of PT–TMDs. Tingting Li et al. successfully prepared the Co_3O_4 nanoneedle arrays supported on the Ni foam (NF@Co_3O_4).[44] Next, the NF@Co_3O_4 was covered by the Ni–B membrane to generate core–shell hybrid. Benefiting from the special interface interaction, NF@Co_3O_4@NiB presented excellent electrochemical performance. In addition, Jingwei Chen and co–workers synthesized the Co_xFe_yS@C compound with a thin carbon layer on the surface based on the prussian blue precursor.[41] The coated carbon layer effectively promotes the energy storage capacity of the Co_xFe_yS@C material. Thus developing more appropriate synthesis approaches for novel PT–TMDs could effectively expand the application in electrocatalysis.

2. Aims of the thesis

The principal goal of this thesis is to establish a facile method for control synthesis of pyrite–type transition metal dichalcogenides as effective catalysts for OER. Particular aims are as follows:

2.1 Synthesis of boron–doped ternary pyrite–type sulfide coated by amorphous boride

The first aim of the thesis is to design pyrite type sulfides as highly active catalysts for OER application. Our previous results found that amorphous polymetallic borides could be efficiently synthesized by liquid–phase–reduction. Moreover, the amorphous polymetallic borides could be scaled up according to the demand. We applied a two–step method, liquid–phase reduction and high–temperature reaction, to fabricate the boron–doped ternary pyrite–type sulfide catalyst. Various characterization instruments and computational simulations were used to analyze the structure of materials and elemental valence analysis. The obtained materials were subjected to OER testing under alkaline conditions.

2.2 Preparation of boron–doped ternary pyrite selenide

Numerous studies had shown that selenides could effectively promote the OER reaction. Meanwhile, valence–engineering could adjust the local electronic structure of the catalysts, further improving their activity and stability. Combining the synthesized amorphous polymetallic borides, we adopted a high–temperature gasification–strategy to synthesize polymetallic selenide. Polymetallic could effectively optimize the electronic structure, due to the difference in atomic radius. In addition, boron doping could also improve the electronic properties of selenides, as the electron-deficient properties. AC–TEM and DFT+U were used to analyze the atomic structure of the pyrite–type selenide.

3. Experimental part – Materials and methods

3.1 Experimental section

3.1.1 Chemicals

Cobalt nitrate ($Co(NO_3)_2·6H_2O$), Nickel nitrate ($Ni(NO_3)_2·6H_2O$), Anhydrous iron chloride ($FeCl_3·6H_2O$), Sodium borohydride ($NaBH_4$), Selenium powder, Sulfur powder were purchased from Sigma–Aldrich. The potassium hydroxide (KOH) and ethanol (absolute) were purchased from Penta. The distilled water (DIW, 18.2 MU) was the solvent for synthesis. All reagents were used without further purification.

3.1.2 Synthesis of pyrite–type B–FeCoNiS$_x$ crystal coated by amorphous FeCoNiB$_x$

A typical redox reaction was used to synthesize a series of amorphous borides (NiB, CoNiB, FeNiB and FeCoNiB). For the synthesis, 0.16 g $Co(NO_3)_2·6H_2O$, 0.29 g $FeCl_3·6H_2O$, and 1.16g $Ni(NO_3)_2·6H_2O$ were added in a reaction flask and dissolved in DI water. After excess $NaBH_4$ solution was added into the flask, a large amount of black precipitation would generate. The precipitation was successively washed with DI water and ethanol to remove the reactants. Then the black precipitation was dried under 60 ℃ for overnight to obtain the black powder of the amorphous borides. Afterward, 0.48 g FeCoNiB and 0.4 g S powder were mixed and added into a quartz boat and transferred to a tube furnace. The mixture was heated to 400 ℃ (heating rate of 5 ℃/min) and reacted for 120 min under N_2 flow. After cooled to room temperature, boron–doped ternary pyrite type sulfide coated by amorphous boride was formed. Similarly, the boron–doped Ni, CoNi and FeNi–based sulfides were synthesized by the same reaction conditions but with the corresponding precursors.

3.1.3 Synthesis of pyrite–type FeCoNiSeB$_x$ catalyst

A two simple steps method was applied to synthesize the series of boron–doped selenides. Similar to the fabrication of sulfides, amorphous borides need to be synthesized in advance. Firstly, the amorphous NiB, FeNiB, CoNiB, FeCoNiB precursors were prepared by the wet chemical approach. 1 mmol amount of $Co(NO_3)_2$, $Ni(NO_3)_2$, and $FeCl_3$ was dissolved in DI water. Subsequently, a moderate amount of $NaBH_4$ solution was added into the mixture of the metal ions solution to generate the black amorphous boride. After repeated washing to remove the reactants, the as–prepared materials dried at 60 °C in an oven overnight. The obtained FeCoNiB and Se powder were placed in the quartz boat with the selenium located on the upstream side. Subsequently, the quartz boat was heated at 450 °C for 2 h under the Ar flow and finally cooled to room temperature to obtain $Fe_5Co_4Ni_{20}Se_{36}B_x$ powder. Similarly, the $NiSe_2B_x$, $FeNi_3Se_8B_x$, and $CoNi_3Se_8B_x$ catalysts were prepared under similar reaction conditions.

3.2 Structural characterizations

The transmission electron microscopy images (TEM), high–resolution transmission electron microscopy (HRTEM), selected area (electron) diffraction (SAED), electron energy loss spectroscopy (EELS) and Energy–dispersive X–ray spectroscopy were collected from JEOL model JEM–ARM–200F microscope operated at 200 kV. X–ray Powder Diffraction (XRD) data were recorded from Rigaku SmartLab using Cu Kα (γ =1.54178 A) radiation. The X–ray photoelectron spectroscopy (XPS) was recorded by an ESCALAB 250Xi XPS system using Mg as the excitation source.

3.3 Electrochemical measurements

The electrochemical tests were carried out in the typical three–electrode system using Autolab electrochemical workstation and CHI 660E workstation in 1M KOH solution. To prepare the electrode, 5 mg of materials were dispersed in the mixture of DI water (750 μL), isopropanol (210 μL), and Nafion solution (40 μL, 5 wt %). After being sonicated for 30 min, homogeneous ink was formed. Then 10 μL ink gradually dripped onto the glassy carbon electrode and dried at room temperature. The saturated calomel electrode (SCE) was used as a reference, while the graphite rod was employed as the counter electrode. Based on the Nernst equation $E(RHE) = E(SCE) + 0.242 + 0.059pH$, the potential of SCE was converted to reversible hydrogen electrode (RHE). The polarization curves were recorded at a scan rate of 1.0 mV s^{-1}. Electrochemical impedance spectroscopy tests were recorded at Autolab electrochemical workstation and Solartron electrochemical workstation (German) with a frequency ranging from 0.01 to 105 Hz.

3.4 Density functional theory calculation

Vienna ab initio simulation package (VASP) was applied for the density functional theory (DFT) calculations.[42] The projected augmented wave (PAW) combined

Perdew–Burke–Ernzerhof (PBE) in the generalized gradient approximation (GGA) to analyze the ion–electron interaction.[43] For the boron–doped ternary pyrite type sulfide system, the cut–off energy for the function was 500 eV while the convergence criteria was 10^{-5} eV in energy and 10^{-2} eV $Å^{-1}$ in force.

The DFT+D3 method was used for describing spin–polarization and van der Waals interactions for the pyrite–type selenide system.[44] Moreover, the GGA + U approach was adopted to correct the coulombic interactions of Ni, Co and Fe, with the corresponding Ueff of 3.4, 3.4, and 3.3 eV, respectively. Similar to the boron–doped ternary pyrite type sulfide system, the cut–off energy and convergence criteria kept the same parameters.

4. Results

4.1 Synthesis of pyrite–type $FeCoNiB_x@Fe_5Co_4Ni_{20}Se_{36}B_x$ for highly efficient OER

In this work, $Fe_5Co_4Ni_{20}Se_{36}B_x$ selenide particles were successfully prepared based on the amorphous $FeCoNiB_x$ to generate the heterostructure ($FeCoNiB_x@Fe_5Co_4Ni_{20}Se_{36}B_x$). To analyze the crystal structure, the XRD Rietveld refinement method was applied to learn the atomic arrangement information.[45] The XRD curve in Figure 1a showed several obvious peaks that belonged to (210), (200), (211), (311), and (321) for the $Fe_5Co_4Ni_{20}Se_{36}B_x$ crystals (JCPDS:88–1711),[46] respectively. The XRD refinement results indicated metal atoms (Fe, Co, Ni) had similar positions while the B atoms mainly existed in the lattice spacing. Some of the B atoms bonded with some metals to form B–M bonds, and other B bonded with Se atoms as shown in Figure 1 B–D. Such a special atomic arrangement structure would promote the modulation of electronic structure.

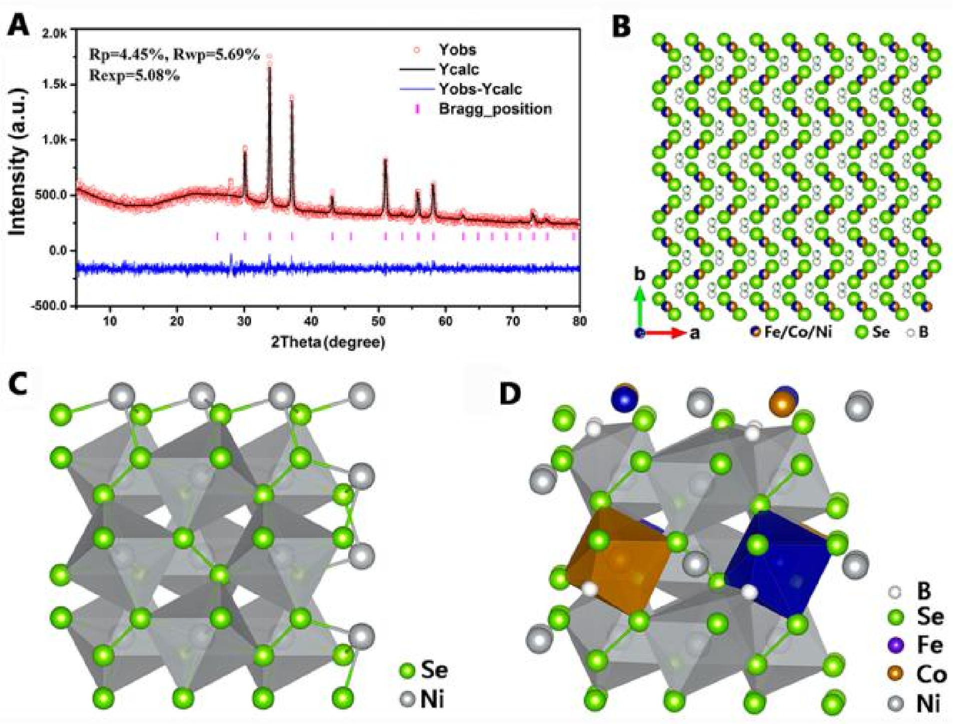

Figure 1. (A) XRD Rietveld refinement and (B) the atomistic model of $Fe_5Co_4Ni_{20}Se_{36}B_x$ crystal. (C, D) Crystal structures of $NiSe_2$ and $Fe_5Co_4Ni_{20}Se_{36}B_x$.

AC–TEM images in Figure 2A clearly showed the crystalline−amorphous structure of the $FeCoNiB_x$@$Fe_5Co_4Ni_{20}Se_{36}B_x$ materials. The $Fe_5Co_4Ni_{20}Se_{36}B_x$ nanoparticles with the size of ~ 50 nm were randomly loaded onto the amorphous $FeCoNiB_x$. SAED pattern in Figure 2B showed the good crystallinity of the $Fe_5Co_4Ni_{20}Se_{36}B_x$, consistent with the XRD curve, while the no diffraction lattice in FFT revealed the typical amorphous structure of the $FeCoNiB_x$ (Figure 2C). The HAADF–STEM and the corresponding EELS images in Figure 2 D, E presented the $Fe_5Co_4Ni_{20}Se_{36}B_x$ particle contained five elements (Fe, Co, Ni, Se, B) and the amorphous $FeCoNiB_x$ had four elements (Fe, Co, Ni, B). Notably, the crystalline−amorphous structure could effectively block the agglomeration of $Fe_5Co_4Ni_{20}Se_{36}B_x$ and provide a 3D accessible structure for the electrolyte, thus facilitating the electrochemical performance.

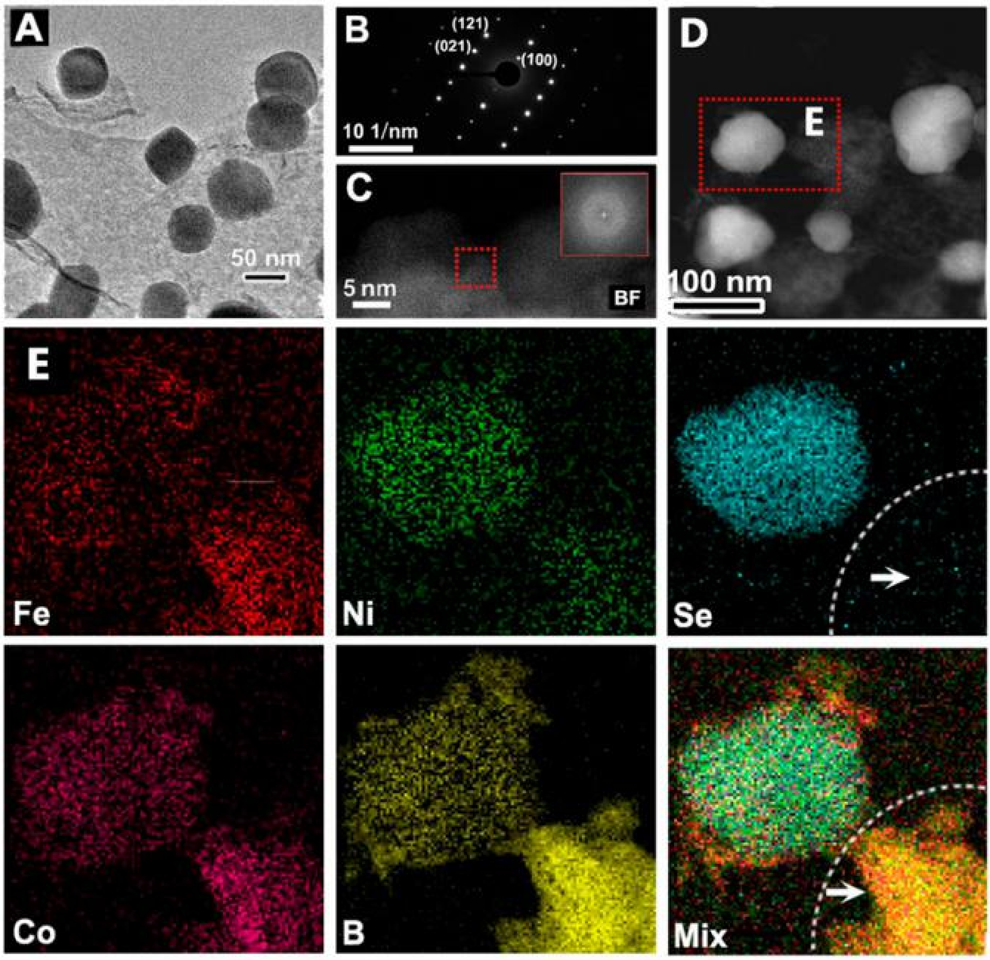

Figure 2. (A) HRTEM and (B) the corresponding SAED pattern of the $Fe_5Co_4Ni_{20}Se_{36}B_x$. (C, D) STEM images of $FeCoNiB_x$ and $FeCoNiB_x@Fe_5Co_4Ni_{20}Se_{36}B_x$. The inserted image in (C) was the FFT. (E) EELS mapping results of the $FeCoNiB_x@Fe_5Co_4Ni_{20}Se_{36}B_x$.

XPS was performed to further analyze the valence state of $FeCoNiB_x@Fe_5Co_4Ni_{20}Se_{36}B_x$. Based on the XPS spectra, the metals in $Fe_5Co_4Ni_{20}Se_{36}B_x$ mainly existed as oxidation states. The peaks at 711.79, 715.26, 725.49, and 729.35 eV (Figure 3A) corresponded to Fe−B, Fe^{3+} $2p_{3/2}$, Fe^{2+} $_{2p1/2}$, and Fe^{3+} $_{2p1/2}$, respectively.[46] The Co 2p spectrum could split into three peaks located at 776.39, 781.68, and 786.75 eV, associated with Co−B, Co^{2+}, and a satellite peak as shown in Figure 3B.[47] The three peaks at 851.6, 856.2, 859.9, and 862.7 eV in Ni $_{2p3/2}$ could be assigned to Ni−B, Ni^{2+}, Ni^{3+} (Figure 3C).[48] The B 1s spectrum result showed two peaks at 185.68 eV and 192.15 eV, which could be assigned as M−B (M = Fe, Co, Ni) and trivalent oxidation states (Figure 36D).[47] The Se 3d XPS spectrum had two peaks at 54.74 eV and 55.73 eV, assigned to Se^{2-} and oxidation state of Se species in the surface of the $FeCoNiB_x@Fe_5Co_4Ni_{20}Se_{36}B_x$ (Figure 3E).[49] These results indicated the electrons could be transferred from the metals to boron and Se atoms. The projected density of states (PDOS) calculated by density functional theory (DFT) found the p orbital of B was overlapped with the orbitals of atoms around B (Figure 3F), including the Se, Fe, Co, and Ni, revealing the B atoms bond with surrounding atoms.

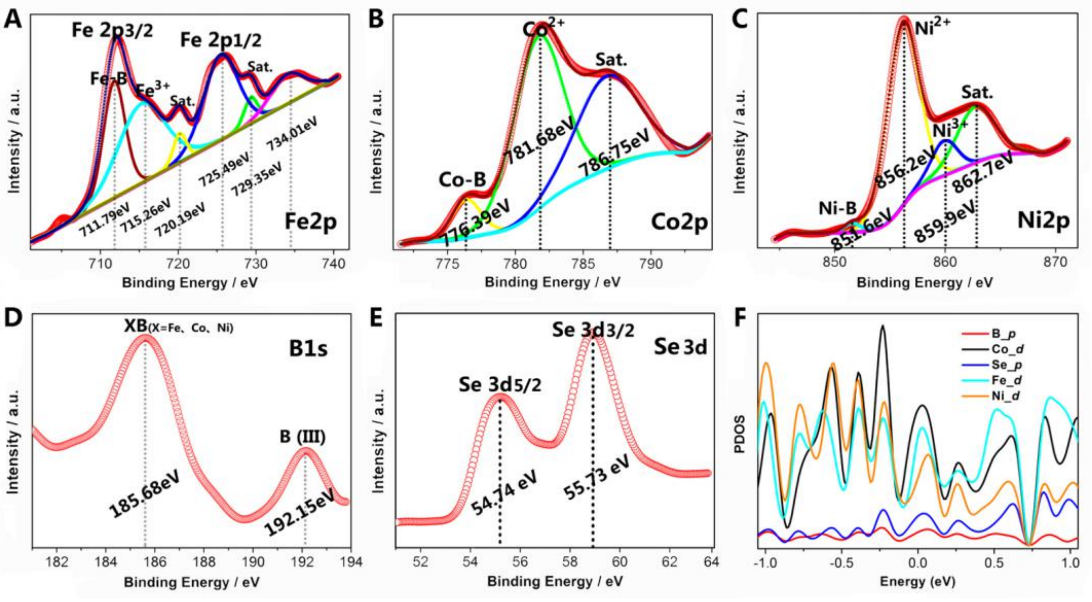

Figure 3. (A–E) XPS spectra of Fe 2p, Co 2p, Ni 2p, B1s, and Se2d. (F) PDOS of $Fe_{0.125}Co_{0.125}Ni_{0.75}Se_2B_{0.2}$.

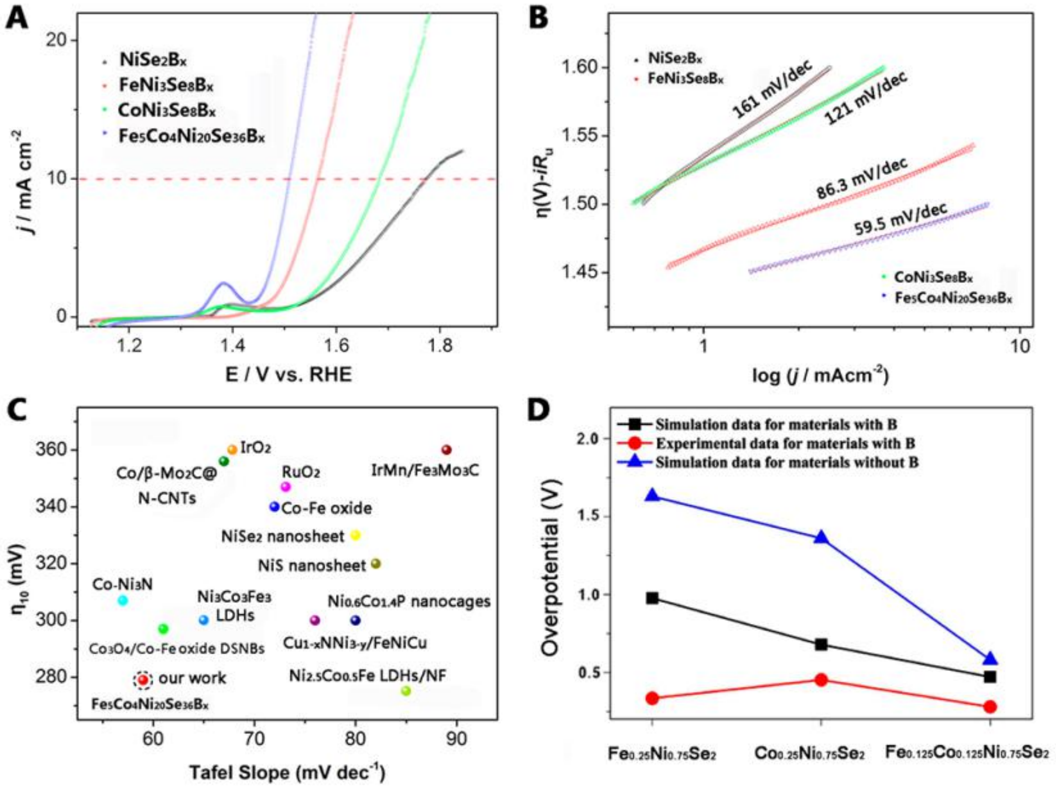

Figure 4. (A) Linear cyclic voltammetry curves of the $NiSe_2B_x$, $FeNi_3Se_8B_x$, $CoNi_3Se_8B_x$, and $Fe_5Co_4Ni_{20}Se_{36}B_x$ samples in 1.0 M KOH under the scan rate of 2 mV s_{-1}. (B) Tafel plots. (C) Comparison the Tafel slopes and overpotentials of

targeted catalyst and other OER catalysts. (D) Comparison of theoretical and experimental results.

The OER performance of the prepared catalysts was tested by a standard three–electrode system in 1.0 M KOH solution. Figure 4A showed that the $Fe_5Co_4Ni_{20}Se_{36}B_x$ exhibited the best OER performance with the overpotential of 279.8 mV under 10 mA cm^{-2}, better than those of $NiSe_2B_x$ (543 eV), $FeNi_3Se_8B_x$ (335 eV), and $CoNi_3Se_8B_x$ (453 mV), respectively. The Tafel slopes in Figure 4B of $Fe_5Co_4Ni_{20}Se_{36}B_x$ was 59.5 mV dec^{-1}, much smaller than those of $FeNi_3Se_8B_x$ (86.3 mV dec^{-1}), $CoNi_3Se_8B_x$ (121 mV dec^{-1}), and $NiSe_2B_x$ (161mV dec^{-1}), respectively, indicating the fast kinetics process. Notably, the $Fe_5Co_4Ni_{20}Se_{36}B_x$ showed excellent OER property among the other catalysts reported recently (Figure 4C). Based on the DFT calculation (Figure 4D), with the increase of metal species, the overpotential of the materials would gradually decrease, and the boron doping could also benefit from reducing the overpotential.

4.2 Synthesis of $Ni_{0.8}Fe_{0.1}Co_{0.1}S_2B_x$@$FeCoNiB_x$ highly efficient OER

In this part, boron–doped ternary pyrite–type sulfides coated by amorphous boride ($Ni_{0.8}Fe_{0.1}Co_{0.1}S_2B_x$@$FeCoNiB_x$, B–TS–H@T–B) was prepared through sulfidation reaction. XRD was performed to analyze the structural information of the obtained crystal. The diffraction results contained several typical peaks which could be assigned as (111), (002), (113) facets of the $Ni_{0.8}Fe_{0.1}Co_{0.1}S_2B_x$ catalyst (Figure 5a).[50] XRD Rietveld refinement further conformed the main phase of the nanocomposite was $Ni_{0.8}Fe_{0.1}Co_{0.1}S_2B_x$ crystal and the corresponding atomic information. Similar to boron–doped polymetallic selenides, the B atoms in $Ni_{0.8}Fe_{0.1}Co_{0.1}S_2B_x$ were mainly embedded in the interstitial site in the lattice as illustrated in the Figure 5b.

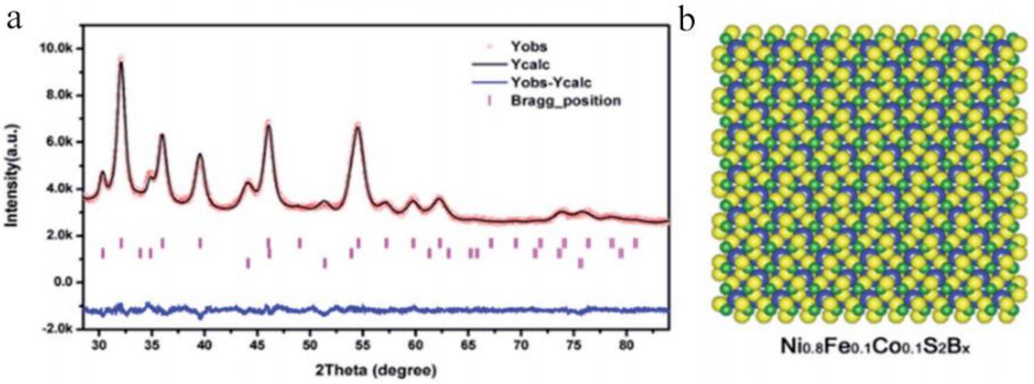

Figure 5. (a) The XRD Rietveld refinement of B–TS–H@T–B. (b) Structural model of the $Ni_{0.8}Fe_{0.1}Co_{0.1}S_2B_x$ catalyst with the S atoms of yellow color, metal atoms (Fe, Co, Ni) of blue color, and the B atoms of green color.

The morphology and atomic arrangement information were collected by AC–TEM and the results were displayed in Figure 6. Enlarged TEM images in Figure 6a–d presented that the amorphous thin layer coated on the surface of the $Ni_{0.8}Fe_{0.1}Co_{0.1}S_2B_x$. HRTEM image in Figure 6e showed the as–prepared boron–sulfide contained different phases of the crystals as the verification of FFT patterns (Figure 6e_1–e_3), which was consistent with the selected area in Figure 6e, corresponding with the XRD refinement results.

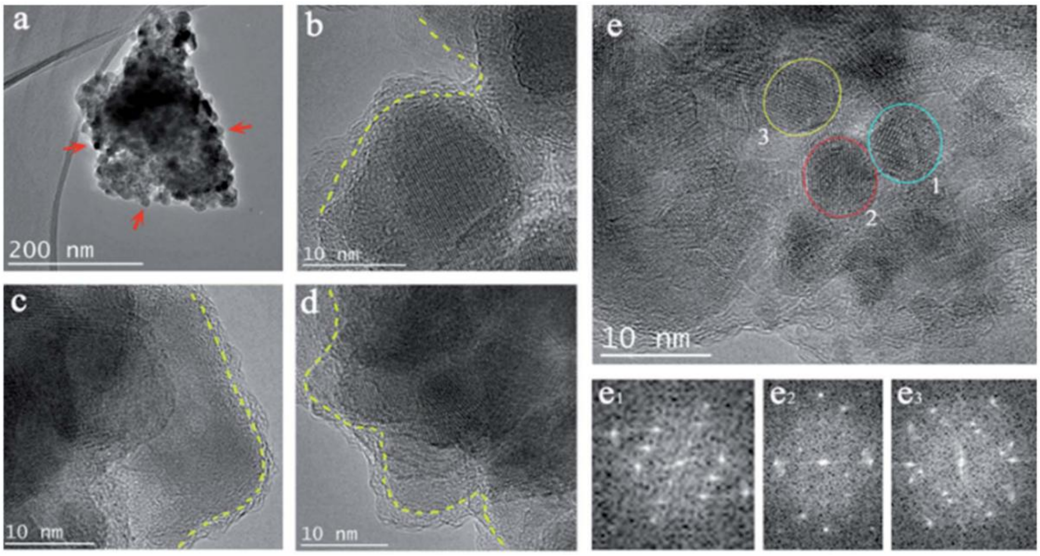

Figure 6. (a–d) Enlarged TEM images of B–TS–H@T–B. (e and e_{1-3}) HRTEM of the material and the corresponding FFT patterns of the selected area in (e).

The STEM image in Figure 5a displayed the morphology of B–TS–H@T–B. This nanocomposite contained numerous particles on the surface. For the crystalline particles, gradually magnified STEM images in Figure 5b, c clearly showed the lattice spacing of ~ 0.27 nm and ~ 0.32 nm, which was consistent with the (002) and (111) planes of $Ni_{0.8}Fe_{0.1}Co_{0.1}S_2B_x$.[51] The lattice angle of (002) and (111) planes was 55°, further explaining the structure of the boron–doped polymetallic sulfides. It should be pointed out that there was a thin amorphous layer on the surface of $Ni_{0.8}Fe_{0.1}Co_{0.1}S_2B_x$, due to the significant difference of the FFT results in Figure 5d, e, exhibiting the crystalline and amorphous heterostructure.

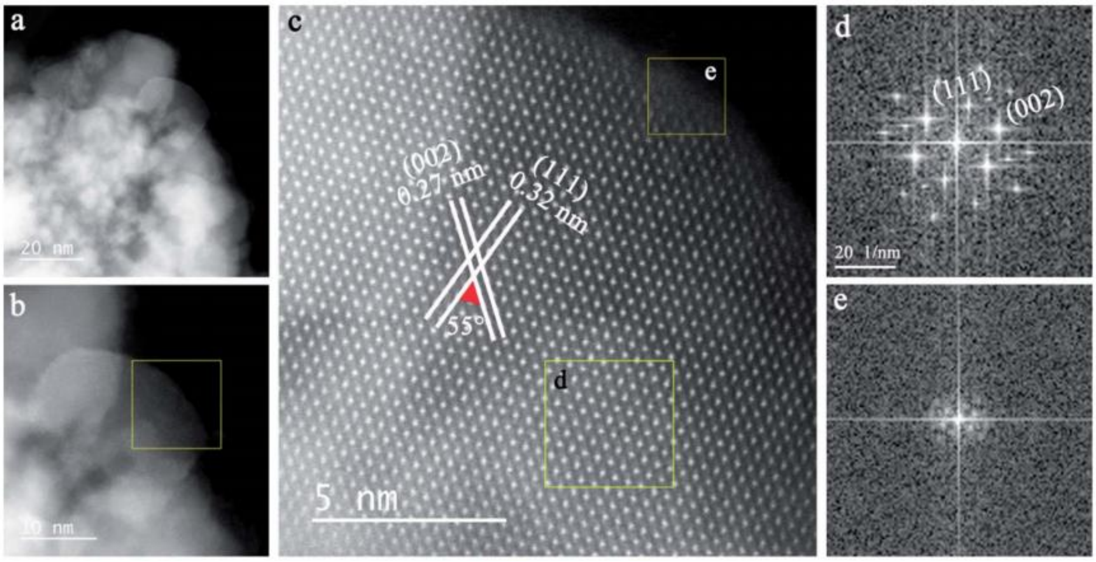

Figure 5. (a) STEM image of the B–TS–H@T–B. (b, c) Magnified STEM images to the atomic level. (d, e) FFT patterns of the selected area in (e).

The chemical valence state of the elements in B–TS–H@T–B was collected by XPS. Survey spectra in Figure 6a found the B2p, S2p, Fe2p, Co2p, and Ni2p elements in the material. The high–resolution XPS spectrum of Fe 2p in Figure 6b were deconvoluted into three peaks at 707.46 eV, 712.78 eV, and 720.38 eV, which would be recognized as Fe^{2+} 2p3/2, Fe^{3+} 2p3/2 and Fe^{2+} 2p1/2, respectively.[46] Additionally, the peaks at 704.92 eV and 708.65 eV were assigned as Fe–B bond and satellite peak. The binding energy positions of the Fe 2p demonstrated the Fe element mainly existed in the oxidation state.[46] Co 2p spectrum in Figure 6c could be fitted into four peaks at 778.99 eV, 780.84 eV, 784.07 eV and 793.99 eV, which could be appointed as Co–B, Co^{2+} 2p3/2, Co^{3+} 2p3/2, and Co^{2+} 2p1/2, respectively.[47] Similarly, the Ni 2p XPS spectrum (Figure 6d) had four fitted peaks at 853.68 eV, 855.35 eV, 859.6 eV and 870.93 eV, which could be assigned as Ni–B, Ni^{2+} 2p3/2, Ni^{3+} 2p3/2 and Ni^{2+} 2p1/2.[48] According to these results, the reduced binding energy represented the loss of electrons from the metals, and partial electrons transferred from the metals to B atoms. The B1s XPS (Figure 6f) had two peaks at 187.22 eV and 192.82 eV, the former was B–M bonds and the latter was contributed of the trivalent state as the adsorbed oxygen.[49] The S 2p spectrum in Figure 6e displayed four peaks at 161.03 eV, 161.97 eV, 163.08 eV, and 163.63 eV, successively belonging to S^{2-}, S 2p3/2, S 2p1/2 and SO$_x$ species.[52] The air environment could result in the surface oxidation of the S atoms on the external positions. Based on the XPS results of the elements, the electrons would transfer from the metallic elements to B and S elements, thus forming abundant high–valence metal atomic sites which were conducive to improving the electrochemical performance of the catalysts.

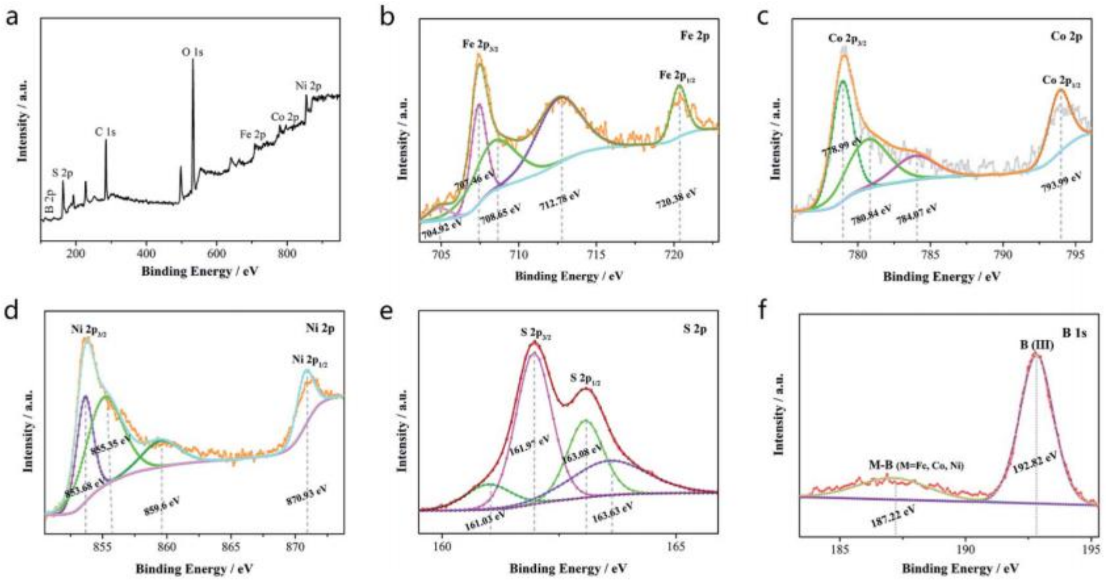

Figure 6. (a) XPS spectrum of B–TS–H@T–B. (b–f) XPS spectrums of Fe 2p, Co 2p, Ni2p, B 1s and S 2p.

The electrochemical performance was tested in 1 M KOH solution with the typical three–electrode system. A linear voltammetry curve was used to record the polarization curve of the samples. As expected, the B–TS–H@T–B presented the best OER activity with the overpotential of 392.4 mV at 50 mA cm^{-2}, which was much lower than that of boron–doped $CoNiS_x$ (459.4 mV, 50 mA cm^{-2}), boron–doped $FeNiS_x$ and boron–doped NiS_x as shown in Figure 7a. Moreover, the target catalyst displayed smaller overpotential even under the higher current density as displayed in Figure 7b. (100 mA cm^{-2} and 150 mA cm^{-2}). The B–TS–H@T–B also had the smallest Tafel slope (64 mV dec^{-1}), while the other samples all had the larger tafel slope (Figure 7c) revealing the faster OER kinetics over the B–TS–H@T–B surface. Furthermore, the B–TS–H@T–B exhibited excellent stability with a retention rate of 76.94% after the 10 h stability test (Figure 7d), revealing the metal doping would contribute to the improvement of activity and stability.

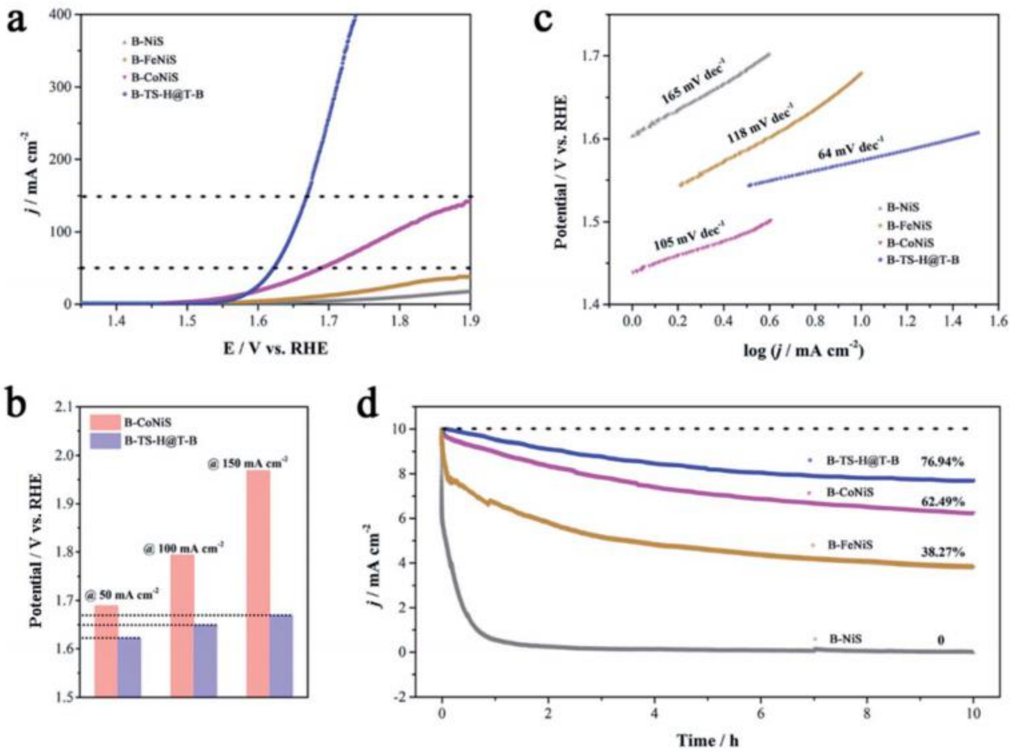

Figure 7. (a) Linear cyclic voltammetry curves of the B–TS–H@T–B, B–NiS, B–FeNiS, and B–CoNiS samples. (b) Overpotentials of the samples under 50 mAcm^{-2}, 100 mAcm^{-2} and 150 mAcm^{-2}, respectively. (c) Tafel slope curves of the four samples. (d) Long–time stability of the as–prepared electrocatalysts.

5. Summary

In this thesis, We focused on designing a facile method to prepare the pyrite–type polymetallic sulfides and selenides for electrocatalytic water splitting. The amorphous membrane coated on the catalysts could enhance the activity of the materials and simultaneously further consolidated the stability of the catalyst. Meanwhile, boron doping could effectively improve the intrinsic electronic structure of the catalyst for the electrocatalytic application. A two–step synthesis process was adopted to obtain the target materials, including the preparation of amorphous borides, and selenization/sulfuration step under megathermal conditions. The presented dissertation successfully establish a facile method to control the synthesis of polymetallic selenides and sulfides with the coating of the amorphous boride layer.

The first goal of the current thesis focused on finding the appropriate preparation methods to from high–quality amorphous borides. We used the wet chemical approach to synthesize the amorphous borides which contained NiB_x, $FeNiB_x$, $CoNiB_x$, and $FeCoNiB_x$ through the reaction between sodium borohydride and metal ion precursors. We used TEM and XRD techniques to analyze the composition and structure of the amorphous borides. Even more, the SAED was also applied to characterize the structure. The synthesized amorphous borides displayed the stacked in layers with a large number of corner and side atoms.

The selenization and sulfuration reaction were carried out in a tubular furnace under the flow of Ar or N_2 gas at above 300 ℃. During the selenization or sulfuration reaction, the vaporized Se or S atoms reacted with the amorphous boride, forming the clusters and then growth to particles. However, the atoms in amorphous boride involved in the reaction would generate the new bond which would drive the surrounding amorphous boride to coat on the surface of the obtained selenide or sulfide particles, finally forming the B–$FeCoNiS_x$@$FeCoNiB_x$ and $FeCoNiSeB_x$@$Fe_5Co_4Ni_{20}Se_{36}B_x$.

B–$FeCoNiS_x$@$FeCoNiB_x$ presented excellent OER activity than B–$FeCoNiS_x$ and $FeCoNiB_x$ with an overpotential of 419 mV vs. RHE under 100 mA cm^{-2} in KOH solution. Additionally, after 10 h stability test, the current density of B–$FeCoNiS_x$@$FeCoNiB_x$ catalyst only dropped 23.06%, much better than B–CoNiS (37.51%) and B–FeNiS (61.73%). The projected density of states (PDOS) results based on the DFT calculation indicated the redistribution of electrons on the metal sites in the B–$FeCoNiS_x$@$FeCoNiB_x$ were conducive to water decomposition.

Additionally, the valence engineered $FeCoNiSeB_x$@$Fe_5Co_4Ni_{20}Se_{36}B_x$ via boron doping exhibited highly efficient OER property. This heterostructure provided a physically anchored structure that could block the aggregation of the $Fe_5Co_4Ni_{20}Se_{36}B_x$ nanoparticles. Moreover, the special heterostructure offered 3D accessible units for the electrolyte during the catalysis. XRD Rietveld refinement result found the boron atoms mainly existed in the interstitial sites of $Fe_5Co_4Ni_{20}Se_{36}B_x$, while the Fe, Co, and Ni atoms co–occupied the same sites. DFT calculation results revealed the boron dopant and binary atomic substitution together contributed to weakening the reaction between the active sites and O intermediates during OER. $FeCoNiSeB_x$@$Fe_5Co_4Ni_{20}Se_{36}B_x$ showed the lowest overpotential of 279.8 mV at 10 mA cm^{-2}, compared to those of $NiSe_2B_x$ (543 mV), $FeNi_3Se_8B_x$ (335 mV), and $CoNi_3Se_8B_x$ (453 mV), respectively.

The work in this thesis illustrated that the pyrite–type sulfides and selenides with boron doping and amorphous layer coating had big potential for energy conversion, due to the special electronic configuration, which may provide a rationally approach for preparing novel electrocatalysts for clean energy application.

6. References

1. Hu, C.; Zhang L.; Gong, J., Recent Progress Made in the mechanism comprehension and design of electrocatalysts for alkaline water splitting. Energy Environ Sci 2019, 12, 2620.

2. You, B.; Sun, Y., Innovative strategies for electrocatalytic water splitting. Acc Chem Res 2018, 51, 1571.

3. Chu, S.; Majumdar, A., Opportunities and challenges for a sustainable energy future. Nature 2012, 488, 294–303.

4. Roger, I.; Shipman, M.; Symes, M., Earth–abundant catalysts for electrochemical and photoelectrochemical water splitting. Nat Rev Chem 2017, 1, 0003.

5. Suen, N.; Hung, S.; Quan, Q.; Zhang, N.; Xu, Y.; Chen, H., Electrocatalysis for the oxygen evolution reaction: recent development and future perspectives. Chem Soc Rev 2017, 46, 337−365.

6. Chu, S.; Majumdar, A., Opportunities and challenges for a sustainable energy future. Nature 2012, 488, 294−303.

7. Zou, X.; Zhang, Y., Noble metal–free hydrogen evolution catalysts for water splitting. Chem Soc Rev 2015, 44 , 5148−5180.

8. Hu, C.; Zhang, L.; Gong, J., Recent progress made in the mechanism comprehension and design of electrocatalysts for alkaline water splitting. Energy Environ Sci 2019, 12, 2620.

9. Shi, Y.; Zhang, B., Recent advances in transition metal phosphide nanomaterials: synthesis and applications in hydrogen evolution reaction. Chem Soc Rev 2016, 45, 1529.

10. Jeon, D.; Park, J.; Shin, C.; Kim, H.; Jang, J. W.; Lee, D. W.; Ryu, J., Superaerophobic hydrogels for enhanced electrochemical and photoelectrochemical hydrogen production. Sci Adv 2020, 6, 1.

11. Lu, H.; Tournet, J.; Dastafkan, K.; Liu, Y.; Ng, Y.; Karuturi, S.; Zhao, C.; Yin, Z., Noble–metal–free multicomponent nanointegration for sustainable energy conversion. Chem Rev 2021, 121, 10271–10366.

12. Reza Gholipour, M.; Dinh, C. T.; Beland, F.; Do, T. O., Nanocomposite heterojunctions as sunlight–driven photocatalysts for hydrogen production from water splitting. Nanoscale 2015, 7, 8187−8208.

13. Uddin, N.; Zhang, H.; Du, Y.; Jia, G.; Wang, S.; Yin, Z., Structural–phase catalytic redox reactions in energy and environmental applications. Adv Mater 2020, 32, 1905739.

14. Li, S.; Gao, Y.; Li, N.; Ge, L.; Bu, X.; Feng, P., Transition metal based bimetallic MOFs and MOF–derived catalysts for electrochemical oxygen evolution reaction. Energy Environ Sci 2021, 14, 1897−1927.

15. Tahir, M.; Pan, L.; Idrees, F.; Zhang, X.; Wang, L.; Zou, J.–J.; Wang, Z., Electrocatalytic oxygen evolution reaction for energy conversion and storage: A comprehensive review. Nano Energy 2017, 37, 136−157.

16. Pan, Q.; Wang, L., Recent perspectives on the structure and oxygen evolution activity for non–noble metal–based catalysts. J Power Sources 2021, 485, 229335.
17. Burke, M.; Enman, L.; Batchellor, A.; Zou, S.; Boettcher, S., Oxygen evolution reaction electrocatalysis on transition metal oxides and (Oxy)hydroxides: activity trends and design principles. Chem Mater 2015, 27, 7549−7558.
18. Peng, L.; Ahmad–Shah, S.; Wei, Z., Recent developments in metal phosphide and sulfide electrocatalysts for oxygen evolution reaction. Chinese J Catal 2018, 39, 1575–1593.
18. Du, J.; Li, F.; Sun, L., Metal–organic frameworks and their derivatives as electrocatalysts for the oxygen evolution reaction. Chem Soc Rev 2021, 50, 2663−2695.
19. Anantharaj, S.; Rao–Ede, S.; Sakthikumar, K.; Karthick, K.; Mishra, S.; Kundu, S., Recent trends and perspectives in electrochemical water splitting with an emphasis on sulfide, selenide, and phosphide catalysts of Fe, Co, and Ni: A review. ACS Catal 2016, 6, 8069−8097.
20. Hunter, B.; Gray, H.; Müller, A., Earth–abundant heterogeneous water oxidation catalysts. Chem Rev 2016, 116, 14120−14136.
21. Siahrostami, S.; Villegas, S.; Mostaghimi, A.; Back, S.; Farimani, A.; Wang, H.; Persson, K.; Montoya, J., A review on challenges and successes in atomic–scale design of catalysts for electrochemical synthesis of hydrogen peroxide. ACS Catal 2020, 10, 7495−7511.
22. Zhang, Y.; Han, C.; Gao, J.; Pan, L.; Wu, J.; Zhu, X.; Zou, J., NiCo–based electrocatalysts for the alkaline oxygen evolution reaction: a review. ACS Catal 2021, 11, 12485−12509.
23. Guo, Y.; Park, T.; Yi, J.; Henzie, J.; Kim, J.; Wang, Z.; Jiang, B.; Bando, Y.; Sugahara, Y.; Tang, J.; Yamauchi, Y., Nanoarchitectonics for transition–metal–sulfide–based electrocatalysts for water splitting. Adv Mater 2019, 31, 1807134.
24. Gao, M.; Zheng, Y.; Jiang, J.; Yu, S., Pyrite–type nanomaterials for advanced electrocatalysis. Acc Chem Res 2017, 50, 2194–2204.
25. Ogawa, S., Magnetic properties of 3d transition ‐ metal dichalcogenides with the pyrite structure. J Appl Phys 1979, 50, 2308.
26. Jiang, H.; He, Q.; Zhang, Y.; Song, L, Structural self–reconstruction of catalysts in electrocatalysis. Acc Chem Res 2018, 51, 2968–2977.
27. He, Z.; Yu, S.; Zhou, Y.; Li, X.; Qu, J., Magnetic field–induced phase–selective synthesis of ferrosulfide microrods by a hydrothermal process: microstructure control and magnetic properties. Adv Funct Mater 2006, 16, 1105−1111.
28. Craig, J.; Vokes, F.; Solberg, T., Pyrite: physical and chemical textures. Miner. Deposita 1998, 34, 82−101.
29. Jin, S., Are metal chalcogenides, nitrides, and phosphides oxygen evolution catalysts or bifunctional catalysts? ACS Energy Lett 2017, 8, 1937.
30. Joo, J.; Kim, T.; Lee, J.; Choi S.; Lee, K., Morphology−controlled metal sulfides and phosphides for electrochemical water splitting. Adv Mater 2019, 31, 1806682.

31. Guo, Y.; Tang, J.; Henzie, J.; Jiang, B.; Xia, W.; Chen, T.; Bando, Y.; Kang, Y.–M.; Hossain, M. S. A.; Sugahara, Y.; Yamauchi, Y. Mesoporous iron–doped $MoS_2/CoMo_2S_4$ heterostructures through organic−metal cooperative interactions on spherical micelles for electrochemical water splitting. ACS Nano 2020, 14, 4141−4152.

32. Yin, J.; Jin, J.; Zhang, H.; Lu, M.; Peng, Y.; Huang, B.; Xi, P.; Yan., C., Atomic arrangement in metal–doped NiS_2 boosts the hydrogen evolution reaction in alkaline media. Angew Chem Int Ed 2019, 58, 18676.

33. Sun, J.; Hu, X.; Huang, Z.; Huang, T.; Wang, X.; Guo, H.; Dai, F.; Sun, D., Atomically thin defect–rich Ni–Se–S hybrid nanosheets as hydrogen evolution reaction electrocatalysts. Nano Research 2020, 13, 2056–2062.

34. Yang, H.; Wang, C.; Zhang, Y.; Wang. Q., Chemical valence–dependent electrocatalytic activity for oxygen evolution reaction: a case of nickel sulfides hybridized with N and S co–doped carbon nanoparticles. Small 2018, 14, 1703273.

35. Nguyen, T.; Su, Y.; Lin, C.; Ting, J., Self–reconstruction of sulfate–containing high entropy sulfide for exceptionally high–performance oxygen evolution reaction electrocatalyst. Adv Funct Mater 2021, 31, 2106229.

36. Liu, H.; He, Q.; Jiang, H.; Lin, Y.; Zhang, Y.; Habib, M.; Chen, S.; Song, L., Electronic structure reconfiguration toward pyrite NiS_2 via engineered heteroatom defect boosting overall water splitting. ACS Nano 2017, 11, 11574.

37. Ni, B.; He, T.; Wang, J.; Zhang, S.; Ouyang, C.; Long, Y.; Zhuang J.; Wang, X.; The formation of $(NiFe)S_2$ pyrite mesocrystals as efficient pre–catalysts for water oxidation. Chem Sci 2018, 9, 2762.

38. Song, Y.; Zhao, X.; Liu, Z., Surface selenium doped hollow heterostructure/defects Co–Fe sulfide nanoboxes for enhancing oxygen evolution reaction and supercapacitors. Electrochim Acta 2021, 374, 137962.

39. Yang, H.; Wang, C.; Zhang, Y.; Wang, Q., Chemical valence–dependent electrocatalytic activity for oxygen evolution reaction: a case of nickel sulfides hybridized with N and S co–doped carbon nanoparticles. Small 2018, 14, 1703273.

41. Chen, J., Li, S., Kumar, V., Lee, P., Carbon coated bimetallic sulfide hollow nanocubes as advanced sodium ion battery anode. Adv Energy Mater 2017, 7, 1700180.

42. Kresse, G.; Furthmuller, J., Efficient iterative schemes for Ab initio total–energy calculations using a plane–wave basis set. Phys Rev B Condens Matter Mater Phys 1996, 54, 11169−11186.

43. Blöchl, P. E., Projector augmented–wave method. Phys Rev B Condens Matter Mater Phys 1994, 50, 17953−17979.

44. Grimme, S.; Antony, J.; Ehrlich, S.; Krieg, S., A consistent and accurate Ab initio parametrization of density functional dispersion correction (DFT–D) for the 94 elements H–Pu. J Chem Phys 2010, 132, 154104.

45. Lin, C.; Tsai, Y.; Johnston, H. E.; Fang, M.; Yu, F.; Zhou, W.; Whitfifield, P.; Li, Y.; Wang, J.; Liu, R.; Attfifield, J.–P., Enhanced photoluminescence emission and thermal stability from introduced cation disorder in phosphors. J Am Chem Soc 2017, 139, 11766−11770.

46. Qiu, B.; Cai, L.; Wang, Y.; Lin, Z.; Zuo, Y.; Wang, M.; Chai, Y., Fabrication of nickel−cobalt bimetal phosphide nanocages for enhanced oxygen evolution catalysis. Adv Funct Mater 2018, 28, 1706008.
47. Kim, J.; Kim, B.; Kim, H.; Kang, K., Recent progress on multimetal oxide catalysts for the oxygen evolution reaction. Adv Energy Mater 2018, 8, 1702774.
48. Zhou, P.; He, J.; Zou, Y.; Wang, Y.; Xie, C.; Chen, R.; Zang, S.; Wang, S. Single–crystalline layered double hydroxides with rich defects and hierarchical structure by mild reduction for enhancing the oxygen evolution reaction. Sci China Chem 2019, 62, 1365–1370.
49. Zuo, Y.; Rao, D.; Li, S.; Li, T.; Zhu, G.; Chen, S.; Song, L.; Chai, Y.; Han, H., Atomic vacancies control of Pd–based catalysts for enhanced electrochemical performance. Adv Mater 2018, 30, 1704171.
50. Sun, Y.; Xu, K.; Wei, Z.; Li, H.; Zhang, T.; Li, X.; Cai, W.; Ma, J.; Fan, H.; Li, Y., Strong electronic interaction in dual–cation incorporated $NiSe_2$ nanosheets with lattice distortion for highly efficient overall water splitting. Adv Mater 2018, 30, 1802121.
51. Sun, R.; Liu, S.; Wei, Q.; Sheng, J.; Zhu, S.; An, Q.; Mai, L., Mesoporous NiS_2 nanospheres anode with pseudocapacitance for high−rate and long−life sodium−ion battery. Small 2017, 13, 1701744.
52. Zhang, G.; Feng, Y.–S.; Lu, W.–T.; He, D.; Wang, C.–Y.; Li, Y.–K.; Wang, X.–Y.; Cao, F., Enhanced catalysis of electrochemical overall water splitting in alkaline media by Fe doping in Ni_3S_2 nanosheet arrays. ACS Catal, 2018, 8, 5431.

7. List of author's publications

7.1 Original publications

Yunpeng Zuo, Dewei Rao, Sainan Ma, Tingting Li, Yuen Hong Tsang, Štěpán Kment, and Yang Chai. Valence engineering via dual–cation and boron doping in pyrite selenide for highly efficient oxygen evolution. ACS Nano, 2019, Volume 13, Issue 10, Pages 11469–11476, https://doi.org/10.1021/acsnano.9b04956. (IF: 15.88)

Yunpeng Zuo, Tingting Li, Ning Zhang, Tianyun Jing, Dewei Rao, Patrik Schmuki, Štěpán Kment, Radek Zbořil, and Yang Chai. Spatially confined formation of single atoms in highly porous carbon nitride nanoreactors. ACS Nano, 2021, Volume 15, Issue 4, Pages 7790–7798, https://doi.org/10.1021/acsnano.1c01872. (IF: 15.88)

Yunpeng Zuo, Dewei Rao, Ning Zhang, Tingting Li, Tianyun Jing, Štěpán Kment, Zdenek Sofer and Yang Chai. Self–reconstruction mediates isolated Pt tailored nanoframes for highly efficient catalysis. J. Mater. Chem. A, 2021, Volume 9, Pages 22501–22508, https://doi.org/10.1039/D1TA05411B. (IF: 12.732)

Tingting Li, Tianyun Jing, Dewei Rao, Xiaotian Jia, Yunpeng Zuo, Štěpán Kment and Radek Zbořil. In situ coating amorphous boride on ternary pyrite–type boron sulfide for highly efficient oxygen evolution. J. Mater. Chem. A, 2021, Volume 9, Pages 12283–12290, https://doi.org/10.1039/D0TA10633J. (IF: 12.732)

7.2 Conference presentations

Self–reconstruction mediates isolated Pt tailored nanoframes for highly efficient catalysis

(poster presentation in “InfoSummit–International Conference on Information Technology Materials” Conference, Chengdu, China, 2021)

Valence engineering in pyrite selenide for highly efficient oxygen evolution

(oral presentation in NANOCON Conference, Brno, Czech Republic, 2021)

8. Souhrn

V této diplomové práci jsme se zaměřili na návrh jednoduché metody přípravy polymetalických sulfidů a selenidů pyritového typu pro elektrokatalytické štěpení vody. Amorfní membrána potažená na katalyzátorech by mohla zvýšit aktivitu materiálů a současně dále konsolidovat stabilitu katalyzátoru. Mezitím by dopování borem mohlo účinně zlepšit vnitřní elektronovou strukturu katalyzátoru pro elektrokatalytickou aplikaci. Pro získání cílových materiálů byl přijat dvoustupňový proces syntézy, včetně přípravy amorfních boridů a kroku selenizace/sulfurace za megatermálních podmínek. Předkládaná disertační práce úspěšně zavádí snadnou metodu řízení syntézy polymetalických selenidů a sulfidů s povlakem amorfní boridové vrstvy.

První cíl této práce byl zaměřen na nalezení vhodných metod přípravy z kvalitních amorfních boridů. Použili jsme mokrý chemický přístup k syntéze amorfních boridů, které obsahovaly NiB_x, $FeNiB_x$, $CoNiB_x$ a $FeCoNiB_x$ prostřednictvím reakce mezi borohydridem sodným a prekurzory kovových iontů. K analýze složení a struktury amorfních boridů jsme použili techniky TEM a XRD. Ještě více, SAED byl také použit k charakterizaci struktury. Syntetizované amorfní boridy zobrazily naskládané vrstvy s velkým počtem rohových a bočních atomů.

Selenizační a sulfurační reakce byly prováděny v trubkové peci pod proudem plynného Ar nebo N_2 při teplotě nad 300 °C. Během selenizační nebo sulfurační reakce odpařené atomy Se nebo S reagovaly s amorfním boridem, vytvořily shluky a poté se rozrostly na částice. Atomy v amorfním boridu zapojené do reakce by však vytvořily novou vazbu, která by přiměla okolní amorfní borid k potažení povrchu získaných selenidových nebo sulfidových částic a nakonec by vytvořily $B–FeCoNiS_x@FeCoNiB_x$ a $FeCoNiSeB_x@Fe_5Co_4Ni_{20}Se_{36}B_x$.

$B–FeCoNiS_x@FeCoNiB_x$ vykazoval vynikající aktivitu OER než $B–FeCoNiS_x$ a $FeCoNiB_x$ s overpotenciálem 419 mV vs. RHE pod 100 mA cm^{-2} v roztoku KOH. Navíc po 10 hodinách testu stability proudová hustota katalyzátoru $B–FeCoNiS_x@FeCoNiB_x$ klesla pouze o 23,06 %, což je mnohem lépe než u B–CoNiS (37,51 %) a B–FeNiS (61,73 %). Výsledky projektované hustoty stavů (PDOS) založené na výpočtu DFT ukázaly, že redistribuce elektronů na kovových místech v $B–FeCoNiS_x@FeCoNiB_x$ vedla k rozkladu vody.

Navíc valenčně upravený $FeCoNiSeB_x@Fe_5Co_4Ni_{20}Se_{36}B_x$ prostřednictvím dopování borem vykazoval vysoce účinnou vlastnost OER. Tato heterostruktura poskytla fyzicky ukotvenou strukturu, která by mohla blokovat agregaci nanočástic $Fe_5Co_4Ni_{20}Se_{36}B_x$. Speciální heterostruktura navíc nabízela 3D přístupné jednotky pro elektrolyt během katalýzy. Výsledek upřesnění XRD Rietveld zjistil, že atomy boru existovaly hlavně v intersticiálních místech $Fe_5Co_4Ni_{20}Se_{36}B_x$, zatímco atomy Fe, Co a Ni společně obsadily stejná místa. Výsledky výpočtu DFT odhalily, že dopant boru a binární atomová substituce společně přispěly k oslabení reakce mezi aktivními místy a O meziprodukty během OER. $FeCoNiSeB_x@Fe_5Co_4Ni_{20}Se_{36}B_x$ vykázal nejnižší nadpotenciál 279,8 mV při 10 mA cm^{-2} ve srovnání s NiSe2Bx (543 mV), $FeNi_3Se_8B_x$ (335 mV) a $CoNi_3Se_8B_x$ (453 mV).

Práce v této práci ukázala, že sulfidy a selenidy pyritového typu s dopováním borem a povlakem amorfní vrstvy měly velký potenciál pro přeměnu energie díky speciální elektronické konfiguraci, která může poskytnout racionální přístup k přípravě nových elektrokatalyzátorů pro aplikace čisté energie.